Development of a robust output-only strain based damage detection technique for wing-like structures, requiring a minimum number of sensors

by

Ulrich Spangenberg

Submitted in partial fulfilment of the requirements for the degree

Master of Engineering

In the Faculty of Engineering, Built Environment and Information Technology

University of Pretoria

Pretoria

2009

Development of a robust output-only strain based damage detection technique for wing-like structures, requiring a minimum number of sensors

by

Ulrich Spangenberg

Supervisor: Prof. P.S. Heyns
Department: Mechanical and Aeronautical Engineering
Degree: Master of Engineering

Summary

In recent years more emphasis has been placed on in-situ condition based monitoring of engineering systems and structures. Aerospace components are manufactured from composite materials more often. Structural health monitoring (SHM) systems are required in the aerospace industry to monitor the safety and integrity of the structure and will ensure that composites reach its full potential within the industry. Damage detection techniques form an integral part of such SHM systems.

With this work a damage detection technique is developed for intended eventual use on composite structures, but starting first on isotropic structures. The damage mechanism that is of interest is delamination damage in composites. A simple numerical equivalent is implemented here however. Two damage indicators, the strain cumulative damage factor (SCDF) and the strain-frequency damage level (SFDL) are introduced. The respective damage indicators are calculated from output-only strain and acceleration response data.

The effectiveness of the system to detect damage in the structure is critically evaluated and compared to other damage detection techniques such as the natural frequency method. The sensitivity to damage and performance of both these indicators is examined numerically by evaluating two deterministic damage cases. The numerical study is enhanced through the use of an updated finite element model. The minimum number of sensors capable of detecting the presence and locate damage spatially is determined from numerical simulations. Monte Carlo type analysis is performed by letting the damaged area vary stochastically and calculating the respective damage indicators.

The model updating procedure from measured mobility frequency response functions (FRFs) is described. The application of the technique to real structures is examined experimentally. Two test structures with two different damage scenarios are examined.

The spatial location and presence of damage can be established from both the SCDF and SFDL values, respectively. The spatial location obtained from the SCDF values corresponded to the known damage location for both the numerical and experimental study. The SFDL proved to be more sensitive than the natural frequency method and could be used to calculate the level of damage within the structure.

Acknowledgements

I wish to express my sincere gratitude to:

The University of Pretoria, for providing the facilities, funds and opportunity to complete my research.

Prof. Heyns, my study leader, who provided guidance and shared his knowledge during my research. Thank you for all your encouragement, hours spent on thinking and assisting me in producing the final product.

My parents, for your help, support and encouragement throughout my studies.

My Sasol laboratory colleagues, for all those who had an open door and whom I could approach for help and your unconditional assistance.

Table of Contents

List of Figures

List of Tables

Nomenclature List

Symbol	Description	Unit
English letter and Symbols		
A	Area	m^2
Ar	Aspect ratio of a wing	
a	Crack size	m
b	Wing span	m
b	Base length	m
C	Constant of the Paris law equation	$m/cycle/(Pa.m^{1/2})^m$
C	Damping matrix	$N.s/m$
c	Chord length	m
c	Damping coefficient	$N.s/m$
E	Young's modulus	Pa
F	Forcing vector	N
f	Frequency	Hz
G	Shear modulus	Pa
H	Transfer function matrix	$Response/N$
h	Height	m
I	Area moment of inertia	m^4
i	Complex operator $\sqrt{-1}$	
K	Stiffness matrix	N/m
K	Stress intensity factor	$Pa.m^{1/2}$
k	Stiffness	N/m
l	Length	m
M	Bending moment	$N.m$
M	Mass matrix	kg
m	Mass	kg
m	Constant in the Paris law equation	
N	Number of cycles	$cycle$
S	Wing planform area	m^2
t	Thickness	m
v	Deflection of a beam	m
v	Velocity	m/s
w	Width	m
X	Response vector	
$\ddot{x}$	Acceleration response	m/s^2
y	Distance from the neutral surface	m
y	y-axis value	m

Symbol	Description	Unit
Greek letters		
γ	Shear strain	
γ	Coefficient of variation	
Λ	Sweep angle	*rad or* °
ε	Strain	
θ	Rotation angle	*rad or* °
κ	Curvature	m^{-1}
λ	Taper ratio	
λ	Wavelength	m
μ	Mean value	
ν	Poisson's ratio	
ρ	Density	kg/m^3
σ	Stress	Pa
σ	Standard deviation	
ω	Circular frequency	rad/s
Subscripts		
a	Acceleration	
ana	Analytical	
d	Damaged structure	
e	Element	
f	Fuselage	
f	Input force (in context of FRF)	
i	Measurement location	
l	Laminate	
$meas$	Measurement line	
n	Natural modes	
num	Numerical value	
o	Undamaged structure	
r	Root of the wing	
r	Modal properties (in context of modal analyses)	
rem	Remaining part	
sg	Strain gauge	
$sound$	Sound	
t	Tip of the wing	
tot	Total	
$trap$	Trapezium	
$tria$	Triangle	
$upper$	Upper limit	
w	Wing	
x	x-direction	
xy	xy-plane	
y	y-direction	

Chapter 1: Introduction and literature study

1.1 Introduction

Structural health monitoring (SHM) of engineering structures and systems in the aerospace/space and automotive industry has been receiving increased attention. In the US, initiatives for research and development of new practices and techniques for structural health monitoring of bridges have started. The Japanese have also launched programmes for structural health monitoring of their infrastructure. The European initiatives focus more on the structural health monitoring of their transportation infrastructure (Wenzel and Pichler, 2005).

Health monitoring of structures are required to ensure their integrity (Staszewski, Boller and Tomlinson, 2004). Structural health is directly related to structural performance and therefore safety. SHM can be used to identify whether a structure needs to be repaired immediately or if repairs can be postponed. Repairs are either directly or indirectly related to cost. It is, for example, directly related to cost through repairs and manufacturing of new parts. Indirect cost is related to downtime of a machine or loss of use of infrastructure (Wenzel et al., 2005). Damage detection techniques form an integral part of a health monitoring system.

Current damage detection methods used for condition assessment of structures are either visual or localised methods (Teughels, Maeck and De Roeck, 2002). These methods include acoustic or ultrasonic, magnetic field, radiography, eddy current and thermal field methods (Lauwagie, Sol and Dascotte, 2002). One disadvantage of local methods is that they are usually limited to detecting damage near or on the surface of the structure (Teughels et al., 2002; Dynamic Design Solutions NV, 2008a; Lauwagie et al., 2002). Other disadvantages of these methods are that the location of the damage has to be known a priori and the part of the structure to be inspected should be accessible to maintenance workers.

Civil engineers, concerned with the safety and maintenance of infrastructure, are aware of the limitations of their current inspection and damage detection methods. There is a need for health monitoring systems that can support the current methods and maybe even overcome their limitations (Wenzel et al, 2005). One of the proposed methods, that may be able to support and possibly overcome the limitations of the current methods, is global damage detection techniques. Global damage detection techniques are non-destructive and are based on the fact that the vibration characteristics of a structure change due to the presence of damage (Pandey, Biswas and Samman, 1991, Teughels et al., 2002, and Maeck, 2003).

There is a growing need in the development of UAVs to have these aircraft fly for super long endurance flights, up to five years (Maneschijn, 2008). UAVs are also designed to be lightweight and are very often manufactured partly from composite materials. The

components manufactured from composites have to be inspected regularly and monitored for the development of damage, specifically delamination damage, to ensure a long service life (Borchardt, 2004).

While wings are currently often only partly manufactured from composites, reduced weight requirements will most likely lead to the wings and tails having to be fully manufactured from composites (Borchardt, 2004). Since some of these UAVs may not land for a few years, damage detection must rely on technology that can be integrated in the wings as well as the UAV's payload bay.

The main damage types that need to be detected in UAVs after manufacture and flights are cracks, delaminations in the skin, debonding between skin and core and defects in the core. The most common type of damage is delamination damage. Due to the fact that the bonds exist underneath the surface of the structure, it is very difficult to detect it visually (Grouve, Warnet, De Boer, Akkerman and Vlekken, 2008).

Aerospace structures are exposed to ambient excitations whilst in-flight. New technologies are arising that make strain based structural health monitoring systems more relevant. There is a definite need to develop a global strain based damage detection method based on output-only data to provide health monitoring of aerospace structures during operation.

These statements motivates the decision to it was decided to develop a structural damage detection technique for use in UAVs. Such a damage detection technique is developed by using output-only strain and acceleration responses. The technique is however first developed on isotropic structures to validate the application and method with the prospect of applying it to fully composite wings. For this system to be integrated into the structure of the UAV it is necessary for it to be small and lightweight with the minimum equipment required. The sensors selected to monitor the dynamics of the structure have to be carefully chosen. The technique therefore focuses on the ideal location of the sensors as well as optimising the number, type and distribution of different sensors to indicate the presence of damage. The main type of damage that is investigated is delamination damage within composites. A numerical equivalent of this type of damage is implemented in a numerical and experimental study.

1.2 Literature study

1.2.1 Global damage detection techniques

It was stated in paragraph 1.1 that global damage detection techniques are based on the fact that the vibration characteristics of a structure change due to the presence of damage. It is generally assumed that damage in the structure causes a decrease in structural stiffness and this change in stiffness becomes apparent in the vibration characteristics of the structure. The natural frequencies and mode shapes are the most common parameters used for damage detection (Teughels et al., 2002). One disadvantage of using natural frequencies is the fact that it is difficult to predict the spatial location of the structural damage from these frequencies. Mode shape

information should be used to uniquely locate an asymmetric damage pattern in symmetrical structures (Maeck et al., 2000). The mode shapes are therefore also monitored to be used in conjunction with the natural frequencies and obtain spatial information on the location of damage. The damping ratio can also be used to identify the presence of damage. As the structure starts to crack, due to damage, the cracks form new surfaces. These new surfaces cause more friction which in turn contributes to damping and thus the damping ratio will increase (Abdel Wahab and De Roeck, 1999). Modal testing is used primarily to determine the natural frequencies, the mode shapes and damping of a structure. It has been used to determine the dynamic characteristics of jet engine blades, rotating machinery and civil engineering structures (Wu, 2004).

Rytter (1993) classifies damage detection into the following four categories:

- Level 1 – Detection: The presence of damage is indicated by the method.
- Level 2 – Localisation: The probable damage location is given by the method.
- Level 3 – Assessment: The information on the size of the damage is given by the method.
- Level 4 – Consequence: The method can predict the safety of the structure for a given damage state.

The aim of global damage detection techniques is directed mainly at the first two damage detection objectives. Various methods have been proposed by different authors to detect and locate damage globally. Some of the methods include looking at modal curvatures, changes in strain energy and the use of flexibility to represent damage and its location (Teughels et al., 2002). The Modal Assurance Criterion (MAC) and the Co-ordinate Modal Assurance Criterion (COMAC) were investigated for their respective sensitivity to damage and it was found that both criteria are not very sensitive to damage in a structure (Pandey et al. (1991) and Abdel Wahab et al. (1999)).

A time response based structural damage detection technique that is able to perform the four main objectives of damage detection was developed by Ngwangwa (2004). This technique was shown to be as much as three times more sensitive to damage than the conventional frequency shift technique. It uses measured operational time responses and compares it to predicted time response through the use of a test statistic. The predicted time responses, for a varying level of damage, are obtained from an updated FE model, thus a time response and test statistic is obtained for a given level of damage. If the value of the measured test statistic is close to the value of a predicted test statistic, the level of damage is estimated from the known level of damage associated with that specific predicted test statistic. Life predictions can then be made from the estimated level of damage by applying the Paris law equation.

Lauwagie et al. (2002) as well as Abdel Wahab, De Roeck, and Peeters (1999) divide damage detection, by means of monitoring modal parameters, into two categories. The first is called “the response-based approach” and the second is termed “the model-based approach”.

1.2.1.1 Response-based approach

In the response-based approach, the modal parameters of the undamaged and damaged structures are compared. This approach is very time efficient, with the disadvantage that the modal parameters before damage should be known and available. Another disadvantage of using this method is that all the different possible damage scenarios at different locations on the structure need to be taken into account (Abdel Wahab et al., 1999).

Pandey et al. (1991) suggested the use of modal curvatures to identify and locate damage in structures. The use of modal curvatures is considered a response-based approach. A cantilever and simply supported beam were used to demonstrate the use of the modal curvatures. It was shown that the absolute changes in the modal curvatures are a maximum in the region of damage.

It is assumed that the damage causes a change in the bending stiffness (the product of area moment of inertia and Young's modulus (EI)) of the structure and therefore the absolute change in modal curvature increases at the damage location. If the damage is increased, the bending stiffness will reduce even further, and the absolute change in modal curvature will increase. The level of damage can therefore be determined from this increase. The curvature is proportional to the bending strain and it is possible to obtain the modal curvature from strain measurements instead of displacements or accelerations (Pandey et al., 1991).

If mode shapes are considered, the modal displacements have a low sensitivity to damage (Pandey et al., 1991; Dynamic Design Solutions, 2008a). The modal curvatures have a much higher sensitivity than the modal displacements. The modal curvatures are very well suited to one dimensional problems of which one dimensional representations and finite element (FE) models can be constructed.

Modal curvatures were used in an analysis performed by Lauwagie et al. (2002). The modal curvatures are determined from the modal displacements by applying a central difference approximation. When modal curvatures are used, the modal curvatures can only provide unscaled stiffness profiles. In order to obtain the absolute scaling of the stiffnesses it is necessary to incorporate the natural frequencies in the analysis.

In the literature the modal curvatures are usually derived from the displacement mode shapes by means of the central difference approximation. Although this appears to be a promising indicator, one of the biggest challenges that remain is to determined accurate modal curvatures from experimental data (Maeck, 2003).

The direct stiffness calculation technique (Maeck, 2003) requires modal curvatures. These curvatures are calculated from displacement mode shapes. The problem with deriving modal curvatures in this manner is the fact that noise in the measurements is amplified. It is therefore necessary to smooth the displacement mode shapes and its derivatives and for this purpose the mixed approach was developed. The mixed approach can directly calculate the curvatures and there is no need to mathematically manipulate the displacement mode shapes. The mixed approach was proven to perform well in

comparison with the central difference scheme, which is mostly used in literature. The technique used to smooth the mode shapes in the mixed approach can be considered as a general smoothing technique for mode shapes and its derivatives.

Abdel Wahab et al. (1999) investigated and validated the use of modal curvatures to detect damage in concrete structures. A potential problem in using modal curvatures of each mode to identify damage was foreseen, as higher modes indicate more peaks corresponding to possible damage locations than expected. A solution to this problem was proposed in the form of a new indicator, termed "curvature damage factor" (CDF). This new indicator is used to average, and thus summarise, the curvature mode shape information into one single number at each measurement point or node of a finite element (FE) model. This method of looking at the average of the modal curvatures was applied practically to the Z24 highway bridge in Switzerland. The CDF is a good indicator of the location of the damage in a structure especially when there are several faults present (Abdel Wahab et al., 1999).

Two damage sensitive indices, the bending moment and residual strain mode shape index, were proposed and investigated by Li, Cheng, Yam and Wong (2002). Both of these indices are derived from strains within the material. The bending moment index is defined in such a manner that it does not require strain information of the undamaged structure. It is a very intuitive way of locating the damage and is easy to implement on a structure. The residual strain mode shape requires information of the undamaged structure. It is defined as the difference at a measurement node between the damaged and undamaged case, which in turn is normalised by the maximum difference between the two cases. The damage in the structure is identified from the peaks of the residual strain mode shape index as defined in equation 1.1 for the r^{th} mode (adapted from Li et al., 2002).

$$\Delta\bar{\varepsilon}_{r,x} = \frac{\left|\Delta\varepsilon_{r,x}(x,y)\right|}{\max\left|\Delta\varepsilon_{r,x}(x,y)\right|} \tag{1.1}$$

with,

$$\Delta\varepsilon_{r,x}(x,y) = \varepsilon_{r,x}(x,y) - (\varepsilon_u)_{r,x}(x,y) \tag{1.2}$$

Equations 1.1 and 1.2 $\varepsilon_{r,x}$ represent the strain mode shape in the x-direction of natural mode r and the difference in strain mode shape is determined with respect to the undamaged strain $(\varepsilon_u)_{r,x}$.

During the numerical validation, the damage was simulated by reducing the thickness of the structure at the damaged location. Both indices could correctly indentify the locations of single and multiple damage areas. The residual strain mode shape index appeared to be more robust as it could easily detect damage even if it is located at a nodal line of a mode. Good correlation was shown between numerical prediction and experimental measurements and both indices proved to be effective in locating damage in a structure (Li, et al, 2002).

The only drawback of this method is the fact that a large number of sensors are needed to identify the damage if it is totally random in nature. Otherwise prior knowledge of probable damage locations should be available and the sensors should be located in these areas.

Farrar and Jauregui (1996) performed an investigation in which five response-based damage identification methods were compared to one another. The comparison was performed by applying the different methods to a common set of damage scenarios. The data for these damage scenarios were obtained from experimentally measured and numerically generated responses from the I-40 Bridge over the Rio Grande in Albuquerque, NM. These methods required the data from the undamaged as well as damaged state of the bridge. All five methods were able to detect damage at its most severe and when the stiffness of the bridge was most adversely affected by the damage. The Damage Index Method was considered to perform the best in all the studied cases. The Mode Shape Curvature method was shown to also perform well. This method could indicate the presence of damage for the studied cases with the exception of two cases.

1.2.1.2 Model-based approach

The second category ("the model-based approach") is an approach where the model parameters of a mathematical model, usually an FE model, are optimised to have correlation between the model and the measured responses. The optimised model parameters are examined to assess the damage in the structure. This approach is calculation intensive and time consuming, but has the advantage that only the modal properties of the damaged structure are needed.

According to Dynamic Design Solutions NV (2008a) the FE model updating based approaches can be classified as either direct or differential. With the direct approach test, data from the undamaged structure is not required. The disadvantage of the direct approach is the fact that the observed inconsistencies can be either due to the damage in the structure or a mismatch between the FE model and the test data. The differential approach uses the updated model of the initially undamaged and damaged structures to localise the damage. The advantage of this approach is the fact that the mismatch between the FE model and the test data can be distinguished from the damage. The disadvantage is that test data before and after damage is required.

It has become standard practice to use an FE model to represent the mathematical or analytical model (Wu, 2004). A mathematical model is constructed and it is used to approximate the structure and its dynamics. In order to perform further dynamic simulations the mathematical model of the system or structure should be validated or updated. One way in which this can be accomplished is by means of an experimental modal analysis. The results from the modal analysis are compared to the mathematical model's results and the model is updated or validated. The process in which the analytical model is updated is commonly known as model updating. Iterative methods have been used to update the model by updating physical model variables (such as Young's modulus, thickness, mass, etc.). This method is iterative as it minimises the difference between the model and the experimental results by means of an optimisation

algorithm. In recent years these sensitivity based finite element model updating techniques have been used for damage assessment (Teughels et al., 2002).

Wenzel et al. (2005) and Teughels et al. (2002) showed that model updating can be used for damage detection which can be used for structural health monitoring. The method of damage detection by means of model updating is described as follows and is shown as a flowchart in Figure 1-1:

1. Tuning a finite element model to the undamaged structure by means of model updating (this is the reference model).
2. Tuning the reference finite element model to the damaged structure by means of model updating (this is the damaged model).
3. The parameters that were tuned to obtain the damaged model can then be used to determine the location of the damage. This can be done by plotting the distribution of the updated model parameters and to see where the greatest changes have occurred.

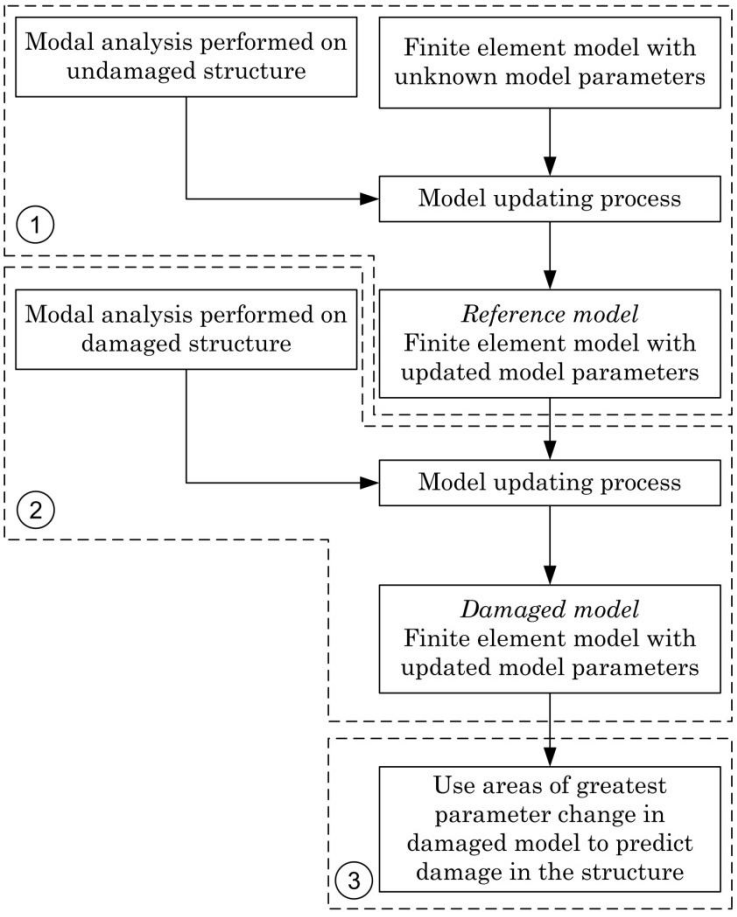

Figure 1-1: Flowchart of the damage detection process by means of model updating (Wenzel et al., 2005)

Teughels et al. (2002) demonstrated this global method to locate damage in a reinforced concrete beam. This model updating method was also applied, with success, to the Z24 highway bridge in Switzerland (Teughels and De Roeck, 2004). The FE model updating method is an efficient vibration-based damage detection technique (Wenzel et al, 2005).

A non-destructive damage detection technique, by means of model updating of an FE model, was applied by Kharrazi, Ventura, Brincker and Dascotte (2002). The structure used for this investigation was a three dimensional four story steel frame. An FE model of the four story structure was constructed. A test setup of the frame was built and damage was introduced into the structure by removing brace beams and by taking out joint connections. Modal analyses were performed on the undamaged and damaged structures. Natural frequencies as well as mode shapes were used to update the model. The undamaged data was used to update the FE model to a reference state. The FE model was updated for a second time with the modal data of the different damage scenarios. The parameter values such as Young's modulus as well as the cross sectional areas and moments of inertia of the beam elements were allowed to be updated. By comparing the elements and the parameters that were updated after the introduction of damage to the reference state, damage could be detected. The predicted damage locations corresponded well to the known damage locations. If the damage introduced in the structure is not large enough to produce an identifiable change in the modal properties, it is not possible to identify or locate the damage.

Lauwagie et al. (2002) discusses the application of the model-based approach to identify the homogeneity of an undamaged beam and to identify the damage pattern within the beam after the introduction of damage. An FE model updating routine was used to identify the longitudinal stiffness properties of a beam and it was shown that it is indeed possible to identify the stiffness properties from the natural frequencies and the modal curvatures. A realistic stiffness distribution for both an undamaged and damaged beam can be obtained from the FE model updating procedure. This procedure was applied to both numerically generated and experimentally measured data and the procedure proved to be stable in both cases (Lauwagie et al., 2002).

1.2.2 Modal analysis

The methodology of measuring the dynamic behaviour of structures and using these measurements to make conclusions on their load carrying capacities and to check modelling assumptions, is very old (Wenzel et al., 2005). Wenzel et al. (2005) mention the application of a free oscillation test as early as 1941.

Experimental modal analysis, for short modal analysis, is used to construct an accurate mathematical model of a structure. By performing a modal analysis, a theoretical or mathematical model is fitted to experimentally measured data, usually in the form of a frequency response function (FRF). The FRFs are constructed from displacement, velocity or acceleration together with force measurements. The modal properties of the system can subsequently be derived from these FRFs by performing an experimental modal analysis (Ewins, 1995). In the following we will generically refer to displacement FRFs, since velocity or acceleration based FRFs can always be used to find the displacement FRFs.

Mode shapes, modal damping ratios and natural frequencies can be obtained from the FRFs and are referred to as the modal properties of the structure. The natural frequencies of a structure can be determined directly from the FRF plots. When a

structure is excited and the forcing function corresponds to the natural frequency of the system, a sharp peak is observed on the FRF. The phase of the response also changes by 180° as the forcing function crosses the natural frequency (Rao, 2004).

The modal analysis, and therefore the FRF measurements, can be used for a wide variety of applications. One of these applications is to use these measurements to validate a mathematical (or FE) model and to check modelling assumptions (Ewins, 1995). Both the natural frequencies as well as the mode shapes can be used to update the FE model. The natural frequencies can be measured with an error around 1%, but the measurements on the mode shapes can be 20% in error (Abdel Wahab et al., 1999).

1.2.2.1 Ambient excitation and vibration monitoring

It is sometimes difficult to measure the force imparted on an operational structure. Other techniques are required to measure and calculate the modal properties of such structures. With the advent of more sensitive measurement equipment and more sophisticated computers and software, it is now possible to perform dynamic measurements on structures that are excited by means of ambient or natural excitation. Ambient excitation is typically associated with sources such as the wind, traffic or impact loads. One of the disadvantages of ambient excitation is that the higher frequency modes are not always excited well by ambient sources (Wenzel, et al., 2005). With ambient excitation it is usually difficult to measure the input forces imposed on the structure. It is therefore usually assumed that the input force is random.

The process of finding the modal model associated with a structure from vibration data is called system identification. In order to perform system identification on a structure that is excited by means of ambient excitation, the stochastic subspace identification (SSI) method originated. This method is used to determine the natural frequencies, modal damping and is able to construct the mode shapes from measurements, without measuring the input force.

The natural frequencies can be determined from measurements made with sensitive accelerometers. The natural frequencies can be determined from the spectrum of the acceleration data measured on the structure. This can be done by applying the fast Fourier transform (FFT) directly to the acceleration data and obtaining the spectrum. In the process described by Wenzel, et al. (2005), it is shown that the various FFTs (from different checkpoints on the structure) can be averaged and normalised in order to obtain a so-called ANSPD (averaged normalized power spectral density) spectrum. From this averaged spectrum the natural frequencies of the structure can be determined.

The mode shapes are determined by comparing the measurements made by the different accelerometers to a reference accelerometer. Scaled mode shapes can be obtained by comparing the measurements from different points to the reference accelerometer. These mode shapes are operational deflection shapes and are a superposition of other natural modes close to the mode under consideration. Only when the modes are well separated will the operational shape resemble the natural mode at the frequency of interest. These operational shapes can be compared to the analytical operational shapes in the MAC and be used for model updating.

These measurements are used to create a dynamic model and the modal model can be reconstructed from the dynamic model. If mass-normalized mode shapes are required, ambient excitation cannot be used as the input force is required to scale the mode shapes (Wenzel et al., 2005).

The SSI method was applied to bridge Z24 in Switzerland. The natural frequencies and the mode shapes were determined from the vibration measurements while the bridge was excited by means of ambient excitation. It was shown that three of the mode shapes changed due to the damage being introduced in the bridge structure (Wenzel et al., 2005).

The structural condition and damage state of a masonry bell-tower was investigated by Gentile and Saisi (2007). The vibration characteristics of the tower were extracted from ambient vibration monitoring and two methods for extracting the modal parameters are described. The first is the peak picking method and the second is known as the frequency domain decomposition (FDD) method. The peak picking method uses the peaks of the auto-spectral densities or the cross-spectral densities to identify the natural frequencies. The FDD method uses the singular value decomposition of the cross-spectral density matrix at each frequency. The peaks of the singular value plot provide and an estimation of the natural frequencies. Both methods provided natural frequency estimates that showed good agreement (Gentile and Saisi, 2007). Both these methods are equivalent to the FFT method described by Wenzel, et al. (2005); except that in this case the auto-spectral or cross-spectral densities instead of the FFT of the response are used to extract the natural frequencies.

1.2.2.1.1 Ambient excitation in aircraft structures

Aircraft structures are subjected to a wide variety of static and dynamic loads during flight and also on the ground. It is possible for the loading on the structure, due to gusts and dynamic manoeuvres, to exceed the maximum allowable limit, but most often the failures can be attributed to fatigue. The highest stressed areas in the aircraft structure are designed to be below the allowable stress limit. These highly stressed areas, however, are the areas where failure, due to fatigue, may occur (Braun, Ewins and Rao, 2002).

Gust loads are often the most critical design load for civil aircraft and is the main source of fatigue loading in the structure. The analysis approach of the response to a gust load can be taken either as a separate discrete event or as a random turbulent sequence. This sequence can be short and may then be considered to be a stationary random process with Gaussian properties. Over longer periods of time, the standard deviation of the gust is not constant but varies randomly with a given probability density function. The 'von Karman' power spectral density function describes how the energy is distributed with frequency. This power spectral density function is often used for the turbulence model (Braun et al., 2002).

Buffeting is another type of aerodynamic excitation that is considered to be random with energy distributed over a wide frequency range. It is defined as the aerodynamic excitation of the vibration modes of the wing or tail structure due to separated flow. It is dependant on the geometry and the flight conditions. Buffeting is associated more with

military aircraft as they fly at high angles of attack. Commercial aircrafts do not fly at these high angles of attack, but buffeting can still occur. Separated flow can occur on the main wing surfaces and then impinges on the tail. This can excite the tail as well as the fuselage modes (Braun et al., 2002).

1.2.2.2 Strain modal analysis

There is a problem with obtaining dynamic strain or stress responses from accelerometer data. The accelerations must be integrated twice to obtain displacements which in turn must be differentiated spatially to obtain strain responses. This leads to difficult mathematical manipulation and the quality of accelerometer data can be insufficient to accurately estimate the dynamic strains and stresses. This problem can be circumvented by directly measuring the strain responses and constructing a strain FRF and if the input force is measured, the strains can be compared to predicted strains obtained from FE models (Vári, 1995).

Ewins and Bernasconi (1989) demonstrated that mass-normalised modal strain fields or strain mode shapes can be computed from the parameters obtained from modal testing with strain gauges as well as displacement transducers. Modal tests as well as numerical analyses were performed on two real structures. The first real structure was a cantilever beam that had an abrupt change in cross section to induce a stress concentration. The computed FE results were compared to both the modal strains obtained directly and through spatial differentiation. The modal strains obtained from differentiation were shown to be less accurate in comparison with the FE modal strains and the modal strains measured directly. The second real structure was a curved plate and in this example the effectiveness of the strain modal tests for measuring multidimensional modal strain fields was illustrated. The multidimensional strain field on the surface of a structure was measured with a strain rosette. The maximum normal stresses that resulted from these measurements for two natural frequencies were determined and compared to an FE model. It was shown that the direction of maximum stresses can be predicted accurately (Ewins et al., 1989).

Strain modal testing provides an alternative to displacement modal testing. Structural modification by means of strain modal testing was investigated by Vári (1995). Strain measurements were carried out in conjunction with displacement measurements and thus strain modal testing was used to complement displacement modal testing. Different structural modification methods together with the advantages and disadvantages to strain modal testing were investigated (Vári, 1995).

Four different analytical equations of the strain FRF were derived and described by Vári (1995). It was shown that the strain mode shape and the displacement mode shape are related to one another by deriving an analytical solution to strain FRF from first principles (Yam, Leung, Li and Xue, 1996). They all showed that the strain FRF matrix is not necessarily square and it is not symmetric, therefore it does not obey the principle of reciprocity, and the analytical equations contain both the displacement and strain mode shapes (Vári, 1995). This is different from displacement FRFs which are symmetrical in form and obey the principle of reciprocity (Ewins, 1995).

If displacement mode shape information is required from the strain frequency response function, there are fundamental changes to be made to the procedure followed when extracting displacement mode shapes from displacement frequency response functions. Vári and Heyns (1997) showed that due to the asymmetry of the strain FRF matrix more test data is required. It is required to measure at least one row and one column of the strain FRF matrix, as both are required to extract displacement and strain mode shapes (Yam et al, 1996). Every element in the strain FRF matrix contains information on the values of m_r, c_r and k_r for all the modes. There are numerous drawbacks to using strain modal testing compared to regular displacement modal testing. Only when the advantages of using strain modal testing are fully utilised, does it become reasonable to perform a strain modal test (Vári, 1995).

One of the advantages of performing strain modal tests is the fact that strain mode shapes are more sensitive to small structural changes than the displacement mode shape. This statement was proved by performing a strain modal analysis on a plate with and without holes cut into it. It was shown that the difference in natural frequencies, obtained from measurements of the plate with and without holes, is quite small. The displacement mode shape did not change significantly even at the circumference of the holes. The strain mode shape showed a significant change at the location of the holes and it was concluded that the strain mode shape is much more sensitive to local structural changes (Yam et al, 1996). The problem frequencies and locations on the structure are directly evident from strain frequency response functions (Vári et al., 1997).

An added advantage of measuring strains lies in the validating of a dynamic finite element model. When strains are measured it can be compared directly to the predicted FE strains. Displacement mode shapes have to be manipulated to obtain the associated stresses and strains. The lower frequency bound of the strain gauge can be advantageous. Strain gauges are commonly used for static measurements, thus the strain gauges used for modal testing can measure in the low frequency range down to static deformation. The piezo-electric accelerometers cannot measure the static deformation of a structure. The strain gauge has an advantage over conventional transducers in terms of size, weight and sensitivity in the low frequency range. Another advantage of strain measurements is that they are incapable of measuring rigid body modes, because rigid body motion is accompanied by no deformation.

When strain modal testing is used for condition monitoring purposes it provides information in four parts (Vári et al., 1997):

- The dynamic characteristics of the structure can be extracted
- The detection of a possible failure in progress
- The unique detection of the location of the possible failure
- The indication of the severity of the failure

The disadvantages of modal analysis by strain gauges include the extraction of displacement mode shapes from strain measurements, which is cumbersome. Strain measurements can become expensive as there might be a need for close spacing of the transducers and the fact that they are not reusable while other modal testing transducers are. One of the main disadvantages is that the requirements for successful

dynamic response measurement are very strict. These requirements include (Vári et al., 1997):

- The bonding quality
- The calibration needed to compensate for lead wire resistive and capacitive effects
- The operational frequency, as at higher frequencies the deformation amplitudes become lower and the dynamic sensitivity decreases

Strain gauges are not the only transducers capable of measuring strains; with the advances in technology it is now possible to measure strains by means of fibre Bragg gratings.

1.2.2.2.1 Modal analysis by means of fibre Bragg gratings

One of the issues with installing a structural health monitoring system on an unmanned aerial vehicle (or UAV for short) is that the sensors or sensing systems must be integrated into the structure of the UAV. Cusano et al. (2006) investigated the use of embedded fibre optic Bragg gratings to perform an experimental modal analysis on the structure of a composite UAV wing. The feasibility of using these fibre Bragg gratings to perform modal analysis was demonstrated and the modal parameters obtained with the Bragg gratings were compared to those obtained from accelerometers and it was shown that they compared very well (Cusano et al., 2006).

The Bragg gratings offer an advantage over other sensors, because it can be integrated in the structure and hardly even change the mechanical properties, as well as measure several parameters simultaneously. It is possible to multiplex fibre Bragg gratings along a single optical fibre, which implies that the strain response of multiple points can be monitored simultaneously (Paolozzi and Gasbarri, 2006). The fibre Bragg gratings have a high resistance to corrosion and fatigue; and protection against lightning and electromagnetic interference is not required.

Paolozzi and Gasbarri (2006) performed a modal analysis on a composite laminated bar, using two optical fibres embedded in the layup and constructed strain FRFs. They obtained the strain mode shape from the strain FRFs and concluded that the results from the strain measurements are consistent with those obtained with accelerometers. In this study a commercial interrogation system unit was used. This unit was limited to a maximum sampling frequency of 50 *Hz* and associated observable frequency of about 20 *Hz* (according to Shannon's sampling theorem). According to Paolozzi et al. (2006) this system is able to measure with a strain resolution lower than 1 $\mu\varepsilon$.

The same analysis that was described by Cusano et al. (2006) is described in the paper by Paolozzi et al. (2006). In this paper the excitation of the wing structure is described as coming from either a hammer impact or from an electromagnetic shaker. The signal used for the shaker was a stepped sine signal as this provides increased energy at each mode of vibration. The strain FRFs were measured with the fibre Bragg gratings. It is implied by definition that the load, which was imparted on the structure, is measured during the measurements of the strain FRFs. The analysis did consider real flight

conditions where the excitation due to flight loads cannot be measured. Instead it was suggested that piezoelectric patches can be embedded in the structure to excite it. In this case the excitation loads can be measured and is therefore known for the subsequent FRF calculations.

1.2.3 Model updating

In practice it is very difficult to create a finite element or analytical model that exactly represents a physical structure or system. Various errors are made during the modelling process, either knowingly or unintentionally. A process known as model updating was developed to minimise the discrepancies between the analytical model and the real structure by adjusting some of the model parameters presumed to be in error. These parameters are usually associated with the mass or stiffness matrix of the analytical model.

Various modelling errors influence the accuracy of FE models. Two common errors are: the modelling of joints and kinematic constraints and distortion in the mesh (Friswell and Mottershead, 1995).

Kinematic constraints of joints must be properly modelled. Joints as well as boundary constraints possess stiffness and perhaps even mass. If the joints are modelled to be completely rigid or the mass is disregarded, discrepancies occur.

When complex structural components are modelled, some elements may become distorted during the meshing process. These distorted elements can cause the determinant of the Jacobian matrix (used to create the element stiffness and mass matrices) to converge to zero. This leads to serious errors in the corresponding element matrices. Such large distortions should be avoided.

Updating of FE models has been used extensively to obtain correlation between mathematical and physical models. This is illustrated by Wu (2004) in his study of a three dimensional mobile crane structure. He used an FE model and modal testing to validate (or update) the model. Wu (2004) concluded that the validity and accuracy of the FE model should be considered and one of the most effective tools to do this is by means of modal testing due to its relative simplicity and low cost.

Model updating is an optimisation process in which the numerical model is updated. The optimisation uses an objective function that is minimised to obtain an updated model, by changing the uncertain model properties (Teughels et al., 2002). As an example of such a function the sum of the squared differences between experimental and numerical modal parameters can be used. Such an objective function $\left(f(a)\right)$ is shown as equation 1.3 (adapted from Wenzel et al., 2005).

$$f(a) = \frac{1}{2}\sum_{j=1}^{m}\left[z_j(a) - \tilde{z}_j\right]^2 \tag{1.3}$$

The experimental and numerical modal parameters are indicated by $\tilde{z}$ and z, respectively. The numerical modal properties are functions of the updating parameters (the a in equation 1.3). These parameters can be material properties, such as Young's modulus, or even geometrical properties, such as thickness. The model updating procedure is illustrated graphically in the form of a flowchart in Figure 1-2; (adapted from Wenzel et al., 2005).

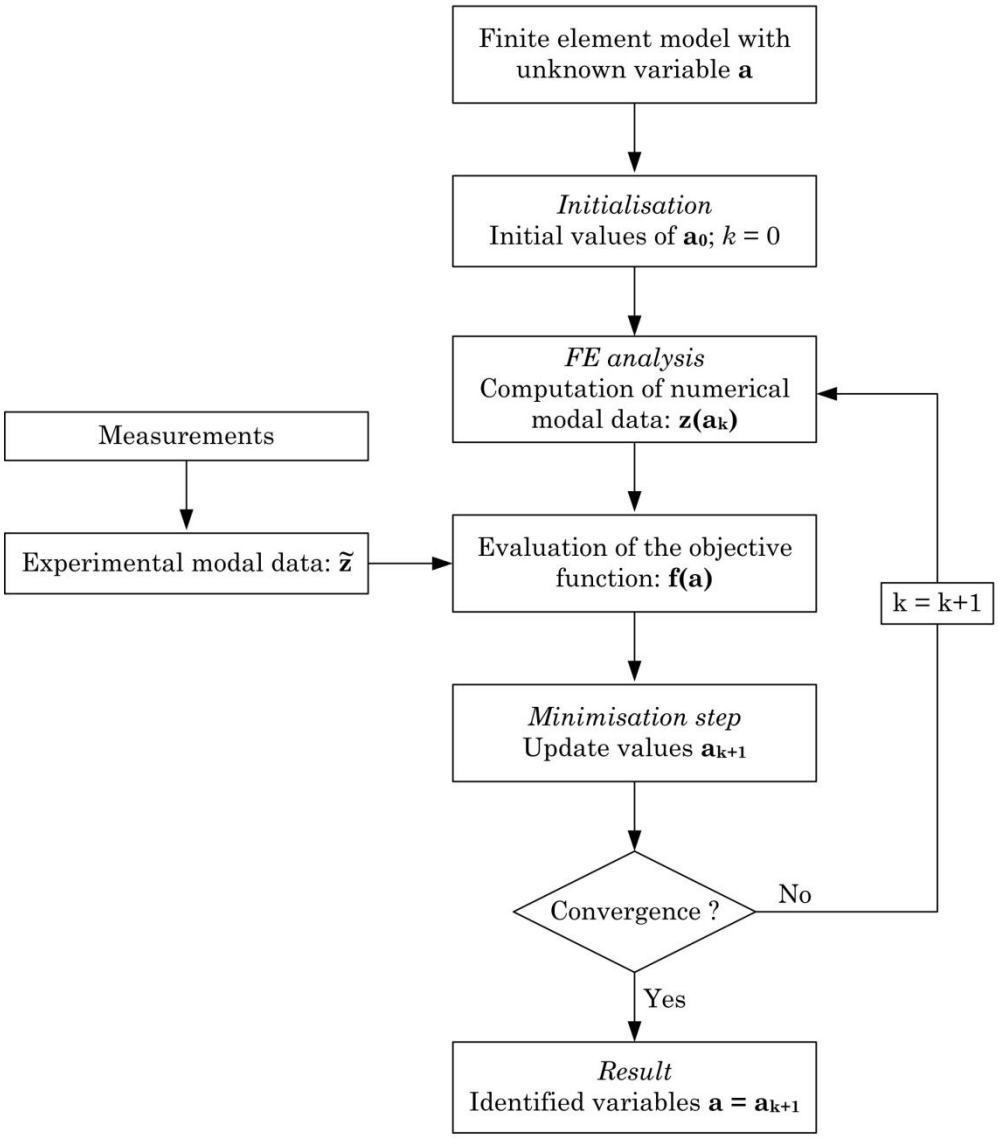

Figure 1-2: Flowchart of the model updating process (Wenzel et al., 2005)

A similar objective function is used by Teughels et al. (2002). A non-linear least squares problem, in which the differences in natural frequencies and mode shapes are expressed as residuals, is considered. The residuals are similar to the difference expression used in brackets in equation 1.3. They are used in the objective function in order to minimise the differences.

Various authors, such as Teughels et al. (2002), Teughels and De Roeck (2004), Lauwagie et al. (2002), Abdel Wahab et al. (1999) and many more, use a sensitivity based model updating approach. In this approach a sensitivity matrix is used in the

optimisation process. The sensitivity matrix is calculated as the gradient of the response with respect to the model parameters as shown in equation 1.4 (adapted from Dynamic Design Solutions NV, 2008b). In equation 1.4, S represents the sensitivity matrix and it is equal to the gradient for the responses (R) with respect to the model parameters (P).

$$[S] = S_{ij} = \left[\frac{\partial R_i}{\partial P_j}\right] \tag{1.4}$$

The gradients of the responses with respect to the model parameters are usually determined by applying the rates of change of eigenvalues and eigenvectors as derived by Fox and Kapoor (1968). They determined exact analytical solutions for the rates of change of eigenvalues and eigenvectors with respect to design variables of choice.

When a sensitivity based model updating approach is used, modal data or frequency response functions can be used. When modal data is used, it is necessary to extract this data by means of a modal analysis, which can introduce errors. It can be more advantageous to use the frequency response functions directly, as there is no need to perform a modal analysis. This appears to be the only advantage over modal data (Friswell et al., 1995).

The use of the sensitivity method in elastodynamics offers various advantages over other updating methods (Cunha and Piranda, 1999). These advantages include: no expansion or condensation is required; the method is very robust with respect to measurement noise and ensures physically meaningful updating results. Some of the disadvantages listed by Cunha et al. (1999) to using sensitivity methods are: an initial FE model which closely represents the real structure is required for fast and reliable convergence and the fact that it requires modes to be paired.

1.2.3.1 The use of damage functions in model updating

Teughels et al. (2002) demonstrate a method to locate damage by establishing an FE model that is tuned to the undamaged structure and comparing this model to an FE model tuned to a damaged structure. This method is illustrated by only updating a single parameter; in this case the stiffness. The stiffness properties of each element were not changed separately. It is possible to vary the stiffness of each element in the FE model. This is rather slow as there are many updating parameters and large computational times are required to compute the sensitivity matrix (Abdel Wahab et al., 1999). When the stiffness of each element is changed individually it causes the sensitivity matrix to become ill-conditioned (Teughels et al, 2002). Realistic damage patterns are also not guaranteed if the stiffness of each element is allowed to vary independently. This is due to the fact that jumps in stiffness properties are allowed when elements are updated individually. The damage pattern therefore loses its physical meaning and is only a mathematical description.

Abdel Wahab et al. (1999) propose the use of a damage function consisting of three parameters. It reduces the number of updating parameters, as only the three parameters defining the damage function, instead of the individual element parameters,

are used in the updating process. This function guarantees a realistic damage pattern, as it is a smooth continuous function.

Maeck et al. (2000) investigate the use of two different techniques to identify and locate damage in reinforced concrete structures. These two techniques are presented and compared to each other.

The first technique determined the damage pattern by means of model updating with the aid of a damage function. This damage function is the same as the damage function proposed by Abdel Wahab et al. (1999).

The second technique is termed direct stiffness calculation. The direct stiffness calculation method uses experimental mode shapes to derive the dynamic bending stiffness of the structure. The main advantage of using this method is that it requires no mathematical model and therefore falls under the response-based approaches. The direct stiffness calculation is based on the basic relation that the dynamic bending stiffness, of a section, is equal to the bending moment, in that section, divided by the curvature. The bending moment is calculated from the inertia forces which can be determined from the experimental natural frequencies and mode shapes. The curvatures, in turn, are calculated from the modal displacements (Maeck, 2003). The direct stiffness calculation technique was also used by Teughels and De Roeck (2004) for comparative reasons.

Maeck et al. (2000) apply both techniques to a reinforced concrete beam subjected to an increasing level of damage. The dynamic bending stiffness (the product of Young's modulus and the area moment of inertia, EI) is calculated by means of the two methods. The first technique only uses natural frequency information to detect damage. The second technique requires mode shape information in order to calculate the bending stiffness. The reduction in the bending stiffness due to damage in the beam is observed and is used to localise the damage. The location of damage could be obtained with both techniques and the predicted location and severity for both techniques corresponded well (Maeck et al., 2000).

Teughels et al. (2002) improved the model updating process by introducing another type of damage function. This damage function can be used to determine the stiffness distribution throughout the FE mesh. This damage function was again used to reduce the number of updating parameters and to guarantee smoothness in updating parameter between adjacent elements.

The damage functions are formulated in accordance with finite element shape functions and it is used to map model parameters, such as Young's modulus, onto a damage element mesh. These elements are used to subdivide the FE model into a grid of damage elements and are therefore a secondary mesh to the primary FE mesh. As with FE models, the accuracy of the damage functions can be increased by refining the mesh (h-refinement) or by increasing the polynomial degree defining the shape function (p-refinement). Each damage element contains the mapping parameter by which the damage function can be multiplied to obtain the original model parameters (Teughels et al., 2002).

The updating parameters become these factors by which each damage function should be multiplied before they are combined. The model updating process is then applied to the damage elements and therefore updates the factors by which each damage function should be multiplied. The model parameters can be derived from the factors of the damage function to obtain usable model parameters.

The model parameters obtained from these functions can be used to represent damaged zones in the structure. Teughels et al. (2002) consider the method to be most applicable to structures whose damage pattern can be presented by a reduction in element bending stiffness. They then illustrate the use of damage functions and damage elements in the model updating process by applying the damage functions in the model updating process to a free-free reinforced concrete beam.

Teughels and De Roeck (2004) illustrate a method of damage detecting by means of updating an FE model with modal data. The differences in natural frequencies as well as the unscaled mode shapes are minimised in order to obtain an updated model. The modal data is derived from ambient vibrations. Damage functions are used to approximate the stiffness distribution and to reduce the number of unknowns. The Gauss-Newton method with the trust region strategy is proposed to improve general sensitivity based model updating methods. The trust region strategy is applied to enforce constraints on the parameters. This trust region only allows the parameters to be varied in a predetermined region and any variation outside this region is not allowed. The trust region method makes the updating process more stable. It is shown that significant improvements in the natural frequencies as well as in the MAC values may be obtained when the model is updated in this way.

The method proposed by Teughels et al. (2004) was applied to a real civil structure, namely the Z24 highway bridge in Switzerland, as was stated in paragraph 1.2.1.2. The torsional and bending stiffness of the bridge girder were used as the updating parameters. The multiplication factors, by which each damage function should be multiplied, were determined by means of optimisation and used to establish a damage pattern, which proved to be a realistic damage pattern. The damage pattern results were compared to the results of the direct stiffness calculation, which showed good correlation.

1.2.4 Structural health monitoring in the aircraft industry

Carbon fibre reinforced polymers are being used more frequently in the aerospace industry due to their high strength to weight ratio. One of the disadvantages of using composites in primary structures is that when they do fail, the damage propagates with little or no indication, accompanied by zero yielding before failure. It is necessary to inspect these structures regularly, but this can be expensive and time consuming.

Structural health and usage monitoring are particularly important in the aircraft industry (Staszewski et al., 2004). Structural health monitoring (SHM) techniques that are applied in industry today are based on pessimistic prediction and require periodic inspection by means of non-destructive testing. These non-destructive testing methods

are usually localised methods. The locations where local damage detection techniques are used are usually areas that are known for a specific type of damage.

The cost and time spent on damage detection and inspection can be reduced by implementing *smart* systems. SHM techniques can detect, characterise and track the damage in such structures. These systems can be integrated in the structure and be used to monitor (sense) and react to certain changes. A need developed to create a SHM system that is both cost-effective and reliable. Such a system can ensure that composites will reach its full potential in the aerospace industry (Oliver, Kosmatka, Hemez and Farrar, 2006).

SHM systems can be used to monitor the structure globally or locally. The global system can monitor the whole structure and determine whether any damage is present. If it is known that damage is present the structure can be inspected in more detail at a specific area. Vibration or modal based damage detection methods are useful for global monitoring of the aircraft structure rather than local monitoring (Staszewski et al, 2004).

Aircraft operators have nominated a couple of typical damage prone locations in composites. Two of these typical locations are (Staszewski et al., 2004):

- areas in composites that are prone to impact damage,
- composite structures with high interlaminar stresses.

A large part of the maintenance is concerned with the health and usage monitoring of the aircraft. The aircraft structure consists mainly of components manufactured from metals and composite materials. The most significant forms of damage, in the aircraft structure, are fatigue crack development in metal structures and impact damage in composite structures (Staszewski et al., 2004).

The parameters and data obtained from the modal analysis have been used with some success to detect damage in aircraft structures (Staszewski et al., 2004). The problem of using modal parameters to detect damage arises from the fact that long cracks are required to provide a change in modal parameters if the cracks are parallel to the loading direction (Staszewski et al., 2004:61).

1.2.5 Model updating and damage detection in composites

Composites originated from the aerospace industry. Due to the development of new materials and new fabrication methods, composites with low density and high strength characteristics have found application in a variety of areas. The mechanical properties of composites are very specific for each type of composite assembly due to the anisotropy and diversity of the materials used and due to the different architectures being used to construct the composite (Cunha et al., 1999).

There exists an inclination to manufacture more UAV components from composite materials. UAVs are no longer inexpensive and simple due to the use of these advanced

materials, but these materials are essential to increase the flight times. There are various advantages and disadvantages to using composites. The advantages of composites include the low weight, excellent corrosion resistance, high resistance to fatigue, reduced machining, the stealth nature, etc. The disadvantages include the high cost, lack of established design criteria, poor energy absorption, etc. (Borchardt, 2004).

Saving in weight, between 15-45% is possible with the use of composites. They are mainly used in moderate load-bearing components, such as the elevators. It is possible to reduce the weight even more, but then the composites will have to be used in higher load-bearing components such as the tail, wings and fuselage.

Structures manufactured from fibre reinforced plastics are usually built up by stacking and bonding layers of these fibres on top of one another. This construction leads to damage types that are different from those found in isotropic materials. The main damage types that need to be detected in UAVs after manufacture and flights are cracks, delaminations in the skin, debonding between skin and core and defects in the core. The most common type of damage is delamination damage. Due to the fact that the bonds exist underneath the surface of the structure, it is very difficult to detect visually (Grouve et al., 2008). Damage in composites eventually leads to failures as is the case with damage in components manufactured from isotropic materials. The detection of these damage types is therefore critical to proper UAV maintenance and a long service life (Borchardt, 2004).

Delaminations in the composite layers are caused by surface impacts. If the energy that is absorbed by the material is greater than a certain threshold, the internal bonding between the layers is broken. This delamination causes the layers to become free to glide along the fibre planes; which causes a reduction in bending stiffness and increase in friction between the layers. The reduction in bending stiffness can be attributed to the fact that delamination causes the area moment of inertia to decrease for the delaminated section. The reduction in bending stiffness may be observed as a decrease in the natural frequency (Grouve et al., 2006) as well as an increase in modal damping (Keye, 2006).

Grouve et al. (2008) investigated the use of a simplified model, based on natural frequency shifts, to detect delamination damage in a plain cantilever beam. The resonant frequencies of a laminated composite beam are sensitive to damage due to delamination. The magnitude of natural frequency shift, due to delamination damage, is dependent on the location as well as the size of the delamination. It was shown that the natural frequencies of such a laminated beam can be measured by means of fibre Bragg gratings.

Strain measurements are not commonly used for condition monitoring. There is a growing need to monitor the strains and subsequently monitor the health of a structure. One such structure is the rotor blades of a wind turbine which are manufactured from a composite material, usually glass fibre-reinforced plastic. These blades are exposed to fluctuating wind loads and are exposed to faults like fatigue and cracks within the blade structure. Strain measurements can be vital to monitoring the structural health of the blades (Hameed, Hong, Cho, Ahn and Song, 2009).

Strain measurements by means of strain gauges are difficult to implement as these sensors are not ideal and robust for long term application. There are, however, new technologies emerging that make long term strain measurement possible. One of these new strain measurement technologies is a fibre Bragg grating that is built-into a fibre optic cable. It can be imbedded into the glass fibre-reinforced plastic of the rotor blades of wind turbines, without overly disturbing the laminate. Once these technologies become cost-effective, condition monitoring systems based on strain measurement will become more relevant (Hameed et al., 2009).

SHM systems can be used to detect damage in composite components (paragraph 1.2.4). UAVs present an ideal platform for research and development of such a SHM system. This development can be aided by an FE model of the UAV. The UAVs are almost entirely manufactured from composites, they fly for extended periods near the edge of their design envelope and because they are unmanned and cost less than manned aircraft, the regulations on using unqualified hardware are not enforced as strictly as for manned aircraft (Oliver et al., 2006).

1.2.5.1 Development of a finite element model for the development of structural health monitoring techniques in composites

In order to perform research and development of a SHM system, Oliver et al. (2006) constructed an FE model of a fully composite wing, performed modal tests on the individual structural components of the wing, as well as the assembled wing, and validated the FE models for further research.

Oliver et al. (2006) constructed a fully composite wing to serve as a test piece, in which the composite material layups and bonding could be chosen before the FE modelling. Four main components were manufactured and assembled, namely the top skin, the bottom skin, the main spar and the aft spar. The layups and composite materials as well as the FE modelling of the individual parts and the assembled wing are described by Oliver et al. (2006).

The FE model updating is not performed directly on the FE model. Instead a meta-model (or model of the FE model) is constructed and updated. Parameters in the meta-model are changed during the updating process and the results exported and implemented in the FE model to obtain a validated model. This FE model can then be used to introduce damage in the modelled structure for further analysis and to validate the developed techniques.

The elements chosen by Oliver et al. (2006) could model the anisotropy of the composite material. Model updating provided significant improvements in the FE model. It was shown that it is necessary to construct FE models of the wing and its components. These models have to be validated to ensure that no misleading results are obtained.

1.2.5.2 Delamination damage in multi-layer composites

The effects of delamination on the natural frequencies and mode shapes of a multi-layered composite plate were studied numerically by Alnefaie (2009) using a three-dimensional FE model. The model took into account the layer orientation as well as the transverse shear effect. It was validated by comparing the natural frequencies of the model to models and experimental results from three other authors. The new FE model proved to be more accurate in all three comparisons.

Dynamic analyses were performed on an intact as well as damaged FE model. The laminates were modelled to ensure that continuity on the displacements and its derivatives at the coincident nodes of the different layers are maintained. The delamination was modelled by detaching the coincident nodes between the layers where the damage is located. It was simulated by a separation of 0.02 mm between the third and the fourth layer from the top. The effects of the delamination sizes upon the natural frequencies, relative displacement between two layers and mode shapes were evaluated.

It was shown that delamination has a less significant effect on the natural frequencies compared to the mode shapes, although the change in natural frequencies increases as both the damage size and mode order are increased. The detection of the damage is mode dependent, as the modes having large displacements in the delaminated region, are affected most by the delamination.

1.2.5.3 Identifying damage in composites by monitoring the modal damping

Keye (2006) investigated a model-based damage detection method to identify and locate delamination damage in carbon fibre reinforced polymers. The method is based on the changes in modal damping due to delamination. The modal damping is determined from an experimental modal analysis as well as from a numerical model. The experimental and numerical damping values are compared through a correlation coefficient, which in turn is used to localise the damage.

This method appears to be very promising since the damage location can be predicted very accurately. However, it appears to be computationally inefficient as all the possible damage locations have to be simulated in order to locate the damaged area. Without prior knowledge of the likely damage location, this is immensely time intensive.

1.3 Scope of work

A definite need for a damage detection method for use in composite aerospace structures, such as UAVs, has been identified from the literature reviewed in paragraph 1.2. This need arose from the fact that aerospace structures are required to further reduce the weight and allow the aircraft to remain airborne for long periods of time. Composite structures are available for this application, but they need to be monitored to ensure its integrity and safety. Technologies such as fibre optic Bragg gratings are becoming more

cost-effective and can be integrated into the composite structure, in order to monitor the structure dynamically. For this reason a vibration based damage detection technique relying on sensors that can be integrated into the structure, which can be used during in-flight conditions and which requires the minimum number of sensors, is developed to ensure that composite structures reach its full potential in the aerospace industry.
A structural damage detection technique for use in UAVs is developed by using output-only strain and acceleration responses. The technique is first developed on isotropic structures to validate the application and method with the prospect of applying it on fully composite wings. For this system to be integrated into the structure of the UAV it is designed to require the minimum equipment. The technique therefore focuses on the ideal location of the sensors as well as on optimising the number, type and distribution of different sensors to indicate the presence of damage. The type of damage that is investigated is delamination damage, as this is one of the most common types of damage in composite structures. The natural frequency shift technique is also sensitive to this type of damage (Grouve et al., 2008). A simplification to delamination damage is made by introducing damage by changing the thickness and hence the area moment of inertia. By changing the area moment of inertia the simulated damage has the same effect as delamination damage in real structures.

Various parameters and functions have been proposed by different authors to indicate the presence and location of damage (Pandey et al. (1991), Abdel Wahab et al. (1999), Maeck et al. (2000), Teughels et al. (2002) and Ngwangwa (2004)). It is widely accepted that damage causes a reduction in bending stiffness (Pandey et al., 1991). It is frequently assumed that the deflections are small and that the structure behaves linearly. The natural frequencies of a structure are dependent on its bending stiffness. Unlike many industrial structures, wing structures do not have redundant members (in order to save weight) and it should therefore be possible to use these natural frequencies to indicate damage. The changes in natural frequencies can generally be measured more accurately than mode shapes and are also good indicators of the presence of damage.

Pandey et al. (1991) showed that modal curvatures are much more sensitive to damage than displacement mode shapes. Modal curvatures provide a good indication of the location of damage. Abdel Wahab et al. (1999) extended the concept of modal curvatures by introducing the CDF (cumulative damage factor) parameter, which is an average of the change in modal curvature. It was shown that the CDF is sensitive to damage and provides a good estimation of the location of the damage.

Gere (2004) shows that the curvature κ or v'' of a beam is proportional to the bending strain ε_x, with the proportionality constant y equal to the distance from the neutral axis to the position where the strain is required. This relationship is known as the strain curvature relation and is shown in equation 1.5. The bending strain can be measured instead of the displacement or its derivatives to construct the modal curvatures (Pandey et al., 1991).

$$\varepsilon_x = -\kappa y = -\frac{d^2 v}{dx^2} y = -v'' y \tag{1.5}$$

Maeck (2003) investigated the use of measured strains to directly calculate the dynamic curvatures rather than determining them from displacement mode shapes. These curvatures are compared with numerically calculated modal curvatures. The conclusion arrived at was that strain gauge measurement seems to be unreliable for dynamic curvature estimation when the excitation levels are small. However, it is suggested that in future research the direct measurement of modal curvatures should be investigated and exploited. New technologies for measuring strains are emerging and condition monitoring systems based on strain measurements are becoming more significant (Hameed et al., 2009).

The flexural formula for calculating the normal stresses σ_x in the beam can be derived from equation 1.5 and the result is shown in equation 1.6 (Gere, 2004). The normal stress is a function of the bending moment M applied to the structure, the distance from the neutral axis y and the area moment of inertia I.

$$\sigma_x = -\frac{My}{I} \tag{1.6}$$

One requirement for the use of the strain-curvature relationship (equation 1.5) and the flexural formula (equation 1.6) is that the geometry of the beam under consideration is symmetrical about the y-axis, as in Figure 1-3. When measurements are carried out, this should be borne in mind.

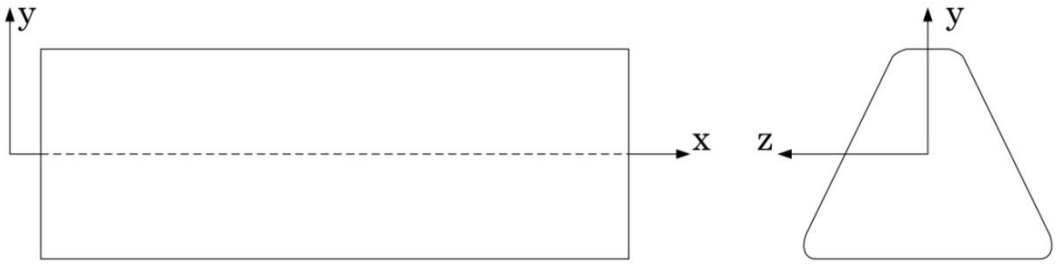

Figure 1-3: Beam used for curvature derivation showing symmetry about y-axis

A limitation of the flexural formula (equation 1.6) is the fact that this equation was derived for the bending of a prismatic beam composed of a homogenous, linear elastic material subjected to pure bending moment. If a beam, that was plane before a bending moment is applied, is subjected to a nonuniform bending moment, shear forces are introduced that cause warping or out-of-plane distortion. The beam will therefore not be plane after the application of the nonuniform bending moment. This warping causes complications in the analysis of such a beam. Extensive research has shown that the normal stresses calculated from the flexural formula (equation 1.6) are not significantly affected by the shear stresses and warping due to nonuniform bending (Gere, 2004). The use of the flexural formula for calculating normal stresses, as well as the accompanying strains, can be justified.

Two new damage parameters are proposed that use the dynamic changes in a structure, due to damage, and build on the parameters that have been developed by other authors. The proposed method depends on the calculation of the curvature directly from the

measured strains. The calculated curvature is used to calculate the CDF as proposed by Abdel Wahab (1999) in equation 1.7.

$$CDF_i = \frac{1}{N}\sum_{j=1}^{N}\left|v''_{o_{j,i}} - v''_{d_{j,i}}\right| \tag{1.7}$$

In equation 1.7 the N represents the total number of modes that is considered, i represents the number of measured locations (from 1 to n) with $v''_{o_{j,i}}$ and $v''_{d_{j,i}}$ representing the curvature of the undamaged and damaged structure, respectively.

It can be seen from equation 1.5 that the curvature multiplied by the distance from the neutral axis (y) is in fact measured when strains are directly measured. It is difficult to reconstruct the curvature from strain measurements if this distance from the neutral axis is not known. This distance will also change as damage is introduced, because the thickness, and thus the distance from the neutral axis, is changed for different levels of damage.

If equation 1.7 is multiplied with the distance from the neutral axis (y) it leads to the result shown in equation 1.8.

$$y_i CDF_i = \frac{1}{N}\sum_{j=1}^{N}\left|v''_{o_{j,i}} y_i - v''_{d_{j,i}} y_i\right| \tag{1.8}$$

The proposed method was developed to be implemented on structures where no artificial excitation is possible. The measured strains are normalised with a reference acceleration measurement to be able to compare the relative changes. Equation 1.5 can now be substituted into equation 1.8 and continuing with the hypothesis and normalising the substituted strain with a reference acceleration response we obtain equation 1.9.

$$\therefore yCDF_i = \frac{1}{N}\sum_{j=1}^{N}\left|\left|\frac{-\varepsilon_{x,o_{j,i}}}{\ddot{x}_o}\right| - \left|\frac{-\varepsilon_{x,d_{j,i}}}{\ddot{x}_d}\right|\right| \tag{1.9}$$

This normalised value is referred to as yCDF and is obtained from the difference between the undamaged $\varepsilon_{x,o_i}/\ddot{x}_o$ and damaged $\varepsilon_{x,d_i}/\ddot{x}_d$ acceleration normalised strain values. Since the structure behaves linearly, the strain also increases linearly with increased excitation force. The yCDF is dimensional with units of $\mu\varepsilon/m/s^2$. This can be non-dimensionalised by dividing the yCDF at a measurement position by the average strain value (of all the modes included in the calculation of the CDF) of the damaged structure at that location. This is given in equation 1.10 and is referred to as the strain (normalised) curvature damage factor or SCDF for short. This is the first new figure of merit for damage detection proposed in this work.

$$SCDF_i = \frac{yCDF_i}{\frac{1}{N}\sum_{j=1}^{N}\left|\frac{\varepsilon_{x,d_{j,i}}}{\ddot{x}_d}\right|} \tag{1.10}$$

The second parameter that is investigated in this study is derived from both the changes in the natural frequencies and the SCDF values, when damage is introduced in the structure. The SFDL (strain-frequency damage level given in equation 1.11) is defined as the root mean square (rms) of the SCDF (strain curvature damage factor, given in equation 1.10) multiplied by the average of the percentage changes in natural frequencies. It is possible to determine natural frequencies from dynamic strain measurements. In this work, accelerometers are included in the response measurements to measure natural frequency.

$$SFDL = \sqrt{\frac{\sum_{i=1}^{n} SCDF_i^2}{n}} \frac{\sum_{j=1}^{N} \Delta f_j}{N} \tag{1.11}$$

with

$$\Delta f_j = 100 \frac{\left| f_o^j - f_d^j \right|}{f_o^j}, j = 1 \; to \; N \tag{1.12}$$

The reasoning behind equation 1.11 is that it should theoretically provide a value equal to zero if the structure is undamaged. The curvatures that are calculated from the strain measurement should remain unchanged and therefore the SCDF at each measurement location should equal zero. The damage indicator (SFDL) would therefore also equal zero and should indicate that no damage is present.

If the structure is damaged and strain is measured near or at the damaged (or delaminated) area, the strain should change due to the reduction in load carrying capability of the structure. The CDF increases due to the change in curvature and it may be expected that the SCDF at the damage location should change significantly. The rms value of the SCDF should show an increase as well. When damage is present, there should be a change in natural frequency associated with it and thus the mean of the change in natural frequency should also increase. If these two parameters are multiplied it provides the SFDL value, which increases as the rms of the SCDF and the mean of the change in natural frequency increase. As the level of damage is increased, the SFDL value should subsequently increase likewise.

The technique developed here is intended for in-flight use on UAVs. It is therefore inappropriate to use an exciter for force input, and ambient excitation is used for dynamic excitation.

The aim of the present study is therefore to develop a strain based damage detection technique capable of detecting whether damage is present in wing-like structures from strain and acceleration measurements with a minimum number of sensors.

The proposed damage detection technique is implemented as follows:

1. Determine the natural frequencies from the ambient acceleration measurement.
2. Extract the acceleration normalised strain values, at the natural frequency positions, from the strain and acceleration transmissibility function for each measurement position.
3. Calculate the SCDF values from the extracted values at each measurement location from equation 1.10.
4. Calculate the SFDL values from equation 1.11.

1.4 Dissertation overview

The dissertation is organised into five chapters and is mainly divided into a numerical and an experimental validation part. The content of each chapter is discussed for easy reference and to provide the overall objective of each chapter:

- **Chapter 1:**

  The main problem and reason for investigation is introduced. The relevant literature on existing damage detection techniques and related topics is reviewed. The basic outline and proposed method is discussed in detail.

- **Chapter 2:**

  The finite element model to be used for numerical investigation is described in detail. The way in which the damage will be modelled is established and discussed.

- **Chapter 3:**

  The proposed damage detection method is analysed by first investigating deterministic damage cases and secondly examining stochastic damage cases. The validity of the method and the two parameters (the SCDF and SFDL) are investigated to prove the method numerically.

- **Chapter 4:**

  The proposed method is investigated experimentally. Two test structures with two different damage cases are considered. The tests are performed to simulate in-flight conditions and to verify that the method can be applied to output-only data.

- **Chapter 5:**

  The work presented in Chapters 2 to 4 is critically evaluated and discussed. Potential future work is identified in Chapter 5.

Chapter 2: Numerical model

The present study focuses on developing a damage detection technique that can in future be applied and incorporated in real composite UAV wing structures. Some simplifications are made to first develop and prove the technique. One of the simplifications is to develop the technique on simplified wing-like structures. The structures that are considered in this study are inspired by the two dimensional top planar view of UAV wings.

Another simplification is made with respect to the material used in the study. It was stated in paragraph 1.2 that most UAVs are manufactured from composite materials. The FE modelling and verification of composite structures can be very time consuming and tedious, as composites are anisotropic. It was decided to rather use a material that can be easily modelled and therefore mild steel is used in this study. Mild steel is an isotropic material of which the properties are very well known and documented. Although the failure modes of composites differ from those of steels, a mathematical equivalent is used and implemented.

2.1 Classification of UAVs

The FE model must be representative of a large number of UAV wings and it would be ideal to classify the different planar wing shapes into a family of wings. The focus is to develop the technique to be applicable to different wings that can be included in the family. The technique therefore depends on certain attributes that are common to the family. A collection of UAVs were studied in order to become familiar with the different typical shapes of these UAV wings.

The United States military have various classifications of UAVs. The widely accepted four category classification of UAVs is show in Table 2-1 (Adapted from Wong, 1997). The four categories are more commonly known as follows: Tier I – *Tactical*, Tier II – *Operative,* Tier II Plus – *Strategic HAE (High Altitude Endurance)* and Tier III Minus – *Strategic LO (Low-Observable) HAE.*

Table 2-1: Classification of UAVs

Category	Designation	Max. altitude	Radius	Speed	Endurance
Tier I	Interim-Medium Altitude, Endurance	Up to 15 000 *ft*	Up to 250 *km*	60-100 *kts*	5 - 24 *hours*
Tier II	Medium Altitude, Endurance	3 000 *ft* to 25 000 *ft*	900 *km*	70 *kts* cruise	More than 24 *hours*
Tier II Plus	High Altitude, Endurance	65 000 *ft* max.	Up to 5 000 *km*	350 *kts* cruise	Up to 42 *hours*
Tier III Minus	Low Observable, High Altitude, Endurance	45 000 *ft* to 65 000 *ft*	800 *km*	300 *kts* cruise	Up to 12 *hours*

From Table 2-1 it is clear that there are different requirements for different types of UAVs. It is intuitive that UAVs that are required to fly for extended periods of time at high altitudes should be larger and heavier. There are different sized UAVs and the relative sizes of the UAVs are compared in Figure 2-1. This comparison is made on the basis of their wing span and gross weight.

The information used to generate Figure 2-1 was obtained from the document, *Unmanned Aircraft Systems Roadmap 2005 – 2030* (2005), posted by the Office of the Secretary of Defence as well as from Wikipedia's General Atomics ALTUS (2008). The information on the UAVs listed in these documents are summarised in Table 2-2. The airfoils used in the construction of the various UAVs are also listed in Table 2-3 and were obtained from Lednicer (2007).

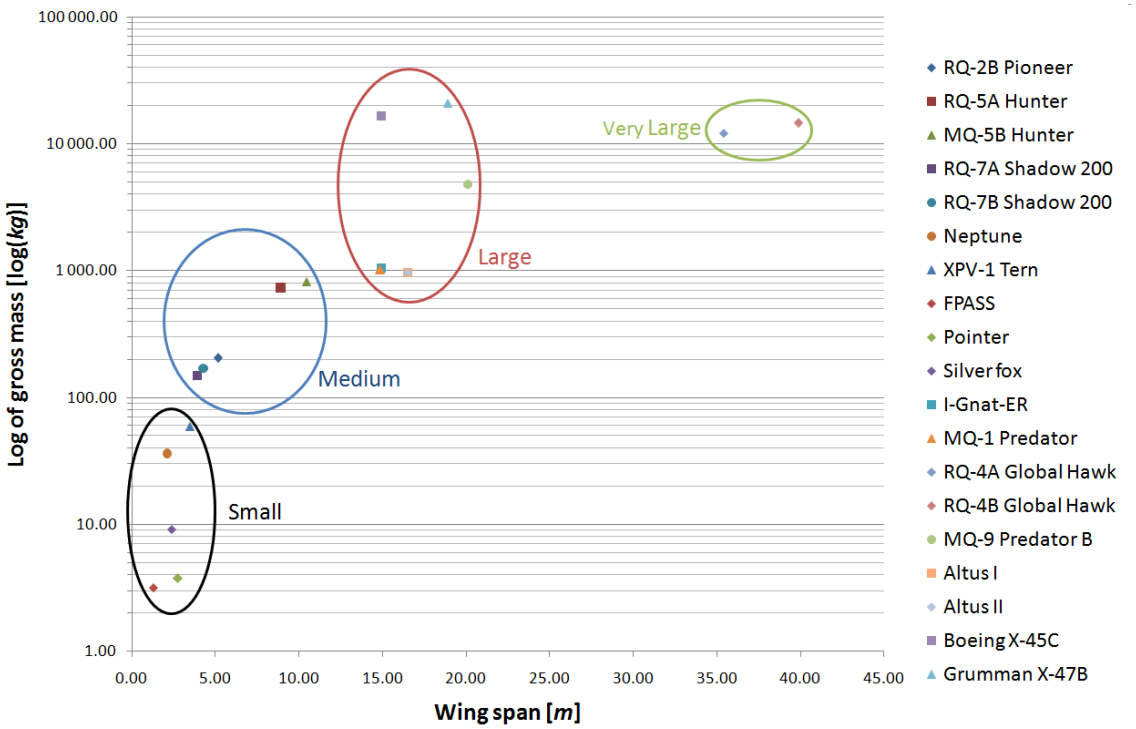

Figure 2-1: Comparison of the mass and size of different UAVs

The information in Table 2-2 can be used to construct different members of the wing family based on the wing span. It is clear from Table 2-3 that there are various airfoil profiles that are used in the construction of the UAVs. It will therefore be very difficult to create a family of wings based on the type of airfoil used. This is also a reason for using a two dimensional planar view for the model.

Table 2-2: UAV specifications

Unmanned aerial vehicle	Max. altitude [*ft.*]	Radius [*km*]	Endurance [*hours*]	Gross mass [*kg*]	Wing span [*m*]
RQ-2B Pioneer	15 000	185.20	5	205.02	5.18
RQ-5A Hunter	15 000	266.69	11.6	734.82	8.90
MQ-5B Hunter	18 000	266.69	18	816.47	10.44
RQ-7A Shadow 200	14 000	125.94	5	148.32	3.90
RQ-7B Shadow 200	15 000	125.94	7	170.10	4.27
Neptune	8 000	74.08	4	36.29	2.13
XPV-1 Tern	10 000	74.08	2	58.97	3.47
FPASS	1 000	11.11	1	3.18	1.31
Pointer	1 000	11.11	2	3.76	2.74
Silver fox	16 000	37.04	10	9.07	2.38
I-Gnat-ER	25 000	277.80	30	1 043.26	14.94
MQ-1 Predator	25 000	926.00	24	1 020.58	14.84
RQ-4A Global Hawk	65 000	10 000.80	32	12 133.60	35.42
RQ-4B Global Hawk	60 000	10 000.80	28	14 628.35	39.90
MQ-9 Predator B	50 000	3 704.00	30	4 762.72	20.12
Altus I	65 000	740.80	24	966.15	16.52
Altus II	65 000	740.80	24	966.15	16.52
Boeing X-45C	40 000	2 222.40	7	16 556.12	14.94
Grumman X-47B	40 000	2 963.20	9	20 865.25	18.90

Table 2-3: Airfoils of the different UAVs

Unmanned aerial vehicle	Airfoil at root	Airfoil at tip
RQ-2B Pioneer	NACA 4415	NACA 4415
RQ-5A Hunter	Unknown	Unknown
MQ-5B Hunter	Unknown	Unknown
RQ-7A Shadow 200	NACA 4415	NACA 4415
RQ-7B Shadow 200	NACA 4415	NACA 4415
Neptune	Unknown	Unknown
XPV-1 Tern	Unknown	Unknown
FPASS	Unknown	Unknown
Pointer	Unknown	Unknown
Silver fox	Unknown	Unknown
I-Gnat-ER	Drela GW-25	Drela GW-27
MQ-1 Predator	Drela GW-19/GW-25	Drela GW-27
RQ-4A Global Hawk	NASA LRN 1015	NASA LRN 1015
RQ-4B Global Hawk	NASA LRN 1015	NASA LRN 1015
MQ-9 Predator B	Drela GW-19/GW-25	Drela GW-27
Altus I	Drela GW-19/GW-25	Drela GW-27
Altus II	Drela GW-19/GW-25	Drela GW-27
Boeing X-45C	Unknown	Unknown
Grumman X-47B	Unknown	Unknown

2.1.1 Wing planform description

The two dimensional planar view of the UAV wing and fuselage is used to create a family of wings representative of real UAVs (paragraph 2.1). One of the main problems is to identify what shape and description can be used to create such a family.

During the wing design phase there are various parameters that need to be selected. This phase usually involves selecting the airfoil, the average chord length ($\bar{c}$), the maximum thickness-to-chord ratio ($(t/c)_{max}$), the aspect ratio ($Ar = b^2/S$), the taper ratio ($\lambda = c_t/c_r$) and the sweep angle (Λ), which is defined for the leading edge as well as for the maximum thickness line. These parameters define the wing planform. An illustration of such a planform including the definition of the parameters is shown in Figure 2-2 (adapted from Corke, 2003).

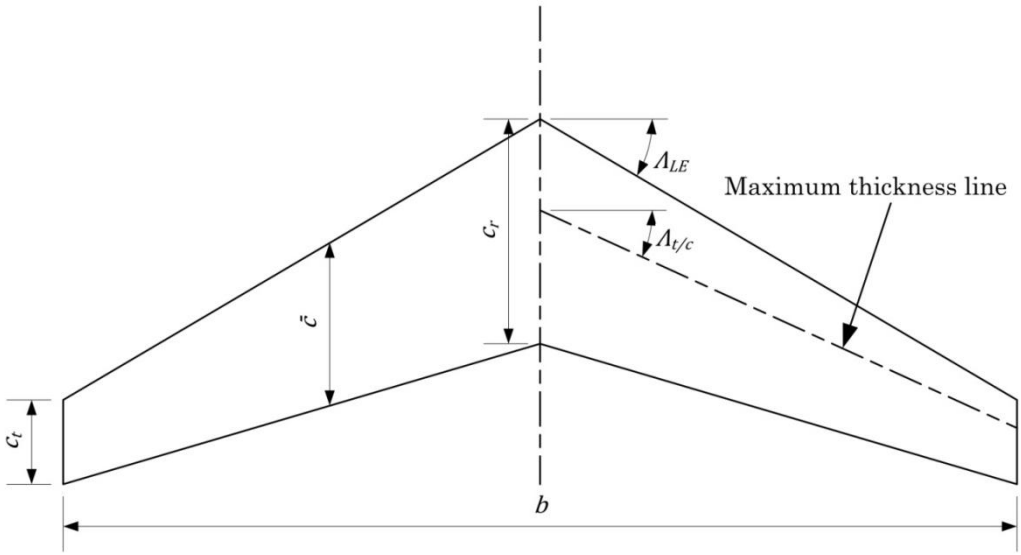

Figure 2-2: Wing planform showing definition of the parameters (adapted from Corke, 2003)

The part of the wing that passes through the fuselage is known as the carry-through and the wing is usually constructed as an integral unit. The carry-through portion has a thickness equal to the maximum thickness-to-chord ratio in order to withstand the large bending moment in the wing (Corke, 2003). The parameters and the definition thereof that are used in the design of the wing planform can be used in the creation of the wing family.

2.1.2 Family of wings

The parameters that are used to design the wing planform of a new aircraft served as inspiration for the generation of a family of wings. The basic layout of the wing planform (Figure 2-2) as well as the parameters used to define it is used to describe the wing area of the family. The size of the fuselage and therefore the carry-through is also included in the family. The basic layout of the wing-like profiles that constitute the family is shown in Figure 2-3. It can be said that the family of wings consists of two wing sections with a fuselage section in between.

The family can be characterised by the wing span (b), the width of the fuselage (l_f), the sweep angle at the leading edge (Λ_{LE}) as well as the chord at both the root and tip of the wing (c_r and c_t). This family can now be used to describe different two dimensional wing planar shapes and sizes. This family is used to develop the damage detection technique and will serve as the basis for numerical and physical modelling, testing and correlation.

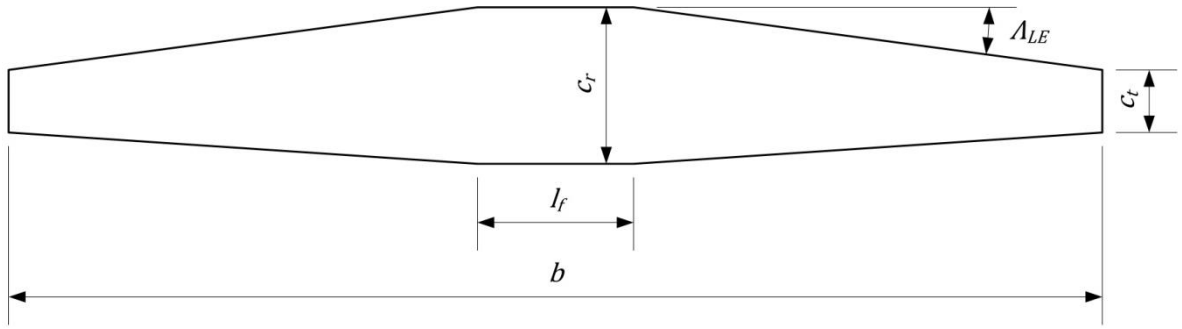

Figure 2-3: Parameter defining the family of wings planform

2.1.2.1 Family of wings compared with real UAVs

Real UAVs are designed on the same basic principles as other aircraft and therefore the proposed family of wings should fit the top planar view of different UAVs. A comparison is made in Figure 2-4 between four different UAVs and the proposed family of wings. The generated profiles (shown in grey) are superimposed on the real planar top view of the UAVs. The figures of the real UAVs used in Figure 2-4 are adapted from *Unmanned Aircraft Systems Roadmap 2005 – 2030* (2005). They are the planar top view of the following UAVs:

a. RQ-4A Global Hawk
b. MQ-1 Predator
c. RQ-2B Pioneer
d. Neptune

The parameters used to generate the wing-like profile (which forms part of the family) are summarised in Table 2-4. The profiles were created by measuring the different parameters defining the family on the sketch, and scaling them with the wing span listed in Table 2-2.

It is evident from Figure 2-4 that the family of wings are able to fit the planar top view of real UAVs very well. The family therefore gives a good representation of the planar view of the wing and can subsequently be used for the development of the damage detection technique. The damage detection technique is developed for a two dimensional view. It is assumed that if the technique can be developed for this family it should be possible to extend the technique to three dimensional wing structures.

Table 2-4: Parameters used to fit the different UAVs

UAV	Wing span (b) [m]	Length of fuselage (l_f) [m]	Sweep angle (Λ_{LE}) [°]	Chord at root (c_r) [m]	Chord at tip (c_t) [m]
RQ-4A Global Hawk	35.42	1.579	7	1.922	0.687
MQ-1 Predator	14.84	0.787	3.2	1.068	0.506
RQ-2B Pioneer	5.18	0.276	0	0.611	0.611
Neptune	2.13	0.604	32	0.774	0.339

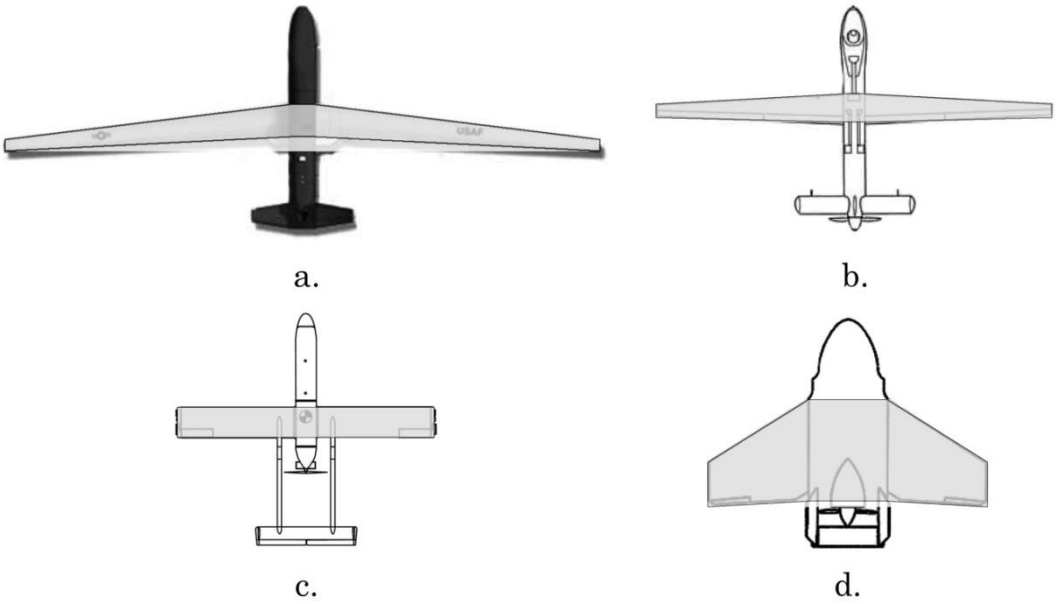

Figure 2-4: Comparison of family to real UAVs (adapted from *Unmanned Aircraft Systems Roadmap 2005 – 2030*, 2005)

2.2 Mathematical model description

The damage detection technique is developed and tested numerically with the aid of an FE model. The FE model can be used to introduce damage in the structure and to monitor the response of the structure and thus develop the damage detection technique.

2.2.1 Finite element model

The geometry of the structure was described in 2.1.2 and can be subdivided into one rectangle and two trapeziums (Figure 2-5). This geometry lends itself to be easily meshed with rectangular or hexahedral elements. This geometry is also ideally suited for the ISO meshing algorithm of Patran (2008). The choice then lies on which elements should be used. There are various advantages and disadvantages to using different elements.

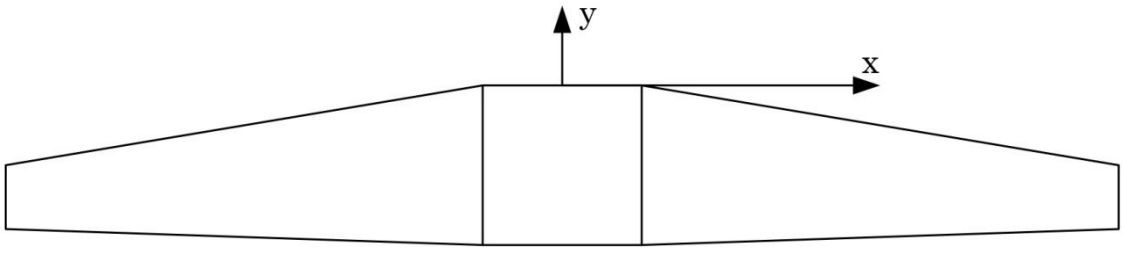

Figure 2-5: Subdivision of the family of wings into a rectangle and two trapeziums

It should be remembered that the geometry possesses a thickness. The family therefore represents a three dimensional geometry. For the sake of this study, it is assumed that the third dimension, thus the thickness, is small compared to the other two dimensions and the family of wings take on the form of a flat plate.

The one possibility is to use hexahedral elements to mesh this three dimensional solid. The advantage to using such an element is the fact that the complete solid is meshed. The displacements, strains and stresses are solved in the x, y and z directions. The disadvantage to using such elements is the fact that there are many more degrees of freedom per element than with two dimensional shell elements. The geometry is also relatively thin and such a solid element is not ideal for meshing thin plates as this could cause problems such as shear locking and ill-conditioning of the element matrices. If a large number of compact three dimensional solids were used in the mesh, the FE model would require far too many degrees of freedom to avoid the problems (Cook, Malkus, Plesha and Witt, 2002).

Another possibility is to mesh the surface of the family of wings with shell elements. The advantage of such an element lies in the fact that the element can model the thickness of the family without increasing the number of degrees of freedom as much as the hexahedral elements would. If an 8-node shell element is used it has 24 degrees of freedom where a 20-node hexahedral element, equivalent to the 8 node quadrilateral, would have 60 degrees of freedom.

In this study normal modes analyses to determine the eigenvalues and eigenvectors of the family of wings, are performed with Nastran as the solver. The most prominent modes are the lateral vibration modes (in the z-direction of Figure 2-5). Due to the thickness being far less than the other two dimensions, the wings can be modelled as plates. Quadratic 8-node shell elements can represent uniform bending correctly and are much more suited to plate bending problems than hexahedral elements (Cook et al., 2002). For this reason the family of wings are surface meshed with 8-node shell elements.

By modelling the structure to have the true dimensions of the real UAV, the FE model can become badly scaled and the effects of shear locking can easily be increased. It would therefore be better to have a model that is adequately scaled without the thickness becoming far less than the other two dimensions. In order to obtain such a model, the parameters defining the family of wing can be normalised with respect to the wing span (b). This would provide a model with a length equal to one unit of length. The normalisation simplifies the experimental structural testing. It would be difficult and expensive to test a plate with the original physical dimensions in the laboratory. The FE model of the family of wings is defined with the origin of the coordinate system located at the centre of the fuselage width as in Figure 2-5. The left edge, of the FE model, will therefore be at -0.5 m and right edge will be at 0.5 m.

The thickness ratio of an aircraft is defined as the thickness to chord ratio. The thickness is normally variable along the length of the wing, since the bending moment and shear forces increase from tip to root. The average thickness ratio for subsonic aircraft is typically 10% and for supersonic aircraft this is equal to 5-8% (Jenkins, Simkin and Rhodes, 1999). The thickness of the four UAVs shown in Figure 2-4 with properties as given in Table 2-4 can be determined if the length of the chord at the root is used and for the calculation it is assumed that they are all subsonic aircraft. The thickness together with the chord of the four UAVs are summarised in Table 2-5.

Table 2-5: Maximum wing thickness of the four different UAVs

UAV	Chord a root (c_r) [m]	Thickness [mm]	Thickness normalised by wing span [mm]
RQ-4A Global Hawk	1.922	192.20	5.426
MQ-1 Predator	1.068	106.80	7.197
RQ-2B Pioneer	0.611	61.10	11.795
Neptune	0.774	77.40	36.34

With the exception of the Neptune wing, the maximum thicknesses of the UAVs are in the order of 10 mm (Table 2-5). The thickness of the structure that is investigated is chosen to be equal to 10 mm which would imply that the thickness will not be too small compared to the length of the wing. It would simplify both the numerical studies as well as provide a realistic experimental structure.

The boundary conditions of the FE model are chosen to be free-free. This is consistent with an aircraft in-flight which is not constrained in any way.

2.2.2 Mesh independence study

The FE method is a numerical approximation of a real structure. One of the problems one is faced with when modelling a structure, is how many elements will provide a good estimate of the real structure. The accuracy of the FE model increases as the mesh is refined. It is always possible to use a very fine mesh, but the time used to solve such a mesh becomes excessively large. The number of elements, used to approximate a structure, should be chosen carefully to obtain a good compromise between accuracy of the FE model and the time taken to solve the system.

In an attempt to find such a compromise, it was decided to consider a member of the wing family for which an analytical solution exists. Such a solution for a rectangular beam is well documented (Rao, 2004), and the accuracy of the FE model can be compared to the analytical solution for this case. A rectangular beam was created from the wing family properties given in Table 2-6 and is shown in Figure 2-6. The FE model was created by using the elements described in paragraph 2.2.1, and the material properties of steel. The material properties are given in Table 2-7 and were obtained from Gere (2004). Free-free boundary conditions are applied in both the FE model and the analytical model to be consistent with the model described in paragraph 2.2.1.

Table 2-6: Wing family and thickness properties used to create a rectangular beam structure

Wing family property	Value
Wing span [m]	1
Length of fuselage [m]	0.04
Sweep angle [°]	0
Chord at root [m]	0.1
Chord at tip [m]	0.1
Thickness [m]	0.01

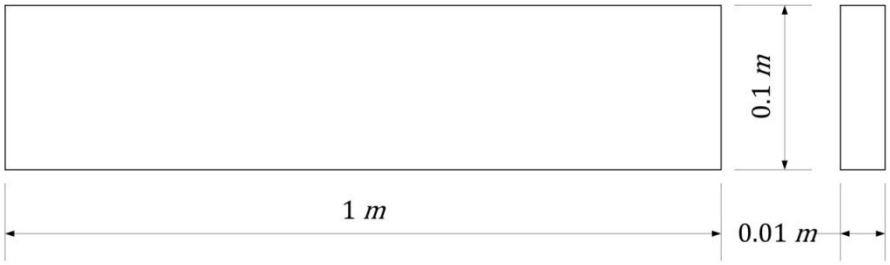

Figure 2-6: Beam used to determine analytical solution to natural frequencies

Table 2-7: Material properties of steel (Gere, 2004)

Property	Value
E (Young's modulus)	210 GPa
ρ (Density)	7850 kg/m^3
ν (Poisson's ratio)	0.3

The analytical solution was determined from equation 2.1, obtained from Rao (2004), for a beam with geometry as defined in Figure 2-6. This solution only provides the vertical natural frequencies (f_n) and therefore only these frequencies are compared. A sample calculation for the first natural frequency (mode 1) of the beam is shown (equation 2.1 to 2.4). βl is a constant for the different natural frequencies determined for different boundary conditions and is provided by Rao (2004). The natural frequencies are a function of the material properties, both Young's modulus E and the density ρ, as well as the geometry defined by the area A and length l.

$$f_n = \frac{(\beta l)^2}{2\pi}\sqrt{\frac{EI}{\rho A l}} \tag{2.1}$$

The area moment of inertia is a function of the width w and the thickness t. It is determined in equation 2.2.

$$I = \frac{1}{12}wt^3 \tag{2.2}$$

$$I = 8.33 \times 10^{-9}\ m^4 \tag{2.3}$$

The area moment of inertia, together with the area ($A = wt$), can now be substituted into equation 2.1 which results in equation 2.4.

$$f_n = 53.166\ Hz \tag{2.4}$$

The natural frequencies for modes 2, 3 and 4 were obtained similarly, but with different βl values. These frequencies are summarised in Table 2-8.

The number of elements used to mesh the beam was varied. The mesh started out with one element through the width and ten elements through the length of the beam. The mesh was refined by doubling the number of elements through the width and the height after each computation. The mesh sizes with their accompanying natural frequencies for the first four vertical modes are shown in Table 2-9. The error values on each numerical

natural frequency $f_{n,num}$ were calculated with respect to the analytical value $f_{n,ana}$ as in equation 2.5 and are shown in Table 2-9. The % error values are plotted in Figure 2-7, to show the convergence of the FE model. Dots in Figure 2-7 correspond sequentially to mesh sizes of Table 2-9.

Table 2-8: Analytical natural frequencies

Vertical mode number	βl value $[m]$	Analytical natural frequency $[Hz]$
1	4.730041	53.166
2	7.853205	146.554
3	10.995608	287.305
4	14.137165	474.929

$$\%Error = \frac{|f_{n,ana} - f_{n,num}|}{f_{n,ana}} \times 100 \tag{2.5}$$

For the first mode of the first mesh size the % error is:

$$\%Error = 0.8540\ \% \tag{2.6}$$

It is clear from Figure 2-7 that when the mesh size is increased there is an overshoot at the 4×40 mesh. This overshoot is due to the numerical calculation and the solution still has to converge. This overshoot reduces from the 16×160 mesh onward and there is an incremental change in % error values and therefore the FE model has more or less converged. There is no real numerical advantage to be gained if the mesh is increased beyond 16×160 elements.

Table 2-9: Mesh size and natural frequency error for mesh independence study

Mesh size $[w_e \times l_e]$	Number of elements	Natural frequency				Average on % Error
		Mode 1	Mode 2	Mode 3	Mode 4	
Analytical	Continuous	53.166	146.554	287.305	474.929	
1×10	10	52.712	144.23	280.56	460.47	
	% Error	0.8540	1.5859	2.3476	3.0445	1.9580
2×20	40	53.07	146.14	286.2	472.59	
	% Error	0.1806	0.2826	0.3845	0.4926	0.3351
4×40	160	53.158	146.61	287.61	475.78	
	% Error	0.0151	0.0381	0.1062	0.1791	0.0846
8×80	640	53.18	146.72	146.72	476.52	
	% Error	0.0263	0.1131	0.2211	0.3349	0.1739
16×160	2560	53.185	146.74	288.02	476.71	
	% Error	0.0357	0.1268	0.2489	0.3749	0.1966
32×320	10240	53.186	146.75	288.04	476.75	
	% Error	0.0376	0.1336	0.2559	0.3834	0.2026
64×640	40960	53.187	146.75	288.04	476.76	
	% Error	0.0395	0.1336	0.2559	0.3855	0.2036

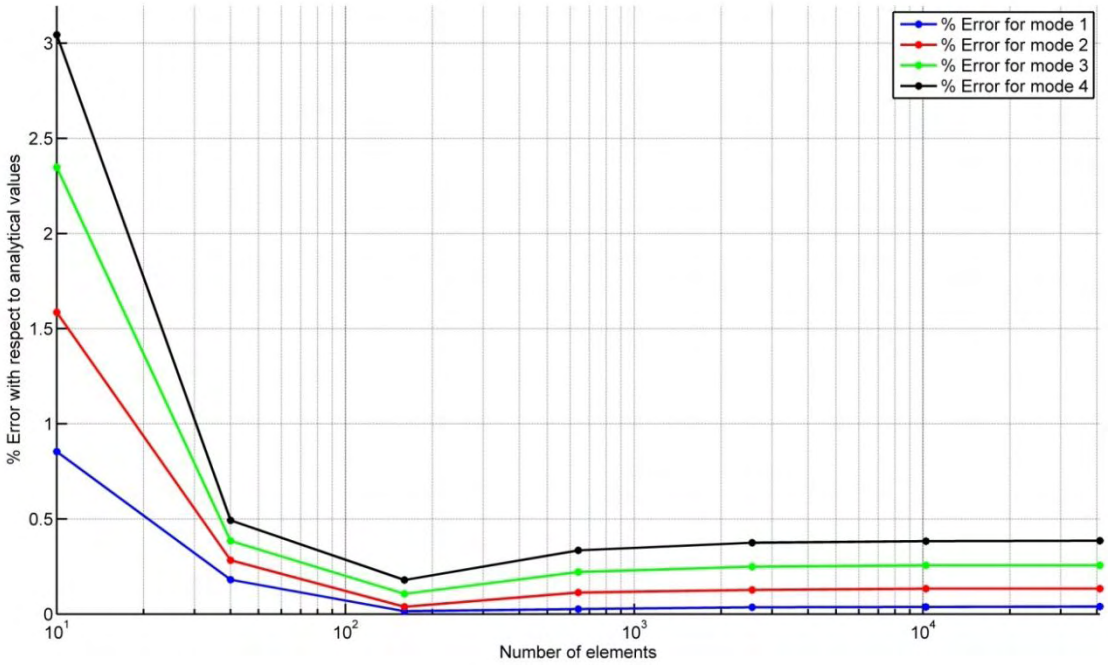

Figure 2-7: % Error to show the convergence of the FE model to the analytical values

A good compromise between accuracy and time spent on solving the system is sought. A time study was performed to establish how long each mesh takes to solve. An average of the time taken to solve the different mesh sizes of Table 2-9, except the 64×640 mesh, was determined. The meshes were solved in Nastran on a computer with the specifications shown in Table 2-10. Four time measurements were made for each of the meshes and their average was determined (Table 2-11). The 64×640 was excluded because the solution more or less converges between the mesh size of 16×160 and 32×320.

Table 2-10: Computer specification

Specification	Value
CPU	Intel Centrino Duo 2.0 GHz, 4 MB L2 cache
Random Access Memory (RAM)	2 GB

Table 2-11: Time taken to solve the different mesh sizes

Mesh size $[w_e \times l_e]$	Time 1 [s]	Time 2 [s]	Time 3 [s]	Time 4 [s]	Average time [s]
1×10	4.1	4	4.7	4.6	4.35
2×20	4.8	4.8	4.5	4.6	4.68
4×40	5.6	5.3	5.7	5.7	5.58
8×80	9.5	9.9	10.7	10.3	10.10
16×160	24.3	24.4	24.4	26.4	24.88
32×320	105.5	104.7	102.4	101.7	103.58

The average on the % error for each frequency at each mesh size (Table 2-9) was plotted against the time taken to solve the different mesh sizes (Table 2-11) and is shown in Figure 2-8. The dots again correspond sequentially to the mesh size in Table 2-11.

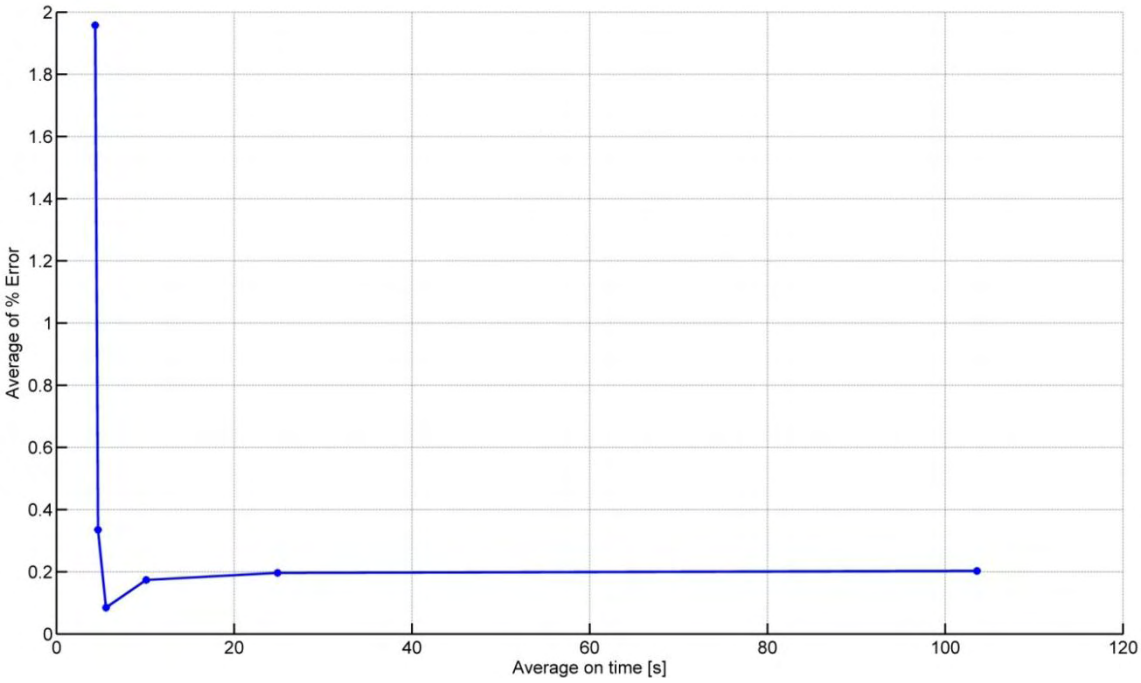

Figure 2-8: The average of % Error versus the time taken to solve the different mesh sizes

It is clear from Figure 2-8 that there is a large increase in solving time between a mesh size of 16×160 and 32×320 (the last two data points). It was established that the FE model converges more or less at a mesh size of 16×160 (Figure 2-7). The great increase in time and the incremental change in % error with a refinement in mesh size therefore warrant the selection of a mesh size more or less equal to 16×160 as there is no gain in refining the mesh, only an increase in time. For other family members that have been normalised with respect to their wing span, this study should give a good indication of the number of elements to be used if the ideal mesh size is more or less equal to 16×160.

Shell elements have inherent shear locking associated with them (Cook et al., 2002). The 16×160 mesh however leads to an element aspect ratio close to 1 with respect to the thickness.

2.2.3 Summary of the mesh size and element type for finite element model

The FE model is based on a family of wings normalised with respect to the wing span. The planar top view of the wings is used and a surface mesh of this view is made. 8-node quadrilateral shell elements with a thickness of 10 *mm* are used and free-free boundary conditions are specified. A mesh size equal or larger than 16 elements through the height of the wing and 160 elements over the length of the wing is desired.

2.3 Dynamic structural model

Dynamic modelling of a structure can be done in various ways. It is possible to directly solve for the time response from the equations of motion obtained from the FE model.

This is however very time consuming if a random input force is used. Another possibility is to calculate the frequency response function (FRF, $H(i\omega)$) of the structure, thus directly calculating the response $\{X\}$, normalised by force $\{F\}$, in the frequency domain (equation 2.7, adapted from Ewins, 1995). The solution of this equation involves the solution of the inverse matrix (dependent on the mass $[M]$, damping $[C]$ and stiffness $[K]$ of the structure), of equation 2.8, for a set of excitation frequencies ω. The solution is faster than the direct solution in the time domain.

$$\{X\} = \left[-\omega^2[M] + i\omega[C] + [K]\right]^{-1}\{F\} \tag{2.7}$$

$$H(i\omega) = \frac{\{X\}}{\{F\}} = \left[-\omega^2[M] + i\omega[C] + [K]\right]^{-1} \tag{2.8}$$

For the proposed method to be implemented, it is necessary to determine the magnitude of the strains at the natural frequencies of interest. If the FE model is solved in the time domain, it is still necessary to convert the response to the frequency domain, after which the magnitude can be determined. If the FRF of the response is determined, it is already in the frequency domain and there is no requirement to convert between domains before any calculations can be performed.

When an FRF of a structure is calculated, it is assumed that the input force, which is used to excite the structure, is also measured. For the proposed method to be implemented on real structures, excited by ambient sources, it is not possible to measure the input force. The method is therefore based on responses only. By computing the FRF, the responses are normalised with respect to the input force and their magnitude relative to input force can be compared. With ambient excitation this relative magnitude is not available and the strain FRF as well as the accelerance FRF are numerically solved and used in subsequent calculations to circumvent this problem. If the strain FRF is divided by the accelerance FRF the transmissibility function between strain and acceleration is obtained. The values of the transmissibility function at the natural frequencies can be used directly in the calculation of the SCDF values of equation 1.10.

There are two different ways of solving the FRF equations. The first is through a direct solver and the second uses a modal solver. The modal solver is preferred as it directly uses the modal damping, which is a function of the critical damping ratio and critical damping value. When the modal solver is used, equation 2.8 is transformed from the physical space to the modal space that decouples the equations of motion. The solution of the uncoupled equations is much faster (MSC.Software Corporation, 2007).

2.3.1 Dynamic structural excitation

The FRFs are computed with a modal solver. There is a question about the excitation of the structure that still has to be answered. In practice, for an aircraft in-flight, the whole wing is excited by a distributed force over the surface of the wing. This force is also random in nature (Braun et al., 2002). In the experimental study however, this distributed loading is difficult to achieve. It was decided to excite the structure at a single

point, within the FE model as well as in the experimental study, in order for the results to be comparable.

The excitation is defined as force normal to the structure, thus out of the plane shown in Figure 2-5. This excitation force is frequency dependent and should be applied over a chosen frequency range. The force used in the FE model has an amplitude of 1 *N* and is defined over a frequency range from 0 to 1350 *Hz*, as this excites the structure up to the 11th mode as shown in Table 3-2.

The excitation force should ideally be located at a position where the force imparted to the structure excites all the modes under consideration, and should not coincide with any of the nodal lines of any of the modes. The normal modes were manually inspected to find a position that is not on or very close to the node or nodal line of a mode. The chosen location have x-y coordinates as shown in Table 2-12 (corresponding to node 4287 of the FE model).

Table 2-12: Coordinates of excitation position

Coordinate	Value [*m*]
x	-0.02652
y	-0.06522

It is possible to perform a pre-test analysis with software such as FEMtools (2008). This allows one to determine the optimum sensor locations. The analysis can be performed by either looking at the normalised modal displacement or by computing the nodal kinetic energy. If the normalised modal displacement method is implemented, the driving point residuals (the location where the excitation and measurement degree of freedom coincide) are computed and compared for a range of mode shapes which are included in the calculation. This analysis provides the ideal sensor locations. Since the drive point residuals are computed, these locations are also ideal excitation positions (Dynamic Design Solutions, 2008b). The position that was determined from inspection was close to a position that was determined by means of the pre-test analysis. It was assumed that this excitation position is adequate for the numerical as well as the experimental study.

2.3.2 Damping in the finite element model

Damping in a structure is usually the most uncertain parameter to predict and may be caused by various mechanisms. One of the main mechanisms of damping is structural or hysteretic damping. This is usually caused by energy dissipation within the material and friction due to connections and between structural components. Damping can be calculated from the logarithmic decrement over decaying oscillations in the time domain. There are other ways in which the damping in the structure can be determined. The modal damping can be estimated from a modal analysis performed on a structure. It is also possible to estimate the damping by updating an FE model with measured FRFs (Dynamic Design Solutions NV, 2008b).

It is necessary to specify damping in the FE model when a frequency response calculation is performed. It is possible to define damping within Patran by specifying the

percentage of critical damping ratio, the hysteretic damping value or the dynamic amplification factor. These values are all interrelated and if one of them is specified, the other two can be determined. The modal damping used in the FE model is estimated from model updating with measured FRFs within FEMtools.

2.3.3 Updated finite element model

The dynamic FE model that was described thus far is an estimate to a real structure. The validity of the model has not been proven and it is not known how well this FE model approximates the real structure. The FE model was updated to improve the correlation between the experimental structure and the numerical estimates. The updating process and the correlation between the FE model and measured data are described in detail in paragraph 4.2.2.

The updated FE model with updated physical material properties as well as updated modal damping is used in the FE model for all the numerical simulations in chapters 3 and 4.

2.4 Strain response calculation

The FE model of the wing family is constructed with the length of the wing in the x-direction and the height of the beam in the y-direction. Such a geometry and mesh is shown in Figure 2-9 for the MQ-1 Predator UAV. This geometry was constructed from the parameters defining the family of wings, which are summarised in Table 2-4. The parameters are normalised with respect to the wing span.

One requirement of the strain-curvature relationship and the flexural formula is that the geometry of the beam should be symmetrical about the y-axis as was shown in Figure 1-3 (paragraph 1.3). This is equivalent to the FE model of the family of wings, being symmetrical about the z-axis of Figure 2-9 when applying the strain-curvature relationship. This is the case as the geometry is symmetrical about the z-axis along the x'-axis (Figure 2-10).

It is required to measure the strains on the surface at a position that is not located on the x'-axis, but rather on the line defined by the x_1-axis (Figure 2-10) that corresponds to one of the lines defined on the FE mesh. The x_1-axis changes its orientation as the symmetry line changes its orientation.

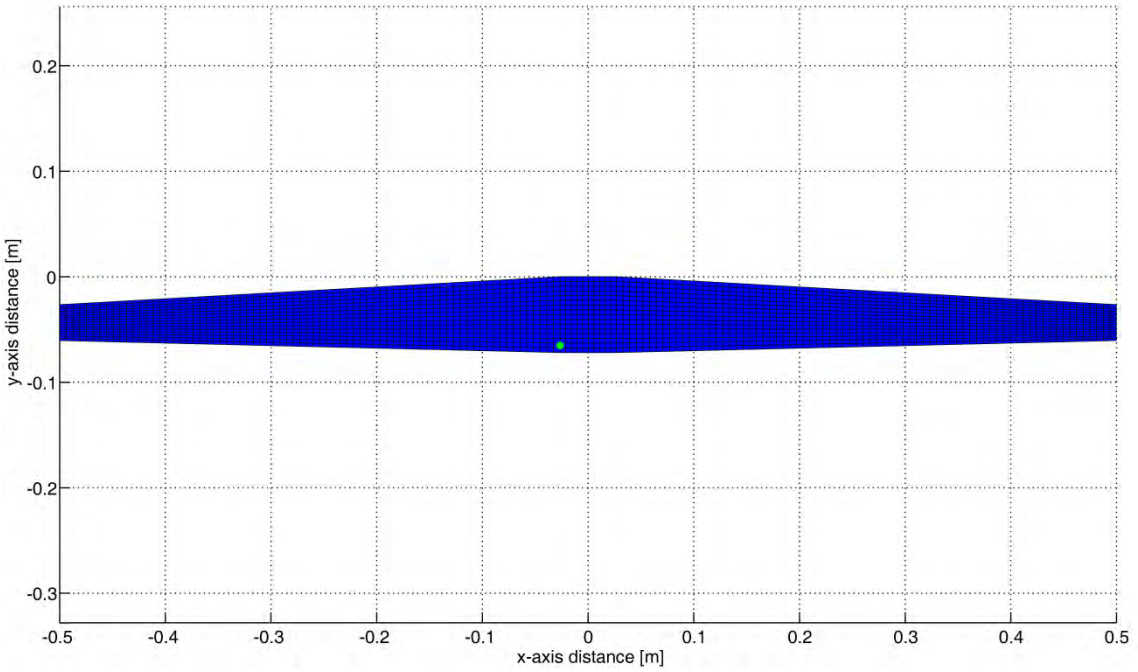

Figure 2-9: Finite element geometry and mesh of the MQ-1 Predator UAV wing planform with excitation position (•)

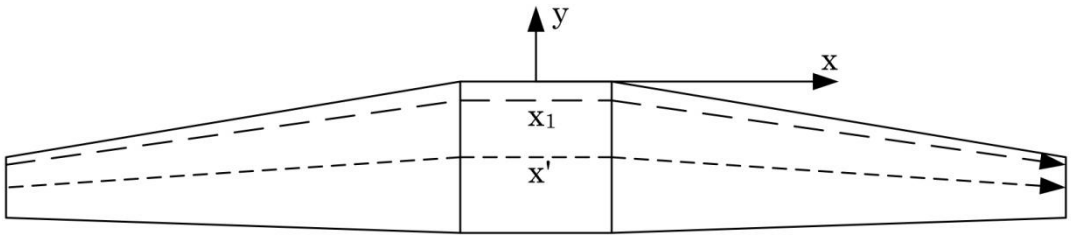

Figure 2-10: Family of wings showing the x'-axis that ensures the geometry remains symmetric about the z-axis and the x_1-axis for measurement purposes

The FE model solves for the strains in the direction of x- and y-axes of Figure 2-9 and Figure 2-10. The strains in the x_1-direction are however required, and a coordinate transformation is necessary. This is shown in Figure 2-11 and the normal strain in the x_1-direction can be calculated by applying equation 2.9 (adapted from Gere, 2004). The transformed strains ε_{x_1} are dependent on the strains in the x- (ε_x) and y-directions (ε_y), the shear strain γ_{xy} and the angle of rotation θ. Although the transformation equation is derived for strains of an element in plane strain, it is applicable to strains of an element in plane stress (Gere, 2004). The thickness dimension of the FE model is much smaller than the length or the height of the FE model. This situation approaches plane stress more than plane strain, but the transformation equations still apply. Even though there might be strain in the z-direction, it does not enter the transformation relationship, because it does not affect the geometrical relationship used in the derivation.

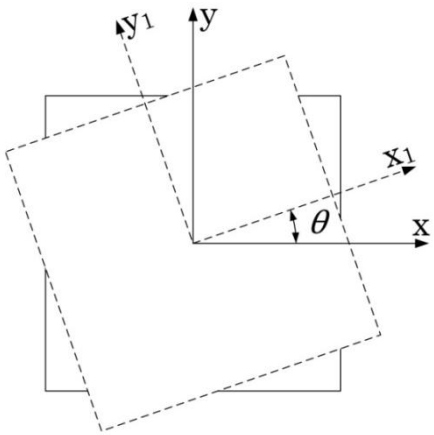

Figure 2-11: Coordinate transformation necessary for the application of the strain-curvature relationship

$$\varepsilon_{x_1} = \varepsilon_x \cos^2\theta + \varepsilon_y \sin^2\theta + \gamma_{xy} \sin\theta \cos\theta \tag{2.9}$$

2.5 Modelling of the structural damage

As was previously argued, isotropic structures are considered in this work as a first step in developing the damage detection technique. The problem with using an isotropic material (mild steel in this case) is the fact that the damage mechanisms associated with this material are different from the damage mechanisms usually found in fibre reinforced composite structures. One of the most common damage scenarios in composites is delamination (Grouve et al., 2008). This type of damage causes a reduction in the bending stiffness of the structure (paragraph 1.2.5).

The problem one is faced with when modelling, is how to model this change in bending stiffness. If the composite structure was built up from layers that are not laminated together (representing a delaminated structure), but instead just held together at the tips, it would have adequate resistance against bending if a pure bending moment was applied to it. This can be attributed to each layer being either in tension or compression and there is no shear force to be transmitted between the layers (Figure 2-12).

The resistance against bending is much less if a shear force is applied to the structure, due to the fact that the layers debonded and therefore cannot transmit the shear force from one layer to the next (Figure 2-13). The shear distribution in each layer causes a bending moment in that layer (Figure 2-13). This bending moment is not carried by the whole structure, but by each individual layer.

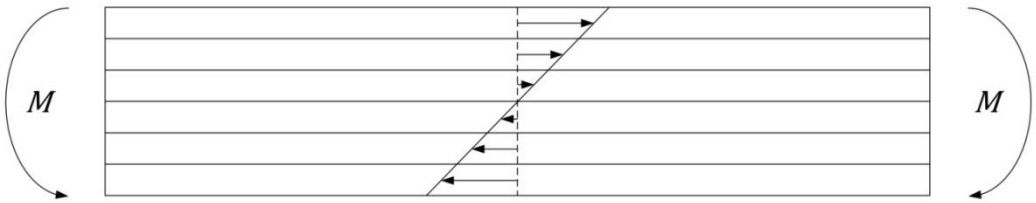

Figure 2-12: Stress distribution due to a bending moment in a delaminated structure

A reduction in bending stiffness is caused by the reduction in the area moment of inertia of the cross section. The structure does not behave as a unit, but rather as individual layers. If the layers are bonded the shear stress can be transmitted between the layers (Figure 2-14) and there is no reduction in bending stiffness as the bending moment is carried by the whole structure.

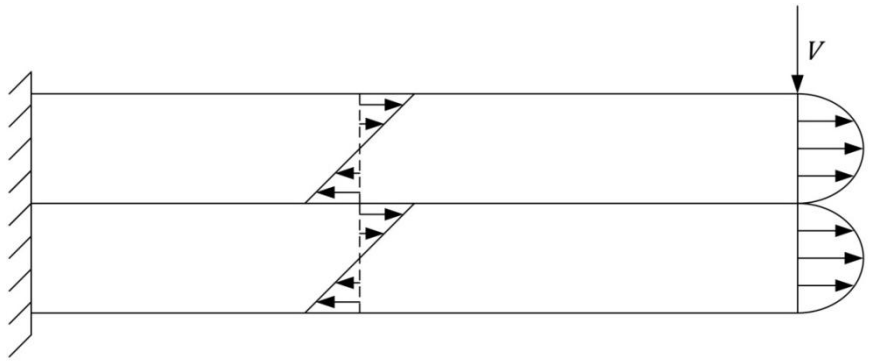

Figure 2-13: Shear and normal stress distribution in a debonded structure

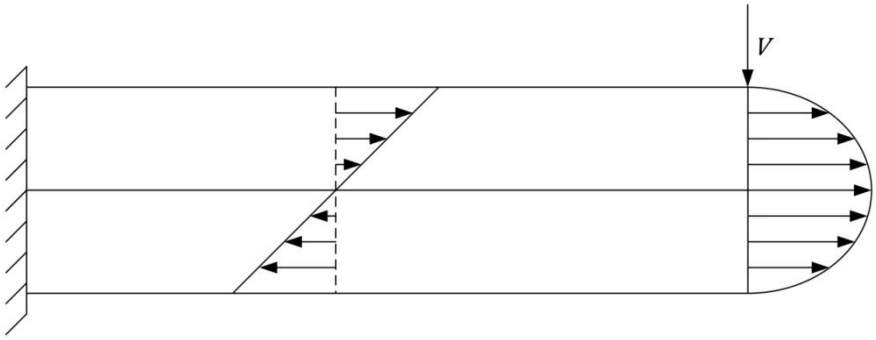

Figure 2-14: Shear and normal stress distribution in a bonded structure

The delamination damage comes from the reduction in area moment of inertia and the reduced bending stiffness associated with it. For a rectangular cross section the area moment of inertia is given by equation 2.2 (repeated in equation 2.10) and it is clear that a decrease in thickness causes the area moment of inertia to decrease.

$$I = \frac{1}{12} w t^3 \tag{2.10}$$

This change in area moment of inertia in turn changes the stress and strain distributions through the cross section, because stress is dependent on the area moment of inertia (Gere, 2004). The change in thickness also changes the value of y (the distance from the neutral surface to the position where the stress is required). If the stress or strain is required on the surface of the structure, the value for y can be substituted with half the thickness of the plate. It can be shown, from the flexural formula of equation 1.6 (repeated in equation 2.11), that the stress would only depend on the thickness (equation 2.13).

$$\sigma_x = -\frac{My}{I} \tag{2.11}$$

$$\sigma_x = -\frac{M\left(\frac{t}{2}\right)}{\frac{1}{12}wt^3} \tag{2.12}$$

$$\sigma_x = -\frac{6M}{wt^2} \tag{2.13}$$

As soon as delamination occurs, the area moment of inertia changes from the expression given in equation 2.10 to the one given in equation 2.14 as a function of the laminate thickness t_l (with reference to Figure 2-15).

$$I = \frac{1}{12}2wt_l^3 \tag{2.14}$$

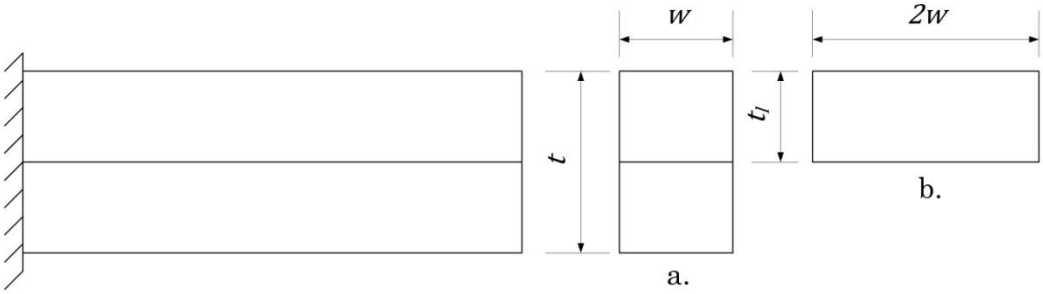

Figure 2-15: Area moment of inertia change due to delamination

This is the same as the effective cross section changing from the one shown in Figure 2-15 a to the cross section of Figure 2-15 b. The area moment of inertia of equation 2.14 is less than the area moment of inertia of equation 2.10. The area moment of inertia of equation 2.14 can be rewritten as a thickness change rather than an increase in width (equation 2.15 with reference to Figure 2-16).

$$I = \frac{1}{12}2wt_l^3 = \frac{1}{12}wt_d^3 \tag{2.15}$$

If equation 2.15 is simplified it leads to a damaged thickness (t_d) value as in equation 2.16.

$$t_d = \sqrt[3]{2}t_l \tag{2.16}$$

The damage and therefore change in area moment of inertia is simulated in the numerical model by changing the thickness at the location of the damage. This will decrease the area moment of inertia as well as change the stress and strain at or near the damage location.

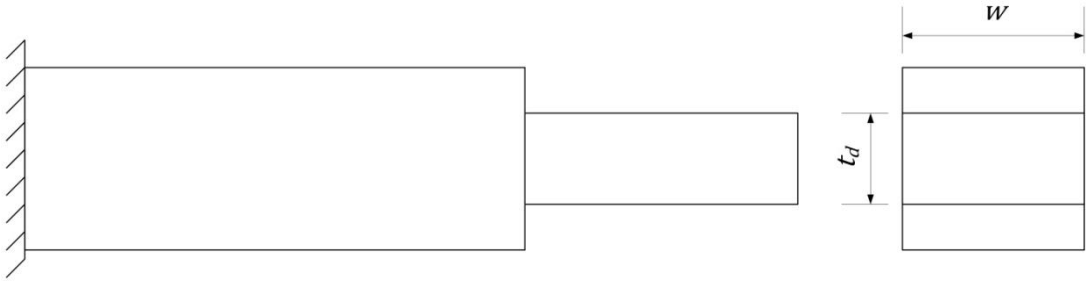

Figure 2-16: Change in thickness to model change in area moment of inertia

The strain at the damage location is sensitive to the delamination size and location between layers. In the derivation of the thickness change due to delamination, a structure with two laminated layers was considered. The strains that are obtained with this method can become erroneous due to the fact that the strains for the delaminated area are effectively at another distance from the neutral axis within the structure than in the case with only a thickness change. When the thickness change is used to model the delamination damage (Figure 2-16), the location of the neutral axis is not changed (Figure 2-17 a). However when delamination occurs, the neutral axis can shift and therefore the strains relative to the neutral axis might be smaller than predicted due to asymmetrical bending about the neutral axis (Figure 2-17 b). The asymmetrical bending case may arise if one or more of the delaminated layers do not contribute to the stiffness of the structure.

The change in thickness (as in Figure 2-17 a) can easily be modelled with shell elements. The asymmetrical bending case is difficult to model as the thickness of the structure will have to be modelled and elements will have to be removed to simulate the damage. The numerical model is used to study the effects of different damage locations and sizes. The best way to model the damage is with a change in thickness and using shell elements. This may not always produce exact results but it assists in the modelling and changes in damage parameters. The time expense for solving an FE model built from shell elements is much less than with hexahedral elements. The shell model is used in spite of a few limitations.

It is possible to change the value of Young's modulus in the damaged area. This causes the bending stiffness to decrease. This approach is easy to implement numerically, but very difficult experimentally. For this reason the change in bending stiffness due to a change in thickness makes more sense, as it can be implemented numerically and experimentally.

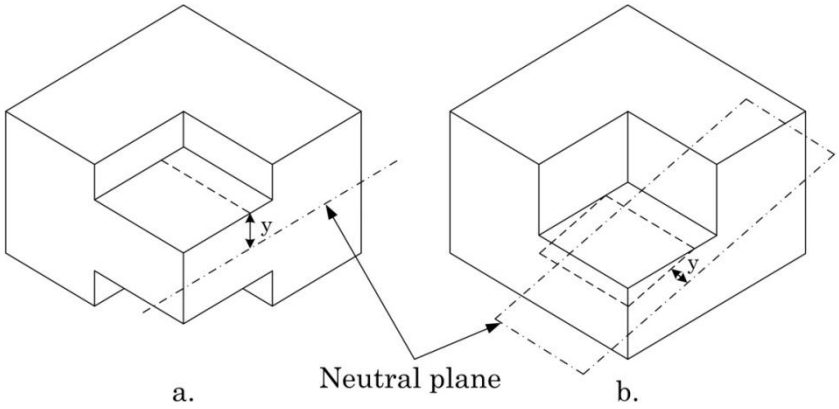

Figure 2-17: Neutral axis location for a symmetrical and asymmetrical structure

2.5.1 Deterministic damage cases

Literature on failure data with respect to the size and shape of delamination damage in UAVs could not obtained. This type of data is rarely recorded and not necessarily published in the public domain as UAVs are often built and operated by the military. Assumptions on the parameters defining the shape and size of the damage had to be made. The damaged area shares the same characteristic parameters as the family of wings. The location of the damage is specified by choosing the parameters shown in Figure 2-18 and Figure 2-19. The parameters of Figure 2-18 locate the damage area, whereas the parameters of Figure 2-19 specify the size of the damage area.

The damage may be varied by varying the thickness of the plate at a known location. One type of damage geometry is investigated and the level of damage at the damage location is varied. The influence of the change in thickness on the shape of the SCDF graph and the SFDL values are investigated with these deterministic cases. The original thickness of the plate is equal to 10 mm. The level of damage at the damaged area is expressed as a percentage of this original thickness t_o according to equation 2.17.

$$\%Damage = 100\frac{t_o - t_d}{t_o} \tag{2.17}$$

The size of the damaged area can be calculated from the parameters defined in Figure 2-19. The area of the damage and the area of the wing section of the family, can thus be computed in the same manner. This can be accomplished by subdividing the shape of Figure 2-19 into a trapezium and a triangle (Figure 2-20). The area of this shape can then simply be computed from equation 2.18. The area of the wing section A_w is a function of the height h and width of the trapezium b_{trap} and the triangle b_{tria}. The total area A_{tot} of the family of wings can be computed from equation 2.19, by using the result of equation 2.18 and the length of the fuselage l_f multiplied by the chord length at the interface of the root and the fuselage c_r.

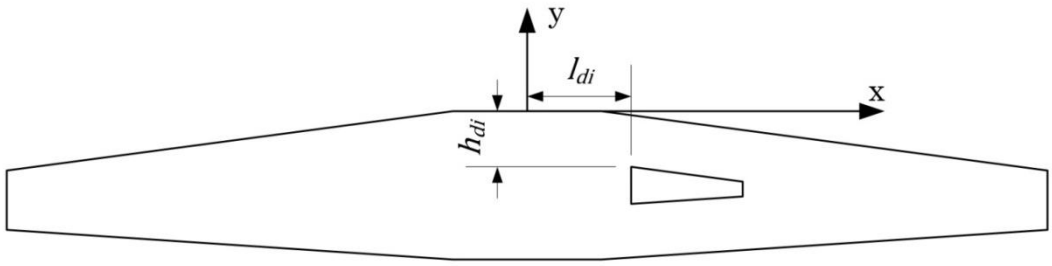

Figure 2-18: Parameters defining the damaged area location with respect to the coordinate system

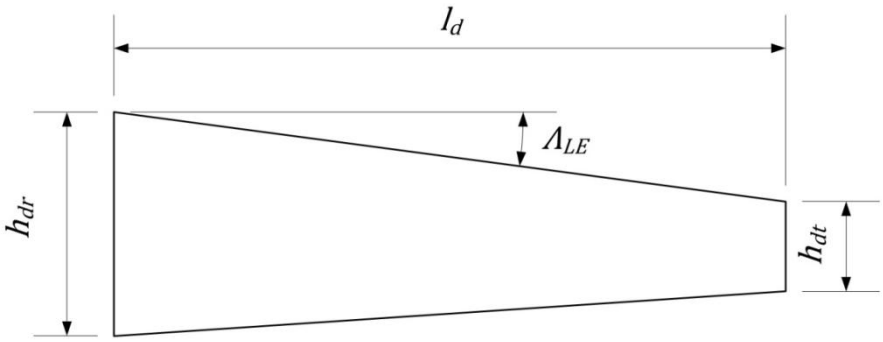

Figure 2-19: Parameters defining the size and profile of the damaged area

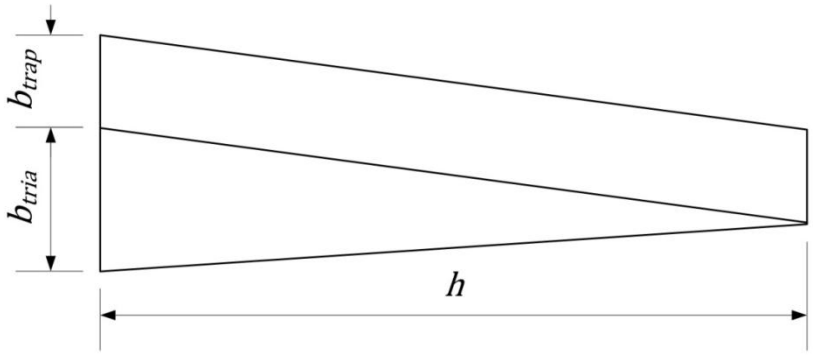

Figure 2-20: Subdivision of wing section for computation of the area

$$A_w = \frac{1}{2} h b_{tria} + h b_{trap} \tag{2.18}$$

$$A_{tot} = 2A_w + l_f c_r \tag{2.19}$$

2.5.2 Stochastic damage cases

The influence of the change in thickness as well as the damage location are studied by varying the location of the damage as well as the thickness of the damaged area stochastically. The stochastic damage cases are used to investigate the way in which the SFDL values are influenced as more sensors are added and the damage level is varied. The same definition of the damaged area described in paragraph 2.5.1 is used.

The parameters allowed to vary are summarised in Table 2-13. The statistical distributions used to vary the size randomly were chosen based on the area on a wing surface that is most prone to fatigue damage due to larger stresses and critical areas or areas which may lead to catastrophic failure once damaged. These areas are mainly located close to the fuselage or at the root of the wings and the part on the airfoil that is the thickest. This part of the airfoil is usually supported by a spar to increase the bending stiffness and reduce the stresses in the airfoil structure. If any of these locations are damaged it could lead to a catastrophic failure of the whole wing.

Table 2-13: Parameters that were allowed to vary randomly

Parameter	Statistical distribution
l_{di}	Exponential
h_{di}	Lognormal
h_{dr}	Uniform
l_d	Uniform
h_{dt}	Dependent on l_d and h_{dr}
t	Dependent on all parameters

The exact form of the statistical distributions used to randomly generate the first three parameters of Table 2-13 are shown in Figure 2-21.

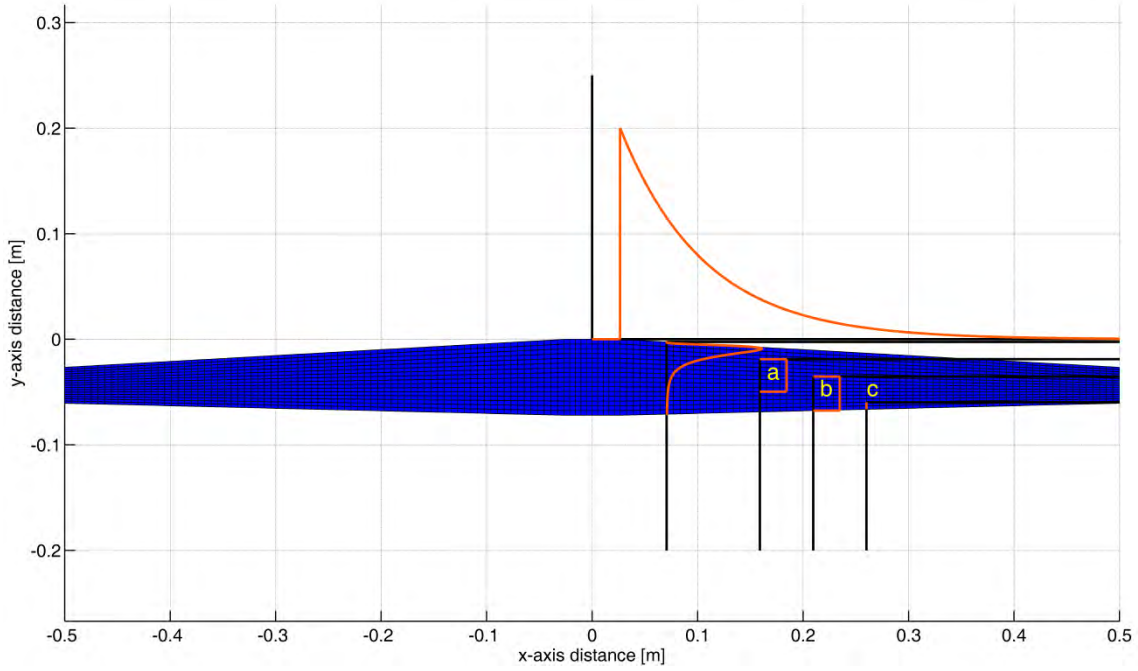

Figure 2-21: Statistical distributions from which the parameters are randomly generated

The parameters of Table 2-13 are randomly varied with Matlab's (2008) *random* algorithm. This algorithm allows the user to specify a statistical distribution and the parameters defining it. The algorithm generates a random value based on the shape of the probability density function of the distribution.

The parameters are generated in the order shown in Table 2-13. The x-distance for the starting point is generated from the exponential distribution. This distribution is chosen since the damage is most likely to occur close to the fuselage. This is a higher stressed area due to the wing acting as a cantilevered beam and fatigue damage will most probably originate here. This distribution has a mean value (μ) of 0.08 and the mean value was chosen for the probability density function to approach zero at the tip of the wing. The distribution is shifted along the x-axis to start where the wing would join the fuselage; therefore the function value starts at zero and reaches the maximum where the wing joins the fuselage.

Once the start location on the x-axis has been generated, the start location on the y-axis can be generated. This is accomplished by defining a lognormal distribution between 0 and 1. A lognormal distribution is chosen as the position of the damage is most likely to start close to the thickest part of the airfoil. This part of the airfoil is the highest stressed area and therefore fatigue will most probably originate here. The mean value $\mu_{h_{di}}$ is dependent on the length (y_{meas}), from the leading edge to the measurement line (Figure 3-2), relative to the wing width w_w at the x-value of the starting location plus a constant value of -0.04 (equation 2.20). The constant value is added to force the distribution to initiate the starting position earlier. This in turn forces the damaged area to be located closer to the thicker airfoil section. The standard deviation of the lognormal distribution $\sigma_{h_{di}}$ is determined from the mean value by using a coefficient of variation (γ) equal to 0.35 (equation 2.21).

$$\mu_{h_{di}} = \frac{y_{meas}}{w_w} - 0.04 \tag{2.20}$$

$$\sigma_{h_{di}} = \gamma \mu_{h_{di}} \tag{2.21}$$

A random value can be generated from a lognormal distribution with the mean and standard deviation calculated from equations 2.20 and 2.21. The y-value of the starting position is then obtained by multiplying the generated random value by the wing width and adding the y-value of the leading edge at the x-starting position. This scales the random value obtained from a lognormal distribution between 0 and 1 to a value located on the wing, between the leading and trailing edge. The starting point of the damaged area is defined from the value obtained from the exponential distribution and the lognormal distribution and this point defines the top left corner node of the damaged area.

The third parameter that has to be generated randomly is the height of the damage at the root side of the wing. This is accomplished by generating a random value from a uniform distribution. This uniform distribution is limited in size. If the damage starting point is more than 10 nodes from the node at the trailing edge, the uniform distribution is defined over 8 nodes from the starting point (distribution a on Figure 2-21). If the starting point is less than or equal to 10 nodes from the bottom, the uniform distribution is defined from the starting point to the node at the trailing edge as for distribution b of Figure 2-21. In both these cases the random value has an equal chance to be generated in the region over which the distribution is defined. This constraint is placed on the region to limit the size of the damage. If this height becomes too great, the damaged area

can become too large and the response might no longer be linear. If the starting point is at a node less than or equal to 3 nodes from the node at the trailing edge, the height of the damage at the root side is set equal to the distance from the starting point to the trailing edge as for plot c in Figure 2-21. After this parameter has been generated, the bottom left corner node of the damaged area is defined.

The following parameter that has to be generated is the length of the damaged area. This is randomly generated from a uniform distribution which is constrained by the height of the damage on the root side h_{dr}. The uniform distribution is limited to the length of the wing beginning at three nodes to the right of the starting node and ending at a value which is proportional to the ratio of the damaged height at the root to the width of the wing remaining from the starting point. This ratio if multiplied by 40% of the remaining wing length from the starting point $(l_{w_{rem}})$, thus the length from the starting point to the tip of the wing, produces the end value of the distribution (equation 2.22).

$$Distribution_{end} = 0.4\frac{h_{dr}l_{w_{rem}}}{w_w} \tag{2.22}$$

The random value generated for the length of the damage, is constrained to the line of nodes passing through the starting node and is therefore dependent on both the starting point and the height on the root side. This parameter then defines the top right corner node of the damaged area.

The height of the damage on the tip side of the wing is dependent on both the length of the damage and the height of the damage on the root side. This parameter is not generated randomly, instead it is located at the node at the intersection of a line drawn to the right of the bottom left node and a line vertically from the top right node of the damaged area. Both these lines are coincident with the element boundaries of the FE model.

The only parameter left to calculate is the thickness of the damaged area. The assumption in this case is that the damaged area will grow due to fatigue during flight. The change in thickness is used to increase the level of damage. As the damaged area is increased it is assumed that it has the same affect as a propagating crack, thus the larger the damaged area, the higher the level of damage.

In the present study a steel structure is investigated and since a function such as the FRF is used it implies the assumption of linearity of the structure and the response. It is therefore assumed that any crack growth due to fatigue falls within the linear regime and that the principles of fracture mechanics hold. The principles of fracture mechanics is used to obtain the relationship between the size of the damage and the thickness of that area. The thickness is related to the level of damage as this is the parameter that changes the characteristics of the structure.

According to the Paris law a relationship between the crack growth rate and the stress intensity range exists as shown in equation 2.23 (Dowling, 2007).

$$\frac{da}{dN} = C(\Delta K)^m \tag{2.23}$$

The ratio change in crack length da to the change in cycles dN is proportional to the stress intensity range ΔK to the power m (a material constant) multiplied by a material constant C.

The value of the stress intensity range is proportional to the stress range and the type of crack. If it is assumed that the loading cycle remains constant, the stress intensity range will remain constant, which implies that the right hand side of equation 2.23 becomes a constant (k_1). The crack growth is then linearly dependent on the cycles that the structure was exposed to (equation 2.24).

$$da = k_1 dN \tag{2.24}$$

It is assumed that the delamination area (A) will grow due to fatigue and therefore the area will increase with an increase in the number of cycles (equation 2.25).

$$dA \propto dN \tag{2.25}$$
$$\therefore k_2 dA = dN \tag{2.26}$$

Since crack size (a_d) gives an indication of the damage level it is assumed that the crack size is related to the thickness through equation 2.27 as the thickness indicates the damage level in the present study.

$$a_d = t_{tot} - t_d \tag{2.27}$$

It is assumed that the crack will always grow from an undamaged length $(a_o = 0)$ and thus the number of cycles initially equals zero $(N_o = A_o = 0)$. This assumption together with the result of equation 2.26 and 2.27 are substituted into equation 2.24 and results in equation 2.28:

$$t_d = t_{tot} - k_1 k_2 A_d \tag{2.28}$$

Equation 2.28 implies that the thickness, used to model the damaged area, is linearly related to the damaged area with the constant equalling the total thickness of the structure. The gradient of the linear relationship needs to be calculated. This constant can be determined if an assumption is made on the size of the damage that will lead to catastrophic failure. It was assumed that when the damage level is equal to 50% $(t_d = 0.5t_{tot})$ and the damaged area equals 13% of the left or right wing area it will lead to a catastrophic failure. The total thickness of the structure was chosen to equal 10 mm and the right wing area for the MQ-1 Predator wing is equal to 0.0251 m^2.

It is possible to calculate the gradient from equation 2.28 with these assumptions and this results in a gradient equal to 1.5323 (equation 2.29).

$$t_d = t_{tot} - 1.5323A_d \tag{2.29}$$

All the parameters defining the damaged area have been defined. It is possible to generate the size and shape of damaged area randomly and to perform simulations to determine the effect of the size and shape on the value of the SFDL.

Chapter 3: Numerical study

This chapter is concerned with the numerical implementation and validation of the proposed method. The performance of the parameters can be judged when it is implemented on a real structure or equivalent numerical model. Vast numbers of test cases can be studied numerically, because changes and simulated measurements can be made relatively quickly in a numerical domain. The FE model created for the family of wings was described in chapter 2 and is implemented in chapter 3 for the numerical study.

The objectives of this chapter are to:

1. Investigate the influence of damage on the change in the two damage indicator values to evaluate the damage detection capabilities of the proposed damage indicators.
2. Investigate the effects of damping on the SCDF values.
3. Study the effects of the way in which damage can present itself in the structure on the damage indicators.
4. Investigate the proposed damage detection method, with accompanying indicators, as it applies to different members of the family of wings.
5. Determine the minimum number of sensors, as well as the placement of these sensors on the structure, to be able to detect and localise damage.
6. Evaluate the performance of the proposed indicators when the damage location is unknown and random.

With reference to Figure 3-1, these objectives will be achieved by:

1. Creating an updated FE model of the MQ-1 Predator wing and numerically studying two distinct deterministic damage cases as the damage level is changed. This analysis is performed in paragraph 3.1.2.1 and 3.1.3.1.
2. Using damage case 1 to numerically study the influence of damping on the SCDF values (paragraph 3.1.2.2).
3. Modelling damage case 2 in two different ways, firstly with a shell element FE model and secondly with a hexahedral element FE model. The data is extracted at the corresponding positions and a comparison between the two models is made (paragraph 3.1.3.2).
4. Creating FE models of other family members and creating deterministic damage cases in these models. The damage detection method is applied to these models and the performance of the proposed indicators is evaluated as it applies to other family members in paragraph 3.2.
5. Stochastically (randomly) varying the location of damage within the FE model of the MQ-1 Predator wing structure and applying the damage detection method to the simulated values. This procedure is carried out whilst the number of sensors

are increased and the change in damage indicator values are examined and evaluated (paragraph 3.3.1).

6. Studying the stochastic variation damage cases and evaluating the performance of the SCDF and SFDL values to localise and indentify the damage in the structure.

Paragraph 3.1.1 serves as a supplement to the deterministic study performed on the MQ-1 Predator wing in paragraphs 3.1.2 and 3.1.3. It is used to describe the natural modes that will be included in the analyses as well as the measurement locations for both acceleration and strain.

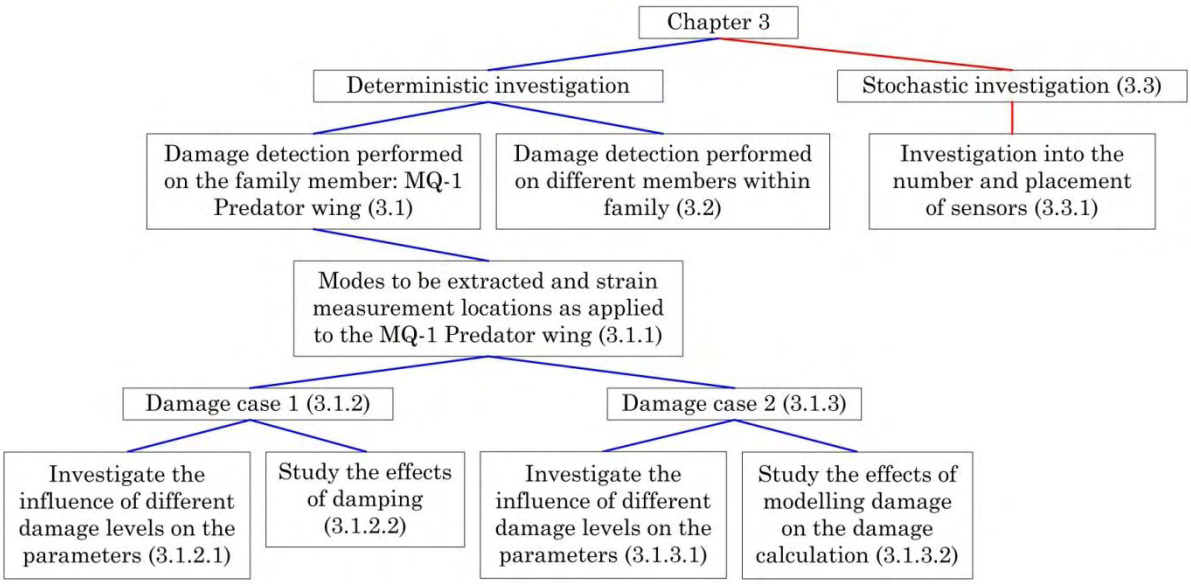

Figure 3-1: Layout of chapter 3

3.1 Deterministic variation of damage location within the MQ-1 Predator wing

The deterministic numerical study of the SCDF values and the damage indicator (SFDL) is conducted on the MQ-1 Predator wing. The FE model of the Predator wing was created by following the modelling method explained in chapter 2. The updated model obtained from the model updating described in paragraph 4.2.2 is used for the numerical study on the MQ-1 Predator wing. The parameters used to construct the geometry were taken from Table 2-4 and normalised with respect to the wing span. These parameters are summarised in Table 3-1. Two damage cases are investigated and applied to the MQ-1 Predator wing.

Table 3-1: Parameters defining the MQ-1 Predator wing geometry

Parameter	Original value	Normalised value
Wing span (b) [m]	14.84	1
Length of fuselage (l_f) [m]	0.787	0.053032
Sweep angle (Λ_{LE}) [°]	3.2	3.2
Chord at root (c_r) [m]	1.068	0.071968
Chord at tip (c_t) [m]	0.506	0.034097

3.1.1 Modes extraction and strain measurement locations

The damage indicator parameters in paragraph 1.3 require the strains at the measurement locations. The vertical bending modes as well as the torsional modes are measured experimentally as these modes are out-of-plane and thus in the z-direction of Figure 2-10. For this reason the vertical bending and torsional modes are considered during the experimental study. The types of modes that were calculated numerically are shown in Table 3-2. In this table VB refers to a vertical bending mode, IPB refers to an in-plane bending mode and T refers to a torsional mode. The numerical analysis was restricted to only 1350 Hz, as there are 9 modes (vertical and torsional modes) of interest up to this frequency. The time required to solve the FE model up to this frequency had to be taken into account. It is possible calculate the response to higher frequencies, but this implies longer solution times. There is a practical limit on the highest frequency that a strain gauge can measure (Hoffman, 1989); however, the strain gauges used during the experimental study can accurately measure up to a frequency of 1350 *Hz* (paragraph 4.1.3.2).

Table 3-2: Type of mode shapes for the undamaged MQ-1 Predator wing (with reference to the updated model)

Mode number	Frequency [*Hz*]	Type
1	61.49	VB
2	155.50	VB
3	296.67	VB
4	378.84	IPB
5	484.97	VB
6	712.17	VB
7	726.27	T
8	837.77	IPB
9	1005.10	VB
10	1191.00	T
11	1321.40	VB

When the numerical simulations and experimental study were performed, restrictions concerning the modes that could be included were observed. During the numerical study it was noticed that modes 6 and 7 cross over at certain levels of damage. It is difficult to identify when this frequency crossover occurs and there are associated difficulties in distinguishing these modes (see paragraph 3.1.2.1). During the experimental study the correlation for the torsional strains at mode 10 was inadequate (paragraph 4.2.3.2). The

test structures are excited to excite the out of plane bending and torsional modes. Mode 4 and 8 are therefore not excited and measured during the experimental study. Modes 4, 6, 7, 8 and 10 are therefore excluded from the numerical study. The modes considered are modes 1, 2, 3, 5, 9 and 11.

To verify the use of the damage indicator (SFDL), the process was started off with as many measurements as possible. These measurement locations were arbitrarily chosen to be 10 locations on the right and left part of the wing with 2 locations on the fuselage. The measurement locations on the wing sections are uniformly spaced throughout the FE model and their positions together with the measurement positions on the fuselage are shown in Figure 3-2. When the measurement line is considered, it can be seen that the measurements are not made on the neutral axis of the structure, which makes it possible to measure the torsional modes, although they are not used in subsequent calculations.

The strains are extracted at the nodes indicated by the yellow circles (Figure 3-2), and these calculated strains serve as estimates to the measured strain. In the experimental investigation the measurements are made at these locations and lies on the x_1-axis (Figure 2-10). The strain values at these nodes are extracted and converted to strains on the x_1-axis and the damage calculation is performed on these transformed strains.

For the numerical study, the accelerance FRF is only calculated at one node. This node serves as the reference acceleration node and the transmissibility functions are calculated by dividing the strain FRFs by the accelerance FRF at the reference node. The reference acceleration is measured at the green circle indicated on Figure 3-2 and the physical location is given in Table 3-3.

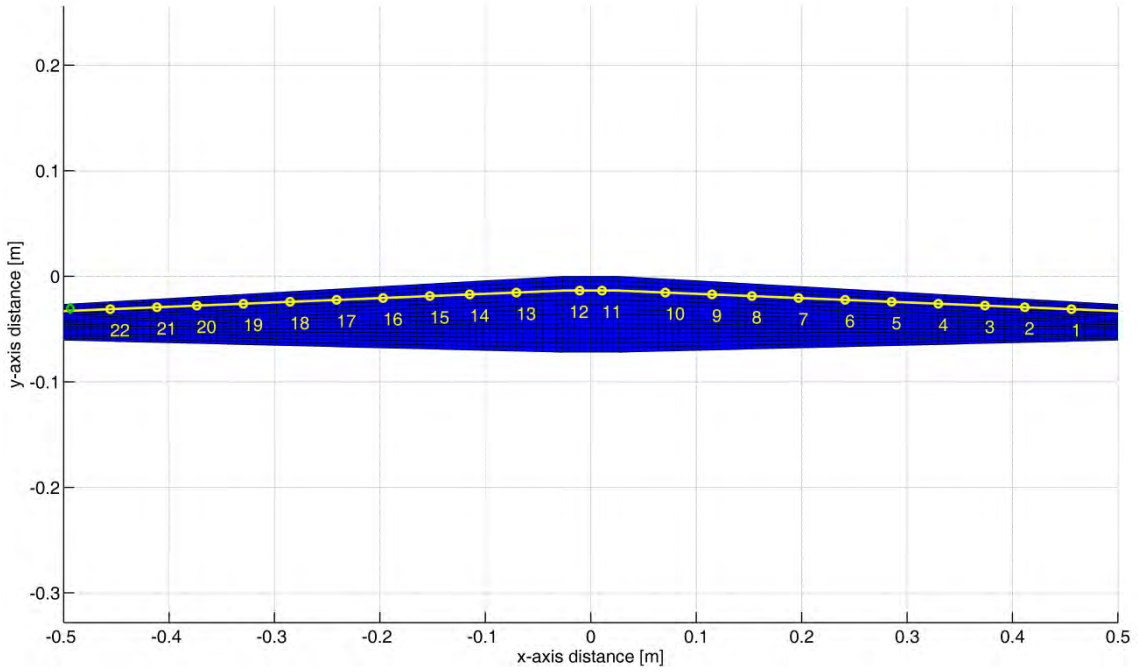

Figure 3-2: Locations and numbers for strain measurements in yellow and location of the acceleration measurement in green for the FE model of the MQ-1 Predator wing

Table 3-3: Coordinates of the acceleration measurement position

Coordinate	Value [*m*]
x	-0.4937
y	-0.0304

The extraction of the modes of interest, the strain and acceleration values are all performed in Matlab (2008). The two damage parameters, the SCDF and the SFDL, are subsequently calculated from the extracted natural frequency, strain and acceleration values by implementing equations 1.10 and 1.11. The two main Matlab scripts used to perform the extraction and the calculations are given in Appendix A.

3.1.2 Damage case 1

Damage was introduced in the Predator wing by choosing the parameters described in paragraph 2.5.1. These values for the first deterministic case are listed in Table 3-4. The size of the damaged area A_d is calculated in equations 3.1 to 3.2 and is shown in Table 3-4. The areas of the right section and the total wing shape of the MQ-1 Predator are calculated in equations 3.3 to 3.7. This results in the damaged area being equal to 8.366% (equation 3.8) of the right wing section and 3.888% of the total area (equation 3.9).

Table 3-4: Parameter values defining the damaged area for case 1

Parameter	Value
l_{di}	89.647 mm
h_{di}	24.639 mm
l_d	88.384 mm
h_{dr}	25.094 mm
h_{dt}	22.443 mm
Λ_{LE}	1.771°
A_d	$2.101 \times 10^{-3}\ m^2$
Ratio of damaged area to the area of right wing section	8.366%
Ratio of damaged area to the area of the complete wing	3.888%

The damaged area is calculated from the length of the damage l_d and the two parameters defining the height at the root h_{dr} and tip h_{dt} of the damaged area.

$$A_d = \frac{1}{2} l_d (h_{dr} - h_{dt}) + l_d h_{dt} \tag{3.1}$$

$$A_d = 2.101 \times 10^{-3}\ m^2 \tag{3.2}$$

The area of the right wing section can be calculated from equation 3.3.

$$A_w = \frac{1}{2} l_w (c_r - c_t) + l_w c_t \tag{3.3}$$

The length of the wing (l_w) is computed from the wing span and the width of the fuselage as in equation 3.4, with b referring to the wing span.

$$l_w = \frac{1}{2}(b - l_f) \tag{3.4}$$

$$l_w = 0.473485\ m \tag{3.5}$$

The result of equation 3.5 can now be substituted into equation 3.3 to obtain the area of the right wing section.

$$A_w = 25.113 \times 10^{-3}\ m^2 \tag{3.6}$$

The total area of the wing shape can now be calculated from equation 2.16 with the result of equation 3.6.

$$A_{tot} = 54.043 \times 10^{-3}\ m^2 \tag{3.7}$$

The percentage of the area that is taken up by the damaged area with respect to the wing and total area is calculated in equation 3.8 and 3.9, respectively.

$$Wing\ ratio = 100\frac{A_d}{A_w} = 8.366\ \% \tag{3.8}$$

$$Total\ ratio = 100\frac{A_d}{A_{tot}} = 3.888\ \% \tag{3.9}$$

Measurement locations 8 and 9 of Figure 3-2 are located close to this damaged area. The location of this damage as well as the measurement locations is shown in Figure 3-3. In this case the load carrying capability is reduced in the damaged area. The remaining undamaged material is in an elevated strain state, because the load is redistributed in the vicinity of the damage. Measurement locations 8 and 9 are located in the undamaged material and therefore an elevated strain is measured (Figure 3-4). It is this feature that is used to indicate the presence and the location of the damage and which, due to its influence on the values of the yCDF and SCDF, in turn changes the SFDL value.

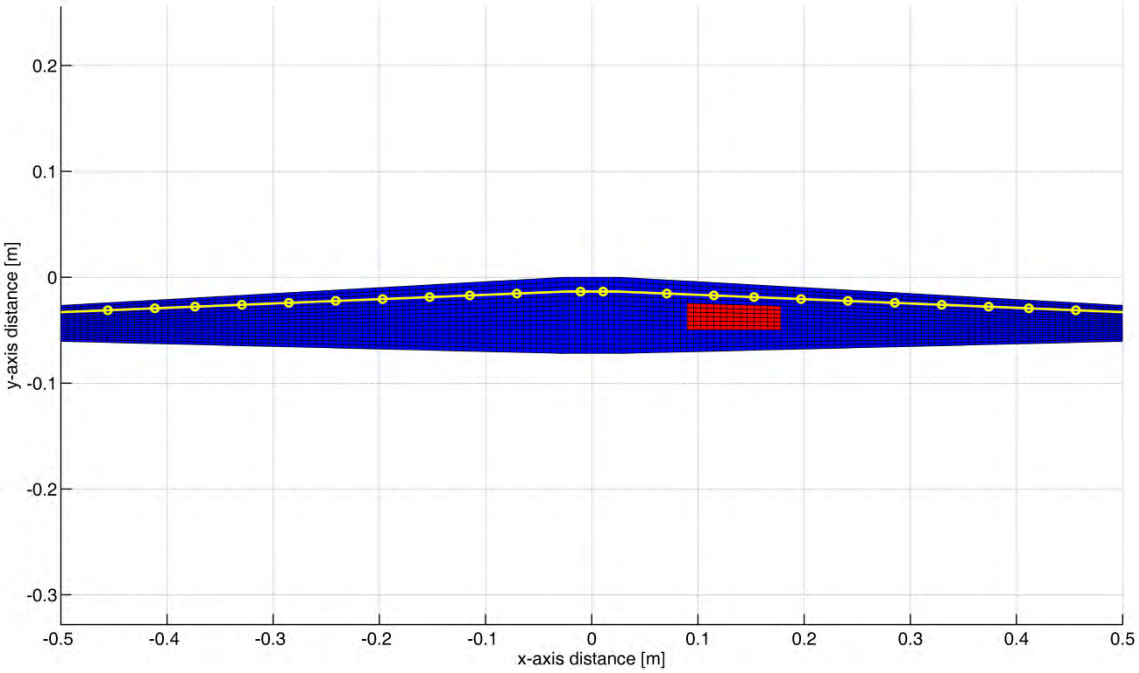

Figure 3-3: Damage location with measurement locations for deterministic damage case 1

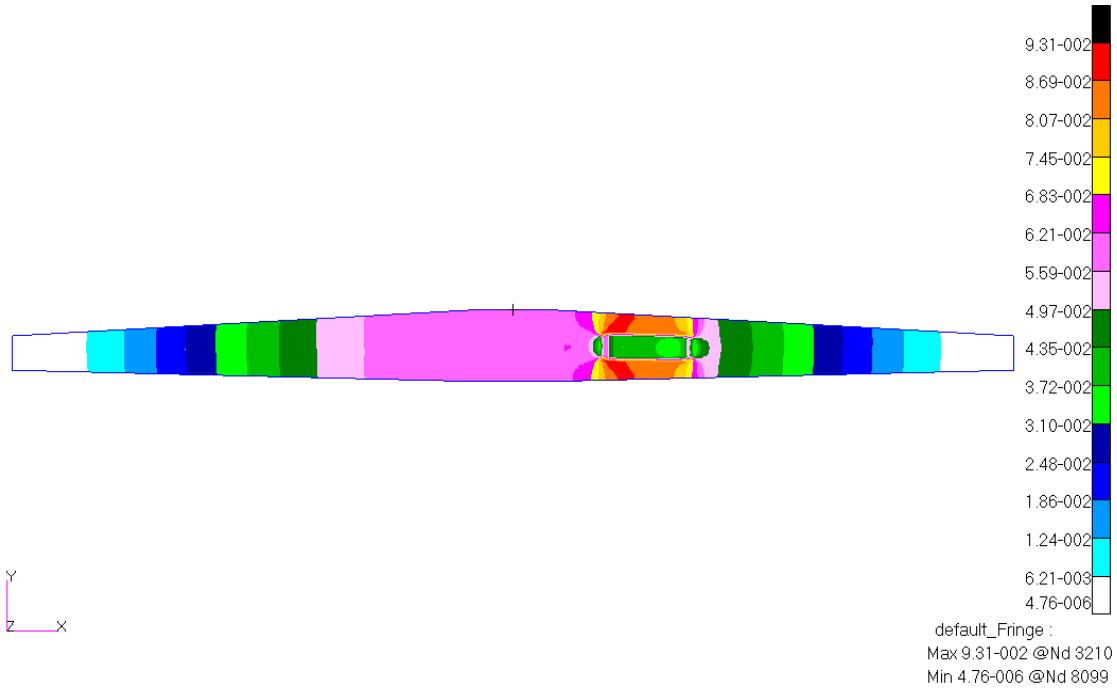

Figure 3-4: Strain field for first bending mode of the wing for case 1 with 50% damage

3.1.2.1 Investigation of different levels of damage for case 1

The level of damage is varied in this section by changing the thickness in the damaged area. The effect of the change in damage levels on the yCDF (equation 1.9), the SCDF (equation 1.10), the change in natural frequency and the damage indicator (SFDL of equation 1.11) values are now investigated. The damage varies from 5% to 50% in 5%

increments, and the thickness changes from 9.5 to 5 *mm* in increments of 0.5 *mm*. The natural frequencies and type of mode are listed in Table 3-5 against the mode numbers extracted from Patran for 10% to 50% in increments of 10% to show the change in natural frequency value as the damage is increased.

In Table 3-5 the type of mode is indicated next to the damage level. If the mode type of the higher damage level corresponds to the mode types of the lower damage level, the mode types are only indicated next to the highest damage level that still shows this correlation. It can therefore be said that for 20% damage modes 6 and 7 were a vertical and torsional mode respectively, but at 30% these two modes swapped around and mode 6 became a torsional mode whereas mode 7 became the vertical bending mode. As damage is introduced in a structure it is possible for frequencies to cross over. In other words the natural modes might change order after the damage was introduced or the damage level is increased. If these frequency crossovers are not known or are neglected, the diagnosis of the damage state will give incorrect results (Rytter, 1993).

When the numerical calculations and comparisons are made, it is difficult to distinguish between vertical bending modes and torsion modes when only natural frequencies and strain values are available. It was therefore decided to exclude modes 6 and 7 as the situation might arise where strains from the vertical bending mode are compared to strains from the original torsional mode.

Table 3-5: Type of mode shapes for damage levels of case 1

Mode number	10% Damage frequency [*Hz*]	20% Damage frequency [*Hz*]	Type	30% Damage frequency [*Hz*]	40% Damage frequency [*Hz*]	50% Damage frequency [*Hz*]	Type
1	60.99	60.51	VB	60.05	59.66	59.33	VB
2	154.65	153.88	VB	153.21	152.69	152.33	VB
3	296.49	296.29	VB	296.08	295.88	295.68	VB
4	379.05	379.25	IPB	379.46	379.66	379.85	IPB
5	482.34	480.07	VB	478.23	476.91	476.14	VB
6	710.15	708.37	VB	701.95	693.51	685.65	T
7	718.68	710.51	T	706.98	705.88	705.17	VB
8	839.04	840.31	IPB	841.58	842.83	844.04	IPB
9	1002.80	1000.60	VB	998.58	996.72	995.15	VB
10	1179.90	1168.70	T	1158.00	1148.10	1139.50	T
11	1316.00	1311.70	VB	1308.50	1306.60	1305.90	VB

Comparisons between the natural frequencies of the modes that are used in the calculation of the SFDL value are shown in Table 3-6 and Table 3-7.

Table 3-6: Comparisons of the natural frequencies for different levels of damage of case 1

Mode number	Undamaged	10% Damage	%Change	20% Damage	%Change	30% Damage	%Change
1	61.49	60.99	0.815	60.51	1.610	60.05	2.340
2	155.50	154.65	0.547	153.88	1.040	153.21	1.470
3	296.67	296.49	0.061	296.29	0.128	296.08	0.199
5	484.97	482.34	0.542	480.07	1.010	478.23	1.390
9	1005.10	1002.80	0.229	1000.60	0.448	998.58	0.649
11	1321.40	1316.00	0.409	1311.70	0.734	1308.50	0.976

Table 3-7: Comparisons of the natural frequencies for different levels of damage of case 1 (continued)

Mode number	Undamaged	40% Damage	%Change	50% Damage	%Change
1	61.49	59.66	2.990	59.33	3.520
2	155.50	152.69	1.810	152.33	2.040
3	296.67	295.88	0.266	295.68	0.334
5	484.97	476.91	1.660	476.14	1.820
9	1005.10	996.72	0.834	995.15	0.990
11	1321.40	1306.60	1.120	1305.90	1.170

A definite change in natural frequency value is evident from Table 3-6 and Table 3-7. The yCDF and SCDF values were calculated for the different damage levels. The yCDF and SCDF are plotted in order to verify whether the location of the damage can be identified from these two damage parameters. An example of such a plot is shown in Figure 3-5 and Figure 3-6 for the yCDF and SCDF, respectively, when the Predator wing is subjected to 50% damage. The yCDF and the SCDF are defined in terms of the number of modes included in its calculation. The plots are therefore made for an increasing number of modes included in the calculation.

It is evident from Figure 3-5 that the yCDF value can indicate the presence of damage, as there is a change in the yCDF value at the known damage location. The location of the damage is clear from the peaks of the plots. The damage location is evident from Figure 3-6 and corresponds to the location predicted by the yCDF. The increase in SCDF value as the level of damage is increased is shown in Figure 3-7 when 6 modes are included in the calculation of the SCDF value. It is clear that the SCDF peaks increase as the level of damage is increased.

The waterfall plot shown in Figure 3-7 does not show high noise levels due to any mathematical manipulation. Figure 3-7 was generated from the SCDF values as calculated from equation 1.10, however, Pandey et al. (1991) used modal curvatures derived from modal displacements and Abdel Wahab (1999) proposed the CDF value to reduce the noise due to the central difference approximation. A comparison can now be made between the SCDF values and the CDF values that were initially proposed by Abdel Wahab (1999). The modal curvatures are derived directly from strain values as in equation 1.5 and the result is substituted into equation 1.8 to calculate the $y_i CDF_i$, more or less equivalent to the CDF value of Abdel Wahab (1999). The variation of this equivalent CDF value as the damage level is increased as is shown in Figure 3-8.

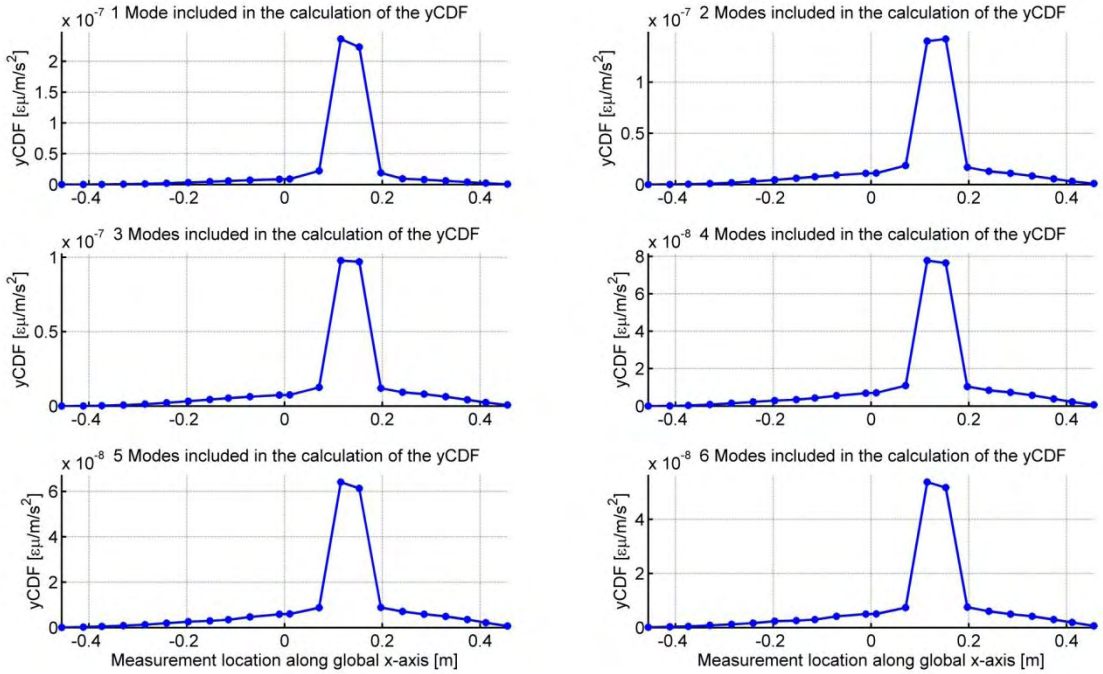

Figure 3-5: yCDF-plots for 50% damage of case 1 for an increasing number of modes

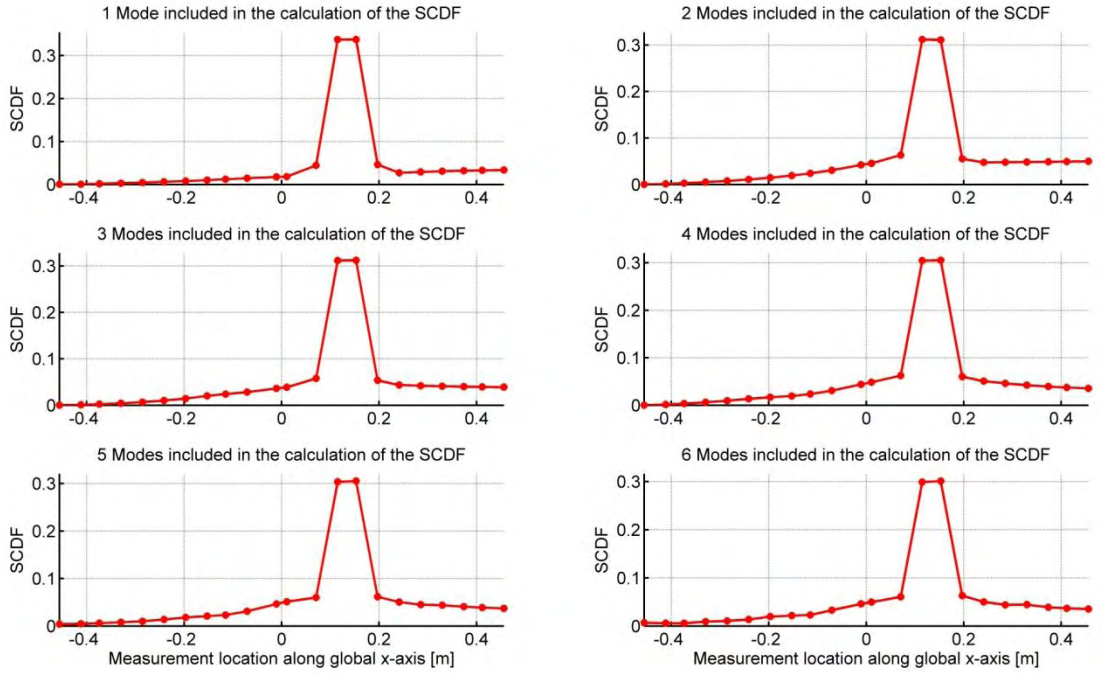

Figure 3-6: SCDF-plots for 50% damage of case 1 for an increasing number of modes

When Figure 3-8 is examined it can be seen that there is mathematical noise in the CDF equivalent values. This type of mathematical noise is also evident from the CDF results published by Abdel Wahab (1999). When the SCDF values of Figure 3-7 are examined it is clear that the noise is less. The SCDF values, with the acceleration normalised strains, provide a clearer graph with less noise present than the CDF equivalent graph and the SCDF value is therefore preferred.

The criteria that is used to determine the damage location is by intuitively identifying the peaks on the SCDF plots. This could however lead to incorrect identification of a damage location. A damage detection method should ideally include criteria to determine whether damage has occurred at a particular location (Farrar et al., 1996). Investigations into such criteria did not form part of the present study. Due to the fact that the peaks can be distinguished quite clearly from Figure 3-6, the criterion to look at the peak values of the SCDF that was applied here will be applied in the rest of the study.

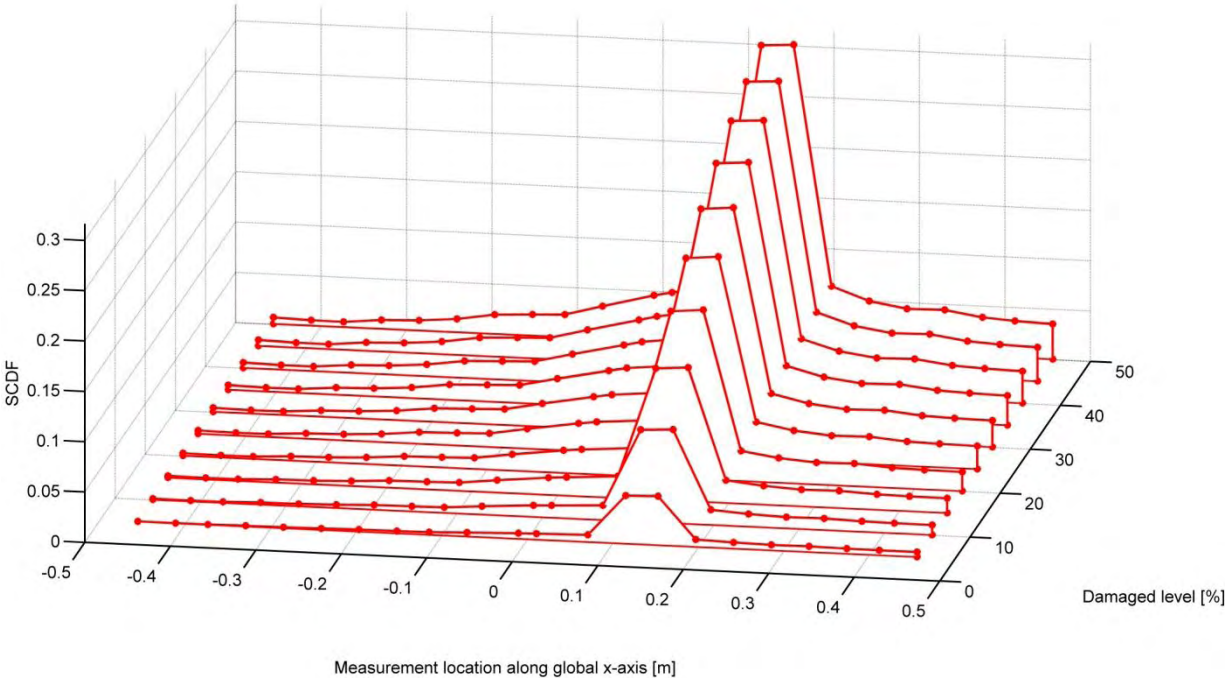

Figure 3-7: Variation of the SCDF values, when 6 modes are included in the calculation, as the damage level is increased for case 1

The plots of Figure 3-5, Figure 3-6 and Figure 3-7 are great for predicting the location of damage, but do not provide a single value to indicate whether damage is present or not. The SFDL was created to provide a parameter that is able to identify whether damage is present or not, by assessing its value.

The effect that the level of damage and the number of modes included have on the SFDL value was studied and a carpet plot showing these effects is drawn as Figure 3-9. When Figure 3-9 is inspected, it can be seen that generally, the SFDL value increases as the level of damage increases. It also appears as if the SFDL values become more constant when 3 or more modes are included. The plot appears to follow a straight line and thus it seems as if the SFDL value increases linearly as the level of damage is increased. This was investigated by fitting a power series, an exponential series and a straight line through the SFDL values when 6 modes are included. These curve fits are shown in Figure 3-10. It is natural to expect that the SFDL value should equal zero when there is no damage present in the structure, thus the curve fits are required to pass through zero (or at least be close to zero) at 0% damage.

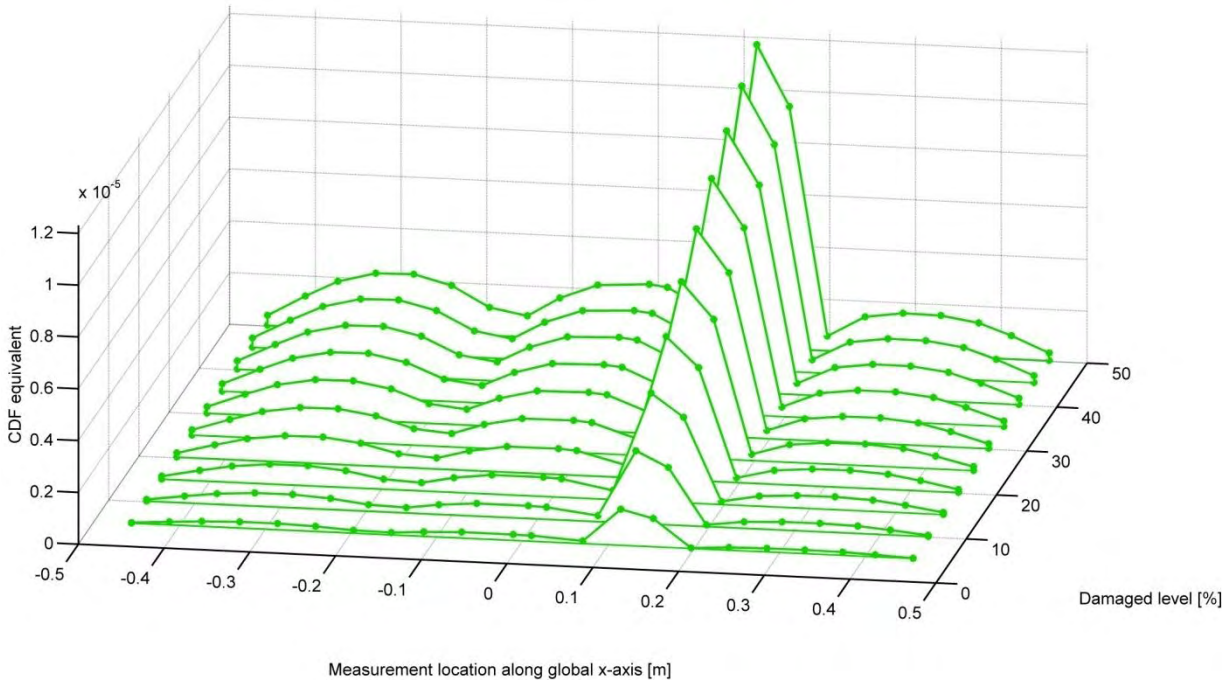

Figure 3-8: Variation of the CDF equivalent values, when 6 modes are included in the calculation, as the damage level is increased for case 1

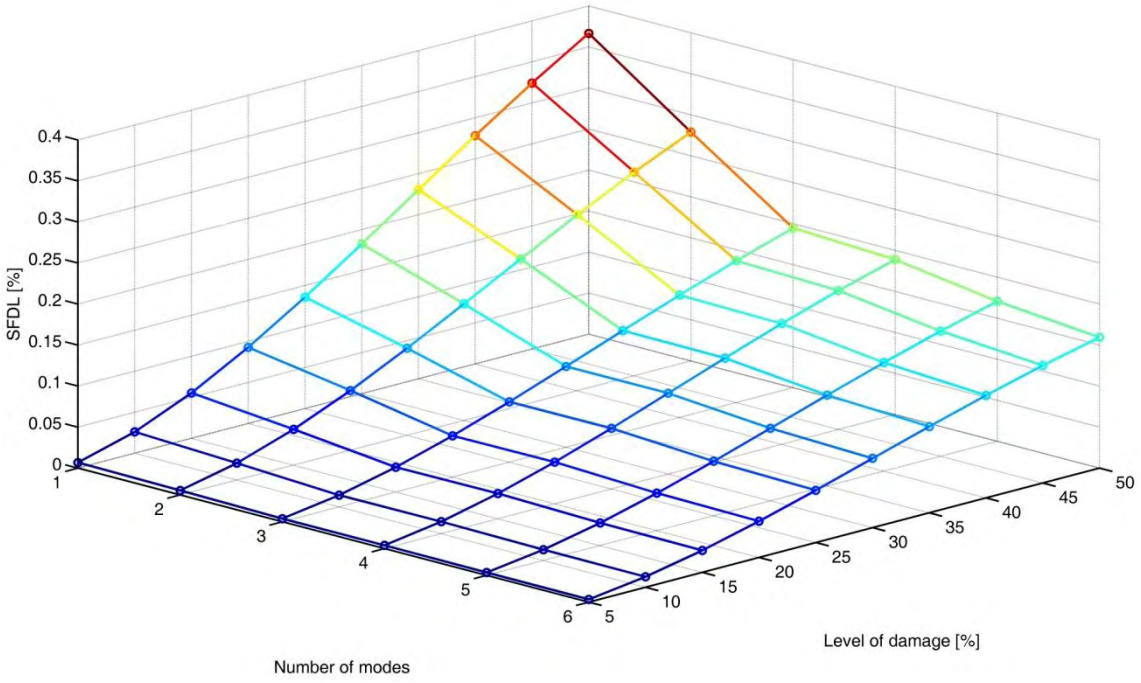

Figure 3-9: Carpet plot showing the effect of the level of damage and number of modes on the SFDL value for case 1

When Figure 3-10 is examined it appears that the power series fit indeed matches the data best, as the r^2 value is the closest to 1, which indicates good correlation. This indicates that the SFDL value increases proportionately through the power law with an exponent of 1.39 to the level of damage if the damaged area is located close to the measurement position. Another question that is raised, when Figure 3-10 is examined, is whether the SFDL value is more sensitive to damage than the natural frequency shift

technique. In order to compare the SFDL value and the natural frequency method, it was decided to use an average of the difference in natural frequency. Therefore an average of the natural frequency for the six modes was determined and compared to the SFDL value determined for the six modes at each level of damage. The result is shown in Figure 3-11.

If Figure 3-11 is examined it is clear that the power series fit (the green curve) matches the data very well. This is visually evident and the correlation coefficient (r^2) verifies the observation, as this value is 1. It can therefore be deduced that the SFDL value is related to the average difference in natural frequency through a power series fit. The exponent of the power series fit is equal to 1.871. This indicates that the SFDL value is almost quadratically as sensitive as the natural frequency method. This observation applies to the case when the damaged area is located close to the measurement locations without including any measurement location.

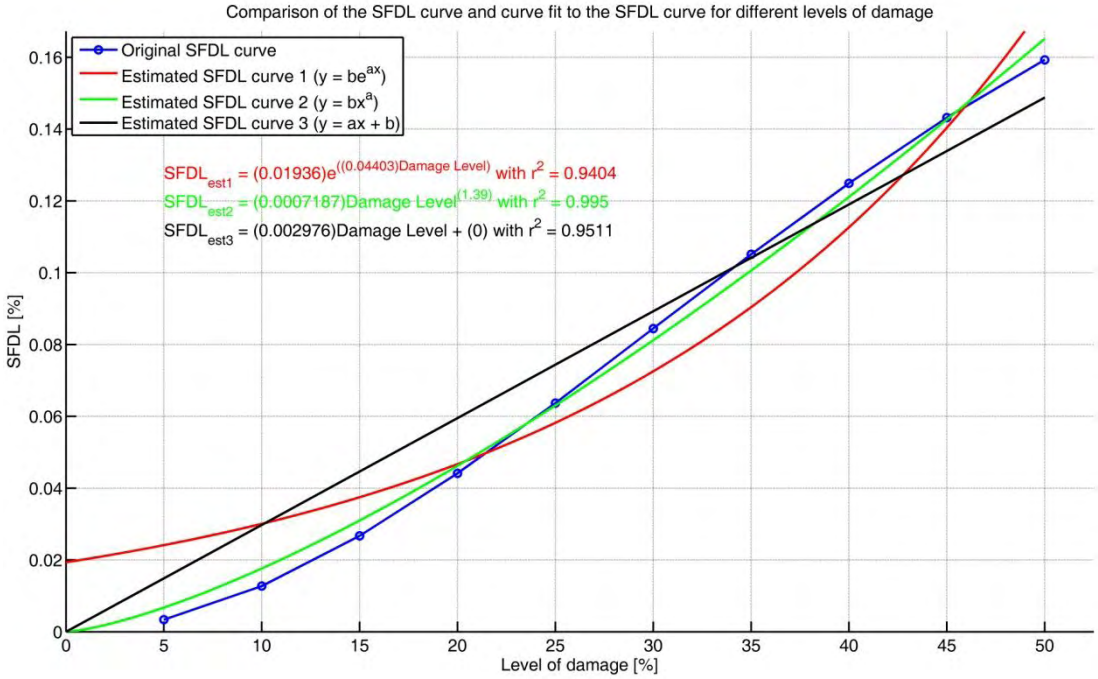

Figure 3-10: Curve fits for the SFDL value compared to the level of damage for case 1

The SFDL value is calculated with the rms value of the SCDF (equation 1.11). The SCDF value, however, is determined by dividing the difference in acceleration normalised strain values by the damaged value of the acceleration normalised strain at location i (equation 1.10). It can be argued that the SCDF can be computed by dividing the difference by the undamaged strain value. The reason for dividing by the damaged strain value was discussed in paragraph 1.3. This reason boils down to the fact that the strain at the damage location decreases and division by a small number produces a very large number. If the measurement location encloses the damaged area the SCDF and SFDL values might increase dramatically. There might be differences in the way the SFDL value scales with respect to the damage level and average difference in natural frequency. The influence of dividing or normalising with the undamaged strain value instead of the damaged strain value was investigated. This investigation was performed by normalising the SCDF and subsequently the SFDL value with the undamaged

normalised strain values. The same type of curve fits used in Figure 3-10 and Figure 3-11, were created and are shown and discussed in Appendix B. The best fits were extracted and compared to the best fits of Figure 3-10 and Figure 3-11, with the results shown in Figure 3-12.

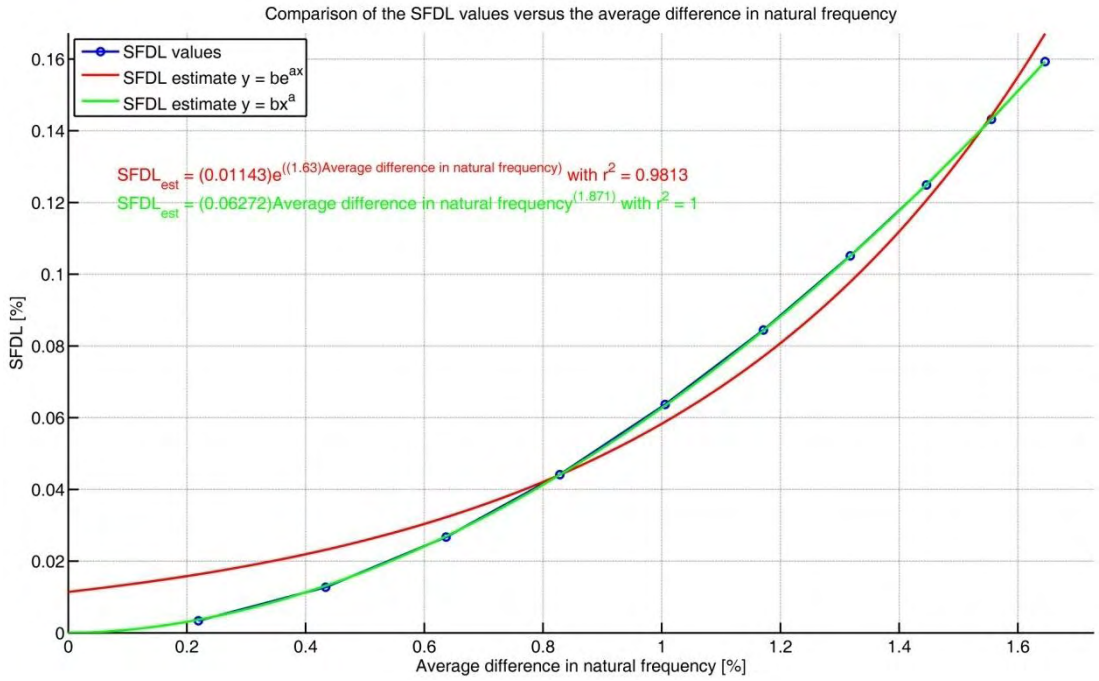

Figure 3-11: Curve fits showing the relation between the SFDL value and the average difference in natural frequency for case 1

When the two comparison plots of Figure 3-12 are examined, it is obvious that the SFDL values calculated from the undamaged normalised SCDF values scale the fastest in both cases. The undamaged exponent differs by 10.79% and 12.61% with respect to the damaged exponents of the two curve fits shown in Figure 3-12, respectively. The exponents are rather close however, and gains obtained by normalising the SCDF and SFDL values with the undamaged values are slim. The normalisation with the damaged strain values are preferred, as they increase at a rate close to the undamaged normalised values and may provide an increased sensitivity when the measurement location is enclosed by the damaged area. The increased sensitivity when the damaged area encloses a measurement location is investigated in more detail in paragraph 3.1.3.1. The scaling of the SFDL when computed from the yCDF instead of the SCDF values is investigated in Appendix B.

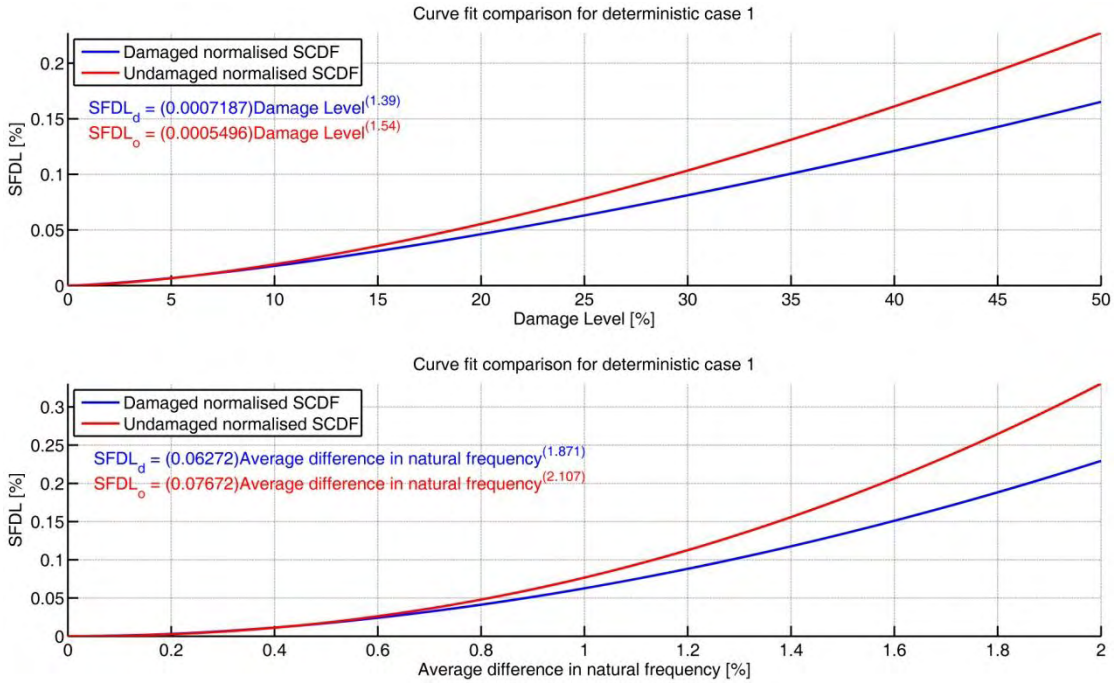

Figure 3-12: Comparison of the scaling of the SFDL value with the SCDF normalised with the damaged and undamaged averaged strains for case 1

3.1.2.2 The effects of damping on the SCDF

Pandey et al. (1991) proposed a method of detecting damage from the differences in modal curvature. The CDF was proposed by Abdel Wahab et al. (1999) and it was shown in paragraph 1.3 that it is possible to calculate the CDF value directly from strain values at the natural frequencies of interest. It can be argued that the SCDF of equation 1.10 can also be determined directly from strain values from a strain FRF at the natural frequency locations. This is a feasible way of determining the SCDF values. It is however not possible to measure a strain FRF whilst the aircraft is in the air. It was decided to use acceleration normalised strain values instead of just strain values alone in the calculation of the SCDF, as the acceleration normalised strain values can be measured during in-flight conditions.

During the investigation of the proposed damage detection method, the SCDF values were initially calculated from strain values obtained directly from strain FRFs. This was done to verify that the method will work from strain values alone, as this is more or less equivalent to the CDF proposed by Abdel Wahab et al. (1999) and it is known that the damage location can be determined from the CDF values. When this investigation was performed it was noticed that the SCDF values calculated from strain values are very sensitive to the absolute strain values at the natural frequency locations.

In practice it might be difficult to measure the FRF response at the resonant frequency with a high degree of accuracy due to the damping in the structure. If the structure is sufficiently damped the response at resonance can be measured relatively accurately (Ewins, 1995). The accuracy of the response measurement at resonance still remains a problem as there might be slight differences in the measured response of two consecutive

measurements. This implies that when two measurements from undamaged structures are compared there might be a difference in strain value, even in the absence of damage, because the strain response value at the natural frequencies could not be measured accurately.

This leads to an investigation of the sensitivity of the SCDF value to damping in the structure and thus its sensitivity to the strain value at resonance. The sensitivity of the SCDF to damping in the structure was investigated by calculating the response of an undamaged structure with modal damping equal to 0.02% of critical damping. The acceleration normalised strain values and strain values at the natural frequency values were extracted from the simulated transmissibility functions and strain FRFs, respectively. The damaged values are the values extracted for deterministic case 1 obtained from the updated model, thus with updated modal damping values, for damage levels ranging from 5% to 50% in increments of 5%. The SCDF values were calculated from equation 1.10 using the acceleration normalised strain values and SCDF values were calculated directly from strain values as shown in equation 3.10.

$$SCDF_i = \frac{\frac{1}{N}\sum_{j=1}^{N}\left|\left|-\varepsilon_{x,o_i}\right| - \left|-\varepsilon_{x,d_i}\right|\right|}{\frac{1}{N}\sum_{j=1}^{N}\left|\varepsilon_{x,d_i}\right|} \tag{3.10}$$

The SCDF values that were obtained for both these calculations are shown in Figure 3-13 for the SCDF calculated from equation 1.10 (top plot) and equation 3.10 (bottom plot).

The damage location is evident from the top plot of Figure 3-13 and these values are comparable to the ones obtained in Figure 3-7. When the bottom plot of Figure 3-13 is examined it is difficult to establish where the damage is actually located. The probable damage locations are erroneous and not even close to the real damage location. It is clear that the SCDF values calculated from the acceleration normalised strain values (equation 1.10) are less sensitive to damping or measurement error of the response at resonance compared to the SCDF values calculated directly from the strain values (equation 3.10).

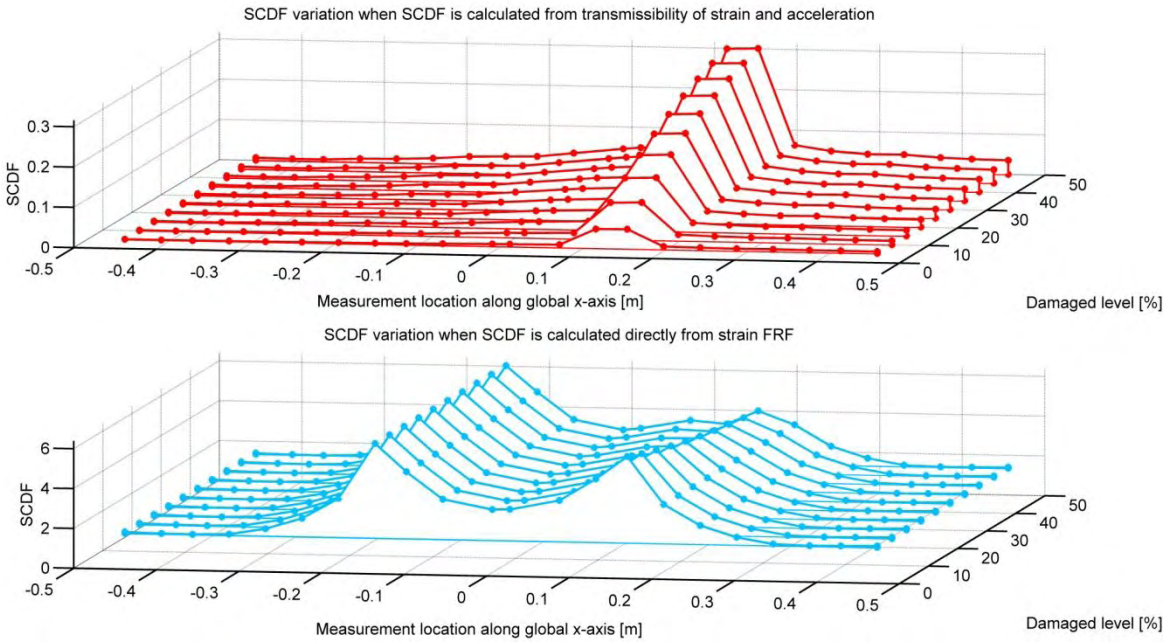

Figure 3-13: Effect of damping on the calculation of the SCDF values

3.1.3 Damage case 2

In the second deterministic case, the damage is in an area that encloses two measurement locations (measurement locations 8 and 9 of Figure 3-2). In this case the reduction in load carrying capability causes a reduction in the strain measured at locations 8 and 9.

The parameters chosen to define the damaged area are summarised in Table 3-8. The damaged area is equal to 6.972% of the right wing section and 3.240% of the total wing area. The x-location of the damaged area remains the same as in case 1, the y-location changed by shifting the damage area upwards. The damage location and the measurement positions for this damage case are shown in Figure 3-14. The strain field distribution for this damage case is apparent from the strain plot of the first vertical bending mode for 50 % damage (Figure 3-15). It is apparent from Figure 3-15 that the measurement locations are in an area with lower strain values compared to the undamaged side of the wing.

Table 3-8: Parameter values defining the damaged area for case 2

Parameter	Value
l_{di}	89.647 mm
h_{di}	3.727 mm
l_d	88.384 mm
h_{dr}	20.912 mm
h_{dt}	18.703 mm
Λ_{LE}	3.2°
A_d	1.751×10^{-3} m^2
Ratio of damaged area to the area of right wing section	6.972%
Ratio of damaged area to the area of the complete wing	3.240%

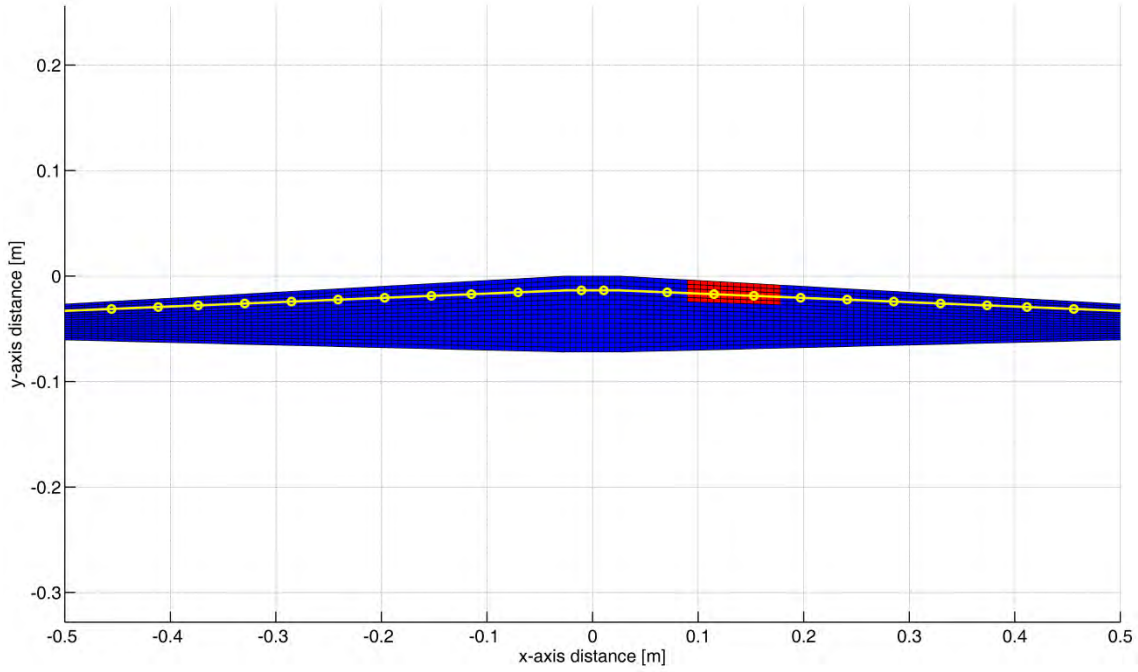

Figure 3-14: Damage location with measurement locations for deterministic damage case 2

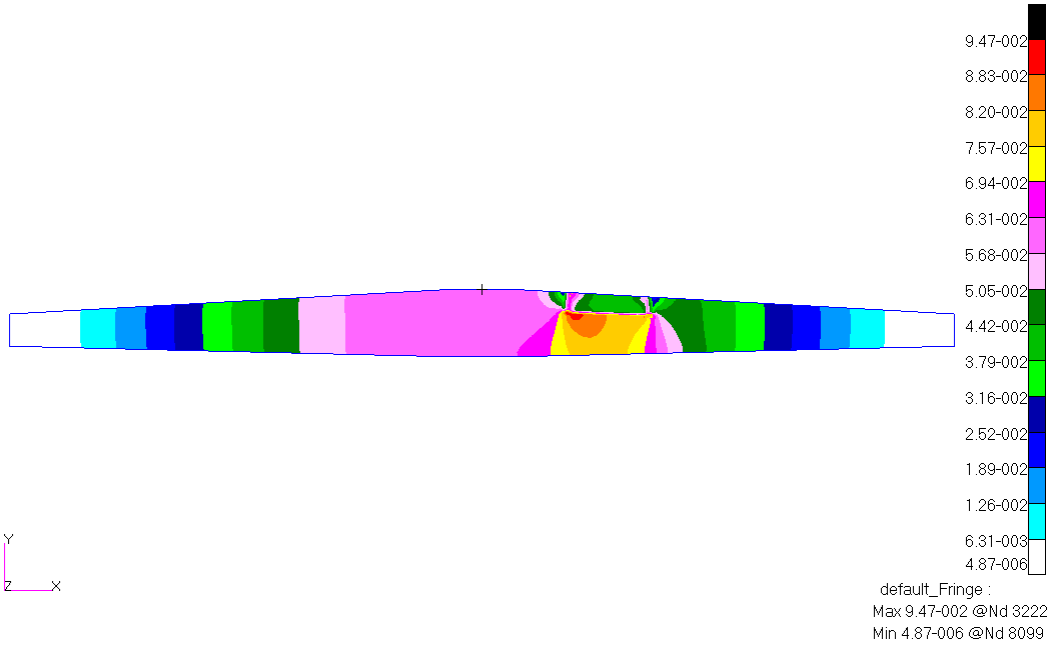

Figure 3-15: Strain field for first bending mode of the wing for case 2 with 50% damage

3.1.3.1 Investigation of different levels of damage for case 2

The damage is varied in the same way as in case 1. The damage is introduced from 5% to 50% in increments of 5%, thus reducing the thickness in the damaged area from 9.5 *mm* to 5 *mm* in increments of 0.5 *mm*. The effects of the changes in thickness on values of the yCDF, the SCDF, the change in natural frequency and the SFDL are investigated. The type of mode for each natural frequency was extracted from Patran (2008) and is listed in Table 3-9 for damage levels at increments of 10%.

Table 3-9: Type of mode shapes for damage levels of case 2

Mode number	10% Damage frequency [*Hz*]	20% Damage frequency [*Hz*]	30% Damage frequency [*Hz*]	40% Damage frequency [*Hz*]	Type	50% Damage frequency [*Hz*]	Type
1	61.06	60.62	60.22	59.86	VB	59.55	VB
2	154.77	154.10	153.52	153.05	VB	152.72	VB
3	296.49	296.28	296.04	295.77	VB	295.48	VB
4	377.64	376.17	374.37	372.11	IPB	369.23	IPB
5	482.69	480.67	479.00	477.76	VB	477.04	VB
6	710.24	708.42	706.78	705.38	VB	703.80	T
7	722.20	717.79	713.14	708.43	T	704.37	VB
8	836.97	835.85	834.33	832.27	IPB	829.49	IPB
9	1002.90	1000.60	998.26	995.92	VB	993.76	VB
10	1184.20	1177.40	1170.70	1164.50	T	1158.80	T
11	1316.20	1311.80	1308.30	1305.90	VB	1304.60	VB

A comparison of the natural frequencies of the modes included in the calculation of the various parameters is given in Table 3-10 and Table 3-11. It is clear from Table 3-10 and

Table 3-11 that there is a definite change in natural frequency value as the damage level is increased. The damage ought to be observed from the change in the SFDL value. Plots of the yCDF and SCDF are made for 50% damage and are shown in Figure 3-16 and Figure 3-17, respectively.

Table 3-10: Comparisons of the natural frequencies for different levels of damage of case 2

Mode number	Undamaged	10% Damage	%Change	20% Damage	%Change	30% Damage	%Change
1	61.49	61.06	0.712	60.62	1.410	60.22	2.070
2	155.50	154.77	0.469	154.10	0.900	153.52	1.270
3	296.67	296.49	0.061	296.28	0.131	296.04	0.212
5	484.97	482.69	0.470	480.67	0.887	479.00	1.230
9	1005.10	1002.90	0.219	1000.60	0.448	998.26	0.681
11	1321.40	1316.20	0.394	1311.80	0.727	1308.30	0.991

Table 3-11: Comparisons of the natural frequencies for different levels of damage of case 2 (continued)

Vertical mode number	Undamaged	40% Damage	%Change	50% Damage	%Change
1	61.49	59.86	2.660	59.55	3.150
2	155.50	153.05	1.580	152.72	1.790
3	296.67	295.77	0.303	295.48	0.401
5	484.97	477.76	1.490	477.04	1.640
9	1005.10	995.92	0.913	993.76	1.130
11	1321.40	1305.90	1.170	1304.60	1.270

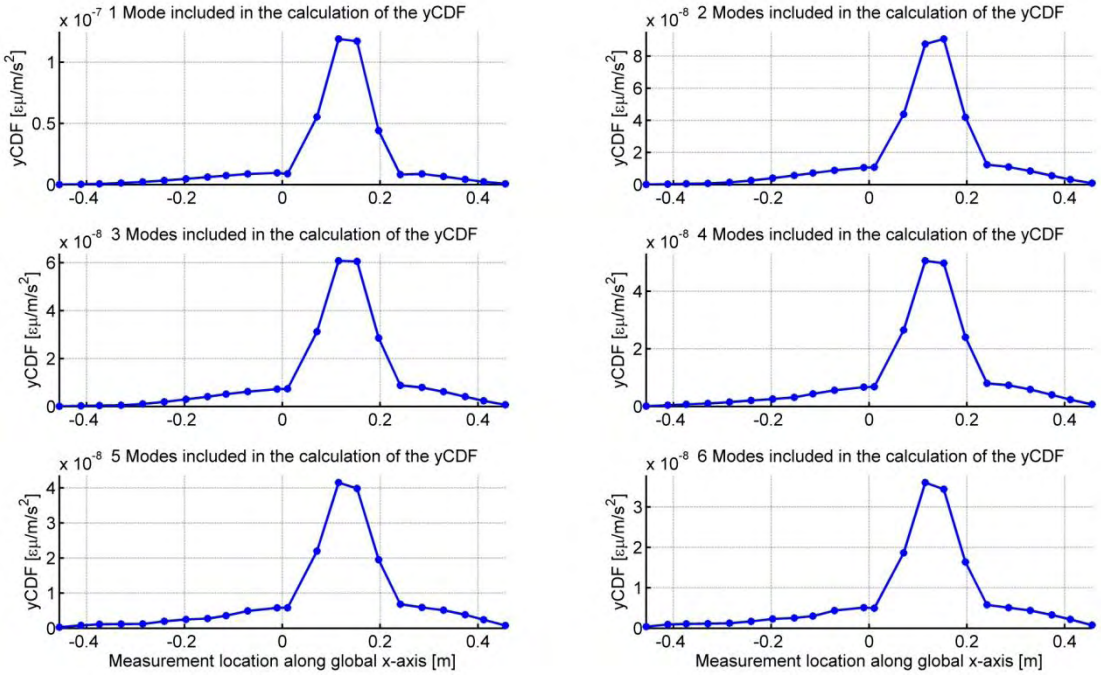

Figure 3-16: yCDF-plots for 50% damage of case 2 for an increasing number of modes

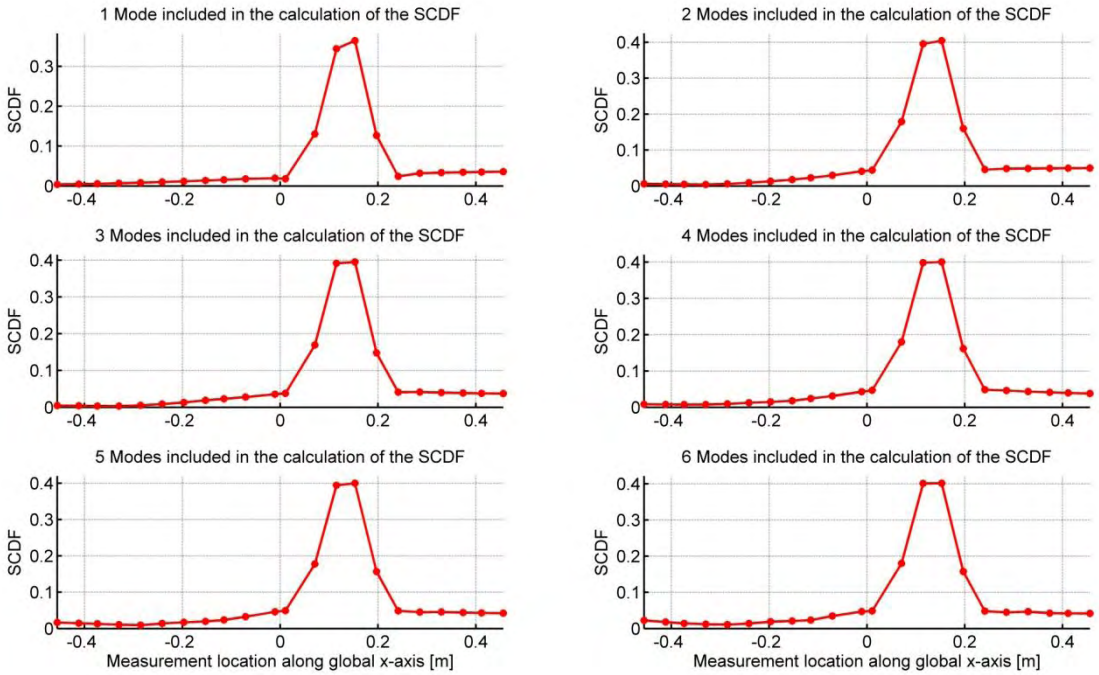

Figure 3-17: SCDF-plots for 50% damage of case 2 for an increasing number of modes

The location of the damage is evident from the plots of Figure 3-16 and Figure 3-17. This location also corresponds to the known damage location. When both of these plots are examined it can be seen that the yCDF and SCDF at positions 7 and 10 are relatively high compared to case 1 where these two values were low in comparison with the peak values at locations 8 and 9 (Figure 3-5 and Figure 3-6). This can be attributed to the fact that measurement locations 7 and 10 are relatively close to the damaged area and the strains are measured close to the damage location where the strains are still recovering to the nominal stress state. This is evident from Figure 3-15, where it can be seen that the measurement locations are located in an area where the strains are still low. This causes the value of the yCDF to become larger at these locations.

If the SCDF values of Figure 3-17 are inspected it can be seen that their values increase towards the right tip of the wing. This can be attributed to the fact that the strains may change very slightly at these locations. Although they are very small on the yCDF plots (Figure 3-16), when these small differences are divided by a strain that is in the order of 1×10^{-6}, their values become more significant on the SCDF plot. The strains are also normalised with respect to the acceleration response on the left side of the wing. The dynamics on the left side of the wing is not influenced by the damage. The strains on the right side normalised by the acceleration response on the left side do show a relative change due to this change in dynamic response. This increase in value can therefore be reduced if the acceleration response of another reference accelerometer, on the right part of the wing, is used for normalisation of the strains on the right wing. This is apparent from the study on the Global Hawk wing in paragraph D.2 of Appendix D, where the SCDF values to the left of the damage remain small in comparison to the values on the right wing section. The aim of this method, however is to use the minimum amount of equipment and sensors and therefore only one reference accelerometer is used.

The variation of the SCDF as the damage level increases is shown in Figure 3-18. It is evident from Figure 3-18 that the SCDF value increases as the level of damage is increased. At the lower damage levels the damage location is not that evident. This can be attributed to the fact that the values next to the damaged location are in the stress concentration area (see Figure 3-15) and the strain value shows a greater change than at the damage location itself. As the damage level is increased the difference in strains at the damage location increases and the damaged location becomes more apparent.

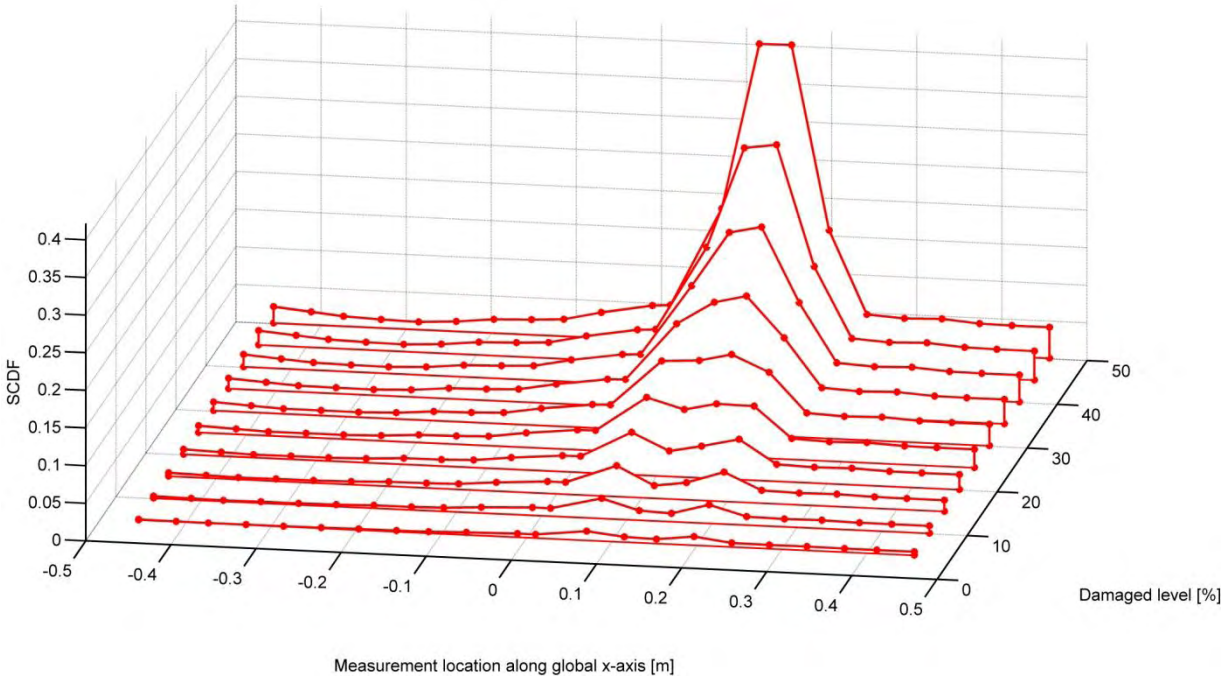

Figure 3-18: Variation of the SCDF values, when 6 modes are included in the calculation, as the damage level is increased for case 2

The variation of the CDF equivalent as the level of damage is increased was determined and this waterfall plot is shown in Figure 3-19. When Figure 3-17 and Figure 3-18 was examined it was observed that the peak values are at the eighth and ninth measurement position from the right. When Figure 3-19 is examined a high level of noise is observed and there are cases where the peak values and thus the damage actually appear to be at the ninth and tenth measurement location. This is erroneous and the SCDF values prove to be more reliable than the CDF equivalent values.

The location of the damage can be obtained from Figure 3-16, Figure 3-17 and Figure 3-18. The SFDL value is computed from the SCDF and the change in this parameter as the number of modes and the damage level is increased, is shown in Figure 3-20.

The SFDL values of Figure 3-20 appear to increase as the level of damage is increased over all the number of modes included. When more modes are included in the calculation, the SFDL value again appears to become constant. The SFDL value for case 2 appears to scale exponentially with an increase in the damage level. This was investigated by again fitting the linear, power series and exponential curves to the SFDL values when 6 modes are included in the calculation and is shown in Figure 3-21.

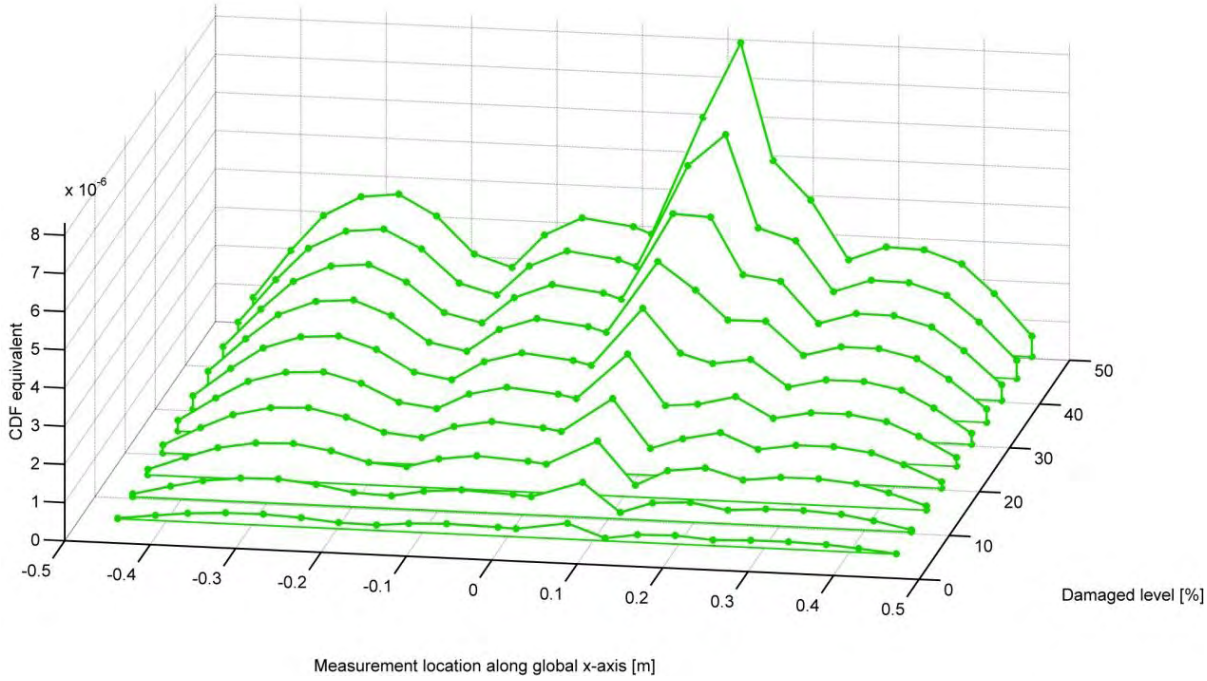

Figure 3-19: Variation of the CDF equivalent values, when 6 modes are included in the calculation, as the damage level is increased for case 2

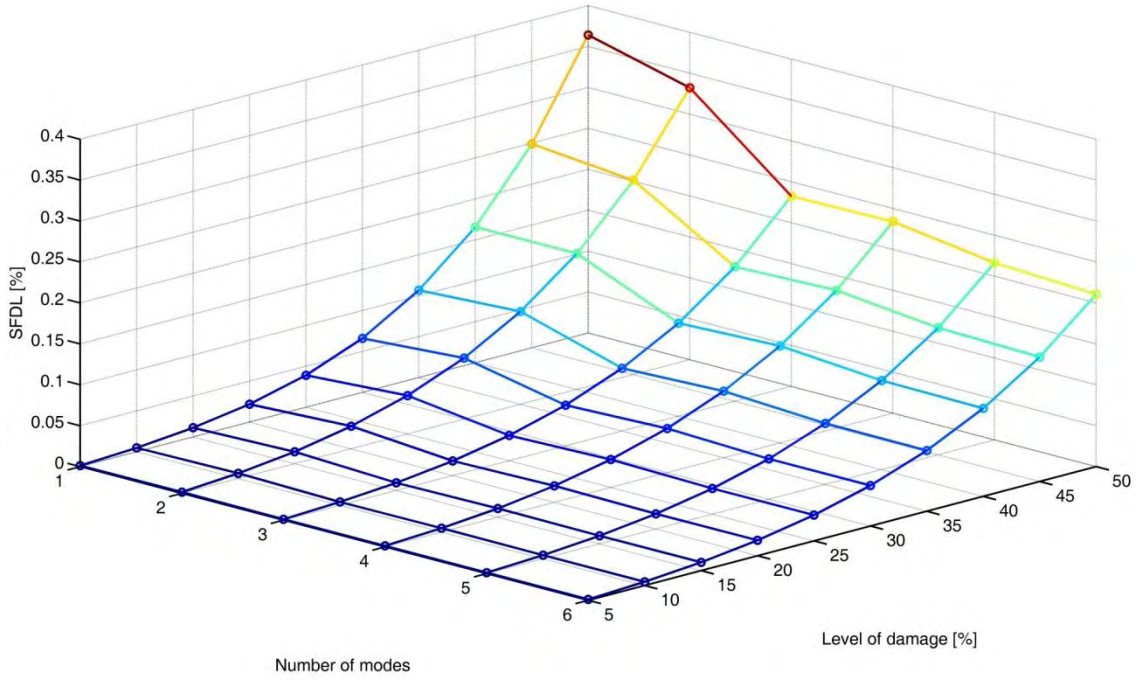

Figure 3-20: Carpet plot showing the effect of the level of damage and number of modes on the SFDL value for case 2

From Figure 3-21 it can be deduced that when the damaged area encloses a measurement location, it appears as if the SFDL scales best as a power series and the r^2 close to 1 enforces this observation. This can be attributed to the fact that the strains in the damaged area decreases rapidly and the yCDF value gets divided by an ever decreasing strain value. When the change in the SFDL value is compared to the average difference in natural frequency the plot of Figure 3-22 is obtained.

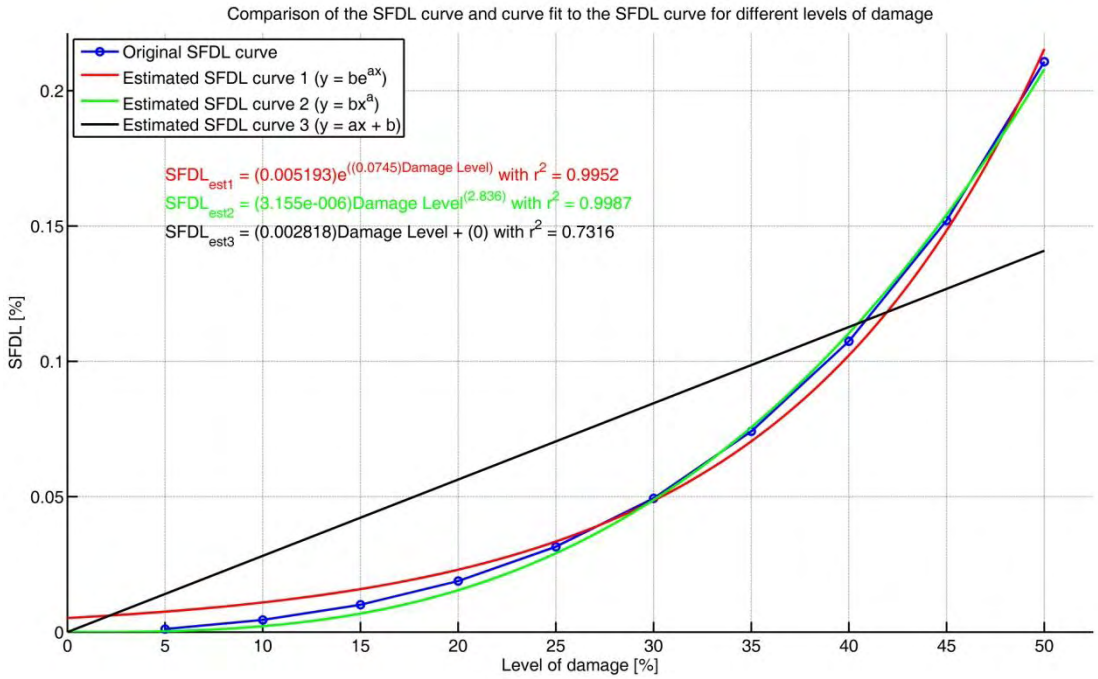

Figure 3-21: Curve fits for the SFDL value compared to the level of damage for case 2

When Figure 3-22 is examined it is observed that the exponential fit is the best fit to the data, as the r^2 value for this fit is closest to 1. The SFDL value therefore appears to scale exponentially with the average difference in natural frequency and therefore is more sensitive than the natural frequency method. This exponential fit is in contrast to case 1 where the best fit was the power law fit.

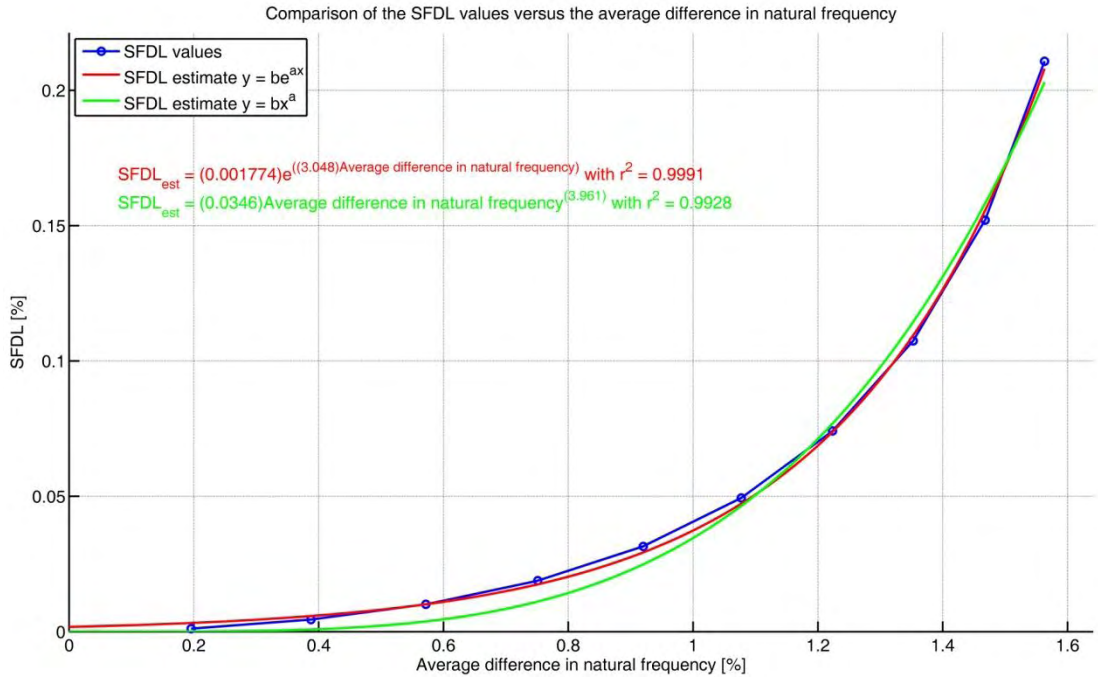

Figure 3-22: Curve fits showing the relation between the SFDL value and the average difference in natural frequency for case 2

The same curve fits are determined when the SCDF and the SFDL values are calculated from the undamaged acceleration normalised strain values (see Appendix B). A comparison of the best curve fits for both the damaged and undamaged normalised SFDL values are made in Figure 3-23.

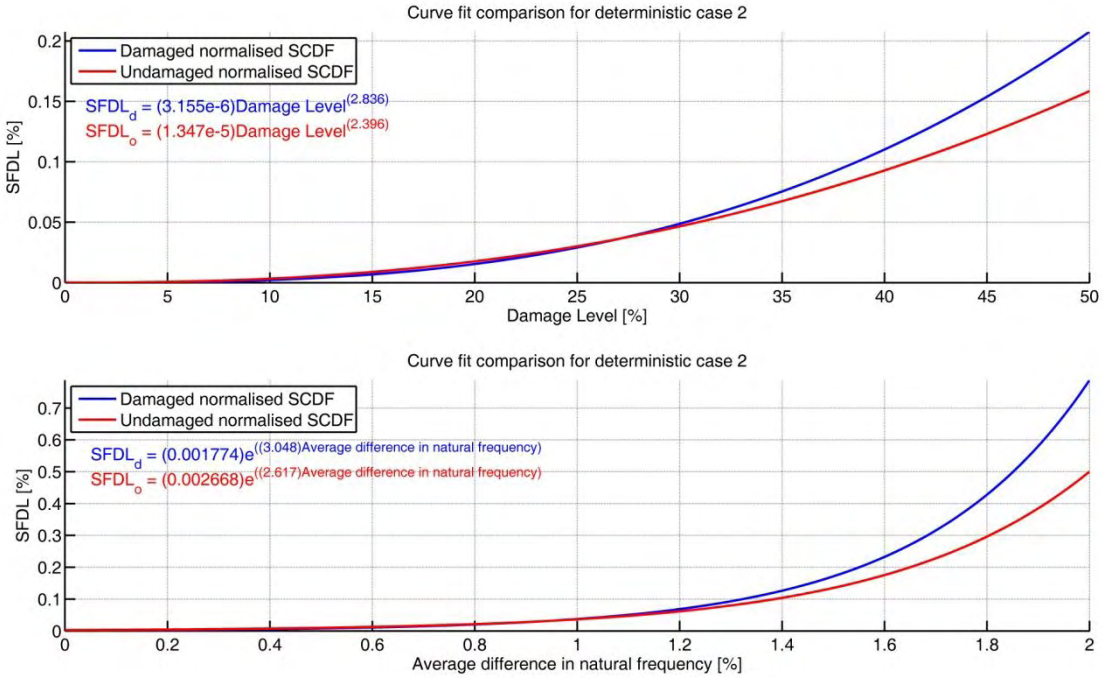

Figure 3-23: Comparison of the scaling of the SFDL value with the SCDF normalised with the damaged and undamaged averaged strains for case 2

Upon examining Figure 3-23, it is clear that the damaged normalised SFDL values increase more rapidly than the undamaged normalised values. The exponent for the power law fit of the undamaged normalised SFDL values differs with 15.5% from the exponent of the damaged normalised SFDL estimate. The fact that the damaged normalised SFDL values scales faster can be attributed to the strain values at the measurement locations being less than the original undamaged value. If the SCDF is normalised with the damaged value it is in effect divided by a smaller number and therefore a larger SCDF value is obtained. For this reason the damaged normalised values are preferred. The scaling of the SFDL when computed from the yCDF instead of the SCDF values is investigated in Appendix C.

3.1.3.2 The effects of damage modelling on the SCDF and SFDL values

There are two possible cases which influence the SCDF and SFDL calculations and values. In the first case the damaged area is close to a measurement location and in the second case the damaged area encloses one or more measurement locations (paragraphs 3.1.2 and 3.1.3, respectively). The modelling of the structural damage was discussed in paragraph 2.5. It was argued that the actual damage scenario might be entirely different from the modelled damage.

The damage modelling and true damage scenario have no impact on the first case, because the strains are measured close to the damaged area. The actual strain values at the damaged location have no influence on the measured strains. This effect is discussed in more detail in paragraph 4.3.1. The situation might arise that the actual damage is completely different from the modelled damage. This difference was discussed in paragraph 2.5 and the effects of this difference in the modelled and actual damage situation are investigated numerically in this paragraph.

This numerical study is performed by generating two FE meshes for the damage size and location of deterministic case 2. In the first case the FE model as discussed in chapter 2 was used to model the damage, however the FE model that was not updated was used. For the second case an FE model consisting of 8-node hexahedral elements was constructed. This model was constructed to have 10 elements through the thickness of the wing-like structure. This number of elements through the thickness was used to be able to simulated damage levels from 10% to 50% by removing one element through the thickness at the damaged location and increasing the damage level by 10%. The excitation node that was used on the shell mesh was not present in the hexahedral mesh, because the hexahedral mesh only had 8 nodes per element. The closest node to the excitation node on the shell mesh was used in the hexahedral mesh. The SCDF and the SFDL values were calculated for each type of mesh for an increasing damage level. The two damage parameters for the two FE meshes are compared in Figure 3-24 and Figure 3-25, respectively.

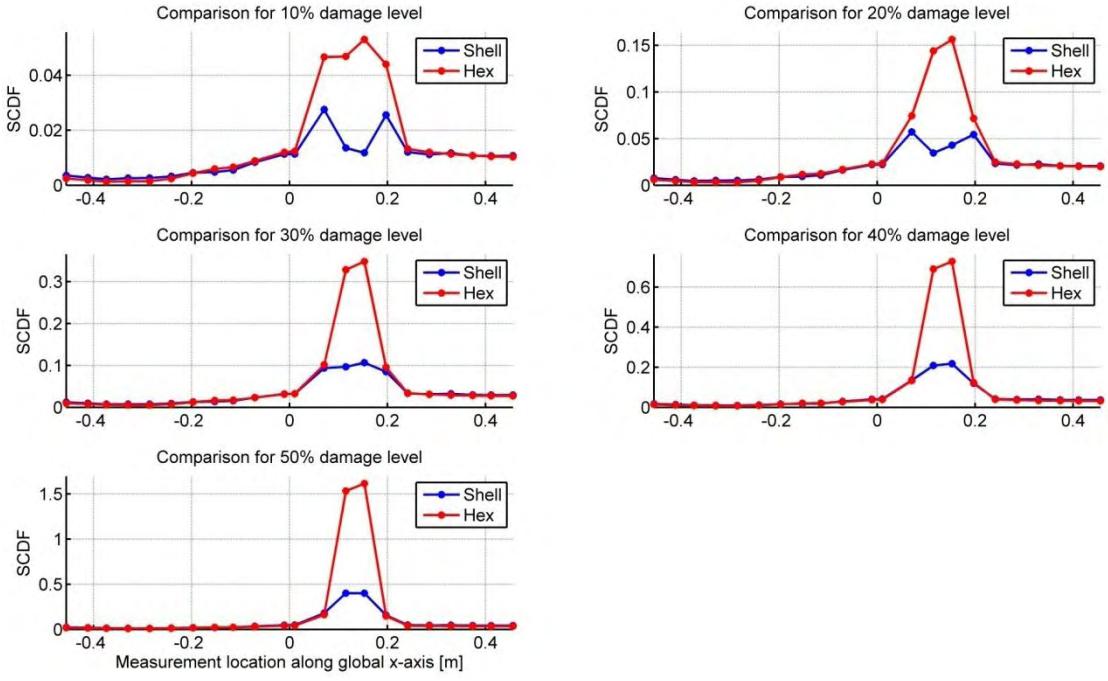

Figure 3-24: Comparison of the level of damage on the SCDF value for the shell and hexahedral mesh of the damaged area

It is evident from Figure 3-24 that the shell and hexahedral meshes differ quite significantly at the damage location. The SCDF values at the rest of the measurement locations correlate well. The difference at the measurement location is attributed to the way in which the damage is modelled. In the shell mesh the neutral axis does not

change, while in the hexahedral mesh the neutral axis is shifted and the strain value at the measurement location is less than in the shell mesh. Due to the lower strain values at the measurement location, the peaks of the SCDF plots are higher for the hexahedral mesh than for the shell mesh. When the SFDL values are calculated from these two SCDF plots, it is expected that the hexahedral mesh should show an increase value compared to the shell mesh, due to the increased SCDF value at the measurement location and this effect is shown in Figure 3-25.

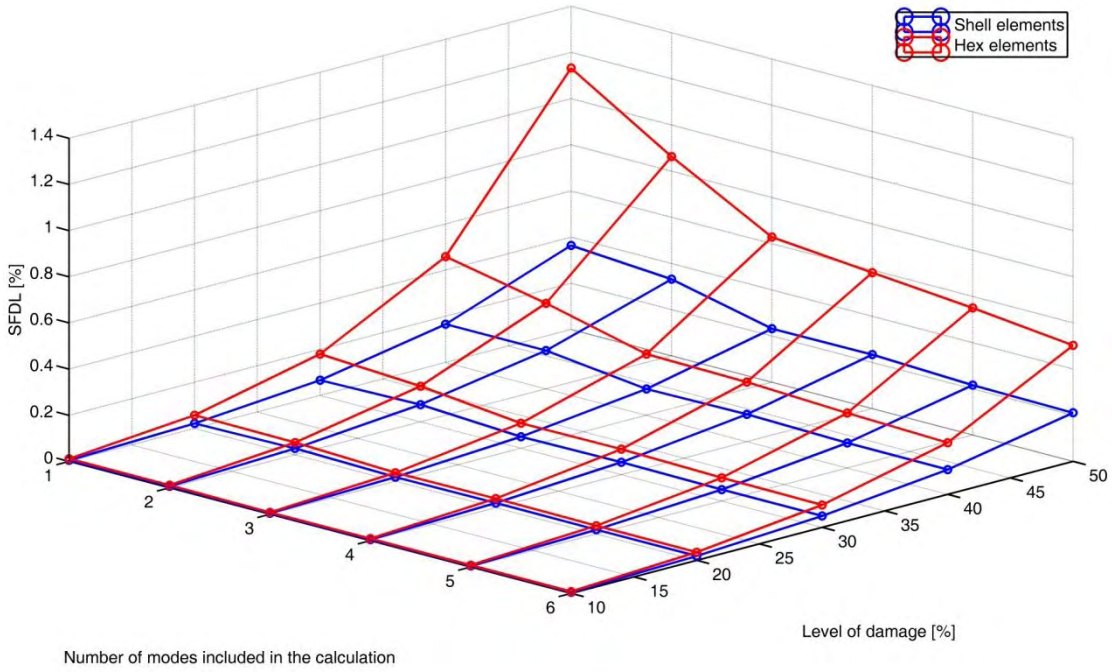

Figure 3-25: Comparison of the change in SFDL value as a function of number of mode included in the calculation and level of damage for the shell and hexahedral meshes

The difference in the SCDF values appears to be a constant factor of around three at the measurement location. A constant factor was determined for the SFDL plot by dividing the SFDL value for the shell mesh at 50% damage and 6 modes by the SFDL value for the hexahedral mesh at the same location. This factor was equal to 2.39 and if all the SFDL values for the shell mesh are multiplied by this factor a SFDL plot that matches better is obtained (Figure 3-26).

It is assumed that the worst case is simulated with the shell mesh because of the lower SCDF and SFDL values. If the method holds and works well for this type of modelling, it should hold for another type of damage scenario. This investigation leads to the conclusion that the method might be more robust if the damaged areas can be avoided when measurement locations are chosen. If these areas are not avoided the damage scenario cannot accurately be predicted and any other predictions might not be valid. If the proposed method is applied to measurement locations close to the damage, the SCDF and SFDL value remain independent of the damage scenario. From these measurements more accurate predictions on the damage level can be made.

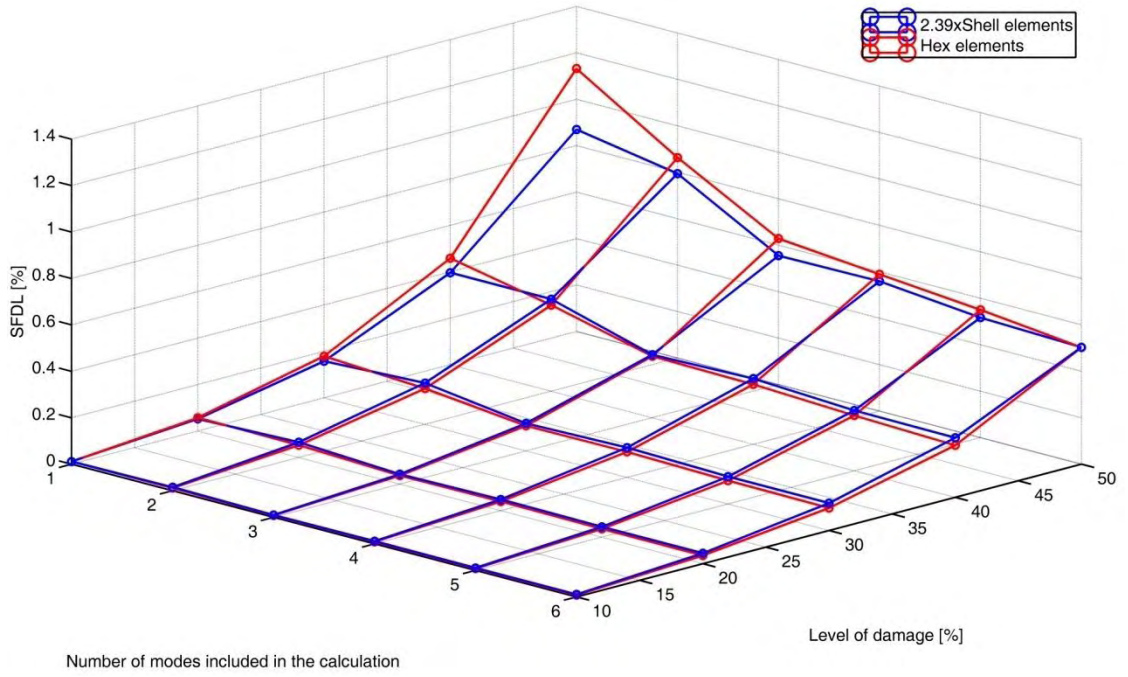

Figure 3-26: Comparison of the change in SFDL value as a function of number of mode included in the calculation and level of damage for the scaled shell and hexahedral meshes

3.1.4 Summary of deterministic damage case 1 and 2

The effect of the changes in damage levels on various damage indicator values were investigated in paragraphs 3.1.2.1 and 3.1.3.1. When the two cases are compared there is one major difference. In case 1 the damage is located close the measurement locations without enclosing any. This leads to a case where the measured strains increase as the damage increases since the load carrying capability of the damaged area reduces and the strains become redistributed through the undamaged part of the structure. The strains in the undamaged part of the structure, where the measurements are made, increases and are therefore able to identify the damage location. In case 2 two measurement locations are enclosed by the damaged area. This leads to a reduction in strains due to a reduction in load carrying capability of the structure in that area.

In comparison with the average change in natural frequency the SFDL values scaled as a power series in case 1 and scaled exponentially in case 2. A comparison of the curve fits to the SFDL values that were obtained in paragraph 3.1.2.1 and 3.1.3.1 are made in Figure 3-27 to compare the rates at which the SFDL values increase with respect to the damage level and the average difference in natural frequency.

The rate of increase of the SFDL value with respect to the damage level is shown in the top plot of Figure 3-27. From this plot it is clear that the SFDL values for case 1 are the largest up to about 42% damage. After this the SFDL increases faster with damage case 2. Thus for lower levels of damage the SFDL for case 1 is able to indicate the presence of damage much earlier than the SFDL for case 2. If an alarm was set for a SFDL value equal to 0.05, it would indicate damage at more or less 20% damage for case 1, but it

would only indicate damage at a level of 30% for case 2. It is evident from the bottom plot of Figure 3-27 that the SFDL value for case 1 appears to scale steadily with respect to the average difference in natural frequency. For case 2 the SFDL value increases dramatically.

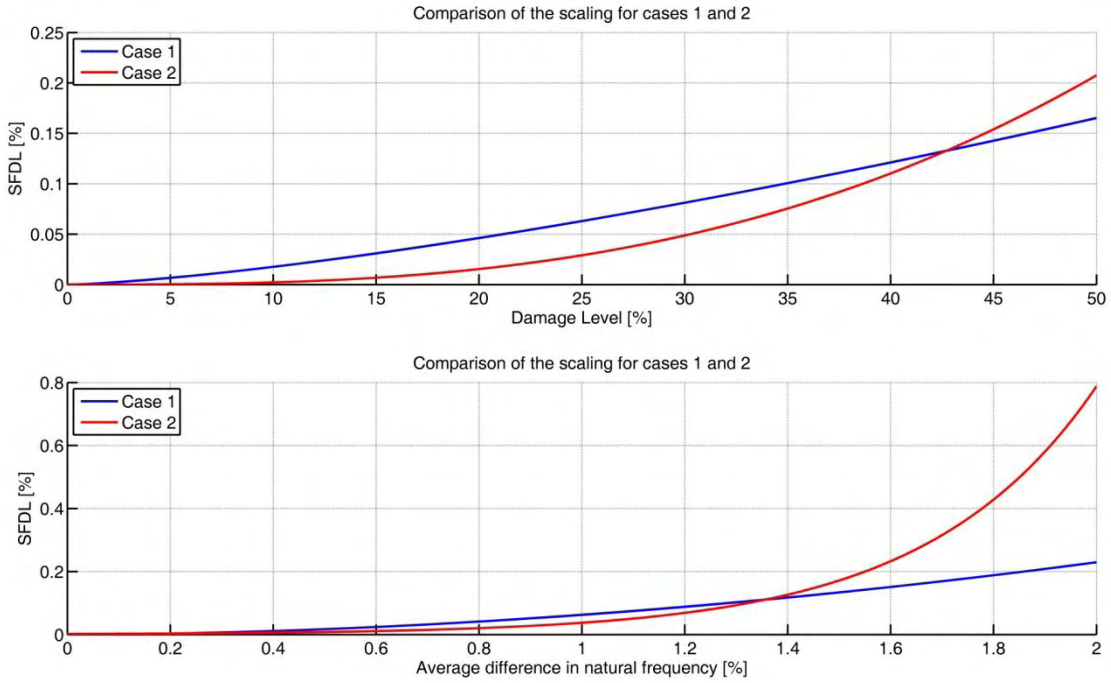

Figure 3-27: Comparison the the SFDL value scaling for cases 1 and 2 with respect to the damage level and the average difference in natural frequency

The proposed SFDL damage indicator appears to increase rapidly compared to both damage level and average difference in natural frequency. This observation is consistent with case 1. It scales as a power series in comparison to both damage level and average difference in natural frequency and is therefore more sensitive to damage than the natural frequency method. If the damage situation changes, as for case 2, the scaling changes and the SFDL is less sensitive to a change in damage, in comparison with case 1, at low levels of damage. The SFDL appears to be more sensitive to damage up to 42% when the measurement location is close to the damage location. For this reason the proposed damage indicator and damage detection method appear to work best when the measurement location is close to, but not enclosed by, the damaged area. It has also proven to be more sensitive to damage than the natural frequency method.

3.2 Deterministic variation of damage location within other wing-like family members

In paragraph 2.1.2 a geometry defining a family of wings was developed. The proposed method is intended to be applicable to this family of wings. One such family member was examined in detail in paragraph 3.1. In order to verify that the method is truly applicable to other family members, it was applied to two other family members. These two are the Neptune and Global Hawk wings, shown in Figure 2-4 with geometrical parameters given in Table 2-4.

The geometry, damage cases and results for these two family members are discussed and shown in Appendix D. The results of this analysis indicate that the method can still reliably predict the damage location from the SCDF values. The SFDL values showed the same type of scaling that was observed in the numerical study performed on the MQ-1 Predator wing. From these analyses the conclusion can be drawn that the proposed method is applicable to other family members.

3.3 Stochastic variation of damage location within the MQ-1 Predator wing

The deterministic numerical study performed in paragraph 3.1, showed that the proposed method appears to be promising. The presence of damage and its location can be identified from the SFDL values and the SCDF plots respectively. In this paragraph the method is investigated further to determine whether the damage can be identified and located if the damaged area and size are varied stochastically. The influence of the location and the size of the damaged area on the SFDL value are studied.

The same procedure, which was used in paragraph 3.1 to calculate and compare the strains at the measurement locations, is used for this investigation. The only difference between the two investigations is the fact that in paragraph 3.1, discrete damage sizes and locations were used to prove the computation and advantage of the SFDL calculation. For the present investigation the size and location of the damaged area varied statistically according to the most likely and critical position that damage can occur as described in paragraph 2.5.2.

3.3.1 Investigation into the number and placement of sensors

The proposed method requires that the strain and acceleration responses be measured via some response measurement transducers such as strain gauges or fibre optic Bragg gratings and accelerometers. There is however only need for one acceleration transducer since the strain response has to be normalised with one reference acceleration response. The minimum number of strain transducers required depends more on the placement of the transducers and whether these locations will allow the detection of damage.

This minimum number of sensors required to detect damage in the structure was studied by varying the number of sensors along the wing and by varying the damage location stochastically. The number of sensors was varied by dividing the wing surface into segments of equal length, depending on the number of sensors used, i.e. if one sensor is used it is placed in the centre of the wing segment of the wing-like structure. The number of sensors is varied along the measurement line that is shown in Figure 3-2.

It was assumed in paragraph 2.5.2 that a damage level of 50% is equivalent to a catastrophic failure. The damage level is therefore restricted to only 50% and the strain sensors are allowed to vary from 1 to 15 on each side of the wing. The number of simulations per number of sensors was limited to 200. The simulations, for the two

damage cases, where the measurement location is close to and inside the damaged area, were performed and initially no distinction between the two cases were made. This yielded the variation of the SFDL value with the number of sensors and the damage level as shown in Figure 3-28. A generally increasing trend in the SFDL values for an increasing level of damage is observed from Figure 3-28. This trend shows that the SFDL value increases as the level of damage is increased and that this increase is not dependent on the number of sensors used. The proposed method and the SFDL value therefore appears to be robust in the sense that for any number of sensors the damage can be detected, although the damage size might be under or over estimated. This is however purely theoretical and no measurement noise is taken into account.

A high level of mathematical noise is also observed in the form of peaks in Figure 3-28. No reliable predictions can therefore be made on the level of damage by simply looking at the SFDL value. The mathematical noise is present due to the modelling and the size and shape of the modelled damage and some of the noise can be attributed to noise present in the average difference in natural frequency (Figure 3-29) with respect to the damage level. Figure 3-29 shows that there is a constant increase in average difference in natural frequency as the damage level is increased.

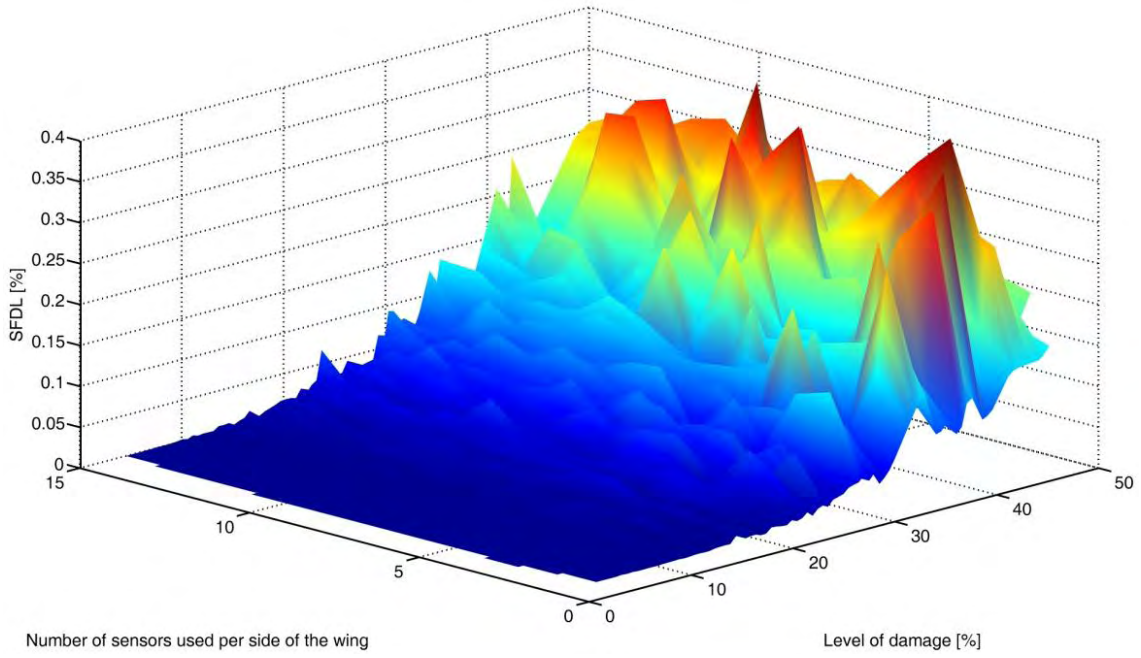

Figure 3-28: The influence of the number of sensors used on the SFDL values for both damage cases

There is a chance that the measurement location falls on the element boundary between damaged and undamaged material or even in an area of high stress concentration within the FE model. This leads to strain values that are not ideal in the sense that they can vary even though the damage level might be the same. Thus the shape and size of the damage might remain constant, but the measured strains might be closer to or further away from the damaged area. The SCDF values will therefore indicate larger or smaller peaks at the damaged location and introduce numerical noise in the calculation of the SFDL value. The SFDL is sensitive to the value of the average difference in natural

frequency and this might also introduce some errors to the value of the SFDL. It is difficult to establish the minimum number of sensors based on the variation shown in Figure 3-28.

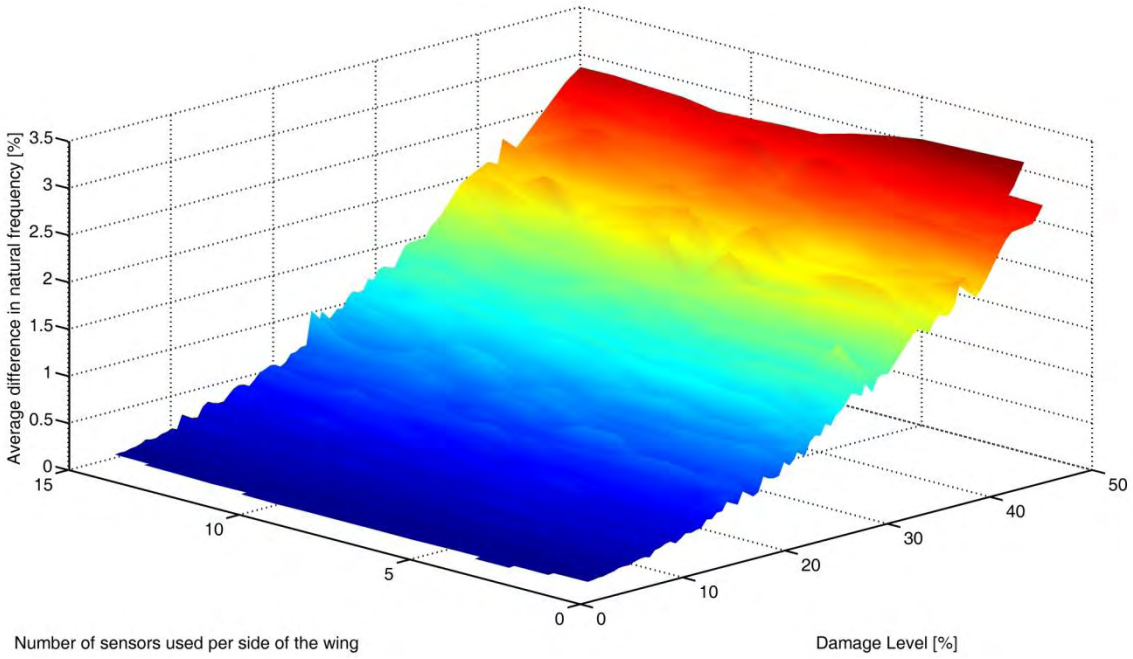

Figure 3-29: Variation of the average difference in natural frequency with respect to the damage level

The two types of damage cases are examined separately to get a better understanding of their effect. The same cases that were simulated for Figure 3-28 are examined; they are just separated into two damage cases. The case where the damage encloses one or more measurement locations is studied first. The variation of the SFDL value with respect to the level of damage and the number of sensors is shown in Figure 3-30. The mathematical noise present in Figure 3-30 can be attributed to the fact that a damage level being equal in size might enclose one measurement location in one case and in the next it might include two measurement locations. The SCDF will indicate one peak in the first case and two peaks in the second. The rms for the second case is much larger and thus the SFDL value will also increase. This damage case is susceptible to various phenomena that can cause it to produce numerical irregularities. The SFDL value for this damage case is very reliant on the strain value at the damaged location.

The SFDL value for 6 sensors on each wing were extracted and compared to the average difference in natural frequency and the level of damage in Figure 3-31 and Figure 3-32, respectively. In Figure 3-31 two curve fits were made to establish any correlation between the two values. Neither curve fit presented a very good fit, but it is observed that the SFDL value increases with an increase in average difference in natural frequency. The SFDL value appears to scale faster than the average difference in natural frequency, which implies that the SFDL is more sensitive than the natural frequency method (the same as the conclusion reached in paragraph 3.1.3.1). Different curve fits were made to the data when the SFDL is compared to the damage level. The power law curve fit provided the best fit and only this fit is shown (Figure 3-32). It is difficult to

make predictions on the damage level from SFDL value because of the noise present in the data. The case where the damage encloses one or more measurement location is therefore undesirable, due to the noise inherent in the SFDL values.

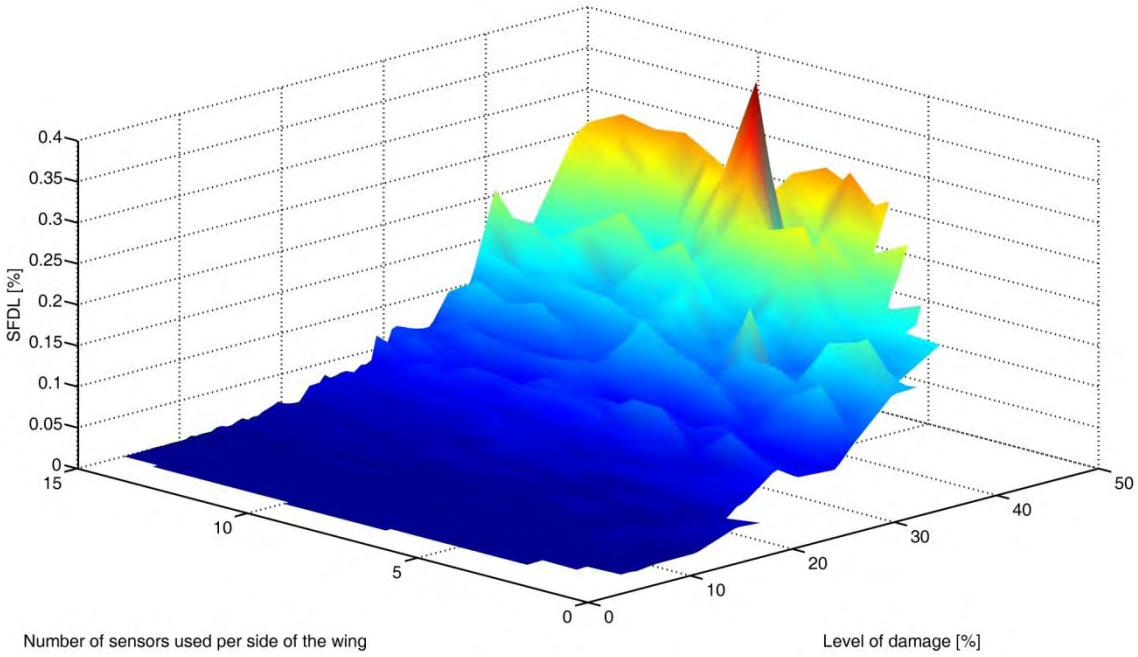

Figure 3-30: The influence of the number of sensors used on the SFDL values for the case where the damaged area encloses measurement location(s)

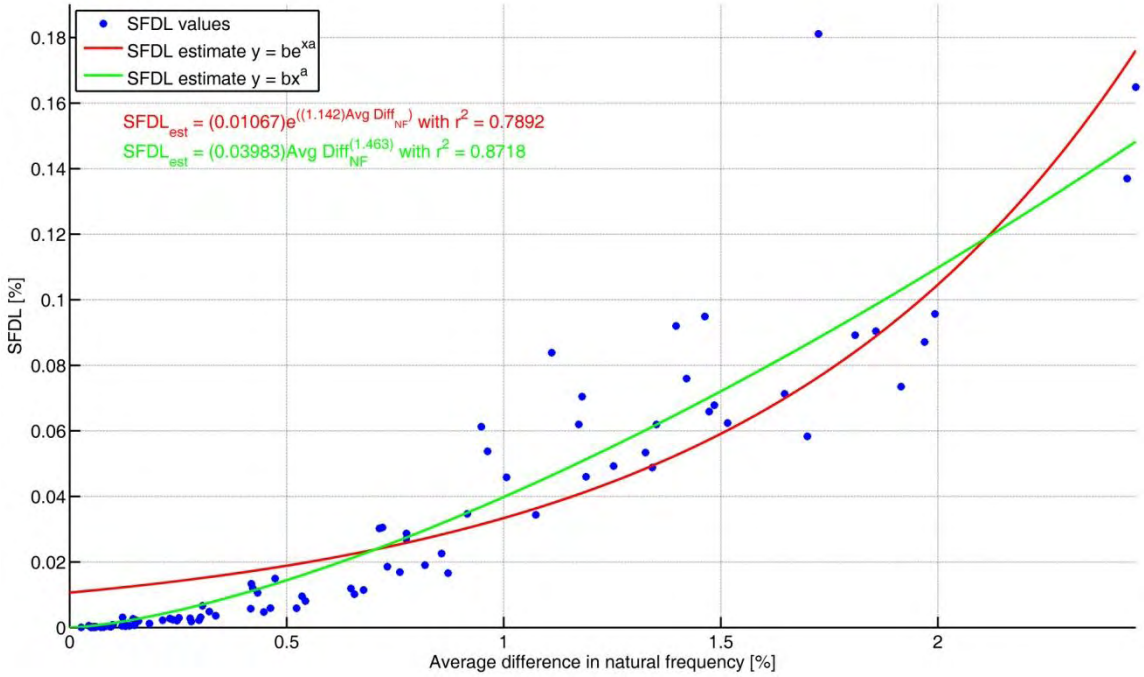

Figure 3-31: Curve fits showing the relation between the SFDL value and the average difference in natural frequency for the case where the damaged area encloses measurement location(s) and 6 sensors have been used

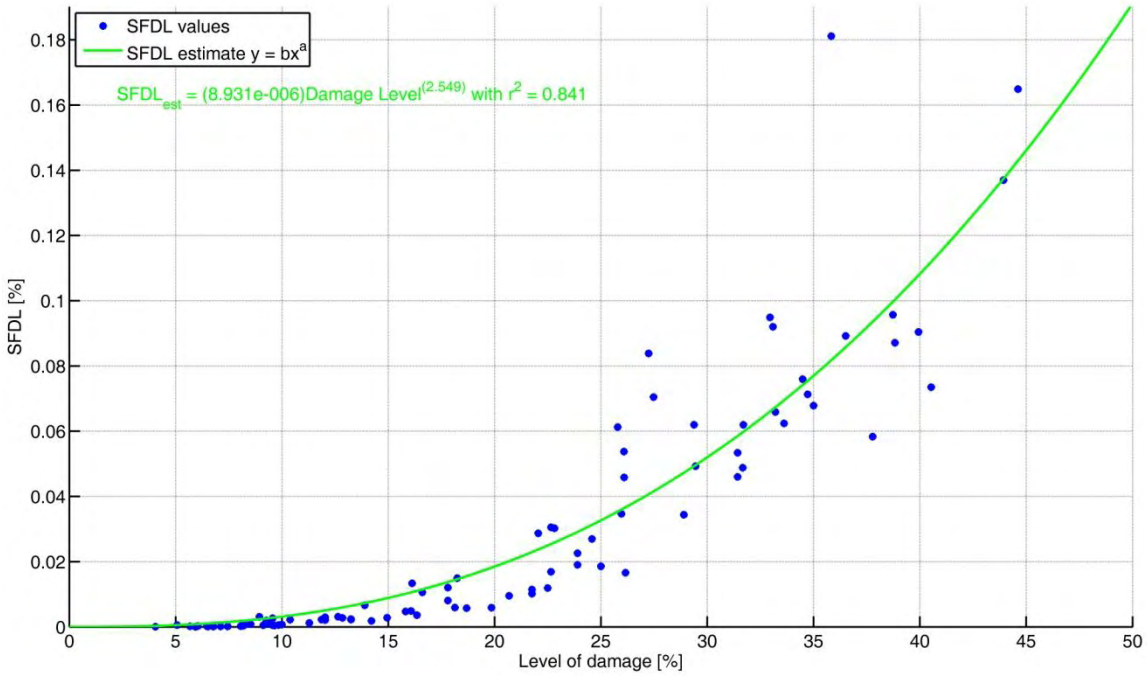

Figure 3-32: Curve fit for the SFDL value compared to the level of damage for the case where the damaged area encloses measurement location(s) and 6 sensors have been used

The variation in the SFDL value for the case where the damaged area is close to the measurement location is shown in Figure 3-33. Figure 3-33 shows a much clearer distinction of the SFDL value for different numbers of sensors. When the number of sensors being used becomes too small the chance that the damaged area is located near the measurement location becomes slim. As the number is increased the increase in SFDL value is smoother as the measurement locations have a greater chance of being located close to the damaged area. The boundary where this transition occurs is not exact. The minimum number of sensors which would still be able to detect the presence of damage has to be determined a little more subjectively. To aid in this choice the number of channels available for measurement and the number of sensors that provides a good indication on the spatial location of the damage area have to be considered.

The SCDF plots for an increasing number of sensors used to detect the damage are shown in Figure 3-34 and Figure 3-35. By evaluating these two figures together with the variation shown in Figure 3-33 the minimum number of sensors that is able to reliably detect the presence of damage as well as provide good spatial resolution can be obtained. It is clear that for a small number of sensors, 5 or less, the spatial resolution and detection capability, are not great. There are more undesirable peaks on the SFDL variation with 5 or less sensors. With 6 or more sensors these undesirable peaks become less prominent and the spatial resolution is increased. An infinite number of sensors theoretically provide the best spatial resolution and perhaps even the best SFDL variation with respect to the damage level. This is not realisable however, as there are limits to the number of channels that can be used for measurements. This leads to a range of minimum sensors that provide damage detection as well as a good spatial resolution. This range is more or less constrained to more than or equal to 6 sensors and less than or equal to 10 sensors to record the strain response with 1 acceleration sensor to record the acceleration response.

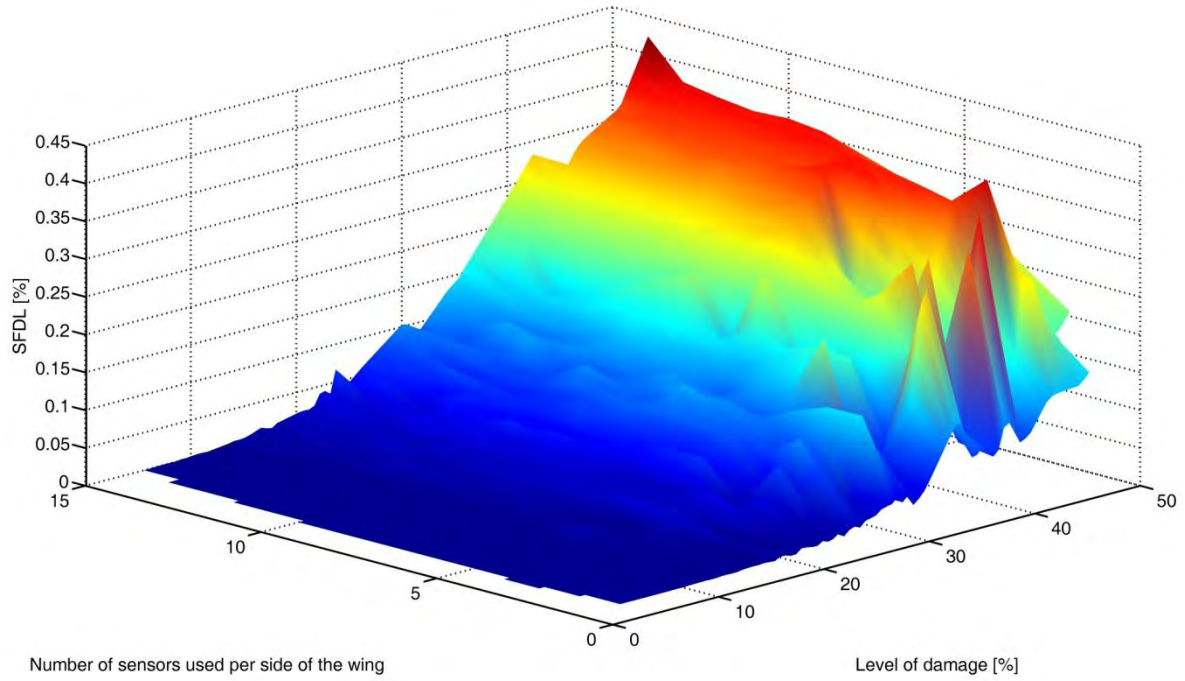

Figure 3-33: The influence of the number of sensors used on the SFDL values for the case where the damaged area is close to the measurement location

This analysis was done in order to establish the minimum number of discrete sensors that is able to reliably indicate the presence of damage as well as its location. There are however methods to produce intermediate results between sensors and it was shown by Farrar et al. (1996) that a cubic spline fit to data can be used to obtain interpolated intermediate data. This intermediate data can be used to determine whether damage is located between discrete sensor locations. If such a fit is made to the measured data it is possible to get away with even less discrete sensors.

The relations between the SFDL value and the average difference in natural frequency and the SFDL and the damage level for six sensors are plotted in Figure 3-36 and Figure 3-37, respectively. When Figure 3-36 is evaluated it is clear that the power law fit provides a good estimate to the data and that the SFDL value is more sensitive to damage than the average difference in natural frequency. Upon examining Figure 3-37 it is clear that the power law fit is a very good estimation to the data as the r^2 value is equal to 0.9511. This is desirable as estimations on the damage level based on the SFDL value can be made. Theoretically it should be possible to monitor the growth of the SFDL value as the damage level increases. A prediction on the damage level can then be made based on a power law fit through the monitored values and comparing this fit to the one obtained in Figure 3-37. The proposed method can therefore theoretically address the third level of damage detection (Rytter, 1993) by giving an indication of the size of the damage.

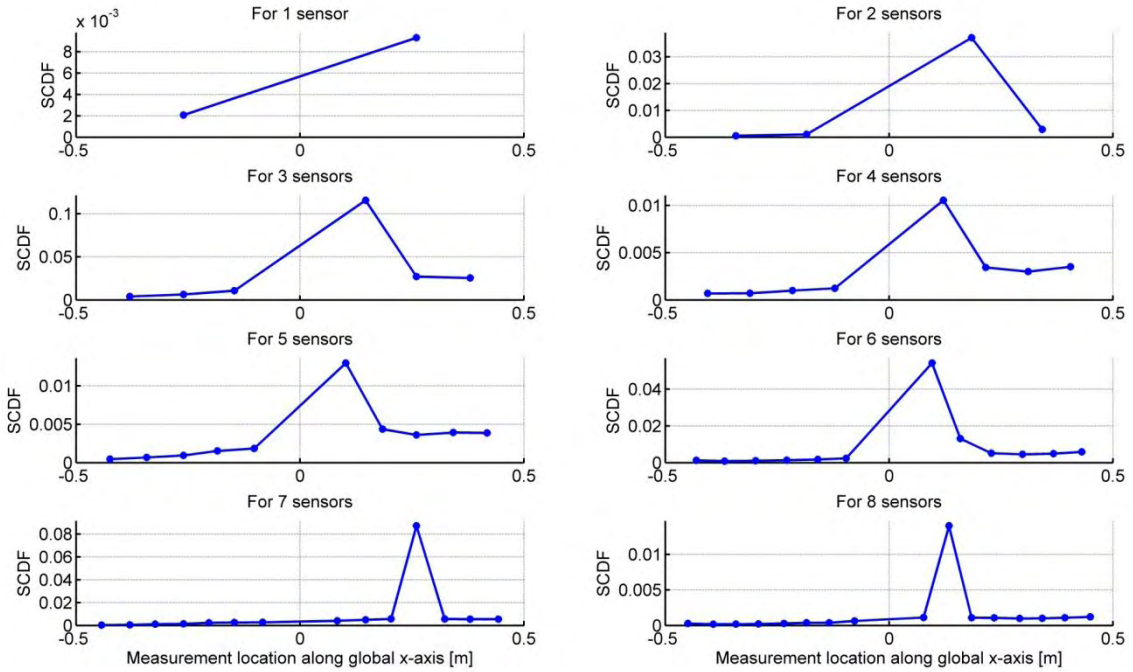

Figure 3-34: SCDF plots for an increasing number of sensors (1-8)

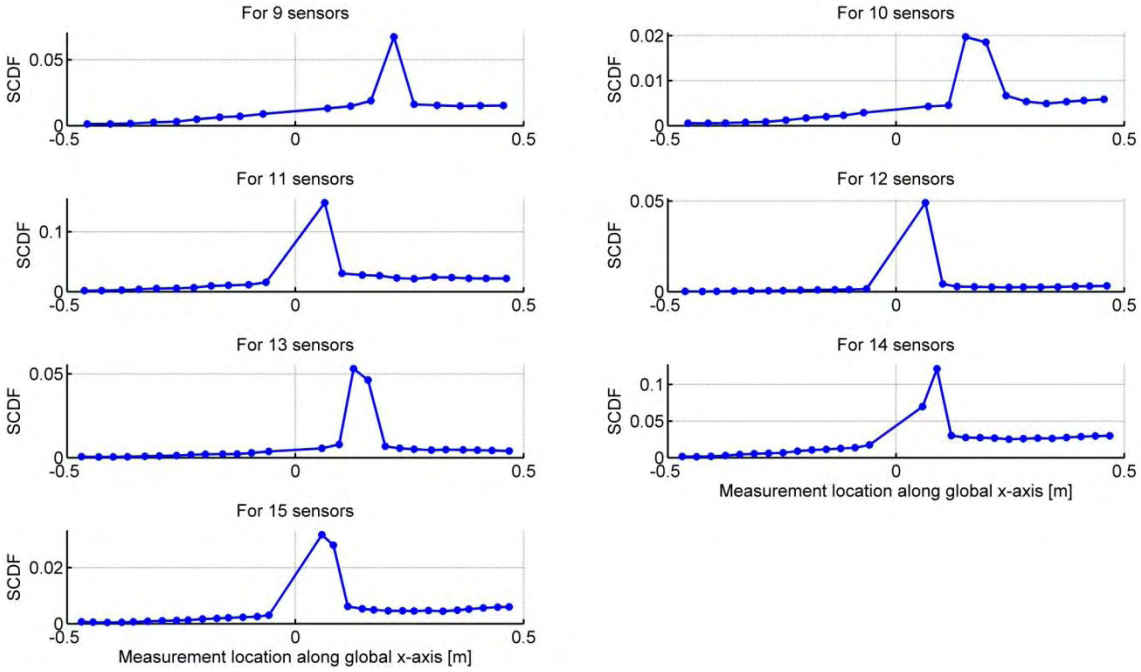

Figure 3-35: SCDF plots for an increasing number of sensors (9-15)

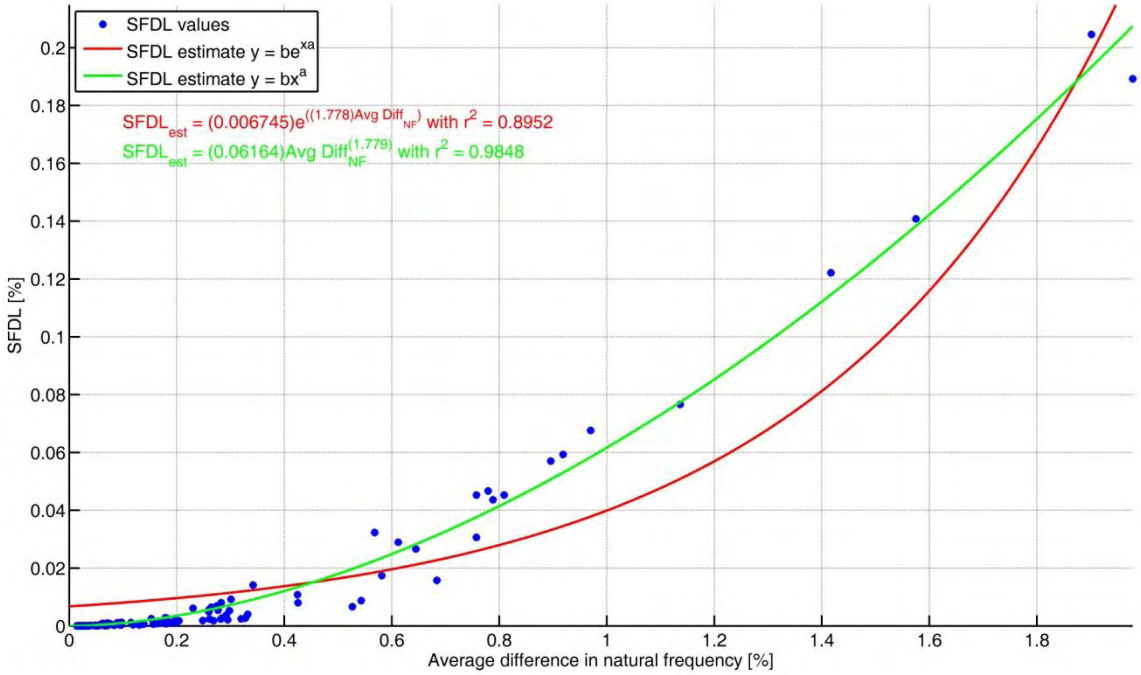

Figure 3-36: Curve fits showing the relation between the SFDL value and the average difference in natural frequency for the case where the damaged area is close to the measurement location and 6 sensors have been used

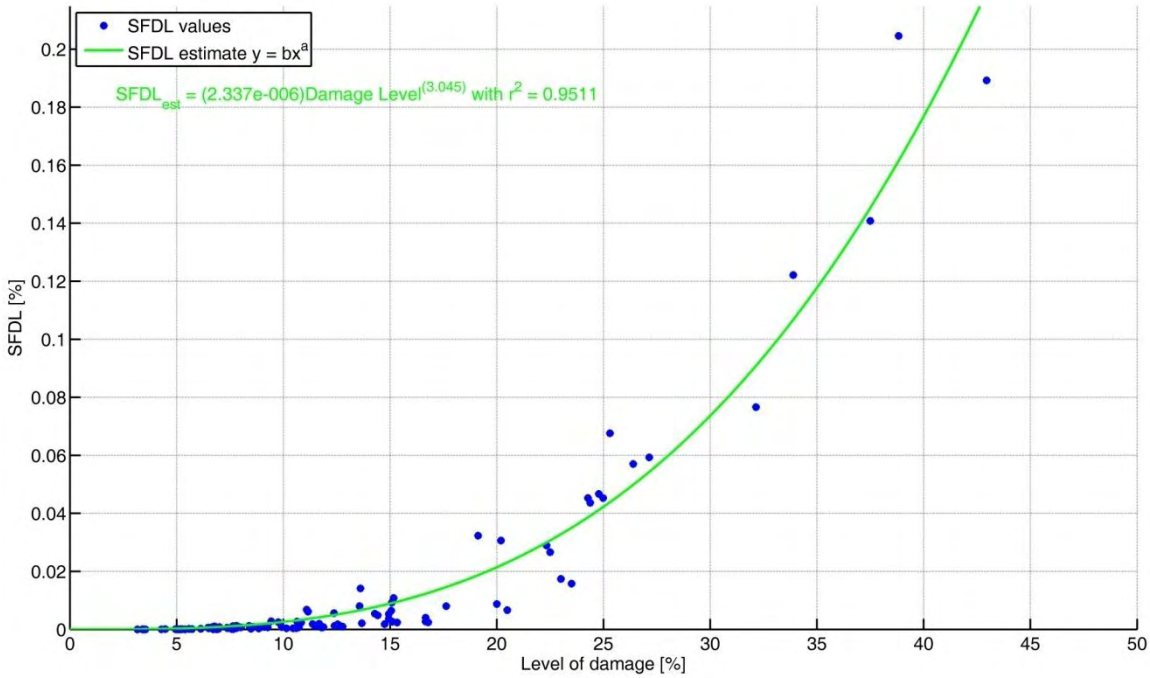

Figure 3-37: Curve fit for the SFDL value compared to the level of damage for the case where the damaged area is close to the measurement location and 6 sensors have been used

3.4 Summary of chapter 3

This chapter was concerned with the numerical study of the damage detection method as it applies to a family of wings. One family member, namely the MQ-1 Predator wing, was

studied in particular. The performance of the proposed damage indicators was evaluated by performing analyses deterministically on the one family member as well as on other family members in paragraphs 3.1.2, 3.1.3 and 3.2, respectively.

3.4.1 Summary of the major findings

In chapter 3 it was shown that:

- It is possible to localise the damage by interpreting the SCDF values.
- The SCDF can correctly indicate the location of the damage as the damage location identified from the SCDF values corresponded to the known damage location.
- There is an increase in SCDF value as the damage level is increased.
- The SCDF has less noise present than a direct calculation of the CDF.
- The presence of damage is indicated by the SFDL value.
- The increase in SFDL value as the damage level is increased can be predicted by a power law equation in the two deterministic cases as well as in the stochastic investigation.
- The SFDL scales quicker than the natural frequency method and is therefore more sensitive to damage than the natural frequency method. This scaling can be approximated by a power law equation or exponential equation depending on the location of damage (either close to, damage case 1, or enclosing, damage case 2, the measurement locations).
- By investigating the normalisation of the SCDF with either the undamaged or damage strain values it was decided to use the SCDF normalised by damaged strains as this provided increased sensitivity when the damage enclosed the measurement locations.
- The method is influenced by the way in which damage can present itself when the damaged area encloses one or more of the measurement locations.
- From the analyses performed on different members of the family of wings, it was shown that the proposed method is applicable to other family members.
- When the number and placement of sensors were investigated, it was found that the minimum number of sensors required to spatially locate the damage within the structure is ideally between 6 and 10 sensors per side of the wing including at least one acceleration sensor.
- It was established from the stochastic simulations that the proposed damage detection method works at its best when the measurement locations are close to the damage location, but not enclosed by the damaged area.
- The stochastic simulations showed that the damage detection method is robust as the method was able to detect the presence of damage (from the SFDL values) as well as localise the damage (from the SCDF values).
- Predictions on the damage level can be made by using the power law estimation to the SFDL values and the measured SFDL value. If a FE model is available, it can be used to estimate the SFDL values as the damage grows and therefore, if the SFDL value is known, the damage level can be estimated.

3.4.2 List of conclusions

The main conclusions that can be drawn from the major findings (3.4.1) are:

- The method can indicate the presence, the location and the level of damage in a structure.
- The SCDF is an improvement on the CDF as there is less noise present in the SCDF values.
- The SCDF is not affected by damping in the structure.
- The SFDL values can be predicted by a power law fit which lends itself to be able to predict the damage level by only measuring the SFDL value.
- The SFDL value is more sensitive to damage than the natural frequency shift technique.
- The method is applicable to other structures in the family of wings.
- The method works at its best when the measurement locations are close to the damaged area, but not enclosed by it.
- The minimum number of sensors was identified to lie between 6 and 10 strain sensors per side of the wing with one acceleration sensor.

Chapter 4: Experimental study

This chapter is devoted to describing the experimental program followed in order to update and validate the FE model as well as investigate the proposed method experimentally.

The objectives of the chapter are to:

1. Update the FE model of the MQ-1 Predator wing for use in the numerical study.
2. Use the updated FE model and correlate the numerical simulations with experimental results.
3. Validate the proposed damage detection method and damage indicators with experimentally measured output-only response data.

With reference to Figure 4-1, these objectives will be achieved by:

1. Performing mobility and strain response measurements with a laser Doppler vibrometer and strain gauges, respectively (paragraphs 4.2.1 and 4.2.3, respectively). Use the measurement results to update the FE model (paragraphs 4.2.2 and 4.2.3.1).
2. Comparing numerical simulations with measured data. This is performed in the model updating stages of paragraphs 4.2.2 and 4.2.3.1 as well as for the strain FRFs and the transmissibility functions in paragraph 4.2.3.2.
3. Using the measurement results described in paragraph 4.2 to calculate the two proposed damage indicators for two experimental cases (paragraph 4.3). In one case the damaged area is located close to the measurement locations (paragraph 4.3.1) and in the second case the damaged area encloses two measurement locations (paragraph 4.3.2). The two experimental damage cases are discrete and are described in paragraph 4.1.4.

The experimental setup that will be used for the mobility as well as the strain measurements is described in detail in paragraph 4.1. The suspension system that is used to realise the boundary conditions during the experimental investigation, is described in paragraph 4.1.1. The excitation attachment is described in paragraph 4.1.2 and the test signals as they apply to the mobility and strain measurements are described in paragraphs 4.1.2.1 and 4.1.2.2, respectively. The configuration, i.e. the measurement locations and measurement systems for the mobility and strain measurements are described in paragraphs 4.1.3.1 and 4.1.3.2, respectively.

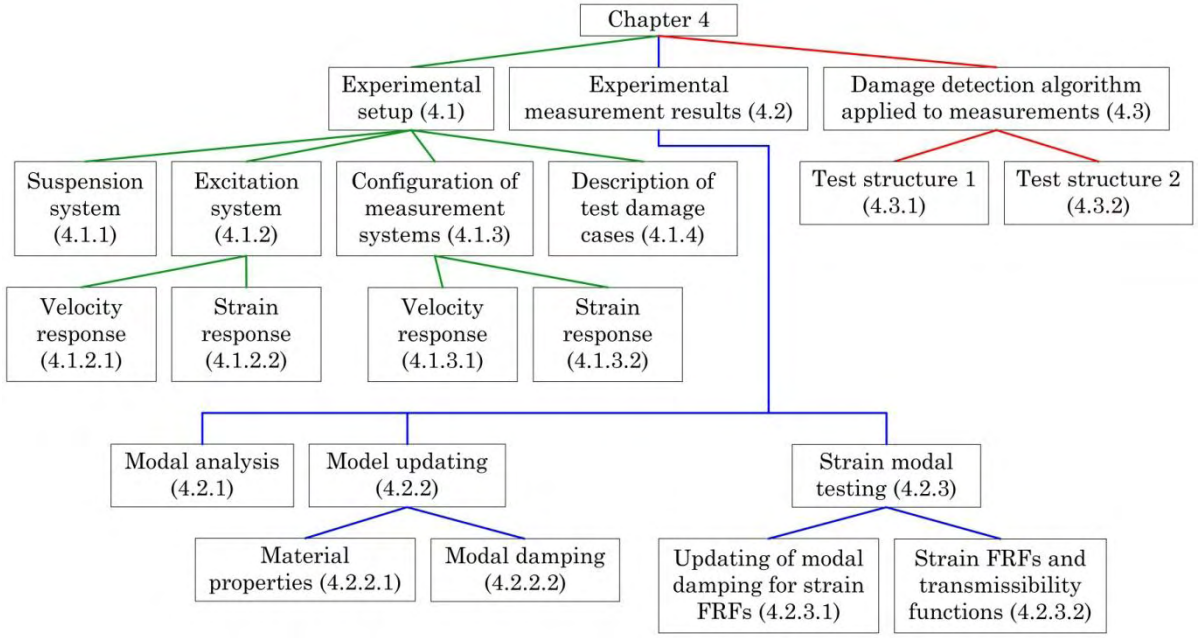

Figure 4-1: Layout of chapter 4

4.1 Experimental setup

The test structure was manufactured to have the same properties and dimensions as the structure used during the numerical study. The structure with geometry as defined in Table 3-1 was laser cut from a 10 *mm* thick mild steel plate with material properties approximately given by those of regular steel as in Table 2-7.

Two types of tests were performed on the test structure. Firstly, mobility measurements with known input excitation were carried out. These measurements were intended for a modal analysis and the results were subsequently used for model updating. The mobility measurements were performed by using a scanning laser Doppler vibrometer to measure the velocity response of the structure. Secondly, a dynamic strain test was performed. During this test dynamic strains and accelerations as well as the input force were measured. These measurements were used for the damage detection calculations and predictions. The basic layout of the two measurement configurations were essentially the same. The two cases differ in the transducers used to measure the response. The subcomponents of each measurement configurations are described in more detail in the subparagraphs of paragraph 4.1.

4.1.1 Suspension of the test structure

The structure was supported horizontally with free-free boundary conditions, because compared to clamped-free or clamped-clamped, it is much easier to realise experimentally and to model numerically.

If a structure is tested with free-free boundary conditions, it exhibits rigid body modes at 0 Hz. Theoretically there are six rigid body modes for all six possible rigid translations and rotations. When testing with free-free boundary conditions it is not always possible

to realise this boundary condition practically. In practice the structure is suspended by very flexible or soft springs, such as elastic bands. This causes the structure to have rigid body modes not necessarily at 0 Hz, but at low frequencies in relation to the bending modes of the structure. In this case low refers to frequencies equal to 10-20% of the first natural frequency.

The first natural mode will be influenced most by the suspension system. A precaution that can be taken to limit this influence is to attach the suspension system as close as possible to the nodal locations of the first mode. It should also be ensured that the suspension system does not add signification damping to a lightly-damped structure (Ewins, 1995).

To establish the best location for the suspension system, the first bending mode of the structure was examined numerically. The FE model used in chapters 2 and 3 was used for this purpose. The first natural mode of the structure is a vertical bending mode. The approximate nodal lines of the first bending mode are indicated by the red dashed lines in Figure 4-2. The positions of these lines were used to determine the support locations.

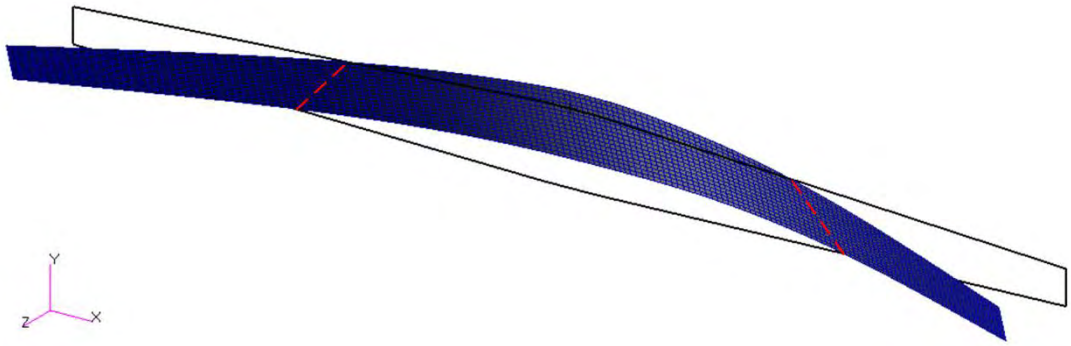

Figure 4-2: The first bending mode of the wing structure showing the nodal lines of the first natural mode

The structure was suspended in the vertical plane and thus it was necessary to drill holes for the suspension system to pass through. The holes were drilled with a 1 *mm* drill bit to ensure minimal mass loss. The locations of the suspension holes as well as the node, in the FE model to which they correspond, are given in Table 4-1 (with respect to the coordinate system defined in Figure 2-10). The ideal location of the suspension system was determined from the FE model, however, when the holes were drilled the actual holes were not drilled at the ideal location, but at a position close to the ideal location. The suspension location is still located relatively close to the nodal line and the influence it has on the first bending mode should be negligible.

Table 4-1: The location of the suspension holes

	Ideal			Actual		
Hole	**x-location [*mm*]**	**y-location [*mm*]**	**Node in FE model**	**x-location [*mm*]**	**y-location [*mm*]**	**Node in FE model**
1	228.5	14.78	2181	159.1	11.2	2731
2	-228.5	14.78	5947	-159.1	11.2	5397

The suspended structure that was used for the experimental measurements is shown in Figure 4-3.

Figure 4-3: The actual suspension location as used for the structure in the experimental study

4.1.2 Excitation of the test structure

When the excitation is considered, care should be taken regarding the attachment of the shaker. The shaker should ideally only excite the structure in the intended direction. The force transducer measures the force that the shaker imparts on the structure. However, it only measures force unidirectionally and thus care should be taken to ensure that only a unidirectional force is imparted on the structure. A stinger is a thin rod that is stiff axially and flexible in bending. It can be used to transmit the force only in the axial direction and thereby constrain the force input to be unidirectional. Any part of the attachment which is on the structure side of the force transducer should be considered to be a part of the structure. The effect such an attachment has is an increase in mass and may even stiffen the structure at the connection point (Friswell et al. (1995) and Ewins (1995)).

Excitation by means of a hammer can be less complicated than excitation by means of a shaker, since no attachment is required. The drawback of this method is the fact that it is sometimes difficult to impart sufficient energy into the structure with a hammer. Shakers are more suitable to impart higher levels of energy into the structure (Friswell et al., 1995). Since free-free boundary conditions are used it is difficult to get repeatable hammer impacts that will excite the structure sufficiently. It was therefore decided to rather use a shaker.

The test structure was suspended in the vertical plane. The shaker that was used to excite the structure dynamically had to be placed in such a manner to excite the structure in the horizontal direction. It was decided to use an electro dynamic shaker (for this setup a Modal 50 was used). This shaker has a large modal mass against which it can react. The shaker can therefore be suspended from chains or ropes to align the shaker with the test piece. This can lead to misalignment errors, where the shaker and thus the force that is imparted on the structure, is not perpendicular to the test structure. One possible way of reducing this misalignment, is to put the shaker on

rollers. On rollers the shaker can still move horizontally and ideally it will only react against the modal mass, the same as in the suspension case. The effects of the two different shaker positions are evaluated and discussed in more detail in paragraph 4.2.1.

The shaker is attached to the structure via a stinger and a load cell (Figure 4-4) at the same location as in the numerical study. This corresponds to node 4287 of the FE model and the location indicated in Table 2-12 which is given in Table 4-2 for convenience. The position is specified with respect to the coordinate system shown in Figure 2-10. The piezoelectric load cell has a sensitivity of 2.359 mV/N. The signal from the load cell was subsequently used to calculate the mobility FRFs.

Table 4-2: Coordinates of excitation position

Coordinate	Value [m]
x	-0.02652
y	-0.06522

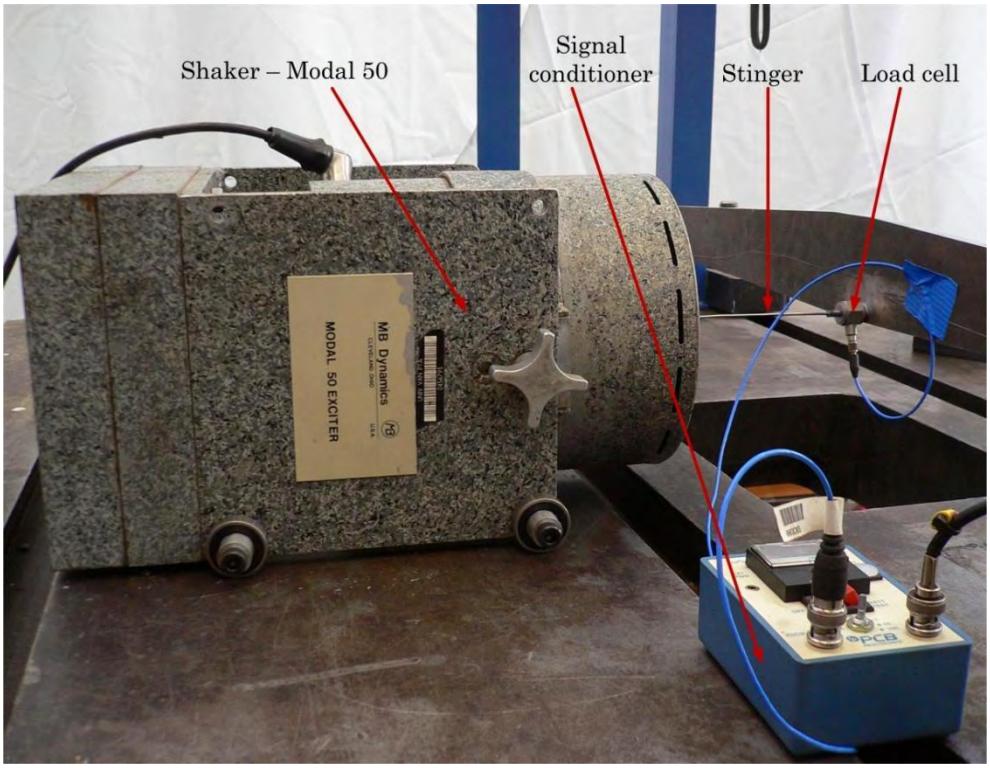

Figure 4-4: The shaker together with the stinger and load cell showing the force transmission path and connection to the structure

4.1.2.1 Excitation for mobility measurements

The mobility measurements were used for modal analysis and model updating purposes. These measurements were made under controlled conditions and did not simulate any real life or in-flight conditions. A periodic chirp function was used to excite the structure. This periodic chirp function is generated by the control computer of the Polytec PSV300 scanning laser Doppler vibrometer and is amplified before the signal goes to the shaker (Figure 4-5).

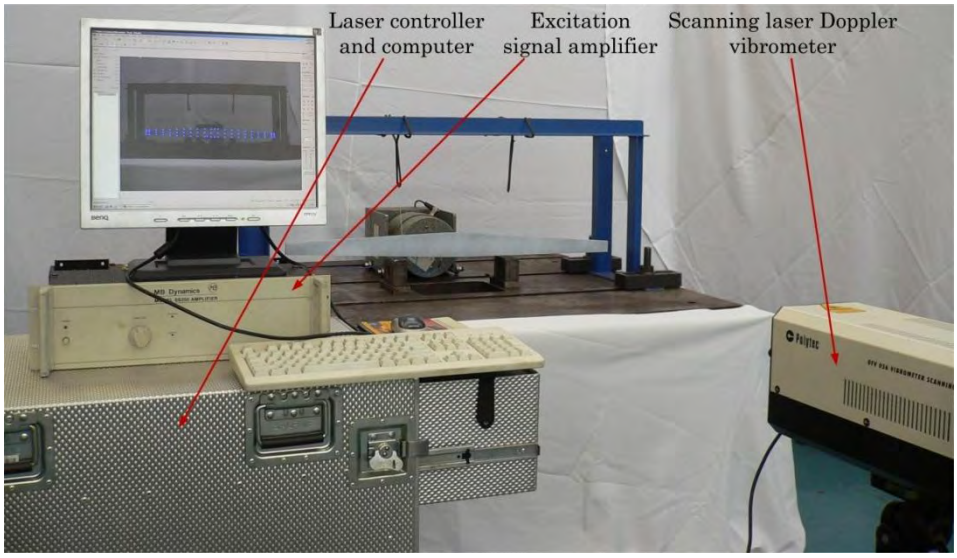

Figure 4-5: Complete modal analysis setup showing the laser and excitation system

During the numerical study the simulations were performed for a frequency range from 0 to 1350 *Hz*. The FE model will therefore have to be updated for this frequency range. The periodic chirp was defined to excite the structure from 5 to 2000 *Hz*, to eliminate the rigid body modes and to include modes up to 2000 *Hz* for model validation.

4.1.2.2 Excitation for strain measurements

The excitation signal for the strain measurement differed from the excitation signal for the mobility measurements in the sense that it had to simulate real flying conditions, and was assumed to be random in nature. The signal was generated by means of Matlab's *rand* function to have energy up to at least 1350 *Hz* for comparison with the numerical model. The signal consisted of randomly generated points with a value between -1 and 1 V. The signal was generated for 13.107 seconds with 2^{16} points defining the function. The signal is equivalent to a signal with a sampling frequency equal to 5000 *Hz*. The eDAQ lite with which the strain and acceleration response was recorded is limited to a choice of sampling frequency of 2000 or 5000 *Hz*. A sampling frequency of 5000 *Hz* was chosen and the reason for this choice is discussed in more detail in paragraph 4.1.3.2. This signal was exported to the control computer of the laser vibrometer. The function generator of the laser was used to excite the structure with this random signal. This random signal was generated to ensure that enough energy up to 2500 *Hz* was present in the excitation force due to the sampling frequency equalling 5000 *Hz*.

4.1.3 Configuration of measurement systems

It was stated at the beginning of paragraph 4.1 that two types of measurements were made. This paragraph describes the two measurement configurations.

4.1.3.1 Mobility FRF measurement

The mobility frequency response of the structure was measured with the Polytec PSV300 scanning laser Doppler vibrometer (Figure 4-5). A measurement mesh was defined as indicated by the blue dots in Figure 4-6. The highest frequency of interest was 1350 *Hz*. The laser was set to measure up to 2 *kHz* with the sampling frequency set to 2.56 times this bandwidth to satisfy Shannon's sampling theorem. The control computer has a built in anti-aliasing filter and therefore no subsequent filtering was necessary. The sensitivity of the laser was set to 10 $mm/s/V$. The laser controller conditioned the signal and the control computer (Figure 4-7) used the conditioned signal together with the load cell signal to calculate the $H_1(i\omega)$ estimator to the mobility at each scan point. 6400 lines were used to define the FRF, which translates into a frequency resolution of 0.3125 *Hz*.

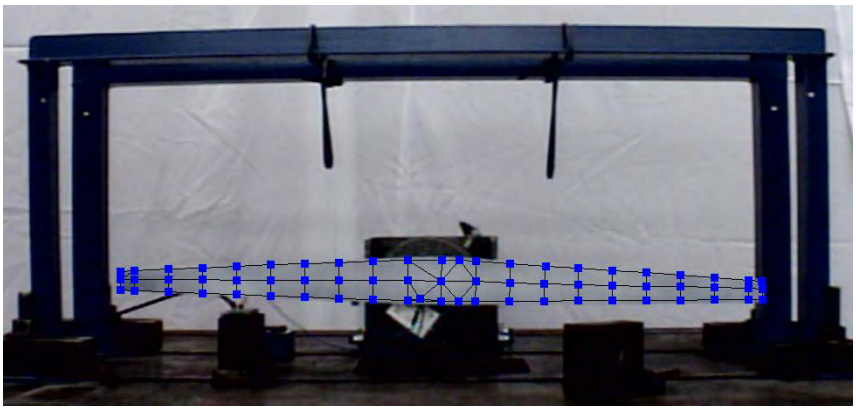

Figure 4-6: Mesh defined over the test structure

Figure 4-7: The laser controller and control computer

4.1.3.2 Strain time-history measurement

Due to the low mass of strain gauges, they are excellent for making dynamic strain measurements. There are, however, two limitations on strain gauges for such measurements. The two factors that should be observed are (Hoffman, 1989):

- The continuous vibration and fatigue characteristics of the strain gauges
- The upper frequency limit of the strain gauges

The continuous vibration and fatigue characteristics of the strain gauge have to do with the number of high amplitude strain (500 to 2000 $\mu m/m$) cycles that the strain gauge can withstand before fatigue failure sets in.

The upper frequency limit is dependent on the ratio of the length of the strain gauge to the wavelength of the response that is measured (l_{sg}/λ). If this ratio grows much larger than 0.1, a discrepancy between the measured strain amplitude and the actual strain amplitude increases. Hoffman (1989) indicates the relationship between the measured to actual amplitude ratio and the strain gauge length to wavelength ratio. For a strain gauge length to wavelength ratio of less than 0.1, the measured and actual amplitude ratio is close to 1. The upper frequency can thus be determined for a given strain gauge length. This calculation can be performed by using the velocity of sound v_{sound} in the material (equation 4.1) and the wavelength λ as the ratio of the speed of sound and the upper frequency limit f_{upper} (equation 4.2). Hoffman (1989) concludes that the commonly used 3 and 6 mm strain gauges will suffice for many dynamic measurement problems.

$$v_{sound} = \sqrt{\frac{E}{\rho}} \tag{4.1}$$

$$\lambda = \frac{v_{sound}}{f_{upper}} \tag{4.2}$$

The strain response was measured with 5 mm 350 Ω 0°/45°/90° rosette strain gauges. The ratio l_{sg}/λ for this strain gauge used on a mild steel plate is calculated to determine the validity of the upper frequency limit. The speed of sound for steel is determined from equation 4.1 and the result is shown in equation 4.3. The wavelength for an upper frequency limit of 1350 Hz is determined from equation 4.2 and the result is shown in equation 4.4.

$$v_{sound} = 4172.2\ m/s \tag{4.3}$$

$$\lambda = 3.83\ m \tag{4.4}$$

The ratio of strain gauge length to wavelength (l_{sg}/λ) is computed in equation 4.5. This value is far less than 0.1 and frequencies up to 1350 Hz can be handled by the strain gauge.

$$\frac{l_{sg}}{\lambda} = 0.001305 \tag{4.5}$$

The strain gauge was used in a quarter bridge configuration as only unidirectional strains without any temperature compensation was required. There is no need for temperature compensation as the measurement period is relatively short and the zero point can be reset before each measurement.

The strain gauges were stuck on a line corresponding to the x_1-axis of Figure 2-10 at the line indicated in Figure 3-2. This ensured that no rotations were necessary and the calculation of the rotated strains from the FE model could be verified. Six strain gauges were attached on the right side of the wing planform and only two strain gauges on the left side (Figure 4-8). The damage was introduced on the right side and therefore more sensors were required here to validate the analytical predicted results. The strain distribution should not change on the left side of the wing planform and therefore two sensors are used here to verify that no change in strain is recorded here.

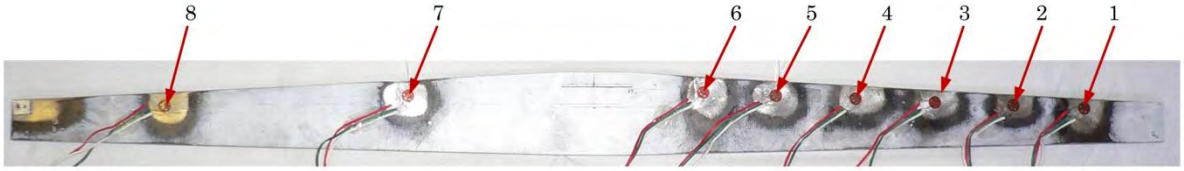

Figure 4-8: Strain gauge distribution and measurement locations

The acceleration response of the structure was recorded together with the strain response. The acceleration response is used to verify the natural frequencies of the structure and is used to normalise the strain response to obtain a measured transmissibility function. The acceleration response was measured at the same location that was used in the numerical study and the coordinates defining the measurement position are given in Table 3-3 and in Table 4-3 for convenience.

Table 4-3: Coordinates of the acceleration measurement position

Coordinate	Value [*m*]
x	-0.4937
y	-0.0304

Damage identification from curvature modes is sensitive to measurement noise and variations in the parameter. This method is effective for systems with small parameter variation and care should be taken during practical implementation to ensure that high quality signals are obtained. These include using anti-aliasing filters and averaging to minimise noise (Li et al., 2002).

A SoMat eDAQ lite data acquisitioning system (Figure 4-9) was used to record the strain as well as the acceleration time histories. The eDAQ only allows the option of a sampling frequency of either 2000 or 5000 *Hz* in the 2500 *Hz* vicinity. Due to this restriction a sampling frequency of 5000 *Hz* was used to ensure that the highest frequency of interest can be measured. The calibration of the measurement equipment as well as signal

conditioning, in the form of anti-aliasing filtering, is performed by the eDAQ. The strain gauge measurement system is shunt calibrated by the internal shunt resistors of the eDAQ lite and no subsequent calibration was required.

The force-time history of the exciter was recorded for FRF calculation purposes. The load cell configuration remained the same as in the mobility measurements described in paragraph 4.1.2. The acceleration response was recorded at only one reference location by the accelerometer. The signal conditioner was used to amplify the signal from the accelerometer as well as the load cell before it was recorded by the eDAQ. The strain gauges were connected to the eDAQ via pigtails with 15 pin connection terminals attached to them. The eDAQ has bridge boards designed specifically for strain gauge measurements that has an internal Wheatstone bridge circuit. The signal was recorded from the internal bridge and therefore does not pass through a signal conditioner. The complete strain measurement system is shown in Figure 4-9.

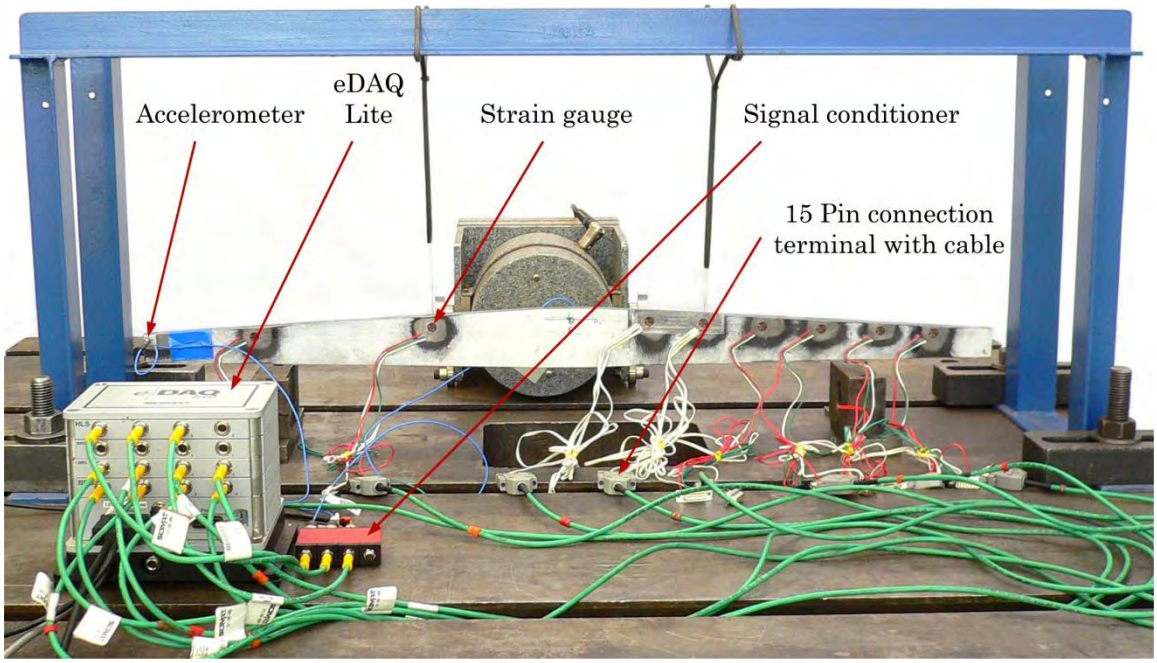

Figure 4-9: The strain measurement system

4.1.4 Damage cases for the experimental study

During the experimental study two cases and thus two test structures were examined. A change in the behaviour (the scaling of the SFDL values) was noticed when the one or more of the measurement locations are enclosed by the damaged area. This gave justification to examine two different cases experimentally. For the first test structure the damage was introduced at a location close to the measurement locations (Figure 4-10 a). It simulates damage with 30% damage, thus having a thickness of 7 mm. The second test structure was used to investigate the case where the damage encloses one or more of the measurement locations (Figure 4-10 b). This structure simulates damage with 50% damage or thickness of 5 mm. Similar cases were studied numerically (paragraph 3.1.2

and 3.1.3.). The damage locations and the respective sizes for the two test structures are summarised in Table 4-4.

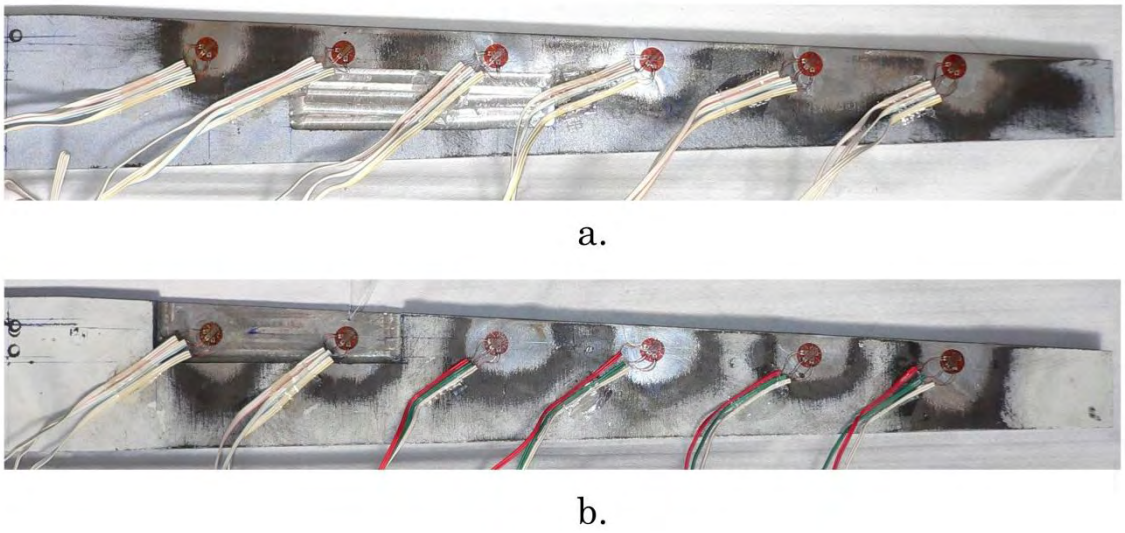

Figure 4-10: Damaged location for test structure 1 and 2

Table 4-4: Parameter values defining the damaged area for test structures 1 (a) and 2 (b)

Damage parameter	Value for test structure 1	Value for test structure 2
l_{di}	133.839 mm	70.708 mm
h_{di}	25.808 mm	2.471 mm
l_d	119.949 mm	113.636 mm
h_{dr}	27.730 mm	25.662 mm
h_{dt}	23.533 mm	22.254 mm
Λ_{LE}	1.771°	3.2°
A_d	$3.074 \times 10^{-3}\ m^2$	$2.715 \times 10^{-3}\ m^2$
t	7 mm	5 mm
Ratio of damaged area to the area of right wing section	12.2439%	10.8125%
Ratio of damaged area to the area of the complete wing	5.6896%	5.0244%

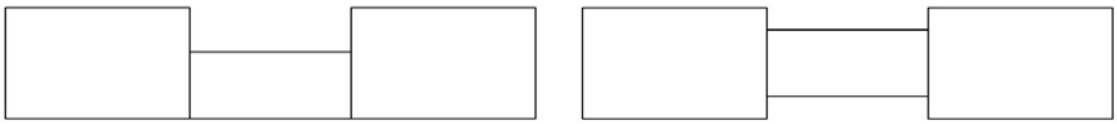

Figure 4-11: Damage introduction in test structure (a) and modelled damage (b)

The damage was introduced to the structure by reducing the thickness at the damage location. This was accomplished by milling the material away at the damage location (Figure 4-11 a). This implied that the physical introduction of damage was not consistent with the way in which the damage was modelled (Figure 4-11 b). This was done to study how the SCDF and SFDL values are influenced if the true damage is different from the modelled damage as there can be many ways in which the damage can present itself in

reality. The modelling of the structural damage was examined in paragraph 3.1.3.2 and investigated experimentally.

4.2 Experimental results

4.2.1 Modal analysis

A modal analysis was performed on the undamaged structure and the results from this analysis were subsequently used to update the FE model. This FE model was used in the numerical study in chapter 3 to numerically simulate and study the proposed damage parameters and the minimum number of sensors that can still indicate the presence of damage. This updated FE model should also be able to predict the strain response more accurately.

The experimental setup for measuring mobility FRFs described in paragraph 4.1 was used for two different sets of mobility FRF measurements. For the first set of measurements, the exciter was hung from cross beams above the experimental table. For the second set, the exciter was placed on rollers on the experimental table.

When the exciter was hung from the cross beam above the table it was difficult to get the shaker to excite only the out-of-plane bending and torsional modes. Due to misalignments, the shaker also excited the in-plane bending modes. An experimental point mobility showing the natural frequencies of the out-of-plane bending and torsion as well as the in-plane bending modes for the first scan with suspended shaker is shown in Figure 4-12. The natural frequencies of these in-plane modes are indicated by the green circles on the measured FRFs (Figure 4-12), but the response of these modes were not measured as only the out-of-plane response could be measured clearly. In an attempt to minimise the misalignment and thus reduce the excitation of the in-plane bending modes, the shaker was placed on rollers. This was done to facilitate easy alignment and movement of the shaker. A comparison of two experimental FRFs at the same location (node 11 and 48 for scans 1 and 2, respectively) are made in Figure 4-13.

From Figure 4-13 it is evident that the excitation of the in-plane bending modes is not influenced by the shaker being either suspended or on rollers. The natural frequencies are still present and have more or less the same magnitude. The misalignment was not solved, but this did not have a great effect on the measurements. The only matter that should be taken into consideration when the modes shapes are extracted from a modal analysis is that the modes obtained at the in-plane bending frequencies will have no physical meaning, as their responses were not accurately measured. Figure 4-13 however demonstrates good repeatability of the measurements, as the two measured FRFs appear to correspond well. The FRF of the second scan with the shaker on rollers appears to be less noisy and was therefore used for the modal analysis.

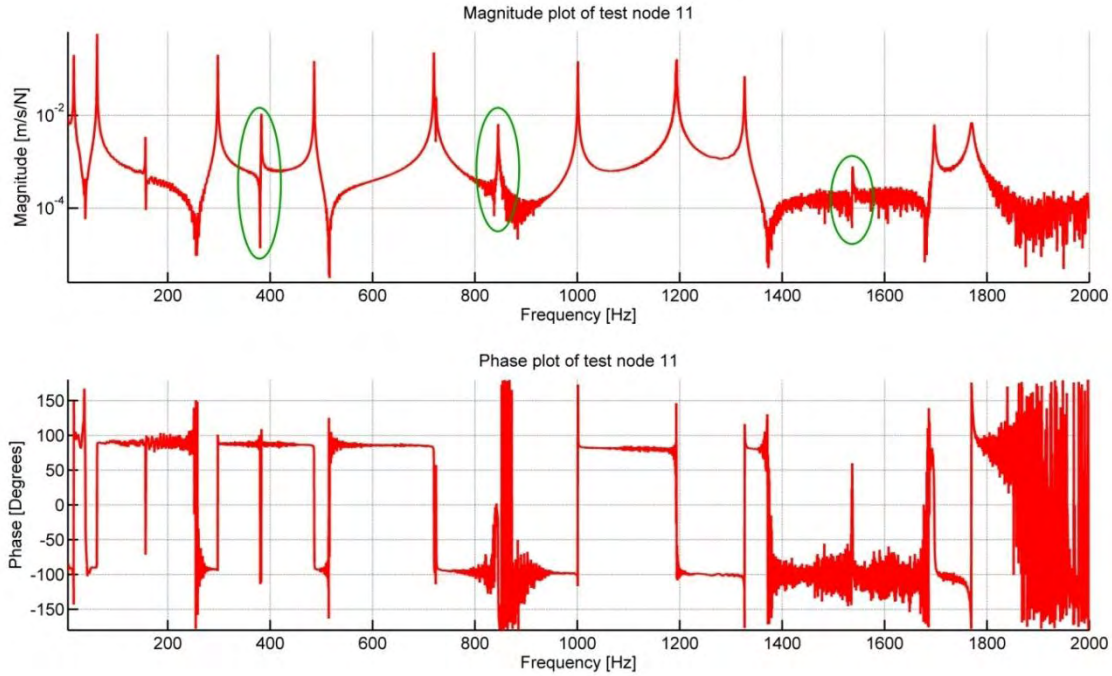

Figure 4-12: A measured point FRF of the first scan, with suspended shaker, indicating the natural frequencies of the in-plane modes at the green circles

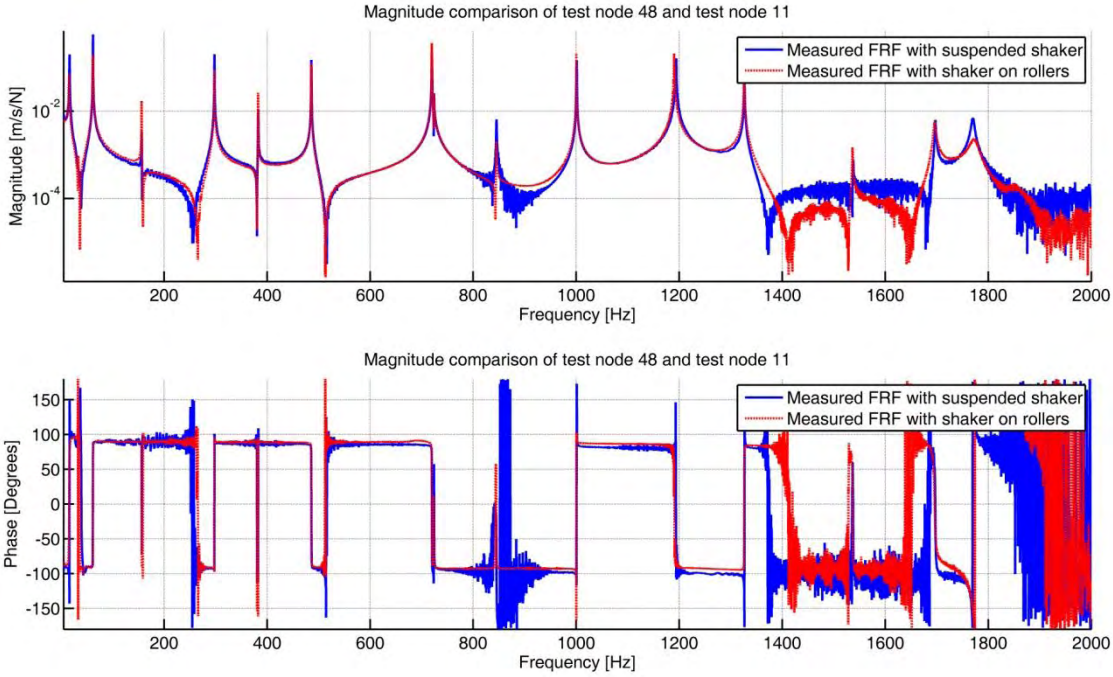

Figure 4-13: Comparison of measured FRFs at the same location for the suspended shaker and shaker on rollers

It is evident from Table 4-5 that a rigid body mode is identified at 15.36 *Hz*. Between the two tests, with the suspended shaker and the shaker on rollers, the stinger was lengthened. It was observed that this rigid body mode was initially at approximately 16.56 *Hz*, when the shaker was suspended. There was a definite change in this rigid body frequency due to the length of the stinger. According to Ewins (1995) it is necessary to check for internal resonance of the drive rod or stinger, as this resonance can introduce

spurious effects on the measured properties. This change in rigid body frequency was not studied further, but it is assumed that it occurs due to the internal resonance of the stinger.

Table 4-5: Type of mode shapes identified during the modal analysis of the undamaged MQ-1 Predator wing

Mode number	Frequency [*Hz*]	Type
1	15.36	Rigid body
2	61.737	VB
3	156.33	VB
4	297.64	VB
5	382.52	IPB
6	485.65	VB
7	719.68	VB
8	724.06	T
9	844.96	IPB
10	1000.3	VB
11	1190.4	T
12	1326.1	VB

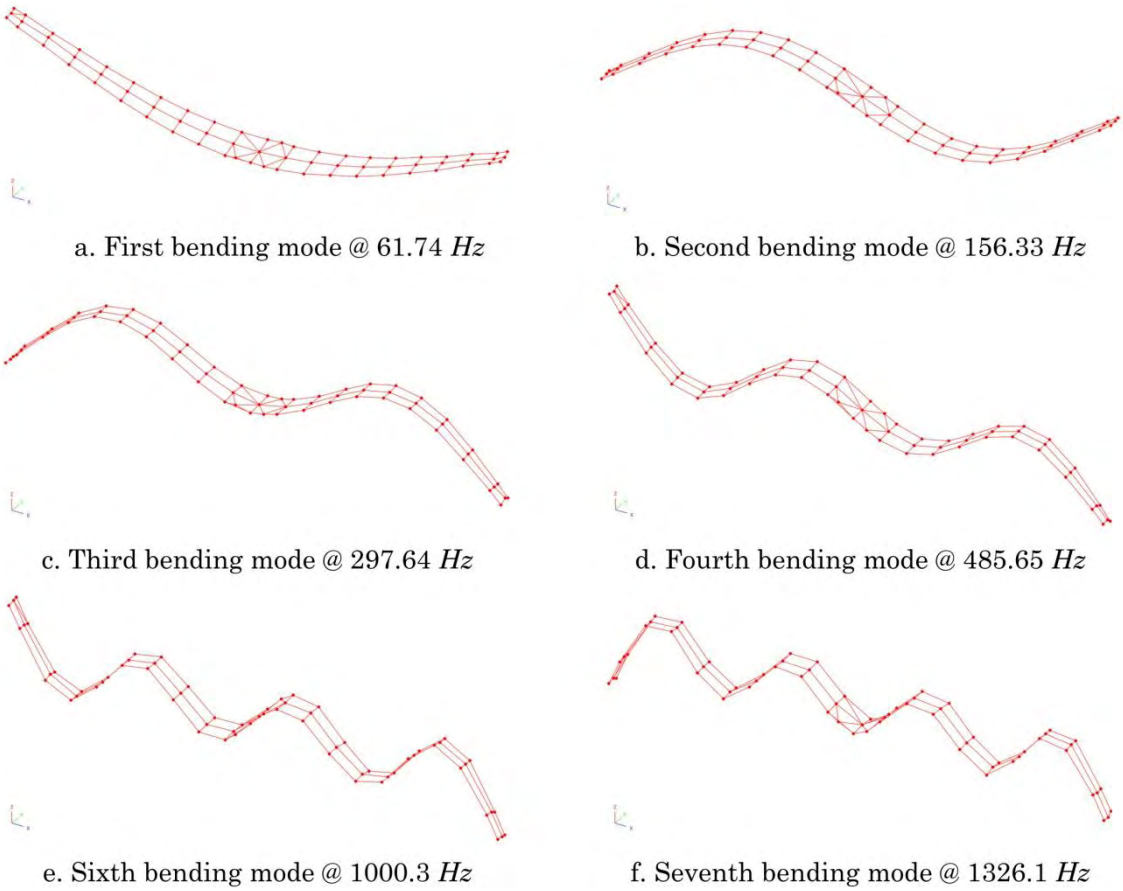

a. First bending mode @ 61.74 *Hz*
b. Second bending mode @ 156.33 *Hz*
c. Third bending mode @ 297.64 *Hz*
d. Fourth bending mode @ 485.65 *Hz*
e. Sixth bending mode @ 1000.3 *Hz*
f. Seventh bending mode @ 1326.1 *Hz*

Figure 4-14: The vertical bending mode shapes extracted by means of the modal analysis that is used in the subsequent analysis

The first rigid body mode should ideally be less than 10-20 % of the first bending mode (Ewins, 1995). This was not the case in the current setup, but the suspension system and rigid body mode, at 15.36 *Hz*, did not appear to influence the first bending mode and a clear and more or less noise free first bending mode shape was identified (Figure 4-14).

4.2.2 Model updating

The boundary condition specified in the initial FE model was free-free. This is however not physically realisable in practice and the suspension described in paragraph 4.1.1 was implemented. The presence and the effects of the suspension system as well as the exciter have to be included in the FE model to obtain good correlation between the numerical and experimental results. It is known that there are some modelling errors in the initial FE model due to the fact that the suspension system and exciter were not included in the initial FE model described in chapter 2.

4.2.2.1 Model updating of the material properties

The natural frequencies and mode shapes were extracted from the modal analysis in paragraph 4.2.1 and were subsequently used to update the material properties and validate the FE model described in chapter 2.

There are errors present when the analytical frequencies are compared to the experimental frequencies especially at pairs 6 and 8 which correspond to the torsional modes (Table 4-6). This is due to the fact that there are some modelling errors present in the FE model of chapter 2 compared to the experimental setup used. These modelling errors are mainly due to the suspension and excitation system used and the material properties of the test structure. When the test structures were laser cut, the material warped and the plate was bent. This could also affect the torsional modes, as this bent shape could increase the torsional stiffness of the test structure. The material properties were unknown although they could be estimated from tabulated values for steel (Gere, 2004).

In order to model the structure to represent the test structure more accurately, the suspension system and shaker systems were modelled. This was accomplished by modelling the suspension system as a grounded spring with spring constants in the x, y and z directions as well as adding a non-structural lumped mass for both the suspension springs and the load cell. The properties for the masses and springs were still unknown and estimations on their values had to be made. The load cell was weighed in order to get an estimation of its mass. The mass of the suspension system was unknown and a value approximately equal to that of the load cell mass was used as an initial estimate. The spring stiffness of the suspension system was estimated by exerting a known force on the spring and measuring its deflection. A linear fit was made through the data and an estimate of the spring constant was obtained. The estimates of the modelling properties of the structure, suspension and excitation systems are summarised in Table 4-7.

Table 4-6: Comparison of the initial FE model and the measured frequencies (with reference to FEMtools solver)

Pair number	FEM mode number	FEM Frequency [*Hz*]	Test mode number	Test Frequency [*Hz*]	Difference [%]
1	1	61.72	2	61.74	-0.03
2	2	155.86	3	156.33	-0.3
3	3	297.47	4	297.64	-0.06
4	5	485.24	6	485.65	-0.09
5	6	720.1	7	719.68	0.06
6	7	735.37	8	724.06	1.56
7	9	1001.46	10	1000.3	0.12
8	10	1215.98	11	1190.4	2.15
9	11	1329.65	12	1326.1	0.27

Table 4-7: Estimated properties of the structure, suspension and excitation systems

Property	Value
E (Young's modulus)	210 GPa
ρ (Density)	7850 kg/m^3
ν (Poisson's ratio)	0.3
Load cell lumped mass	0.026 kg
Suspension system lumped mass	0.02 kg
Suspension stiffness in x, y and z direction	690 N/m

The frequencies of the FE model, with the added suspension and excitation properties, were compared to the measured frequencies and it became clear that better correlation was shown at the torsional modes of pairs 6 and 8 (Table 4-8). The paring for Table 4-8 remained the same as in Table 4-6. There is however a loss in accuracy of the frequencies of the bending modes. A compromise solution that fits both the bending and torsional modes was found from the model updating process.

Table 4-8: Comparison of the FE model, with added suspension and excitation systems, and the measured frequencies of the first test structure (with reference to FEMtools solver)

		Initial FE model			Updated FE model		
Pair number	Test Frequency [*Hz*]	FEM Frequency [*Hz*]	Difference [%]	MAC values [%]	FEM Frequency [*Hz*]	Difference [%]	MAC values [%]
1	61.74	61.4	-0.55	99.4	61.5	-0.39	99.5
2	156.33	154.79	-0.99	99.8	155.52	-0.52	99.9
3	297.64	296.04	-0.54	99.7	296.77	-0.29	99.7
4	485.65	482.68	-0.61	98.6	485.21	-0.09	98.4
5	719.68	712.24	-1.03	98.3	712.71	-0.97	97.4
6	724.06	728.28	0.58	96.4	730.86	0.94	96.4
7	1000.3	999.95	-0.04	99	1006.12	0.58	99
8	1190.4	1204.31	1.17	99	1199.24	0.74	98.1
9	1326.1	1318.59	-0.57	95.6	1323.25	-0.21	94.7

There are different methods of comparing measured (experimental) and predicted (analytical) modal properties. One of the methods in which mode shape vectors can be compared is through the use of the modal assurance criterion (MAC). The MAC matrix indicates the degree of correlation between two mode shape vectors. When two mode

shape vectors are closely matched, a value close to or equal to unity should be obtained. This is not always the case and it is possible to obtain values less than unity within the MAC matrix. These deviations from unity can be caused by different factors (Ewins, 1995):

- The analytical model is incorrect
- There might be nonlinearities in the test structure
- Noise in the measured data making the estimates of the mode shape vectors inaccurate
- Poor modal analysis of the experimental data which leads to poor mode shape vectors

The MAC values for the FE and test mode shapes are also included in Table 4-8 and it can be seen that the lowest correlation initially is equal to 95.6% and is equal to 94.7% after updating. It can be concluded that the model is correct and the measured data and modal analysis provided satisfactory mode shapes.

Before commencing any model updating, it is essential to decide which parameters to update. A sensitivity analysis of the different modelling properties provides one with an estimation to which properties are most likely to lead to a better updated model. This sensitivity analysis was performed within FEMtools and it was established that the model was not sensitive to any changes in stiffness properties of either the material or the suspension system. The model proved to be much more sensitive to mass properties of the material as well as the suspension and excitation systems. The mass properties were therefore selected for updating. The properties were allowed to be updated globally and no local changes were allowed. In total there were four modelling properties assigned for updating which included the density of the structure as well as the three masses of the suspension and excitation system. After updating these parameters an FE model that correlated with frequencies less than 1% error was obtained. The effects of the model updating on the natural frequencies and mode shapes are shown in Table 4-8.

It is evident from Table 4-8 that a compromised FE model with good correlation was obtained. The natural frequencies differ with a maximum difference equal to 0.94%. The MAC values stayed more or less constant, although slight changes are observed.

The updated values of the uncertain model properties that were used in the updating process are summarised in Table 4-9.

Table 4-9: Updated properties of the suspension and excitation systems

Property	Value
E (Young's modulus)	210 GPa
ρ (Density)	7723.78 kg/m^3
ν (Poisson's ratio)	0.3
Load cell lumped mass	0.0607 kg
Suspension system lumped mass on right	0.0348 kg
Suspension system lumped mass on left	0.0225 kg
Suspension stiffness in x, y and z direction	690 N/m

One of the parameters that changed the most is the mass density of the structure. The mass density is still acceptable for a steel structure. Due to different alloying metals used the mass density can vary. Test structure 1 was weighed after the introduction of damage and the volume of the structure was calculated. The mass density was calculated and is equal to 7813.27 kg/m^3. The mass density obtained from model updating is less than this calculated density, but the difference might be due to the volume of the test structure being different from the calculated volume. The measured and updated densities are in the vicinity of the original estimated density and therefore the updated density remains valid.

Mobility measurements were made on the second test structure to verify that the FE model was still valid and could provide a good approximation to the second structure. In Table 4-10 the natural frequencies and mode shapes obtained from the modal analysis of the second test structure is compared to the FE natural frequencies. The pair numbers are the same as in Table 4-6. It is clear that the FE model is still accurate in representing the dynamics of the second test structure with the largest difference in natural frequency being equal to 1.14%.

Table 4-10: Comparison of the FE model, with added suspension and excitation systems, and the measured frequencies of the second test structure (with reference to FEMtools solver)

Pair number	Test Frequency [Hz]	FEM Frequency [Hz]	Difference [%]	MAC values [%]
1	62.04	61.5	-0.87	99.6
2	156.59	155.52	-0.68	99.7
3	298.24	296.77	-0.49	99.5
4	486.63	485.21	-0.29	99
5	720.94	712.71	-1.14	97.4
6	727.18	730.86	0.51	97.2
7	1002.4	1006.12	0.37	98.1
8	1194.9	1199.24	0.36	97.1
9	1328.2	1323.25	-0.37	95.5

4.2.2.2 Updating of the modal damping

Due to FRFs being used in the numerical study there is another property of the FE model that is very uncertain and this is the modal damping. It is possible to update the modal damping within FEMtools to allow better correlation on the FRFs. The modal damping is updated by using the raw measured FRFs and comparing them to the analytical FRFs. An initial estimate for the modal damping across the frequency range was set equal to 2×10^{-4} or 0.02% of the critical damping value.

The modal damping was updated in FEMtools with the mobility measurements made during the modal analysis phase. This provided a good estimation of the modal damping with respect to the mobility measurements (Figure 4-15).

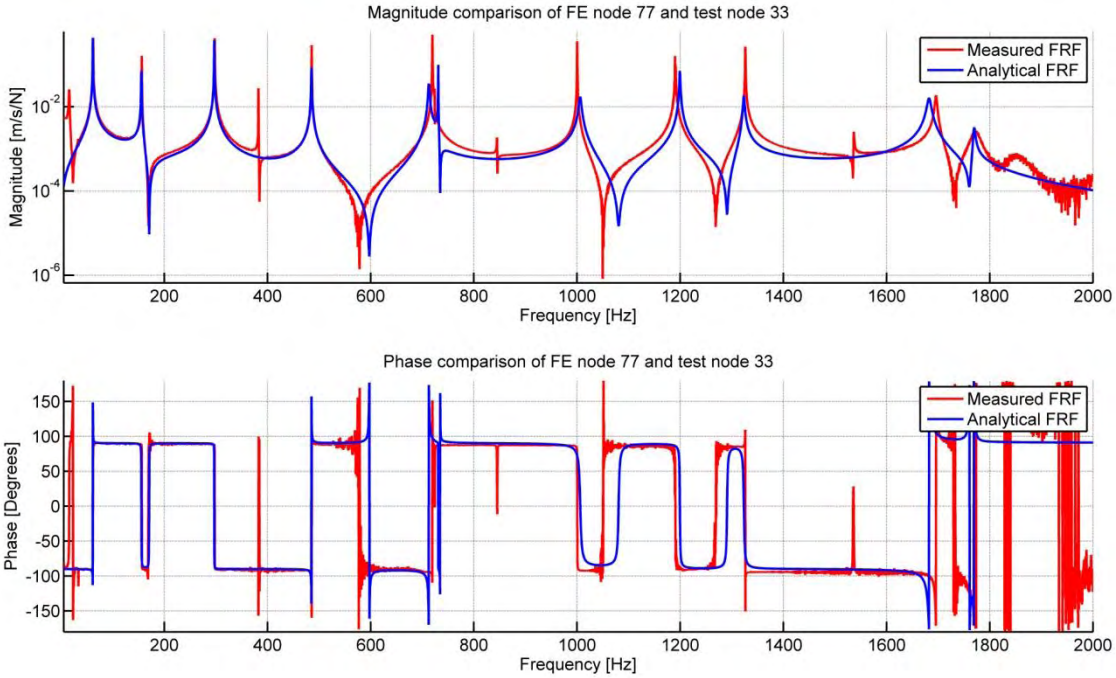

Figure 4-15: FRF comparions of the measured and test FRFs after updating of the modal damping

4.2.3 Strain modal testing

The setup described in paragraph 4.1.3.2 was used and the strain responses of both test structures for undamaged and damaged configuration were carried out. The two FRF estimators, $H_1(i\omega)$ and $H_2(i\omega)$, have different sensitivities to noise close to or at resonance and antiresonance. Ewins (1995) showed that the $H_2(i\omega)$ estimator might be a better indicator near resonance than the $H_1(i\omega)$ estimator, due to this difference in sensitivity to noise. The FRFs were calculated from the $H_2(i\omega)$ estimator due the fact that it is less sensitive to noise at the resonance frequency. The $H_2(i\omega)$ estimator is shown in equation 4.6 (Ewins, 1995).

$$H_2(i\omega) = \frac{S_{aa}(i\omega)}{S_{af}(i\omega)} \tag{4.6}$$

The auto-spectral density function (S_{xx}) of the response (either acceleration or strain) was calculated with Matlab's *pwelch.m* algorithm. A Tukey window with length of 9825 points was specified for the required windowing of the measurements. The number of overlapping points was set equal to 4913 points which equates to 50% of the window length. The number of Fast Fourier Transform (FFT) points used in the calculation was set equal to 2^{14}, which provided a frequency resolution of 0.305 *Hz*. The cross-spectral density function (S_{xf}) between the response and the force was calculated with Matlab's *cpsd.m* algorithm with the same parameters used with the *pwelch.m* algorithm.

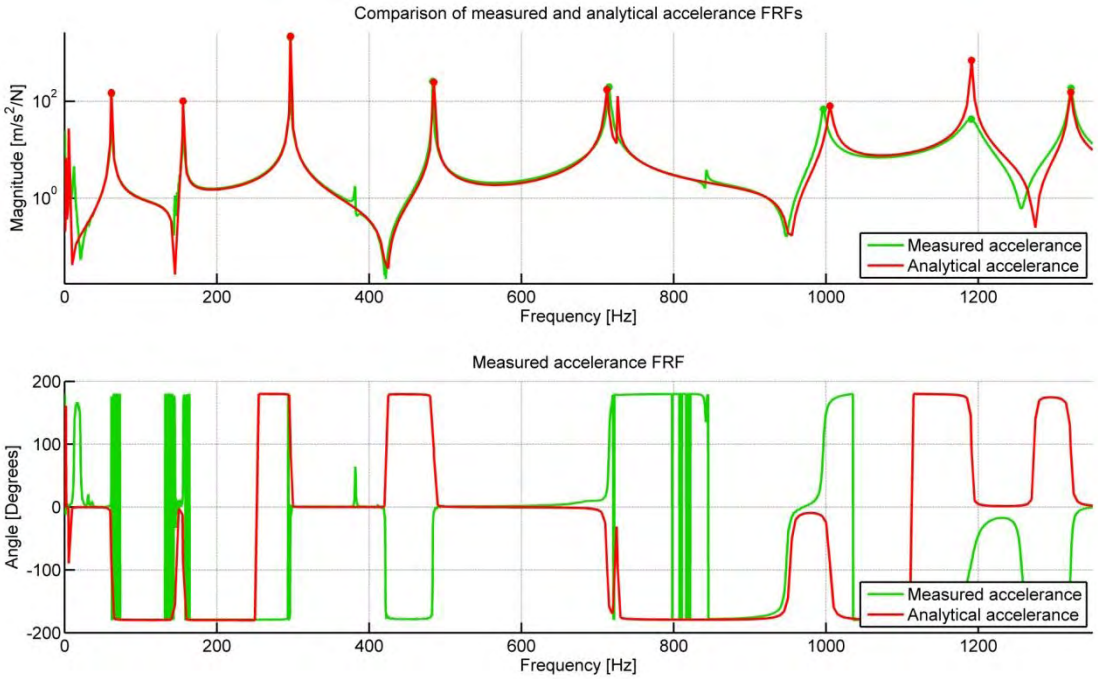

Figure 4-16: Comparison of the measured and analytical accelerance FRF at the reference accelerometer

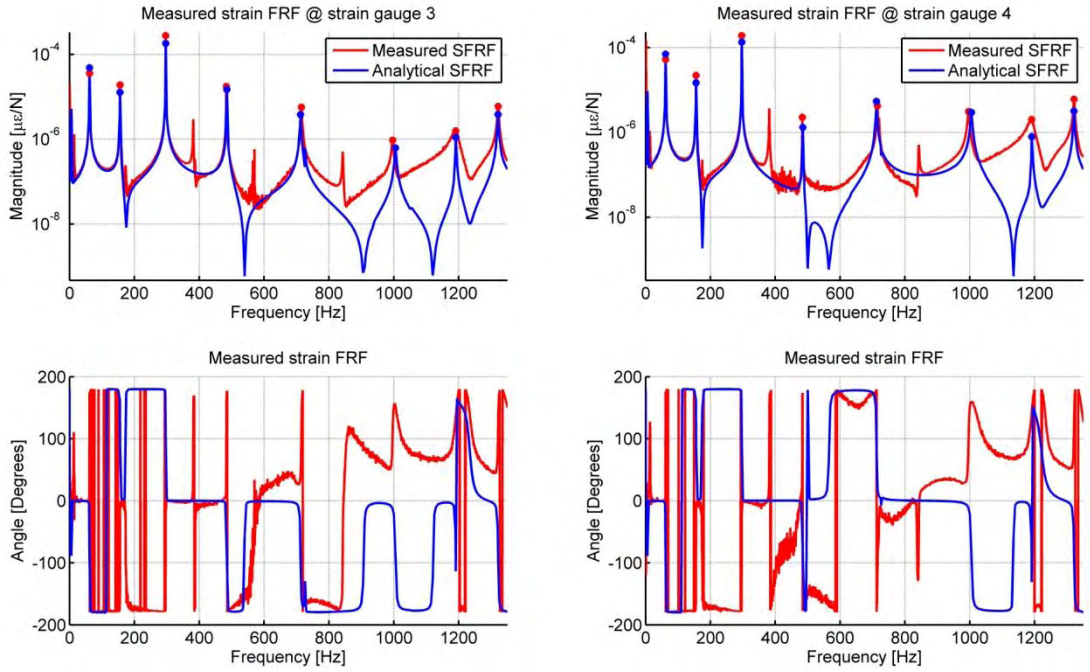

Figure 4-17: Strain FRF comparison before updating the modal damping in Matlab

The transmissibility function of the strain and the acceleration data was determined in a similar manner. This function is calculated from equation 4.7 in which the cross-spectral density is not calculated with respect to the input force, but rather with respect to the acceleration. The auto-spectral and cross-spectral densities used in the calculation of the transfer function were calculated with the *pwelch.m* and *cpsd.m* algorithms, respectively.

$$H_2(i\omega) = \frac{S_{sgsg}(i\omega)}{S_{sga}(i\omega)} \tag{4.7}$$

The measured and analytical accelerance is shown in Figure 4-16 and it is clear that very good correlation was obtained. A comparison of two measured and predicted strain FRFs are shown in Figure 4-17.

4.2.3.1 Updating of modal damping for strain FRFs

In paragraph 3.1.2.2 it was proven that the SCDF values are not sensitive to the damping when calculated from the transmissibility function between strain and acceleration. The strain FRFs were examined and it was observed that the modal damping obtained from the FRF updating in FEMtools was not adequate (Figure 4-17). Although the method is not reliant on the strain FRFs, it was decided to update the FE model for a second time using the strain FRFs. This was done to ensure that there are no errors introduced due to the modal damping values used in the FE model. The modal damping was updated with an algorithm written in Matlab (2008) to specifically update the modal damping to obtain better correlation with respect to the peak values at the natural frequencies. The peak strain values at the natural frequencies of the analytical model were compared to the measured peak strain value at the corresponding mode. The modal damping was updated until the peak strain values correlated closely. This provided a better estimation of the modal damping in the strain FRFs as can be seen from Figure 4-18.

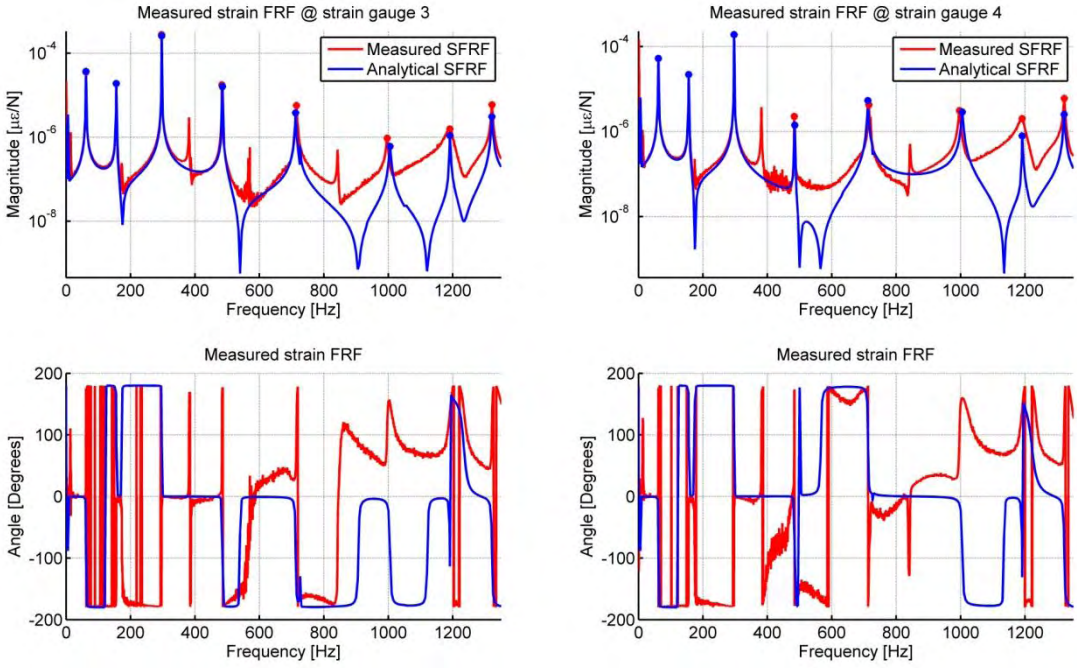

Figure 4-18: Strain FRF comparison after updating the modal damping in Matlab

4.2.3.2 Strain FRF and transmissibility measurements

The measured strain FRF for strain gauge 3 and 4 of Figure 4-8 as well as the correlation with the analytical strain FRF at these locations are shown in Figure 4-18.

When Figure 4-18 is examined it can be seen that the measured and analytical strain FRFs correlate well in the natural frequency regions. The correlation worsens from 800 *Hz* onwards, although there are times when it improves in the region of the natural frequency, as can be seen from the strain FRF at gauge 4 compared to the one at gauge 3.

There are some areas where the correlation is not good at all, especially at the second torsional mode at 1190.4 *Hz* (seventh indicated dot on Figure 4-18). The strain measurements were made on an axis where the strains induced by the vertical bending modes are the largest. It is known that maximum shear stresses and strains due to torsion are normally orientated at 45° to the principal planes (Gere, 2004). The torsional modes are, however, excited during the experiment (Figure 4-15). It is suspected that the shear strains due to the torsional modes are not excited very well on the x_1-axis and therefore cannot be measured with sufficient accuracy on the x_1-axis.

The strain responses were measured with 0°/45°/90° rosette strain gauges and thus the strain at 45° to the x_1-axis was measured. The measured strains on the 45° were compared to the analytical strains that were rotated through 45° with respect to the x_1-axis and the correlations for two strain gauges are shown in Figure 4-19.

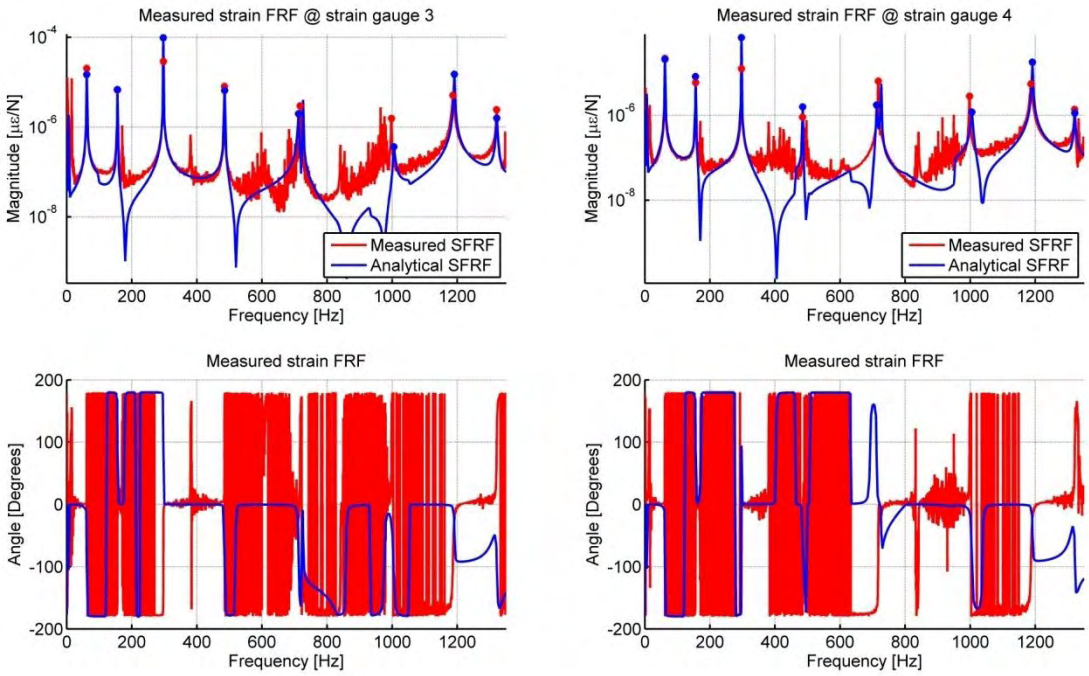

Figure 4-19: Strain FRF compasison of the strains rotated by 45° from the x_1-axis

Since the torsional mode located at 1190.4 *Hz* cannot be predicted with sufficient accuracy from the strains on the x_1-axis, it was decided to neglect this mode during the

damage identification process. It was observed during the deterministic numerical study in paragraph 3.1 that the vertical bending and torsional mode located close to 720 *Hz* (or close to the fifth circle in Figure 4-16) can cross over at certain levels of damage. This may not be distinguishable in practice by only looking at the natural frequencies and transmissibility function between the strain and the acceleration and are neglected during subsequent calculations.

The damage detection technique is based on the values of the transmissibility function at the natural frequency values. A comparison of the measured and predicted transmissibility function is shown in Figure 4-20. If Figure 4-20 is inspected it is clear that the analytical and measured transmissibility functions correlate well, except in the region of the second torsion mode at a frequency of 1190.4 *Hz*. This confirms the decision to neglect this mode during subsequent calculations.

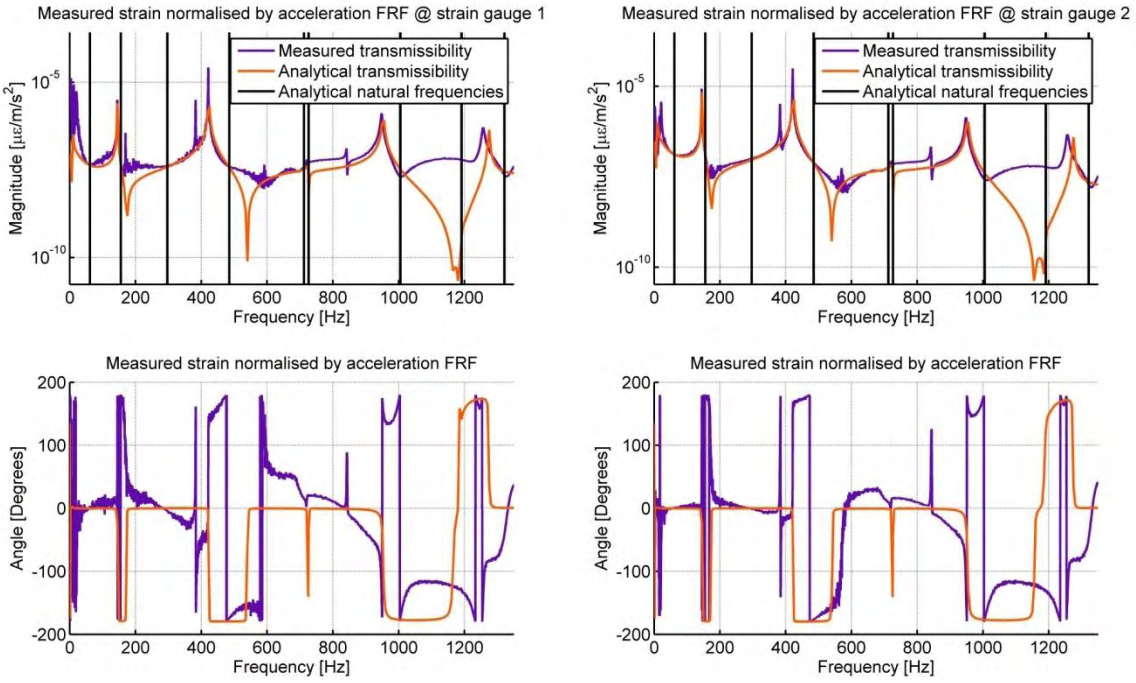

Figure 4-20: Comparison of the experimental and analytical transmissibility function

4.3 Damage detection algorithm applied to measurements

The first step of the damage identification method is to determine the natural frequencies of the structure. The natural frequencies of the structure were determined by implementing two methods. For the first method the natural frequencies were obtained from the peaks of the accelerance FRF (Figure 4-16). This will however not be possible for an in-flight aircraft because the load, used to calculate the FRF, cannot be measured in-flight. To make the method applicable to in-flight monitoring the second method used output only data. The natural frequencies were obtained from the auto-spectral density plot of the acceleration response in accordance with the peak picking method for ambient measurements described by Gentile et al. (2007). The analytical natural frequencies were used as a priori knowledge to extract the natural frequencies from the peaks of

auto-spectral density plot. This spectral plot is shown in Figure 4-21 and the corresponding measured natural frequencies are indicated by the red dots in Figure 4-21.

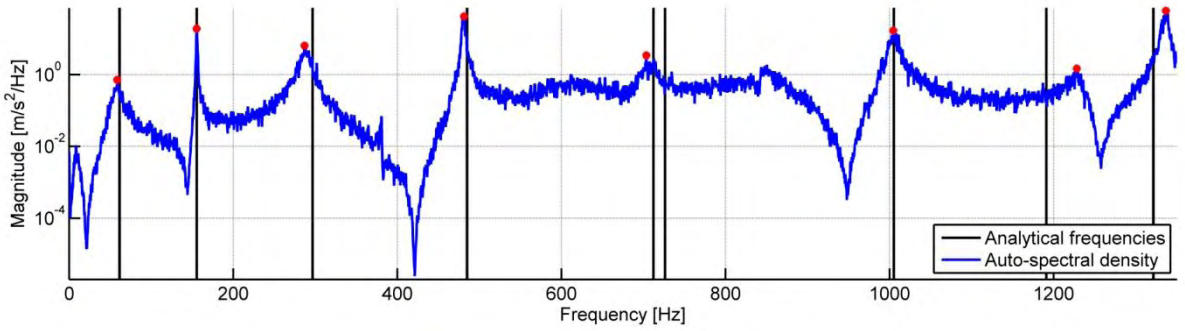

Figure 4-21: Auto-spectral density plot of acceleration response of the first undamaged test structure

The natural frequencies of the six modes of interest, obtained from the analytical model, are compared to the measured frequencies of both test structures obtained from the accelerance FRF and from the ambient measurements in Table 4-11 and Table 4-12, respectively. The analytical natural frequencies of Table 4-11 to Table 4-14 have been obtained from the Nastran solver.

Table 4-11: Comparison of analytical (Nastran solution) and measured natural frequencies obtained from the accelerance FRF of the undamaged structures

		Test structure 1		Test structure 2	
Mode	**Analytical**	**FRF – Measured [*Hz*]**	**%Error**	**FRF – Measured [*Hz*]**	**%Error**
1	61.49	61.65	0.248	61.65	0.248
2	155.50	155.64	0.090	155.94	0.286
3	296.67	296.33	0.116	296.94	0.090
5	484.97	483.40	0.324	484.62	0.072
9	1005.10	996.40	0.866	997.62	0.744
11	1321.40	1321.72	0.024	1321.72	0.024

Table 4-12: Comparison of analytical (Nastran solution) and measured natural frequencies obtained from ambient measurements of the undamaged structures

		Test structure 1		Test structure 2	
Mode	**Analytical**	**Ambient – Measured [*Hz*]**	**%Error**	**Ambient – Measured [*Hz*]**	**%Error**
1	61.49	58.59	4.715	58.59	4.715
2	155.50	155.33	0.106	155.64	0.090
3	296.67	286.87	3.305	286.87	3.305
5	484.97	481.26	0.765	481.87	0.639
9	1005.10	1004.33	0.076	1004.03	0.107
11	1321.40	1336.67	1.156	1330.87	0.717

Table 4-11 clearly shows that the analytical and measured natural frequencies correlate well with the largest error equal to 0.866%. If Table 4-12 is examined, however, the errors become much larger with the largest error being equal to 4.715%. It is difficult to extract the modal properties from ambient measurements (Gentile et al., 2007) and there

are various reasons for the ambient measurements to differ from the analytical natural frequencies. These reasons may have to do with the amount of energy imparted to the structure as well as measurement and excitation location.

During the second step of the damage detection method, the strain values at the natural frequency values are extracted. This was done for the transmissibility measurements (also referred to as ambient measurements) to obtain acceleration normalised strain values at each of the natural frequencies. The SCDF values at each measurement location were calculated from the extracted acceleration normalised strain values by implementing equation 1.10.

In the final step of the method, the SFDL value is calculated from the rms of the SCDF and the natural frequency difference as defined in equation 1.11. This procedure was followed for both test structures and the results are discussed independently.

4.3.1 Test structure 1

The natural frequencies obtained from the FRF as well as the ambient measurements for test structure 1 are compared to the analytical predicted frequencies in Table 4-13.

Table 4-13: Comparison of analytical (Nastran solution) and measured natural frequencies for the damaged test structure 1

Mode	Analytical	Analytical average difference in natural frequency [%]	FRF Measured [*Hz*]	%Error	Ambient Measured [*Hz*]	%Error	Ambient average difference in natural frequency [%]
1	59.69	2.932	60.12	0.720	58.59	1.837	0.000
2	150.31	3.135	151.67	0.906	151.37	0.703	1.277
3	293.94	2.397	294.19	0.085	286.87	2.407	0.851
5	479.89	2.059	479.74	0.032	478.21	0.350	0.797
9	992.48	1.899	986.94	0.558	991.21	0.128	0.899
11	1303.40	1.809	1304.93	0.118	1314.09	0.820	1.031

The natural frequencies determined from the FE model relates well to the FRF measured natural frequencies. The ambient measured natural frequencies show less agreement with the analytical results and an error as large as 2.407% is observed (Table 4-13).

The SCDF values for an increasing number of modes included in the calculation at the different measurement locations were computed from equation 1.10. The analytical predicted SCDF values for the same location and size of damage were computed and the comparison of the predicted and measured SCDF values is shown in Figure 4-22.

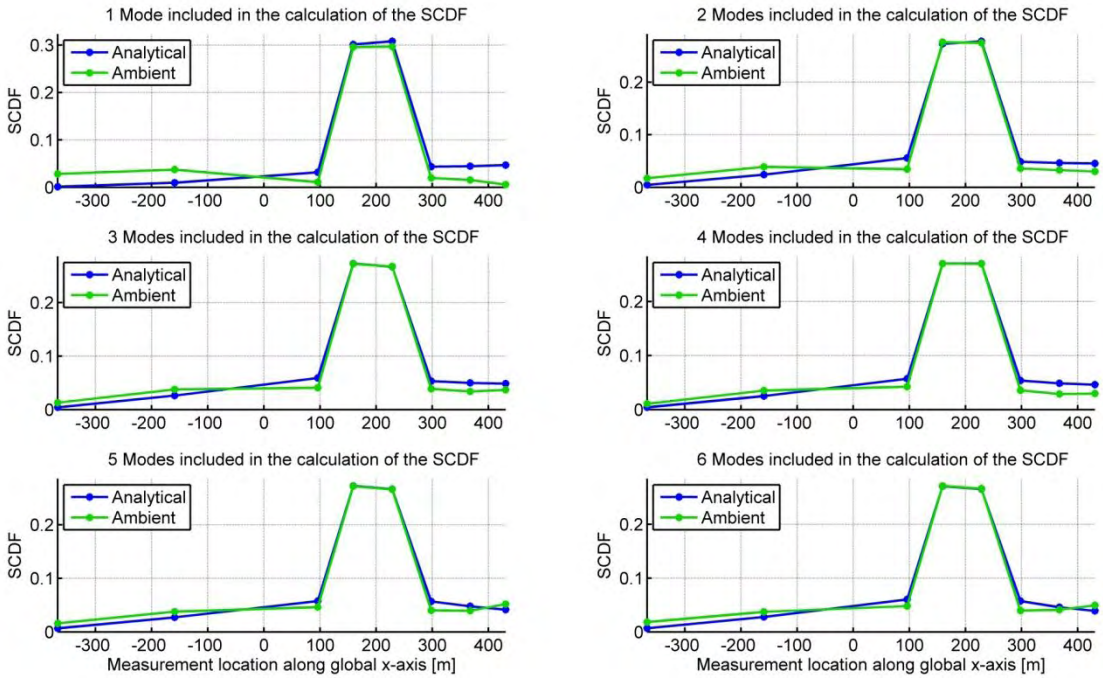

Figure 4-22: Measured and predicted SCDF values for test structure 1

Figure 4-10 showed that the damaged location is close to the fourth and fifth strain gauge from the right. This is evident from Figure 4-22 as there is a definite peak at the fourth and fifth dot from the right. This corresponds with the known damage location as shown in Figure 4-10 for test structure 1. The damaged location can be identified from the ambient SCDF plots. There is a strong correlation between the predicted and measured SCDF values. The damage location as well as the amplitude can therefore be correctly predicted by the FE model. Although the damage that was introduced in the test structure was different from the modelled damage, the FE model still produced SCDF values that compare very well with measured values. This is due to the fact that the strains outside the damaged area change proportionally in the FE model and in the test although the real damage scenario in fact differs from the modelled one.

It can be assumed that the method will consistently predict the same SCDF values even though the real damage might be completely different from what was modelled if the measurement location is outside the damaged location. This provides a way to predict the damage level from the SFDL curve fits as in Figure 3-37, as well as size and location as the SCDF values are consistent.

The rms of the SCDF values of Figure 4-22 was determined and multiplied by the average difference in natural frequency to determine the SFDL values as in equation 1.11. The comparison between the predicted and measured SFDL values for different amounts of modes included is shown in Figure 4-23.

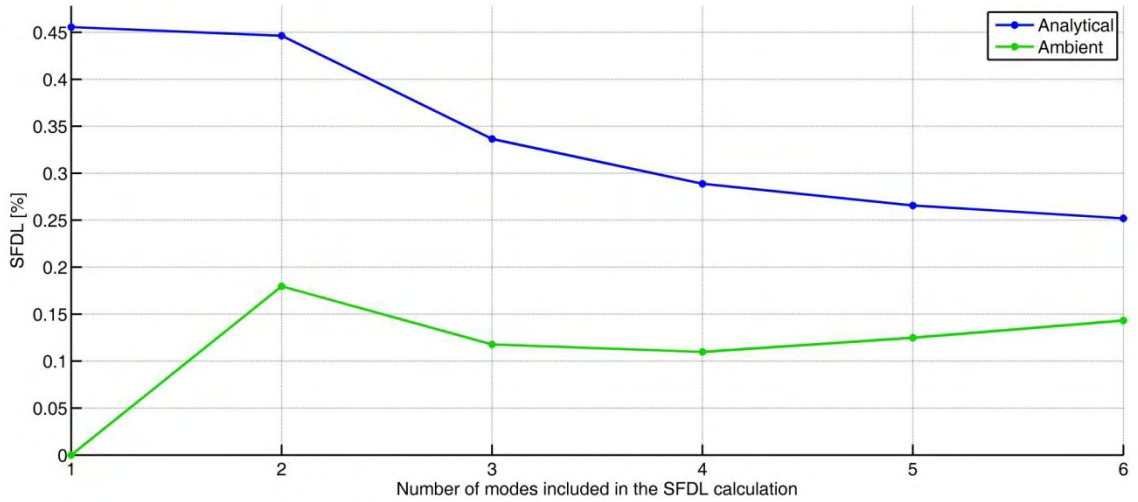

Figure 4-23: Predicted and measured SFDL value fot test structure 1

If Figure 4-23 is examined it is seen that the predicted and measured SFDL values differ significantly. As the number of modes increases the two SFDL values seem to converge. This is interesting to note, as the SCDF values related closely, therefore the only difference in the two calculations can come from the natural frequency difference. When the natural frequency values of the analytical model were compared to the natural frequencies obtained from the ambient measurements, large errors were observed (Table 4-13). As more modes are included in the calculation these differences appear to average out and therefore closer agreement is obtained when more modes are included. The statement that the difference in SFDL value comes from the difference in natural frequencies was examined. The SCDF values of the ambient case were used in the calculation of the ambient SFDL value. The average difference in analytical measured natural frequencies was used in the calculation of the ambient SFDL to show the influence of the ambient measured natural frequencies (Figure 4-24).

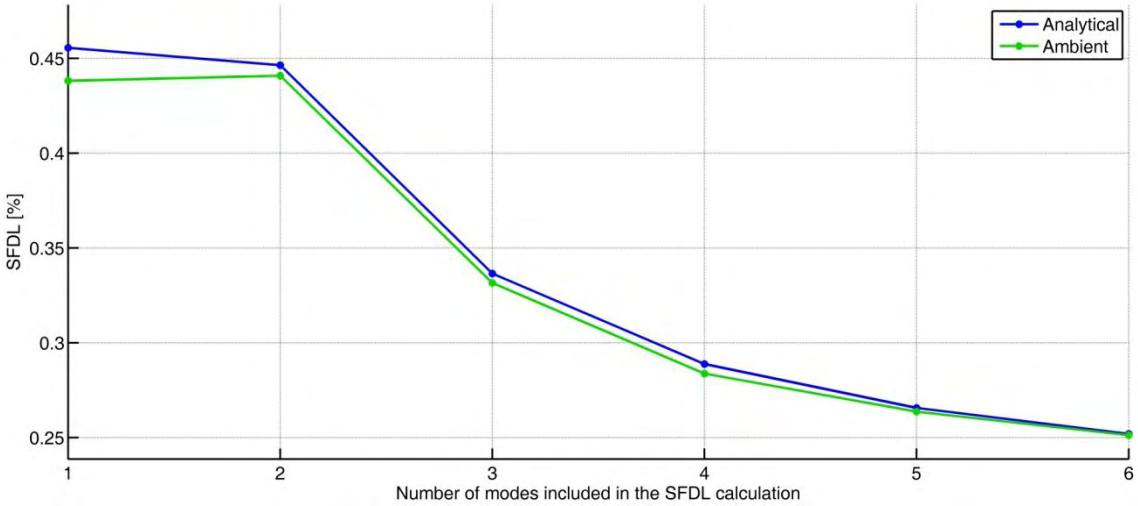

Figure 4-24: Comparison of the predicted and measured SFDL values when the same averaged difference in natural frequencies is used in the SFDL calculation

It is evident that much better correlation can be obtained when the average difference in natural frequency is the same for the predicted and analytical SFDL calculation (Figure 4-24). The difference can therefore be accredited to the natural frequency difference. For this reason the SFDL calculation appears to be sensitive to the average change or difference in natural frequency. Care should therefore be taken to ensure that the natural frequencies obtained from ambient measurements are measured accurately. The SCDF is not sensitive to this change in difference in natural frequency as the correlation between the predicted and measured SCDF values were good even though the frequencies where the acceleration normalised strain values were extracted, are different from the analytical case.

4.3.2 Test structure 2

The natural frequencies of test structure 2, obtained from the FRF as well as the ambient measurements, are compared to the analytical predicted frequencies in Table 4-14.

Table 4-14: Comparison of analytical (Nastran solution) and measured natural frequencies for the damaged test structure 2

Mode	Analytical	Analytical average difference in natural frequency [%]	FRF Measured [*Hz*]	%Error	Ambient Measured [*Hz*]	%Error	Ambient average difference in natural frequency [%]
1	58.43	4.986	58.90	0.808	58.59	0.285	0.000
2	151.64	3.734	152.59	0.625	151.98	0.223	1.176
3	293.95	2.795	293.58	0.126	286.87	2.410	0.784
5	474.44	2.639	479.13	0.988	478.21	0.795	0.778
9	986.35	2.484	981.14	0.528	991.21	0.493	0.878
11	1300.10	2.339	1311.95	0.912	1322.94	1.757	0.831

Table 4-14 shows that the predicted and FRF measured natural frequencies are again closely related, but there are still large errors when the ambient natural frequencies are compared to the analytical natural frequencies. This can again have an adverse effect on the SFDL value.

The SCDF values for test structure 2 were calculated from equation 1.10 and a comparison between the measured and predicted SCDF values is made in Figure 4-25. If Figure 4-25 is examined, it is evident that the damaged location can be established from the SCDF plot. The measured and predicted values show an increase in SCDF value at the fifth and sixth measurement location which corresponds to the damaged location of Figure 4-10 for test structure 2.

It is evident from Figure 4-25 that the predicted and measured SCDF values do not correlate well at all. This can be attributed to the way in which the damage was modelled and the way in which it was introduced experimentally (as discussed in paragraph 3.1.3.2). It was noticed that the predicted strains at the damage location are

higher than the measured strains. The strain values predicted at the damage location were 1.4966 times higher than in the measured case.

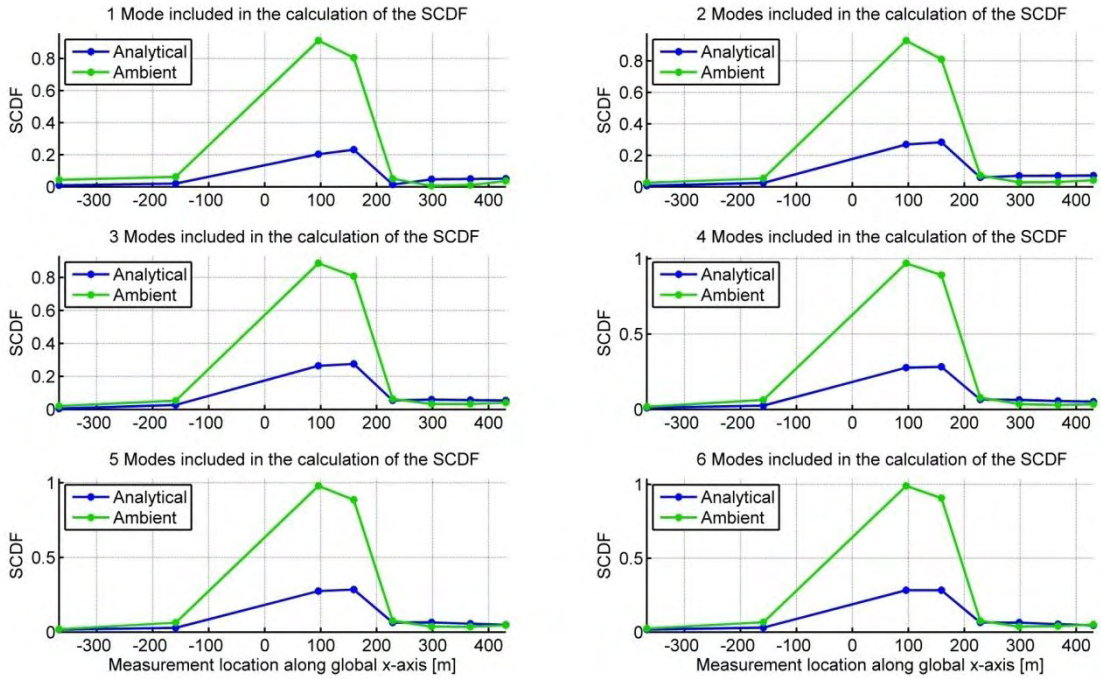

Figure 4-25: Measured and predicted SCDF values for test structure 2

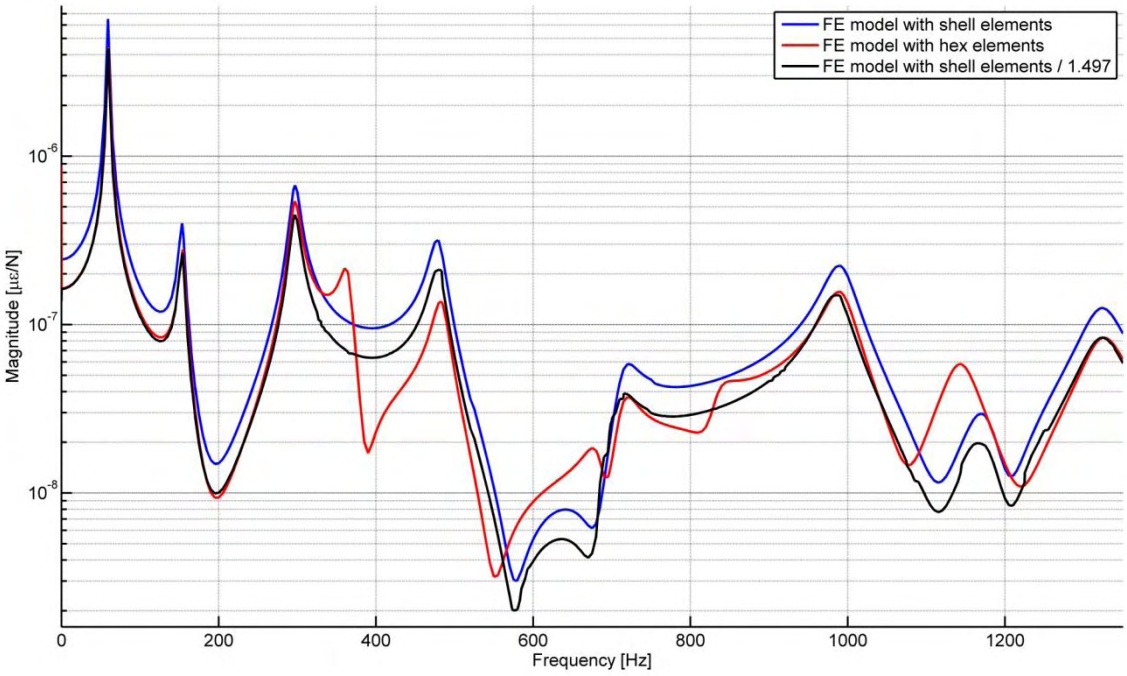

Figure 4-26: Comparison of the strain FRF for the hexahedral and shell FE models used to model the damage of test structure 2

In order to investigate this effect an FE model of the structure was built from hexahedral elements and elements at the damage location were removed to create a model with the same damaged area and size as the test structure. The strain FRF at one of the

measurement location that was enclosed by the damage area was extracted and plotted against the value obtained from the original shell FE model (Figure 4-26). The 1.4966 factor was again observed and if the strain FRF obtained from the shell model is divided by this factor the correlation improved significantly (Figure 4-26).

The strain values at the damage location, obtained from the shell FE model, were divided by this factor. The measured and predicted SCDF plots were again compared and much better agreement was obtained (Figure 4-27).

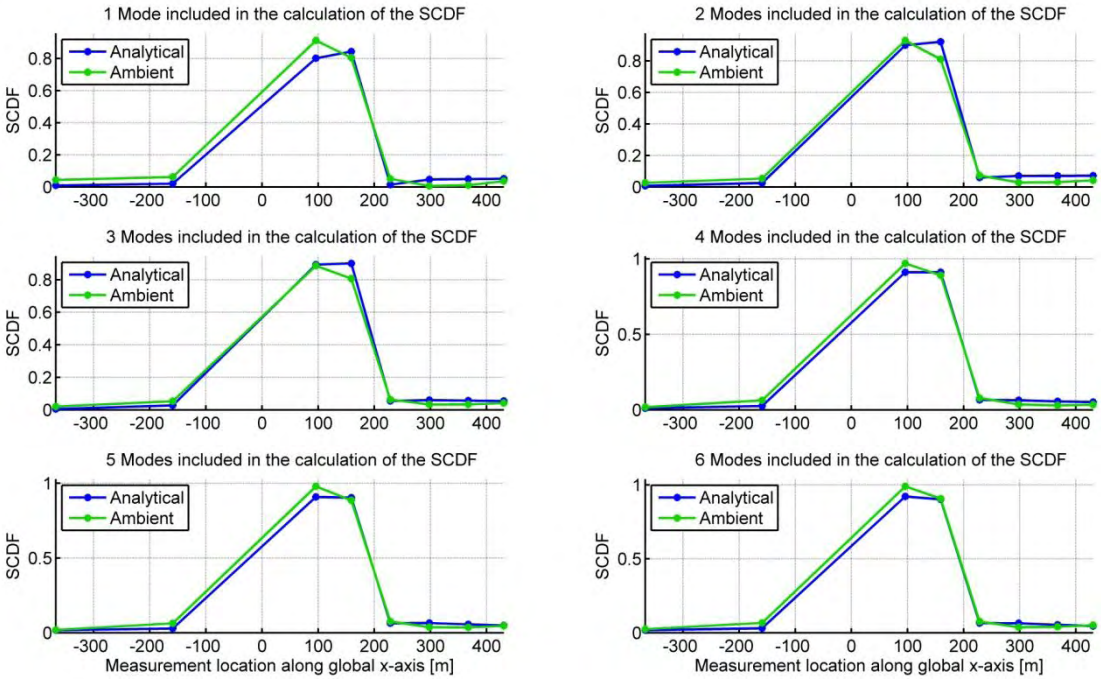

Figure 4-27: SCDF comparison for strain values divided by 1.4966 at the damage location

It can be deduced that the SCDF values are very sensitive to the true value of the strain at the damage location. If the real damage situation is different from the modelled one, these values will differ significantly. In paragraph 4.3.1 the statement was made that the damage level and size can be predicted accurately when the damaged area is close to the measurement locations, because the SCDF values remained consistent even though the true damage and modelled damage differed. In the case of test structure 2, this is not the case; the SCDF values are not consistent and may differ significantly if the true damage is different to the modelled case. The damage level cannot be predicted if the SCDF values are inconsistent. This proves that the case of test structure 1 is more desirable as predictions on the damage level can be made.

The SFDL values for the predicted (original values without compensation for the strains at the damaged location) and measured results are compared in Figure 4-28. The correlation appears to be better than expected, since the SCDF values did not show any correlation for the predicted values of Figure 4-25. This is however not valid due to the large differences in SCDF values and the fact that the ambient measured frequencies could not be measured with sufficient accuracy (Table 4-14).

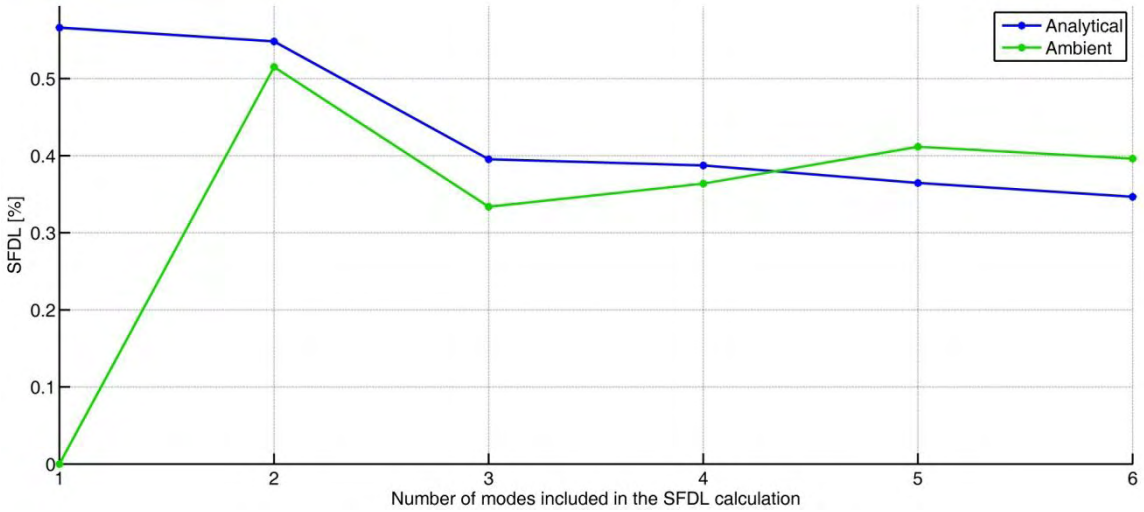

Figure 4-28: Comparison of predicted and measured SFDL value from original SCDF curve

The strains at the damaged location were compensated for as in Figure 4-27. These SCDF curves were used in the calculation of the SFDL values and the comparison of the predicted compensated SFDL and measured SFDL values is made in Figure 4-29. This shows that the correlation is deficient. The only other factor that can influence the SFDL value is the average difference in natural frequency. The analytical average difference in natural frequency was used in the calculation of the ambient measured SFDL value and the comparison is shown in Figure 4-30. The correlation obtained when the average difference in natural frequency is the same is improved and the conclusion that the SFDL value is very sensitive to the average difference in natural frequency, which was made in paragraph 4.3.1, is reinforced.

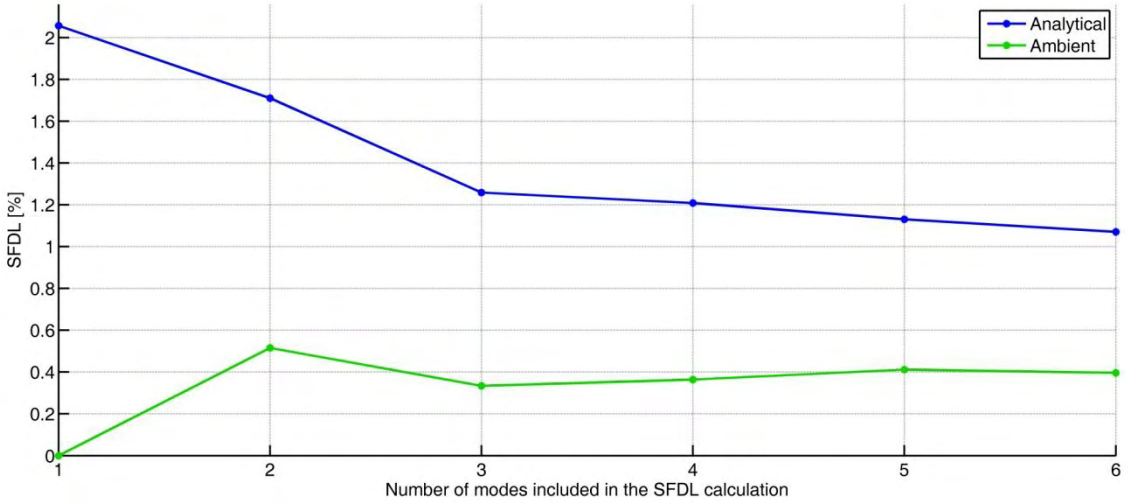

Figure 4-29: Comparison of the predicted and measured SFDL values obtained from the scaled SCDF curve

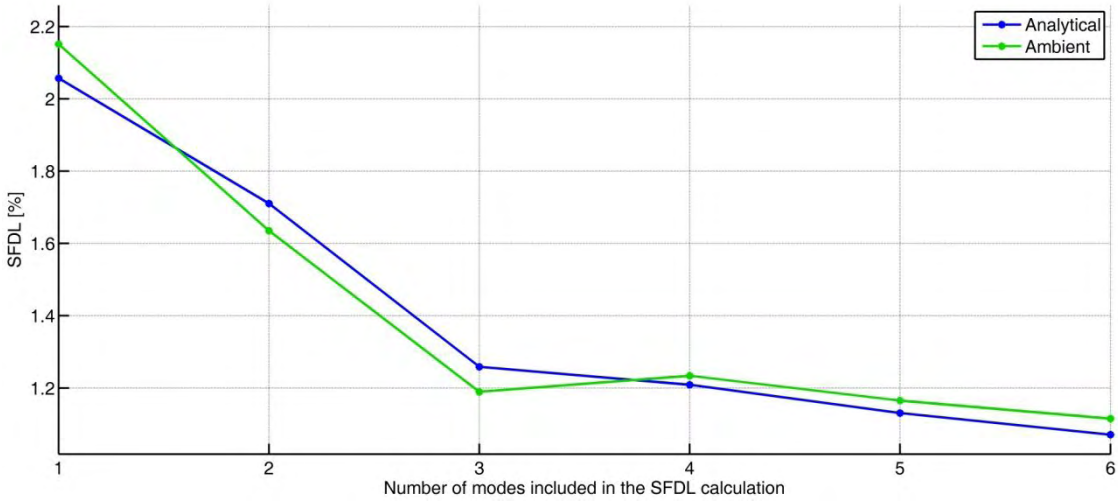

Figure 4-30: Comparison of the predicted and measured SFDL values from the scaled SCDF curve when the same averaged difference in natural frequencies is used in the SFDL calculation

4.4 Summary of chapter 4

Chapter 4 was mainly concerned with the experimental verification of the proposed method and damage indicators. The experimental setup was described in detail (paragraph 4.1), the results for updating as well as strain measurements were presented and discussed (paragraph 4.2) and the proposed damage detection method was applied to measurements performed on the MQ-1 Predator wing (paragraph 4.3).

4.4.1 Summary of major findings

In chapter 4 it was shown that:

- The numerical model correlated well with experimental measurements of mobility FRFs, accelerance FRFs and strain FRFs after updating the model.
- The numerical model correlated well with the measured transmissibility functions obtained from output-only data.
- The natural frequencies obtained from the FRFs of the numerical simulations matched closely to the experimental FRF measurements.
- The natural frequencies obtained from ambient measurements did no show the same level of correlation, which could be the results of various factors, such as insufficient excitation of the modes, placement of the excitation system and/or accelerometer.
- The SCDF values showed that they are not sensitive to the measurement error on the natural frequencies. Although the natural frequencies measured obtained from ambient measurement did not correspond closely to the numerical simulations, the SCDF values calculated at these ambient frequencies showed good correlation with numerically simulated SCDF values.
- The damage location predicted from the SCDF values corresponded to the known damage location for both test structures.

- The SFDL values are sensitive to the measurement error of the ambient measured natural frequencies as it is a function of the measured natural frequencies.
- The finding that the method is influenced by the way in which damage presents itself in a real structure (paragraph 3.4.1) is confirmed in paragraph 4.3.2.
- The SFDL value can be used to indicate the presence of damage. However, the magnitude of the measured SFDL value did not match the values of the numerical simulation and it would therefore not be possible to make any predictions on the damage level based on the SFDL value.

4.4.2 List of conclusions

The conclusions that can be drawn from the major findings (4.4.1) are:

- The numerical model correlated well with experimentally measured FRFs, transmissibility functions and natural frequencies from the FRFs.
- The SCDF values are robust with respect to measurement errors as well as measurement noise.
- The location of damage can be correctly identified from the SCDF values as the known damage location corresponded to the one predicted by the SCDF values for both test structures.
- The SFDL value indicated the presence of damage although it is less robust to measurement error than the SCDF values.
- The method proved to be able to predict the presence and location of damage from output-only measured data.

Chapter 5: Conclusion

5.1 General conclusions

A global damage detection technique that is able to detect the presence of damage, its location and the damage level, was presented. This method is a response based method and it was designed to work with ambient excitation, thus it was able to perform the damage detection from output-only data. The data required by the method are the acceleration and strain response data before and after damage is introduced. The damage detection technique can therefore be classified as a response based method requiring output-only data of the undamaged and damaged structure and is able to address the third level of damage detection (Rytter, 1993).

Two parameters, the strain cumulative damage factor (SCDF) and the strain-frequency damage level (SFDL) were presented. The first parameter (the SCDF value) was derived from the cumulative damage factor or CDF originally created and presented by Abdel Wahab et al. (1999). The second parameter (the SFDL value) is a newly proposed damage indicator which is based on the rms of the SCDF values and the average difference in natural frequency. Both these parameters are calculated and monitored during the damage detection process. The spatial location of the damaged area is obtained from the SCDF values. The SFDL value provides a single value that can be monitored for the commencement of damage. This value can also be used to assess the damage level present in the structure.

Numerical simulations were performed with the aid of an updated FE model to investigate the effect of an increasing damage level on the SCDF and the SFDL values when the damage location is deterministic and known. The updated FE model was obtained by performing model updating in FEMtools with modal properties obtained from a modal analysis of mobility FRFs. The FE model and the experimentally measured values correlated well. The method is applied to two other members of the family of wings and numerically the presence and location of the damage could be identified (Appendix D). The method is therefore relevant and applicable to other members of the family of wings.

The damage location could be predicted from the SCDF values and corresponded to the known damage location. It was shown that the SCDF value had less noise present and could predict the location more reliably than the CDF equivalent value calculated directly from the strain values. This is an improvement on the CDF. The SCDF values at or near the damaged area showed an increase in value as the damage level was increased. Damping in the structure and accurate measurement of the values of the strain and acceleration transmissibility function did not appear to affect the SCDF value significantly and it can be concluded that the SCDF value is not very sensitive to damping.

The SFDL value increases in value as the damage level increases. However, it becomes more constant as more modes are included in the calculation, since this leads to better averaging. The SFDL value is more sensitive to damage than the natural frequency method. There is different scaling of the SFDL value depending on whether a measurement location is enclosed by the damaged area or not.

In the present study the SCDF value was calculated by dividing the difference in the acceleration normalised strains by the damaged values. It was shown that the SFDL values for this calculation scales slower than the SFDL value calculated from the SCDF when the difference is divided by the undamaged strain values. If the damaged areas can be avoided it might actually be better to calculate the SCDF from the undamaged values. If the damage in this case encloses a measurement location the SFDL values scale even slower (Appendix B). It is therefore suggested that the SCDF should be calculated from the difference divided by the damaged values, as this works well in both damage cases and is able to still scale relatively quick even if a measurement location is close to the damaged area.

Numerical simulations were performed on stochastically varied damage location and size. This was done to study the robustness of the damage detection technique and to establish the minimum number of sensors that can be used to still reliably indicate the presence of damage. The effect of randomly varying the size and location of the damaged area on the SFDL value was investigated and it was observed that the presence of damage can be indentified by the SDFL value for any damage size and location. The SFDL value indicated to be more reliable and scale more predictably when the damaged area does not enclose one or more measurement locations. There is a problem associated with the damage case where one or more measurement locations are enclosed by the damaged area. The delamination damage in different damage cases can differ and if the strains are measured at the damage location no predictions can be made as the strains are different for the different damage cases. The situation where the measurement location is close to but not at the damaged area is preferred, as these values remain constant irrespective of the real damage situation at the delaminated area. Predictions on the damage level can be made from the SFDL values when they remain more constant.

The minimum number of strain sensors was determined to lie in a range from 6 to 10 sensors per side of the wing and at least 1 acceleration sensor is required. This number of sensors provides good spatial resolution without using too many acquisition channels. It is assumed that this number of sensors can be applied to other wing-like structures in the family of wings; however this was not investigated any further. It should also be kept in mind that the measurement locations should be close to the damaged area, for the strain sensors to be in a location where the strain values change due to damage. If the sensors are too far away it will lie in a nominal stressed area and the damage cannot be detected from changes in strain values.

An experimental study was performed to investigate the validity of the proposed method on real structures. The study was performed by exciting the structure with a random force equivalent to ambient sources during in-flight operation. The output-only data, the measured strains and acceleration, were used to calculate the transmissibility function

and the SCDF and SFDL values were calculated from these measurements. It was proven that the damage location obtained from the SCDF values corresponded to the known damage location. The measured and numerically predicted SCDF values correlated very well even from noise polluted measurements. The SCDF value shows to be robust, as the measured values correspond very well to the predicted values. The amount of measurement noise and any measurement error did not influence the SCDF too much. The SCDF values are related to the modal curvatures as both are derived from the strains in the structure. It is very difficult to determine accurate modal curvatures from experimental modal displacement data (Maeck, 2003). The current method uses measured strains normalised by acceleration to estimate the SCDF and there are no mathematical manipulations required to obtain the strains during the calculation. This helps to make the SCDF calculation an alternative to the CDF calculated from displacement derived modal curvatures. More accurate estimates to the modal curvatures can be obtained by measuring the strains directly.

The SFDL values showed that it is very sensitive to the measurement of the natural frequencies and any measurement error affected the SFDL values. The SFDL value is less robust than the SCDF, as it is sensitive to any measurement error in natural frequency. If this technique is implemented care should be taken in measuring and extracting the natural frequencies to ensure that the correct natural frequency values are obtained. This can be accomplished by placing the accelerometer in an area of large accelerations and ensuring that the excitation of the wing and its natural modes are sufficient.

5.2 Future research

The proposed damage detection technique has been proven to work on a wing-like homogenous steel structure. The strain measurements were made with strain gauges and the excitation was provided by an actuator. There is room for further research to implement the technique on a real composite wing which consists of ribs, spars and an outer skin. The technique still has to be proven when strain measurements are made with optical fibre Bragg gratings, although in principle it should work. Finally the whole system has to be proven for an UAV in real flight conditions to prove that the ambient sources of excitation do indeed excite the structure sufficiently to be able to measure the natural frequencies and modes together with the acceleration and strain response accurately.

References

Abdel Wahab, M. M. & De Roeck, G. (1999). Damage detection in bridges using modal curvatures: Application to a real damage scenario. *Journal of Sound and Vibration,* 226(2):217-235.

Abdel Wahab, M. M., De Roeck, G. & Peeters, B. (1999). Parameterization of damage in reinforced concrete structures using model updating. *Journal of Sound and Vibration,* 228(4):717-730.

Alnefaie, F. (2009). Finite element modelling of composite plates with internal delamination. *Composite Structures*, 90:21-27.

Borchardt, J.K. (April 2004). Unmanned aerial vehicles spur composites use. *Reinforced Plastics*, 28-31.

Braun, S.G., Ewins, D.J. & Rao, S.S. (2002:87-97). *Encyclopedia of vibration*. San Diego: Academic Press.

Cook, R.D., Malkus, D.S., Plesha, M.E. & Witt, R.J. (2002). *Concepts and applications of finite element analysis*. 4th edition. Hoboken: John Wiley & Sons.

Corke, T.C. (2003). *Design of aircraft*. Upper Saddle River: Prentice Hall.

Cunha, J. & Piranda, J. (1999). Application of model updating techniques in dynamics for the identification of elastic constants of composite materials. *Composites Part B,* 30:79-85.

Cusano, A., Capoluongo, P., Campopiano, S., Cutolo, A., Giordano, M., Felli, F., Paolozzi, A. & Caponero, M. (2006). Experimental modal analysis of an aircraft model wing by embedded fibre Bragg grating sensors. *IEEE Sensors Journal*, 6(1):67-77.

Dowling, N.E. (2007). *Mechanical behaviour of materials. Engineering methods for deformation, fracture, and fatigue*. 3rd edition. Upper Saddle River: Prentice Hall.

Dynamic Design Solutions NV (2008a). *Validation and updating of FE models for structural analysis*. Pretoria: Esteq Engineering.

Dynamic Design Solutions NV (2008b). *FEMtools model updating theoretical manual*. Leuven: Dynamic Design Solutions.

Ewins, D.J. (1995). *Modal testing: Theory and practice*. Taunton: Research Studies Press.

References

Ewins, D.J. & Bernasconi, O. (1989). *Application of strain modal testing to real structures*. Proceedings of the 7th International Modal Analysis Conference (IMAC) 1453-1464. Las Vegas.

Farrar, C. & Jauregui, D. (1996). *Damage detection algorithms applied to experimental modal data from I-40 bridge*. Technical report: LA-13074-MS. New Mexico, Los Alamos National Laboratory.

FEMtools version 3.3.1 (1994-2008). (Computer Software). Leuven: Dynamic Design Solutions NV.

Fox, R.L. & Kapoor, M.P. (1968). Rates of change of eigenvalues and eigenvectors. *AIAA Journal,* 6:2426-2429.

Friswell, M.I. & Mottershead, J.E. (1995). *Finite element model updating in structural dynamics*. Dordrecht: Kluwer Academic Publishers.

Gentile, C & Saisi, A. (2007). Ambient vibration of historic masonry towers for structural identification and damage assessment. *Construction and Building Materials*, 21:1311-1321.

Gere, J.M. (2004). *Mechanics of materials*. 6th edition. Belmont: Thomson – Brooks/Cole.

Grouve, W.J.B., Warnet, L., De Boer, A., Akkerman, R. & Vlekken, J. (2008). Delamination detection with fibre Bragg gratings based on dynamic behaviour. *Composites Science and Technology*, 68:2418-2424.

Hameed, Z., Hong, Y.S., Cho, Y.M., Ahn, S.H. & Song, C.K. (2009). Condition monitoring and fault detection of wind turbines and related algorithms: A review. *Renewable & Sustainable energy reviews*, 13:1-39.

Hoffman, K. (1989). *An introduction to measurements using strain gages*. Darmstadt: Hottinger Baldwin Messtechnik GmbH.

Jenkins, L.R., Simkin, P. & Rhodes, D. (1999). *Civil jet aircraft design*. Burlington: Butterworth-Heinemann.

Keye, S. (2006). Improving the performance of model-based damage detection methods through the use of an updated analytical model. *Aerospace Science and Technology,* 10:199-206.

Kharrazi, M.H.K., Ventura, C.E., Brincker, R & Dascotte, E. (2002). *A study on damage detection using output-only modal data.* Conference proceedings of the 20th International Modal Analysis Conference (IMAC). California, Los Angeles.

Lauwagie, T., Sol, H. & Dascotte, E. (2002). *Damage identification in beams using inverse methods*. Paper presented at the 2002 International Seminar on Modal Analysis (ISMA): Leuven, Belgium.

References

Lednicer, D. (2007). *The incomplete guide to airfoil usage*. Available from: http://www.ae.uiuc.edu/m-selig/ads/aircraft.html#conventional (Accessed 2009-01-16).

Li, Y.Y., Cheng, L., Yam, L.H. & Wong, W.O. (2002). Identification of damage locations for plate-like structures using damage sensitive indices: strain modal approach. *Computers & Structures*, 80:1881-1894.

MATLAB version 7.6.0.324 (R2008a) (1984-2008). (Computer software). Natick, Massachusetts: The MathWorks.

Maeck, J. (2003). *Damage assessment of civil engineering structures by vibration monitoring*. Doctoral dissertation. Leuven: Katholieke Universiteit Leuven.

Maeck, J., Abdel Wahab, M., Peeters, B., De Roeck, G., De Visscher, J., De Wilde, W.P., Ndambi, J.-M. & Vantomme, J. (2000). Damage identification in reinforced concrete structures by dynamic stiffness determination. *Engineering Structures,* 22:1339-1349.

Maneschijn, A. (2008). *Continuous airworthiness challenges in unmanned aircraft systems*. Paper presented at the Technical Aerospace and Unmanned Systems Conference (TAUSC 2008): Somerset West, RSA.

MD Nastran R3 (2008). (Computer software). Santa Ana, Calfornia: MSC.Software Corporation.

MSC.Software Corporation (2007). *Dynamic analysis using MD Nastran and MD Patran*. Pretoria: Esteq Engineering.

Ngwangwa, H.M. (2004). *Assessment of structural damage using operational time response*. Masters dissertation. Pretoria: University of Pretoria.

Office of the Secretary of the Defence's Unmanned Aircraft Systems Roadmap 2005 – 2030 (2005). Available from: www.fas.org/irp/program/collect/uav_roadmap2005.pdf (Accessed 2009-01-15).

Oliver, J.A., Kosmatka, J.B., Hemez, F.M. & Farrar, C.R. (2006). Validating finite element models of composite aerospace structures for damage detection applications. *Proceedings of SPIE – the international society for optical engineering*, 6176:79-90.

Pandey, K. A., Biswas, M. & Samman, M. M. (1991). Damage detection from changes in curvature mode shapes. *Journal of Sound and Vibration,* 145(2):321-332.

Paolozzi, A. & Gasbarri, P. (2006). *Dynamic analysis with fibre optic sensors for structural health monitoring*. 9th Paper presented at the meeting of RTO-MP-AVT-141. Neuilly-sur-Seine, France. Available from: http://www.dtic.mil/cgi-bin/GetTRDoc?AD=ADA479893&Location=U2&doc=GetTRDoc.pdf (Accessed 14 July 2009).

References

Patran R1 (2008). (Computer software). Santa Ana, Calfornia: MSC.Software Corporation.

Rao, S.S. (2004). *Mechanical vibrations*. 4th edition. Upper Saddle River: Prentice Hall.

Rytter, A. (1993). *Vibration based inspection of civil engineering structures*. Ph.D. Thesis. Aalborg: University of Aalborg.

Staszewski, W., Boller, C. & Tomlinson, G. (2004). *Health monitoring of aerospace structures: Smart sensor technologies and signal processing*. Chichester: Wiley.

Teughels, A., Maeck, J. & De Roeck, G. (2002). Damage assessment by FE model updating using damage functions. *Computers and Structures*, 80:1869-1879.

Teughels, A. & De Roeck, G. (2004). Structural damage identification of the highway bridge Z24 by FE model updating. *Journal of Sound and Vibration,* 278:589-610.

Vári, L.M. (1995). *Structural modification using strain modal testing*. Masters dissertation. Pretoria: University of Pretoria.

Vári, L.M. & Heyns, P.S. (1997). Strain modal testing – A Critical Appraisal. *R & D Journal*, 13(3):83-90.

Wenzel, H. & Pichler, D. (2005). *Ambient vibration monitoring*. Chichester: Wiley.

Wikipedia's General Atomics ALTUS (2008). Available from: http://en.wikipedia.org/wiki/General_Atomics_ALTUS (Accessed 2009-01-16).

Wong, K.C. (1997). *Aerospace industry opportunities in australia. Unmanned aerial vehicles (UAVs) - Are they ready this time? Are we?* Paper presented at the meeting of the Royal Aeronautical Society. Sydney, Australia.

Wu, J. (2004). Finite element modelling and experimental modal testing of a three-dimensional framework. *International Journal of Mechanical Sciences*, 46:1245–1266.

Yam, L.H., Leung, T.P., Li, D.B. & Xue, K.Z. (1996). Theoretical and experimental study of modal strain analysis. *Journal of Sound and Vibration*, 191(2):251-260.

Appendix A: MATLAB scripts

A.1 MATLAB script used to extract strain and acceleration response

The following code was used to change the *.bdf-input file of the FE model to be analysed by Nastran. The properties of the elements at which damage is located are changed in the *.bdf-input file, the Nastran solver is called to solve the FE model and Patran is recalled to access the results file and generate report files from which the strain and acceleration responses can be extracted. The values of the extracted responses and various other variables are saved so they can be accessed by other programs and functions. This program was used for all the numerical calculations throughout chapters 3 and 4. This program will be referred to as *Nastran.m* and is one of the main programs.

```
clc;
close all;
clear all;

%This program will be used to change the thickness and the damaged area in
%the *.bdf input file to Nastran. Nastran is recalled to solve the *.bdf
%and generates the *.xdb input. Patran is launched and the *.xdb is read
%and a report on the strains at the natural frequencies is generated. This
%report is read and the strains in the x1-coordinate system is calculated
%and saved.

Deterministic = 'Y';
Wing_Measurement_Vec = [1 2]; % 3 4 5 6 7 8 9 10 11 12 13 14 15];

%Perform the main program in a loop
Num_Meas = 1;
% for Num_Meas = 1:length(Wing_Measurement_Vec)
for Run_No = 1:10%1:200

    %Define constants that will be used
    Thickness_Total = 0.01;
    Damage = [0.0095 0.009 0.0085 0.008 0.0075 0.007 0.0065 0.006 0.0055 0.005];

    disp(['THIS INFORMATION IS FOR RUN NUMBER ',num2str(Run_No),' AND ',num2str(Wing_Measurement_Vec(Num_Meas)),'
MEASUREMENTS']);
    disp('------------------------------------------------------------');
    disp('------------------------------------------------------------');
    disp(' ');

    %Define the measurement numbers and the measurement line location
    tic
    N_Wing_Measurement = 10;%Wing_Measurement_Vec(Num_Meas); %was 10; %Number of measurements on the left and right wing
planform
    N_Fuselage_Measurement = 2; %was 2; %Number of measurements on the fuselage part of the planform
    Measurement_Row = 14; %was 9;%Define the row on the FE model on which the measurements will be made
                          %with the bottom row being 1 as defined by the
                          %Predator wing
    Ana_Nat_Freq = [61.493 155.5 296.67 378.84 484.97 712.17 726.27 837.77 1005.1 1191 1321.4]; %As determined from Patran
    NF_Mode_Numbers = [1 2 3 5 9 11]; %This is a vector containing the mode numbers of the vertical bending modes
    Measure_Loc = 1; %Defines the FRF at which the comparison will be plotted

    %Define the Matlab *.mat file
    File_Location = 'D:\Nagraads\Meesters\Matlab codes\Predator .mat files for the discrete cases\';
%     File_Location = ['D:\Nagraads\Meesters\Matlab codes\Stochastic simulations\',num2str(N_Wing_Measurement),' Wing
sensors\'];
%     Mat_File = [File_Location,['Predator_Stochastic_',num2str(N_Wing_Measurement),'_Sensors_Damage_Case'],num2str(Run_No)];
%     Mat_File = [File_Location,'Predator_Stochastic_No_Damage.mat'];
%     Mat_File = [File_Location,'Predator_FRF_damage_case_test',num2str(Run_No),'0'];
    Mat_File = [File_Location,'Predator_FRF_damage_case3_',num2str(Run_No),'0'];
%     Mat_File = [File_Location,'Predator_FRF_damage_case1_orig_damp_',num2str(Run_No),'0'];
%     Mat_File = [File_Location,'Predator_FRF_test_no_damage'];
%     Mat_File = [File_Location,'Predator_FRF_orig_damp_no_damage'];

    %Define the *.bdf file from which the node locations and the element
    %connectivity can be read
    File = 'D:\Nagraads\Meesters\Patran FEM\FEM models\Predator wing\Predator_parametric_wing_Original.bdf';

    %Delcare the filename that will serve as the reference *.bdf
    File_Original = 'Predator_parametric_wing_updated.bdf';
%     File_Original = 'Predator_parametric_wing_ori_damp.bdf';
    File_Modified = 'Predator_parametric_wing_Modified.bdf';
    File_Result_Output_Session_File = 'Result_Output_Session_File.ses';
    File_Result_Output_Session_File_Modified = 'Result_Output_Session_File_Modified.ses';
```

Appendix A: MATLAB scripts

```
    %Open the file and read the contents into a matrix
    fid = fopen(File_Original);
    Out = textscan(fid,'%s','delimiter','\n','whitespace','');
    fclose(fid);
    Out = char(Out{1});

    %Define the constants that define the damaged area
    %The damage area is defined
    if upper(Deterministic) == 'Y'
%         ldi = 133.839e-3; %Test case 1 with 30% damage
%         hdi = 25.808e-3;
%         ld =  119.949e-3;
%         hdr = 27.73e-3;
%         hdt = 23.533e-3;
%         Damaged_Thickness = Damage(Run_No);
%         ldi = 70.708e-3; %Test case 2 with 50% damage
%         hdi = 2.471e-3;
%         ld =  113.636e-3;
%         hdr = 25.662e-3;
%         hdt = 22.254e-3;
%         Damaged_Thickness = Damage(Run_No);
%         ldi = 89.647e-3; %Deterministic case 1
%         hdi = 24.639e-3;
%         ld =  88.384e-3;
%         hdr = 25.094e-3;
%         hdt = 22.443e-3;
%         Damaged_Thickness = Damage(Run_No);
%         ldi = 89.647e-3; %Deterministic case 2
%         hdi = 3.727e-3;
%         ld =  88.384e-3;
%         hdr = 20.912e-3;
%         hdt = 18.703e-3;
%         Damaged_Thickness = Damage(Run_No);
        ldi = -348.485e-3; %Deterministic case 3 (Originally 9 in Predator modes.docx)
        hdi = 47.894e-3;
        ld =  -44.192e-3;
        hdr = 11.554e-3;
        hdt = 10.670e-3;
        Damaged_Thickness = Damage(Run_No);
        %Calculate  the area of the two wing sections and the total area of the
        %family of wings. The area of the damage will be calculated and will be
        %expressed as a percentage of the wing and total areas.
        [Ratio_Dam_Wing,Ratio_Dam_Tot] = Wing_area_calculation(ld,hdr,hdt);
    else
        Ratio_Dam_Wing = 0.5;
        while Ratio_Dam_Wing < 1
        %Obtain the damage parameters
            [ldi,hdi,ld,hdr,hdt,Damaged_Thickness,Ratio_Dam_Wing] =
Stochastic_Generation_Damage_Location(File,Thickness_Total);
        end
    end

    %Extract the elements & nodes at the damaged location
    Figure_Count = 0;
    Sweep_Ans = 'Y';

[Node_Measured_Left,Node_Measured_Middle,Node_Measured_Right,Measured_Elements_Data,Elements_Inside_Damage,Damage_Corner_Node
s,Theta_Right,Theta_Left] = ...;

Damaged_Area_Elements(N_Wing_Measurement,N_Fuselage_Measurement,Measurement_Row,File,ldi,hdi,ld,hdr,hdt,Figure_Count,Sweep_An
s);
    Measured_Nodes = [Node_Measured_Right Node_Measured_Middle Node_Measured_Left]; %This is the nodelist required by the
session file

    %Determine if a measurement location is inside the damaged area and
    %save a logical to represent it
    Count_Inside = 0;
    for ii = 1:length(Measured_Nodes)
        Pos = find(Elements_Inside_Damage(2:end,:) == Measured_Nodes(ii));
        if ~(isempty(Pos))
            Count_Inside = Count_Inside + 1;
        end
    end
    if Count_Inside > 0
        Measure_Loc_Inside_Damage = 1;
    else
        Measure_Loc_Inside_Damage = 0;
    end
    pause(1);
    Finish_Tot = 0;
    Finish = toc;
    Finish_Tot = Finish_Tot + Finish;
    disp(' ');
    disp('Finished with the initial definition and calculation');
    disp(['of the damaged area                                    ',num2str(Finish,6),' seconds']);

    %Find the elements at which the measurements are made and the elements that
    %fall within the damaged area
    Measured_Elements = sort(Measured_Elements_Data(1,:));
    Element_No_Inside_Damage = sort(Elements_Inside_Damage(1,:));

    %Change the element group at which the measurements are made
    %Find the line $ Elements for group : Output_Elements
    tic
    Pos_Elements = find(Out(:,1) == '$' & Out(:,2) == ' ' & Out(:,3) == 'E' & Out(:,4) == 'l' & ...
              Out(:,5) == 'e' & Out(:,6) == 'm' & Out(:,7) == 'e' & Out(:,8) == 'n' & ...
              Out(:,9) == 't' & Out(:,10) == 's' & Out(:,11) == ' ' & Out(:,12) == 'f' & ...
              Out(:,13) == 'o' & Out(:,14) == 'r' & Out(:,15) == ' ' & Out(:,16) == 'g' & ...
              Out(:,17) == 'r' & Out(:,18) == 'o' & Out(:,19) == 'u' & Out(:,20) == 'p' & ...
              Out(:,21) == ' ' & Out(:,22) == ':' & Out(:,23) == ' ' & Out(:,24) == 'O' & ...
              Out(:,25) == 'u' & Out(:,26) == 't' & Out(:,27) == 'p' & Out(:,28) == 'u' & ...
```

Appendix A: MATLAB scripts

```
            Out(:,29) == 't' & Out(:,30) == '_' & Out(:,31) == 'E' & Out(:,32) == 'l');
    Temp_Out = Out(1:Pos_Elements,:);
    First_Time = 0;
    Count = 0;
    for ii = 1:length(Measured_Elements)
        if First_Time == 0
            Temp_Out(Pos_Elements+1,1:8) = 'SET 1 = ';
            Count2 = 8;
        end
        First_Time = 1;
        String = num2str(Measured_Elements(ii));
        if ii ~= length(Measured_Elements)
            String2 = [String,','];
        else
            String2 = String;
        end
        if Count2+length(String)+1 <= size(Out,2)
            Temp_Out(Pos_Elements+1+Count,Count2+1:Count2+length(String2)) = String2;
            Count2 = Count2 + length(String)+1;
        else
            Count = Count + 1;
            Count2 = 0;
            Temp_Out(Pos_Elements+1+Count,Count2+1:Count2+length(String2)) = String2;
            Count2 = Count2 + length(String)+1;
        end
    end
    Pos_Title = find(Out(:,1) == 'T' & Out(:,2) == 'I' & Out(:,3) == 'T' & Out(:,4) == 'L' & Out(:,5) == 'E') - 4; %Minus 4
to include the acceleration node
    Temp_Out(end+1:end+size(Out(Pos_Title:end,:),1),:) = Out(Pos_Title:end,:);
    clear Out
    Out = Temp_Out;
    clear Temp_Out
    Finish = toc;
    Finish_Tot = Finish_Tot + Finish;
    disp('Finished with the definition of the element group at');
    disp(['which the measurements are made                    ',num2str(Finish,6),' seconds']);

    %Change the damaged elements to show the correct property type
    tic
    Pos_CQuad = find(Out(:,1) == 'C' & Out(:,2) == 'Q' & Out(:,3) == 'U' & ...
                     Out(:,4) == 'A' & Out(:,5) == 'D' & Out(:,6) == '8');

    %Ensure that all the elements are initially undamaged
    PID = 1;
    Out(Pos_CQuad,18) = num2str(PID);

    %Change the damaged elements to the damaged elements property ID
    for ii = 1:length(Element_No_Inside_Damage)
        Pos_Change_Element_Prop = find(str2num(Out(Pos_CQuad,10:17)) == Element_No_Inside_Damage(ii));
        PID = 2;
        Out(Pos_CQuad(Pos_Change_Element_Prop),18) = num2str(PID);
    end
    Finish = toc;
    Finish_Tot = Finish_Tot + Finish;
    disp('Finished with the location and redefinition of the');
    disp(['damaged elements properties                        ',num2str(Finish,6),' seconds']);

    %Sort the Text so all the elements with PID 1 is at the top and all those
    %with PID of 2 is at the bottom
    tic
    Pos_PSet = find(Out(:,1) == '$' & Out(:,2) == ' ' & Out(:,3) == 'P' & ...
                    Out(:,4) == 's' & Out(:,5) == 'e' & Out(:,6) == 't');
    Pos_Referenced_Material = find(Out(:,1) == '$' & Out(:,2) == ' ' & Out(:,3) == 'R' & ...
                                   Out(:,4) == 'e' & Out(:,5) == 'f' & Out(:,6) == 'e' & ...
                                   Out(:,7) == 'r' & Out(:,8) == 'e' & Out(:,9) == 'n' & ...
                                   Out(:,10) == 'c' & Out(:,11) == 'e' & Out(:,12) == 'd' & ...
                                   Out(:,13) == ' ' & Out(:,14) == 'M' & Out(:,15) == 'a' & ...
                                   Out(:,16) == 't' & Out(:,17) == 'e' & Out(:,18) == 'r' & ...
                                   Out(:,19) == 'i' & Out(:,20) == 'a' & Out(:,21) == 'l' & ...
                                   Out(:,22) == ' ' & Out(:,23) == 'R' & Out(:,24) == 'e' & ...
                                   Out(:,25) == 'c' & Out(:,26) == 'o' & Out(:,27) == 'r' & ...
                                   Out(:,28) == 'd' & Out(:,29) == 's');
    Temp_Out_Up_To_Pset1 = Out(1:Pos_PSet(1),:);

    %Change the thickness of the damaged area
    Temp_Out_Pset_2 = Out(Pos_PSet(2)-2:Pos_PSet(2),:);
    Input_Thickness = num2str(Damaged_Thickness);
    Temp_Out_Pset_2(2,25:25+length(Input_Thickness(2:end))-1) = Input_Thickness(2:end);

    Temp_Out_Referenced = Out(Pos_Referenced_Material:end,:);
    Count1 = 0;
    Count2 = 0;
    for ii = 1:length(Pos_CQuad)
        if str2num(Out(Pos_CQuad(ii),18)) == 1
            Count1 = Count1 + 2;
            Temp_Out_Quad_1(Count1-1:Count1,:) = Out(Pos_CQuad(ii):Pos_CQuad(ii)+1,:);
        elseif str2num(Out(Pos_CQuad(ii),18)) == 2
            Count2 = Count2 + 2;
            Temp_Out_Quad_2(Count2-1:Count2,:) = Out(Pos_CQuad(ii):Pos_CQuad(ii)+1,:);
        end
    end
    Finish = toc;
    Finish_Tot = Finish_Tot + Finish;
    disp(['Finished with the sorting operation                ',num2str(Finish,6),' seconds']);

    %Assemble the output file and write the text
    tic
    Out = [Temp_Out_Up_To_Pset1;Temp_Out_Quad_1;Temp_Out_Pset_2;Temp_Out_Quad_2;Temp_Out_Referenced];
    Textwrite(File_Modified,Out);
    Finish = toc;
    Finish_Tot = Finish_Tot + Finish;
    disp(['Finished writing the modified file                 ',num2str(Finish,6),' seconds']);
```

Appendix A: MATLAB scripts

```
    %Run Nastran to solve the *.bdf
    Time = RunNastran(File_Modified,0,0,1,1);
    disp(['Finished with the Nastran run                    ',num2str(Time),' seconds']);
    Finish_Tot = Finish_Tot + Time;

    %Create a nodelist inside the session file so the values at these nodes
    %are the only output in the result files
    %Open the session file and read the contents into a matrix
    tic
    fid = fopen(File_Result_Output_Session_File);
    Out = textscan(fid,'%s','delimiter','\n','whitespace','');
    fclose(fid);
    Out = char(Out{1});

    Pos_Node_List = find(Out(:,1) == 's' & Out(:,2) == 't' & Out(:,3) == 'r' & ...
                         Out(:,4) == 'i' & Out(:,5) == 'n' & Out(:,6) == 'g' & ...
                         Out(:,7) == ' ' & Out(:,8) == 'N' & Out(:,9) == 'o' & ...
                         Out(:,10) == 'd' & Out(:,11) == 'e' & Out(:,12) ==  'L' & ...
                         Out(:,13) == 'i' & Out(:,14) == 's' & Out(:,15) == 't' & ...
                         Out(:,16) == '[' & Out(:,17) == '1' & Out(:,18) == '0' & ...
                         Out(:,19) == '0' & Out(:,20) == '0' & Out(:,21) == ']');
    for ii = 1:length(Measured_Nodes)
        if ii == 1
            Nodes_for_List(1:length(num2str(Measured_Nodes(ii)))+1) = [num2str(Measured_Nodes(ii)),' '];
        elseif Measured_Nodes(ii) ~= Measured_Nodes(end)
            Nodes_for_List(end+1:end+length(num2str(Measured_Nodes(ii)))+1) = [num2str(Measured_Nodes(ii)),' '];
        else
            Nodes_for_List(end+1:end+length(num2str(Measured_Nodes(ii)))) = num2str(Measured_Nodes(ii));
        end
    end
    Node_List = ['NodeList = "Node ',Nodes_for_List,'"'];
    String_Change_Node_List = ['string NodeList[',num2str(length(Node_List)+2),']'];
    Out(Pos_Node_List,1:length(String_Change_Node_List)) = String_Change_Node_List;
    Out(Pos_Node_List,length(String_Change_Node_List)+1:length(String_Change_Node_List)+5) = ' ';
    Out(Pos_Node_List+1,1:length(Node_List)) = Node_List;
    Textwrite(File_Result_Output_Session_File_Modified,Out);
    Finish = toc;
    Finish_Tot = Finish_Tot + Finish;
    disp(['Finished correcting the output session file          ',num2str(Finish,6),' seconds']);

    %The session file that will create the result files (mag.txt and
    %phase.txt) is played and the modified session file is used
    tic
    PatranPath = 'D:\MSC.Software\Patran\2008_r1\bin\';
    evalstr = ['!' PatranPath 'Patran.exe -sfp ' File_Result_Output_Session_File_Modified];
    eval(evalstr)
    Finish  = toc;
    Finish_Tot = Finish_Tot + Finish;
    disp(['Finished running Patran to generate output files     ',num2str(Finish,6),' seconds']);

    %Extract the strains and the phases from the mag.txt and phase.txt
    %files
    tic
    Output_File_Mag = 'mag.txt';
    Output_File_Phase = 'phase.txt';
    [Strain_Mag_Scaled,Freq] = Read_Patran_Output(Output_File_Mag);
    [Strain_Phase_Deg,Freq] = Read_Patran_Output(Output_File_Phase);
    Strain_Mag = [Strain_Mag_Scaled(:,1,:) Strain_Mag_Scaled(:,2:4,:)./1e8];
    Strain_Phase = [Strain_Phase_Deg(:,1,:) Strain_Phase_Deg(:,2:4,:).*(pi/180)];

    %Add part to extract the acceleration data
    Ana_File_Real = 'Acc_FRF_Real.txt';
    Ana_File_Imag = 'Acc_FRF_Imag.txt';
    [Ana_Acc_Real,Ana_FRF_Freq] = Read_Patran_Output(Ana_File_Real);
    [Ana_Acc_Imag,Ana_FRF_Freq] = Read_Patran_Output(Ana_File_Imag);
    i = sqrt(-1);
    Ana_Acc_Z = squeeze(Ana_Acc_Real(1,4,:)) + i.*squeeze(Ana_Acc_Imag(1,4,:));
    Ana_Acc_Mag_Z = abs(Ana_Acc_Z);
    Ana_Acc_Phase_Z = angle(Ana_Acc_Z);

    Finish = toc;
    Finish_Tot = Finish_Tot + Finish;
    disp(['Finished reading the output from the text files      ',num2str(Finish,6),' seconds']);

    %Transform the strain output from the xy-axis to the x1y1-axis
    %Extract the x1 values on the left wing
    Nodes_Pos_Left = zeros(1,length(Node_Measured_Left));
    for ii = 1:length(Node_Measured_Left)
        Nodes_Pos_Left(ii) = find(Strain_Mag(:,1,1) == Node_Measured_Left(ii));
    end
    Strain_x1_Left = zeros(length(Freq),length(Node_Measured_Left));
    for ii = 1:length(Nodes_Pos_Left)
        X_Strain_Mag = squeeze(Strain_Mag(Nodes_Pos_Left(ii),2,:));
        X_Phase = squeeze(Strain_Phase(Nodes_Pos_Left(ii),2,:));
        X_Strain = X_Strain_Mag.*exp(i.*X_Phase);
        Y_Strain_Mag = squeeze(Strain_Mag(Nodes_Pos_Left(ii),3,:));
        Y_Phase = squeeze(Strain_Phase(Nodes_Pos_Left(ii),3,:));
        Y_Strain = Y_Strain_Mag.*exp(i.*Y_Phase);
        XY_Strain_Mag = squeeze(Strain_Mag(Nodes_Pos_Left(ii),4,:));
        XY_Phase = squeeze(Strain_Phase(Nodes_Pos_Left(ii),4,:));
        XY_Strain = XY_Strain_Mag.*exp(i.*XY_Phase);
        Strain_x1_Left(:,ii) = X_Strain.*(cos(Theta_Left))^2 + Y_Strain.*(sin(Theta_Left))^2 +
XY_Strain*sin(Theta_Left)*cos(Theta_Left);
    end

    %Extract the x1 values on the right wing
    Nodes_Pos_Right = zeros(1,length(Node_Measured_Right));
    for ii = 1:length(Node_Measured_Right)
        Nodes_Pos_Right(ii) = find(Strain_Mag(:,1,1) == Node_Measured_Right(ii));
    end
    Strain_x1_Right = zeros(length(Freq),length(Node_Measured_Right));
```

Appendix A: MATLAB scripts

```
    for ii = 1:length(Nodes_Pos_Right)
        X_Strain_Mag = squeeze(Strain_Mag(Nodes_Pos_Right(ii),2,:));
        X_Phase = squeeze(Strain_Phase(Nodes_Pos_Right(ii),2,:));
        X_Strain = X_Strain_Mag.*exp(i.*X_Phase);
        Y_Strain_Mag = squeeze(Strain_Mag(Nodes_Pos_Right(ii),3,:));
        Y_Phase = squeeze(Strain_Phase(Nodes_Pos_Right(ii),3,:));
        Y_Strain = Y_Strain_Mag.*exp(i.*Y_Phase);
        XY_Strain_Mag = squeeze(Strain_Mag(Nodes_Pos_Right(ii),4,:));
        XY_Phase = squeeze(Strain_Phase(Nodes_Pos_Right(ii),4,:));
        XY_Strain = XY_Strain_Mag.*exp(i.*XY_Phase);
        Strain_x1_Right(:,ii) = X_Strain.*(cos(Theta_Right))^2 + Y_Strain.*(sin(Theta_Right))^2 +
XY_Strain*sin(Theta_Right)*cos(Theta_Right);
    end

    %Extract the x1 values in the middle
    Nodes_Pos_Middle = zeros(1,length(Node_Measured_Middle));
    for ii = 1:length(Node_Measured_Middle)
        Nodes_Pos_Middle(ii) = find(Strain_Mag(:,1,1) == Node_Measured_Middle(ii));
    end
    Strain_x1_Middle = zeros(length(Freq),length(Node_Measured_Middle));
    for ii = 1:length(Nodes_Pos_Middle)
        X_Strain_Mag = squeeze(Strain_Mag(Nodes_Pos_Middle(ii),2,:));
        X_Phase = squeeze(Strain_Phase(Nodes_Pos_Middle(ii),2,:));
        X_Strain = X_Strain_Mag.*exp(i.*X_Phase);
        Strain_x1_Middle(:,ii) = X_Strain;
    end

    %Combine the measured strains in one matrix
    Strain_x1_Complex = [Strain_x1_Right Strain_x1_Middle Strain_x1_Left];
    Strain_x1 = abs(Strain_x1_Complex);

    %Calculate the strain FRFs normalise by the accelerance FRF
    Strain_x1_Normalised = zeros(size(Strain_x1_Complex,1),size(Strain_x1_Complex,2));
    for ii = 1:size(Strain_x1_Complex,2)
        Strain_x1_Normalised(:,ii) = Strain_x1_Complex(:,ii)./Ana_Acc_Z;
    end

    Finish = toc;
    Finish_Tot = Finish_Tot + Finish;
    disp(['Finished with the conversion from xy to x1y1-axis    ',num2str(Finish,6),' seconds']);

    %Extract the strain values at the natural frequencies of interest
    tic
    Patran_NF_Pos = zeros(length(Ana_Nat_Freq),1);
    Patran_Ana_Nat_Freq = zeros(length(Ana_Nat_Freq),1);
    NF_Strain_x1 = zeros(length(Ana_Nat_Freq),size(Strain_x1_Complex,2));
    for ii = 1:length(Ana_Nat_Freq)

        %Extract the analytical natural frequencies from Patran
        [Min,Patran_NF_Pos(ii)] = min(abs(Freq - Ana_Nat_Freq(ii)));
        Patran_Ana_Nat_Freq(ii) = Freq(Patran_NF_Pos(ii));

        %Extract the acceleration and strain values at the natural frequencies from
        %the analytical model
        for jj = 1:size(Strain_x1_Complex,2)
            NF_Strain_x1(ii,jj) = Strain_x1(Patran_NF_Pos(ii),jj);
        end
    end
    MStrain_Freq_NF_Loc = Patran_Ana_Nat_Freq;
    MStrain_x1_NF_Loc = NF_Strain_x1(NF_Mode_Numbers,:);
    MStrain_x1_NF_Loc_Normalised = abs(Strain_x1_Normalised(Patran_NF_Pos(NF_Mode_Numbers),:));

    %Compute the natural frequency lines
    Count = 1;
    NM_Freq(Count) = 0;
    NM_Freq_Line(Count) = 0;
    for ii = 1:length(NF_Mode_Numbers)
        Count = Count + 1;
        NM_Freq(Count) = MStrain_Freq_NF_Loc(NF_Mode_Numbers(ii)) - exp(-MStrain_Freq_NF_Loc(NF_Mode_Numbers(ii)));
        NM_Freq_Line(Count) = 1e-10;
        Count = Count + 1;
        NM_Freq(Count) = MStrain_Freq_NF_Loc(NF_Mode_Numbers(ii));
        NM_Freq_Line(Count) = 1.1*max(max(MStrain_x1_NF_Loc));
        Count = Count + 1;
        NM_Freq(Count) = MStrain_Freq_NF_Loc(NF_Mode_Numbers(ii)) + exp(-MStrain_Freq_NF_Loc(NF_Mode_Numbers(ii)));
        NM_Freq_Line(Count) = 1e-10;
    end

    Finish = toc;
    Finish_Tot = Finish_Tot + Finish;
    disp(['Finished extracting the strains at the NF locations  ',num2str(Finish,6),' seconds']);

    %Save the file
    tic

    %The newly calculated matrices are added to the orginal *.mat file
    save(Mat_File,'Freq','Strain_x1','Node_Measured_Right','Node_Measured_Middle',...
                  'Node_Measured_Left','MStrain_x1_NF_Loc',...
                  'Damage_Corner_Nodes','Damaged_Thickness','Elements_Inside_Damage',...
                  'Measured_Elements_Data','Measured_Nodes','Measurement_Row',...
                  'NF_Mode_Numbers','N_Fuselage_Measurement','N_Wing_Measurement',...
                  'Theta_Right','Theta_Left','hdi','hdr','hdt','ldi','ld','Measure_Loc_Inside_Damage',...
                  'Ana_Nat_Freq','MStrain_Freq_NF_Loc','NF_Strain_x1',...
                  'Patran_Ana_Nat_Freq','Patran_NF_Pos','Ana_Acc_Z','Ana_FRF_Freq',...
                  'Strain_x1_Normalised','MStrain_x1_NF_Loc_Normalised');
    Finish = toc;
    Finish_Tot = Finish_Tot + Finish;
    disp(['Finished saving the *.mat file for later use         ',num2str(Finish,6),' seconds']);

    %Display the total time
    disp(' ');
    disp('--------------------------------------------------------------------');
```

```
    disp(['Finished with the program of RUN NUMBER ',num2str(Run_No),' in         ',num2str(Finish_Tot,6),' seconds']);
    disp('------------------------------------------------------------------------');
    disp(' ');
    pause(2);

    %Clear the unecessary variables
    clear Count Count1 Count2 Damage Damage_Corner_Nodes Damaged_Thickness Element_No_Inside_Damage ...
          Elements_Inside_Damage File File_Modified File_Original File_Result_Output_Session_File ...
          File_Location File_Result_Output_Session_File_Modified Finish Finish_Tot First_Time Freq Input_Thickness ...
          MStrain_x1_NF_Loc Mat_File Measure_Loc Measured_Elements Measured_Elements_Data Measured_Nodes ...
          Measurement_Row Min NF_Mode_Numbers NM_Freq NM_Freq_Line N_Fuselage_Measurement N_Wing_Measurement ...
          Node_List Node_Measured_Left Node_Measured_Middle Node_Measured_Right Nodes_Pos_Left Nodes_Pos_Middle ...
          Nodes_Pos_Right Nodes_for_List Out Output_File_Mag Output_File_Phase PID PatranPath Pos_CQuad ...
          Pos_Change_Element_Prop Pos_First_BM Pos_Elements Pos_Node_List Pos_PSet Pos_Referenced_Material Pos_Title ...
          Ratio_Dam_Tot Ratio_Dam_Wing Strain_Mag Strain_Phase Strain_x1 Strain_x1_Left Strain_x1_Middle ...
          Strain_x1_Right String String2 String_Change_Node_List Temp_Out_Pset_2 Temp_Out_Quad_1 Temp_Out_Quad_2 ...
          Temp_Out_Referenced Temp_Out_Up_To_Pset1 Theta_Left Theta_Right XY_Phase XY_Strain X_Phase X_Strain ...
          Y_Phase Y_Strain ans evalstr fid hdi hdr hdt ii jj ld ldi Measure_Loc_Inside_Damage Count_Inside ...
          Pos Time Strain_Mag_Scaled Strain_Phase_Deg Strain_x1_Complex XY_Strain_Mag X_Strain_Mag Y_Strain_Mag ...
          Ana_Nat_Freq Figure_Count MStrain_Freq_NF_Loc NF_Strain_x1 Patran_Ana_Nat_Freq Patran NF_Pos Sweep_Ans ...
          Ana_Acc_Imag Ana_Acc_Mag_Z Ana_Acc_Phase_Z Ana_Acc_Real Anna_Acc_Z Ana_FRF_Freq Ana_File_Imag Ana_File_Real ...
          Patran_NF_Pos i Ana_Acc_Z MStrain_x1_NF_Loc_Normalised Strain_x1_Normalised Thickness_Total

    %Delete the files that were written by Nastran and Patran that are
    %redundant
    try
        eval('delete patran.ses.*');
    catch ME_Ses
    end
    try
        eval('delete Results.db.jou');
    catch ME_db_jou
    end
    try
        eval('delete Results.db');
    catch ME_db
    end
    try
        eval('delete predator_parametric_wing_modified.xdb');
    catch ME_xdb
    end
    try
        eval('delete mag.txt');
    catch ME_Mag
    end
    try
        eval('delete phase.txt');
    catch ME_Phase
    end
    try
        eval('delete Acc_FRF_Real.txt');
    catch ME_Acc_Real
    end
    try
        eval('delete Acc_FRF_Imag.txt');
    catch ME_Acc_Imag
    end
    clear ME_Ses ME_db_jou ME_db ME_xdb ME_Mag ME_Phase ME_Acc_Real ME_Acc_Imag
end %For the loop over the main program
% end %For the loop counting the number of measurements
```

The program *Nastran.m* recalls the function *Damaged_Area_Elements.m*. This code is used to calculate the nodes at which the measurements are made and calculate the rotation that the extracted strains should go through to lie on the measurement line based on the specified measurement row. The damaged elements are identified within this function and is given to *Nastran.m* to change the material properties of these elements in the *.bdf-file.

```
function [Node_Measured_Left,Node_Measured_Middle,Node_Measured_Right,...
          Measured_Elements_Data,Elements_Inside_Damage,Damage_Corner_Nodes,Theta_Right,Theta_Left,Figure_Count] = ...
          Damaged_Area_Elements(N_Wing_Measurement,N_Fuselage_Measurement,...
          Measurement_Row,File,ldi,hdi,ld,hdr,hdt,Figure_Count,Sweep_Ans)

%This function will be used to calculate the elements that are enclosed by
%the damaged area. This will serve as the input to the Nastran.m file which
%changes the elements and runs Nastran from Matlab.
%
%The ouput to the function is defined as follows:
%
%Node_Measured_Left     - The measurement nodes on the left wing
%Node_Measured_Middle   - The measurement nodes on the fuselage
%Node_Measured_Right    - The measurement nodes on the right wing
%Measured_Elements_Data - The element data (node numbers and nodes
%                         connectivity) of the measured nodes. These are
%                         the 4 elements that share the common measured
%                         nodes for the calculation of the average stress
%                         at that node
%Elements_Inside_Damage - The element data which described those elements
%                         inside the damaged area
%Damage_Corner_Nodes    - The nodes at the four corners of the damaged area
%Theta_Right            - The angle (in radians) of the rotation from the
%                         xy to the x1y1 axis for the right wing
%Theta_Left             - The angle (in radians) of the rotation from the
```

Appendix A: MATLAB scripts

```
%                       xy to the x1y1 axis for the left wing
%
%The input to the function is defines as follows:
%
%N_Wing_Measurement     - Number of measurements on the left and right wing
%                         planform
%N_Fuselage_Measurement - Number of measurements on the fuselage part of
%                         the planform
%Measurement_Row        - Define the row on the FE model on which the measurements will be made
%                         with the bottom row being 1 as defined by the
%                         Predator wing
%File                   - The *.bdf filname from which the node and element
%                         data can be read
%ldi                    - Defines the x-location of the node at which the
%                         damage starts
%hdi                    - Defines the y-location of the node at which the
%                         damage starts
%ld                     - Defines the length of the damaged area
%hdr                    - Defines the height of the damaged area at the
%                         root
%hdt                    - Defines the height of the damaged area at the tip

%Load and define new constants
[N_Elem,N_Nodes] = Constants;%Global Hawk - Constants_Global_Hawk %Neptune - Constants_Neptune;% Predator - Constants;
Measured_Nodes = 'None';
Answer_for_all = 'Yes';

%Read the nodes location and the element connectivity from the file
[x_Loc,y_Loc,Element_Data,Node_Data] = Read_Elements_Node_Data(File,Measured_Nodes,N_Elem,N_Nodes,Answer_for_all);
%Extract the corner nodes
for ii = 1:length(Element_Data)
    if ii == 1
        Temp_Corner_Nodes(:,1) = Element_Data(3:6,ii);
    else
        Temp_Corner_Nodes(end+1:end+4,1) = Element_Data(3:6,ii);
    end
end
Temp_Corner_Nodes = sort(Temp_Corner_Nodes);
Element_Corner_Nodes = Temp_Corner_Nodes(1);
Count = 1;
for ii = 2:length(Temp_Corner_Nodes)
    if Temp_Corner_Nodes(ii) ~= Temp_Corner_Nodes(ii-1)
        Count = Count + 1;
        Element_Corner_Nodes(Count,1) = Temp_Corner_Nodes(ii);
    end
end
Pos_Corner_Nodes = zeros(length(Element_Corner_Nodes),1);
for ii = 1:length(Element_Corner_Nodes)
    Pos_Corner_Nodes(ii) = find(Node_Data(1,:) == Element_Corner_Nodes(ii));
end
Corner_Node_Data = Node_Data(:,Pos_Corner_Nodes);
clear Temp_Corner_Nodes

%Sort the nodes from bottom to the top to identify the measurement
%locations
N_Wing_FEM_Measurements = N_Wing_Measurement + 2;
N_Fuselage_FEM_Measurements = N_Fuselage_Measurement + 2;
RCount = 1; %The rows go from bottom to top
CCount = 1; %The columns go from right to left with respect to the predator wing
Corner_Node_Data_Sort(1,1,1:4) = Corner_Node_Data(:,1);
for ii = 2:length(Corner_Node_Data)
    RCount = RCount + 1;
    if Corner_Node_Data(3,ii) > Corner_Node_Data(3,ii-1)
        Corner_Node_Data_Sort(RCount,CCount,1:4) = Corner_Node_Data(:,ii);
    else
        CCount = CCount + 1;
        RCount = 1;
        Corner_Node_Data_Sort(1,CCount,1:4) = Corner_Node_Data(:,ii);
    end
end
Count = 1;
for ii = 2:size(Corner_Node_Data_Sort,2)
    if Corner_Node_Data_Sort(Measurement_Row,ii,3) == Corner_Node_Data_Sort(Measurement_Row,ii-1,3)
        if Count == 1
            Fuselage_Pos(Count) = ii-1;
        end
        Count = Count + 1;
        Fuselage_Pos(Count) = ii;
    end
end

%The damage location is calculated
x_di = ldi;
y_di = -hdi;

Distance_di = sqrt((x_di - Corner_Node_Data(2,:)).^2 + (y_di - Corner_Node_Data(3,:)).^2);
[Min_Distance,Pos_Min_Distance] = min(Distance_di);
x_FEM_di = Corner_Node_Data(2,Pos_Min_Distance);
y_FEM_di = Corner_Node_Data(3,Pos_Min_Distance);
FEM_di_Node = Corner_Node_Data(1,Pos_Min_Distance);
for R_Count = 1:size(Corner_Node_Data_Sort,1)
    for C_Count = 1:size(Corner_Node_Data_Sort,2)
        if Corner_Node_Data_Sort(R_Count,C_Count,1) == FEM_di_Node
            Pos_di = [R_Count C_Count];
        end
    end
end

%Extract the nodes in the column next to the damage initiation position
Nodes_Close_to_di = [Corner_Node_Data_Sort(Pos_di(1),Pos_di(2)-1,1) Corner_Node_Data_Sort(Pos_di(1),Pos_di(2)+1,1)];
Pos_Nodes_Close_to_di(1) = find(Corner_Node_Data(1,:) == Nodes_Close_to_di(1));
Pos_Nodes_Close_to_di(2) = find(Corner_Node_Data(1,:) == Nodes_Close_to_di(2));
```

Appendix A: MATLAB scripts

```
% if abs(Corner_Node_Data(2,Pos_Min_Distance+1) - Corner_Node_Data(2,Pos_Min_Distance) < 1e-5) & ...
%    (Corner_Node_Data(2,Pos_Min_Distance+1) > Corner_Node_Data(2,Pos_Min_Distance))
%     x_Node_Above_FEM_di = Corner_Node_Data(2,Pos_Min_Distance+1);
%     y_Node_Above_FEM_di = Corner_Node_Data(3,Pos_Min_Distance+1);
% else
%     x_Node_Above_FEM_di = Corner_Node_Data(2,Pos_Min_Distance-1);
%     y_Node_Above_FEM_di = Corner_Node_Data(3,Pos_Min_Distance-1);
% end
% Distance_Node_Above_FEM_di = sqrt((x_FEM_di - x_Node_Above_FEM_di).^2 + (y_FEM_di - y_Node_Above_FEM_di).^2);
% Distance_FEM_di = sqrt((x_FEM_di - Corner_Node_Data(2,:)).^2 + (y_FEM_di - Corner_Node_Data(3,:)).^2);
% Pos_Nodes_Close_to_di = find((Distance_FEM_di < 2*Distance_Node_Above_FEM_di) &...
%                              (abs(Corner_Node_Data(2,:) - x_FEM_di) > 1e-5) &...
%                              (abs(Corner_Node_Data(3,:) - y_FEM_di) < 0.5*Distance_Node_Above_FEM_di));
% if length(Pos_Nodes_Close_to_di) < 2
%     Pos_Nodes_Close_to_di = find((Distance_FEM_di < 3*Distance_Node_Above_FEM_di) &...
%                                  (abs(Corner_Node_Data(2,:) - x_FEM_di) > 1e-5) &...
%                                  (abs(Corner_Node_Data(3,:) - y_FEM_di) < 0.5*Distance_Node_Above_FEM_di));
% end

%Fit a straight line through the points that are close to the start of the
%damage
Ini_del_x = Corner_Node_Data(2,Pos_Nodes_Close_to_di(1)) - Corner_Node_Data(2,Pos_Nodes_Close_to_di(2));
Ini_del_y = Corner_Node_Data(3,Pos_Nodes_Close_to_di(1)) - Corner_Node_Data(3,Pos_Nodes_Close_to_di(2));
Ini_Gradient = Ini_del_y/Ini_del_x;
Ini_Constant = y_FEM_di - Ini_Gradient*x_FEM_di;
Ini_X = [-0.5 0.5];
Ini_Y = Ini_Gradient*Ini_X + Ini_Constant;
if x_di > 0
    Distance_Edge_Node = sqrt((Ini_X(2) - Corner_Node_Data(2,:)).^2 + (Ini_Y(2) - Corner_Node_Data(3,:)).^2);
else
    Distance_Edge_Node = sqrt((Ini_X(1) - Corner_Node_Data(2,:)).^2 + (Ini_Y(1) - Corner_Node_Data(3,:)).^2);
end
[Min,Pos_Edge_Node_Line] = min(Distance_Edge_Node);
del_x = Corner_Node_Data(2,Pos_Edge_Node_Line) - x_FEM_di;
del_y = Corner_Node_Data(3,Pos_Edge_Node_Line) - y_FEM_di;
Gradient = del_y/del_x;
Constant = y_FEM_di - Gradient*x_FEM_di;
X = [-0.5 0.5];
Y = Gradient*X + Constant;
Sweep_Angle = abs(atan(Gradient));
Sweep_Angle_Deg = Sweep_Angle*180/pi;
if upper(Sweep_Ans) == 'Y'
    disp(['The sweep angle of the damaged area is equal to ',num2str(Sweep_Angle_Deg,6),' degrees']);
end

%Create the damaged area from damage area definition parameters
%Locate the top corner opposite the initiation position
X_at_ld = x_FEM_di + ld;
Y_at_ld = Gradient*X_at_ld + Constant;
Distance = sqrt((X_at_ld - Corner_Node_Data(2,:)).^2 + (Y_at_ld - Corner_Node_Data(3,:)).^2);
[Min_Distance,Pos_Min_Distance] = min(Distance);
X_FEM_at_ld = Corner_Node_Data(2,Pos_Min_Distance);
Y_FEM_at_ld = Corner_Node_Data(3,Pos_Min_Distance);

%Locate the bottom corner underneath the initiation position
Y_at_hdr = y_FEM_di - hdr;
X_at_hdr = x_FEM_di;
Distance = sqrt((X_at_hdr - Corner_Node_Data(2,:)).^2 + (Y_at_hdr - Corner_Node_Data(3,:)).^2);
[Min_Distance,Pos_Min_Distance] = min(Distance);
X_FEM_at_hdr = Corner_Node_Data(2,Pos_Min_Distance);
Y_FEM_at_hdr = Corner_Node_Data(3,Pos_Min_Distance);

%Locate the bottom corner at the farthest end
Y_at_hdt = Y_FEM_at_ld - hdt;
X_at_hdt = X_FEM_at_ld;
Distance = sqrt((X_at_hdt - Corner_Node_Data(2,:)).^2 + (Y_at_hdt - Corner_Node_Data(3,:)).^2);
[Min_Distance,Pos_Min_Distance] = min(Distance);
X_FEM_at_hdt = Corner_Node_Data(2,Pos_Min_Distance);
Y_FEM_at_hdt = Corner_Node_Data(3,Pos_Min_Distance);
Damage_Corner_Nodes = [x_di X_at_hdr X_at_hdt X_at_ld;y_di Y_at_hdr Y_at_hdt Y_at_ld];

%Locate the elements that are inside the damaged area
%First locate the elements that is in the x bound
x_Bound = sort([x_FEM_di X_FEM_at_ld]);
Pos_Nodes_Inside_x_Bound = find((Corner_Node_Data(2,:) > x_Bound(1)) & (Corner_Node_Data(2,:) < x_Bound(2)) & ...
                               abs(Corner_Node_Data(2,:) - x_Bound(1)) > 1e-5 & ...
                               abs(Corner_Node_Data(2,:) - x_Bound(2)) > 1e-5);
Nodes_Inside_x_Bound = Corner_Node_Data(:,Pos_Nodes_Inside_x_Bound);

%Fit straight lines for the y bounds
del_x_Top = x_FEM_di - X_FEM_at_ld;
del_y_Top = y_FEM_di - Y_FEM_at_ld;
Gradient_Top = del_y_Top/del_x_Top;
Constant_Top = y_FEM_di - Gradient_Top*x_FEM_di;
del_x_Bot = X_FEM_at_hdr - X_FEM_at_hdt;
del_y_Bot = Y_FEM_at_hdr - Y_FEM_at_hdt;
Gradient_Bot = del_y_Bot/del_x_Bot;
Constant_Bot = Y_FEM_at_hdr - Gradient_Bot*X_FEM_at_hdr;

Count = 0;
for ii = 1:length(Nodes_Inside_x_Bound)
    X_Top = Nodes_Inside_x_Bound(2,ii);
    X_Bot = X_Top;
    Y_Top = Gradient_Top*X_Top + Constant_Top;
    Y_Bot = Gradient_Bot*X_Bot + Constant_Bot;
    if (Nodes_Inside_x_Bound(3,ii) > Y_Bot) & (Nodes_Inside_x_Bound(3,ii) < Y_Top) &...
       abs(Nodes_Inside_x_Bound(3,ii) - Y_Bot) > 1e-5 & abs(Nodes_Inside_x_Bound(3,ii) - Y_Top) > 1e-5
        Count = Count + 1;
        Nodes_Inside_Damage(:,Count) = Nodes_Inside_x_Bound(:,ii);
    end
end
```

Appendix A: MATLAB scripts

```
%The elements inside the damaged area are extracted
Count = 0;
for ii = 1:length(Nodes_Inside_Damage)
    for jj = 1:4
        Pos = find(Element_Data(2+jj,:) == Nodes_Inside_Damage(1,ii));
        if isempty(Pos) == 0
            Count = Count + 1;
            Elements_Inside_Damage_Pos(Count) = Pos;
        end
    end
end
Elements_Inside_Damage_Original = Element_Data(:,Elements_Inside_Damage_Pos);

%Eliminate the duplicates in Elements_Inside_Damage
Count = 0;
Elements_Inside_Damage(:,1) = Elements_Inside_Damage_Original(:,1);
for ii = 2:size(Elements_Inside_Damage_Original,2)
    Count_Unequal = 0;
    for jj = 1:size(Elements_Inside_Damage,2);
        if Elements_Inside_Damage_Original(1,ii) ~= Elements_Inside_Damage(1,jj)
            Count_Unequal = Count_Unequal + 1;
        end
    end
    if Count_Unequal == size(Elements_Inside_Damage,2)
        Count = Count + 1;
        Elements_Inside_Damage(:,Count) = Elements_Inside_Damage_Original(:,ii);
    end
end

%Calculate the measurement nodes
Interp_Right = linspace(Corner_Node_Data_Sort(Measurement_Row,1,2),...
                        Corner_Node_Data_Sort(Measurement_Row,Fuselage_Pos(1),2),N_Wing_FEM_Measurements);
Interp_Left = linspace(Corner_Node_Data_Sort(Measurement_Row,Fuselage_Pos(end),2),...
                       Corner_Node_Data_Sort(Measurement_Row,end,2),N_Wing_FEM_Measurements);
Interp_Middle = linspace(Corner_Node_Data_Sort(Measurement_Row,Fuselage_Pos(1),2),...
                         Corner_Node_Data_Sort(Measurement_Row,Fuselage_Pos(end),2),N_Fuselage_FEM_Measurements);
for ii = 1:length(Interp_Right)
    Distance_Right = abs(Interp_Right(ii) - Corner_Node_Data_Sort(Measurement_Row,:,2));
    [Min,Pos_Distance_Right(ii)] = min(Distance_Right);
    Distance_Left = abs(Interp_Left(ii) - Corner_Node_Data_Sort(Measurement_Row,:,2));
    [Min,Pos_Distance_Left(ii)] = min(Distance_Left);
end
Node_Measured_Right = Corner_Node_Data_Sort(Measurement_Row,Pos_Distance_Right(2:end-1),1);
Location_Node_Measured_Right = squeeze(Corner_Node_Data_Sort(Measurement_Row,Pos_Distance_Right(2:end-1),2:3));
Node_Measured_Left = Corner_Node_Data_Sort(Measurement_Row,Pos_Distance_Left(2:end-1),1);
Location_Node_Measured_Left = squeeze(Corner_Node_Data_Sort(Measurement_Row,Pos_Distance_Left(2:end-1),2:3));
for ii = 1:length(Interp_Middle)
    Distance_Middle = abs(Interp_Middle(ii) - Corner_Node_Data_Sort(Measurement_Row,:,2));
    [Min,Pos_Distance_Middle(ii)] = min(Distance_Middle);
end

%Calculate the gradient to calculate the angle through which the xy-axis
%should be rotated to find the x1y1-axis strain values
del_x_Right = Location_Node_Measured_Right(1,1) - Location_Node_Measured_Right(end,1);
del_y_Right = Location_Node_Measured_Right(1,2) - Location_Node_Measured_Right(end,2);
del_x_Left = Location_Node_Measured_Left(1,1) - Location_Node_Measured_Left(end,1);
del_y_Left = Location_Node_Measured_Left(1,2) - Location_Node_Measured_Left(end,2);
Gradient_Right = del_y_Right/del_x_Right;
Gradient_Left = del_y_Left/del_x_Left;
Theta_Right = atan(Gradient_Right);
Theta_Left = atan(Gradient_Left);

Node_Measured_Middle = Corner_Node_Data_Sort(Measurement_Row,Pos_Distance_Middle(2:end-1),1);
Measured_Nodes = [Node_Measured_Right Node_Measured_Middle Node_Measured_Left];

%The elements inside the damaged area are extracted
Count = 0;
for ii = 1:length(Measured_Nodes)
    for jj = 1:4
        Pos = find(Element_Data(2+jj,:) == Measured_Nodes(ii));
        if isempty(Pos) == 0
            Count = Count + 1;
            Measured_Elements_Pos(Count) = Pos;
        end
    end
end
Measured_Elements_Data = Element_Data(:,Measured_Elements_Pos);

%The finite element mesh is plotted for graphical conformation that the
%correct elements has been selected for the level of damage
if nargin < 10
    figure(1)
    clf;
else
    Figure_Count = Figure_Count + 1;
    figure(Figure_Count);
    clf;
end
% subplot(2,1,1)
set(gca,'FontSize',14);
hold on

%Find nodes 8045 (accelerometer), 4287 (excitation), 2731 and 5397
%(suspension)
Count = 0;
for ii = 1:size(Corner_Node_Data_Sort,1)
    for jj = 1:size(Corner_Node_Data_Sort,2)
        if Corner_Node_Data_Sort(ii,jj,1) == 8045
            Acc_Row_Pos = ii;
            Acc_Column_Pos = jj;
            Acceleration_X_Loc = Corner_Node_Data_Sort(ii,jj,2);
            Acceleration_Y_Loc = Corner_Node_Data_Sort(ii,jj,3);
```

```
        end
        if Corner_Node_Data_Sort(ii,jj,1) == 2731 | Corner_Node_Data_Sort(ii,jj,1) == 5397
            Count = Count + 1;
            Susp_Row_Pos(Count) = ii;
            Susp_Column_Pos(Count) = jj;
            Susp_X_Loc(Count) = Corner_Node_Data_Sort(ii,jj,2);
            Susp_Y_Loc(Count) = Corner_Node_Data_Sort(ii,jj,3);
        end
    end
end

%Plot the FE model
for ii = 1:N_Elem
    Element_No = Element_Data(1,ii);
    Corner_Nodes = Element_Data(3:6,ii);
    for jj = 1:4
        Pos(jj) = find(Corner_Node_Data(1,:) == Corner_Nodes(jj));
    end
    Corner_Nodes_x = Corner_Node_Data(2,Pos);
    Corner_Nodes_y = Corner_Node_Data(3,Pos);
    patch(Corner_Nodes_x,Corner_Nodes_y,'b');%,'FaceColor','none');
end

%Plot the damaged area
for ii = 1:length(Elements_Inside_Damage_Pos)
    Element_No = Element_Data(1,Elements_Inside_Damage_Pos(ii));
    Corner_Nodes = Element_Data(3:6,Elements_Inside_Damage_Pos(ii));
    for jj = 1:4
        Pos(jj) = find(Corner_Node_Data(1,:) == Corner_Nodes(jj));
    end
    Corner_Nodes_x = Corner_Node_Data(2,Pos);
    Corner_Nodes_y = Corner_Node_Data(3,Pos);
    patch(Corner_Nodes_x,Corner_Nodes_y,'r');%'c');
end

xlabel('x-axis distance [m]');
ylabel('y-axis distance [m]');
axis equal
grid on

set(gca,'LineWidth',1);
hold off
```

The function *Wing_area_calculation.m* is recalled by the main program and is used to calculate the wing area by implementing equations 2.18 and 2.19.

```
function [Ratio_Dam_Wing,Ratio_Dam_Tot,Damaged_Area] = Wing_area_calculation(ld,hdr,hdt)

%This function will be used to calculate the are of the two wing sections
%and the total area of the family of wings. The area of the damage will be
%calculated and will be expressed as a percentage of the wing and total
%areas.
%
%The input to the function is defined as follows:
%
%ld  - The length of the damage
%hdr - The height of the damage at the root
%hdt - The height of the damage at the tip
%
%The output of the function is defined as follows:
%
%Ratio_Dam_Wing - The ratio of the damage to the left or right wing
%Ratio_Dam_Tot  - The ratio of the damage to the complete wing

%Recall the other contacts
[N_Elem,N_Nodes,Node_Measured_Right,Node_Measured_Middle,Node_Measured_Left,b,lf,lw,cr,ct] = Constants;

%Define the constants defining the damage area and the wing area
Dam_btrap = hdt;
Dam_btria = hdr-hdt;
Dam_h = ld;
if cr > ct
    b_trap = ct;
    b_tria = cr-ct;
else
    b_trap = cr;
    b_tria = ct-cr;
end
h = lw;

%Calculate the respective areas
Damaged_Area = abs(0.5*Dam_h*Dam_btria + Dam_h*Dam_btrap);
Wing_Area = abs(0.5*h*b_tria + h*b_trap);
Total_Area = abs(2*Wing_Area + lf*cr);

%Calculate the percentage area consumed by the damaged area with respect to
%the wing area and the total area
Ratio_Dam_Wing = Damaged_Area/Wing_Area*100;
Ratio_Dam_Tot = Damaged_Area/Total_Area*100;
disp(['The percentage damaged area with respect to the wing area is  ',num2str(Ratio_Dam_Wing),'%']);
disp(['The percentage damaged area with respect to the total area is ',num2str(Ratio_Dam_Tot),'%']);
disp(['The damaged area is equal to ',num2str(Damaged_Area,8),' m^2']);
```

A.2 Script to calculate the relevant damage indicator values

The second main program is used to calculate the SCDF and SFDL values for the different cases and will be referred to as the *Parameter_Calculation_Stochastic.m* algorithm.

```
clc;
close all;
clear all;

%This program will be used to load the different damage cases generated
%from the stochastic analyses that were performed in Nastran.m and compute
%the yCDF, SCDF and the DI values. It compares the natural frequencies
%before and after damage to each other. It will also be used to calculate
%the parameter, to visualise the effect of the damage on it. It uses the
%READ_NODES_LOCATION function to etract the XYZ-positions of the nodes.

Answer_Plot_Area = input('Do you want to plot the damaged area? ((Y)es/(N)o) ','s');
Answer_Plot_SCDF = input('Do you want to plot the yCDF and SCDF? ((Y)es/(N)o) ','s');
Answer_Plot_DIvsDI = input('Do you want to plot the SFDL vs SFDL from yCDF comparison ((Y)es/((N)o) ','s');
Answer_Cases = input('What cases would you like to compare? (1 - Damage inside, 2 - Damage outside, 3 - Both) ','s');
disp(' ');

Figure_Count = 0;
Sweep_Ans = 'N';
Count = 0;
%For loop over all the damaged cases
for Run_No = 1:1%200
    disp(['THIS INFORMATION IS FOR RUN NUMBER ',num2str(Run_No)]);
    disp('------------------------------------------------------------');
    disp('------------------------------------------------------------');
    disp(' ');

    %The constants that is applicable to this FE model
    [N_Elem,N_Nodes] = Constants;

    %The undamaged and damage strain values at the measurement locations are
    %loaded and the frequencies and strains are stored for use later on
%     File_Location = 'D:\Nagraads\Meesters\Matlab codes\Predator .mat files for the discrete cases\';
    File_Location = 'D:\Nagraads\Meesters\Matlab codes\Stochastic simulations\12 Wing sensors\';
    Mat_File = [File_Location,'Predator_Stochastic_No_Damage.mat'];
%     Mat_File = [File_Location,'Predator_FRF_test_no_damage.mat'];
%     Mat_File = [File_Location,'Predator_FRF_no_damage.mat'];
%     Mat_File = [File_Location,'Predator_FRF_orig_damp_no_damage'];
%     File_Location = 'D:\Nagraads\Meesters\Matlab codes\Predator .mat files for the discrete cases\Hex mesh comparison\No
Damage\';
%     Mat_File = [File_Location,'Predator_Hex_No_Damage.mat'];
    load(Mat_File);

    %The undamaged frequencies and strains are declared as variables, otherwise
    %there will be a conflict with the damaged variables
    Undamaged_Freq = Patran_Ana_Nat_Freq(NF_Mode_Numbers);
%     Undamaged_Strain_x1 = MStrain_x1_NF_Loc;
    Undamaged_Strain_x1 = MStrain_x1_NF_Loc_Normalised;

    %Specify the amount of damage for the correct mat file to be loaded
    Mat_File = [File_Location,'Predator_Stochastic_12_Sensors_Damage_Case',num2str(Run_No)];
%     Mat_File = [File_Location,'Predator_FRF_damage_case_test',num2str(Run_No),'0'];
%     Mat_File = [File_Location,'Predator_FRF_damage_case3_',num2str(Run_No),'0.mat'];
%     File_Location = 'D:\Nagraads\Meesters\Matlab codes\Predator .mat files for the discrete cases\Hex mesh comparison\50%
Damage\';
%     Mat_File = [File_Location,'Predator_Hex_50_Damage.mat'];
    load(Mat_File);

    Run_Program = 0;
    if Answer_Cases == '1' & Measure_Loc_Inside_Damage == 1
        Run_Program = 1;
    elseif Answer_Cases == '2' & Measure_Loc_Inside_Damage == 0 %& Damaged_Thickness < 0.0095
        Run_Program = 1;
    elseif Answer_Cases == '3'
        Run_Program = 1;
    end

    if Run_Program == 1
        Count = Count + 1;
        if upper(Answer_Plot_Area) == 'Y'
            %Recreate the damaged position and plot it to verify the location of
            %the damage
            File = 'D:\Nagraads\Meesters\Patran FEM\FEM models\Predator wing\Predator_parametric_wing_Original.bdf';

[Node_Measured_Left,Node_Measured_Middle,Node_Measured_Right,Measured_Elements_Data,Elements_Inside_Damage,Damage_Corner_Node
s,Theta_Right,Theta_Left,Figure_Count] = ...;

Damaged_Area_Elements(N_Wing_Measurement,N_Fuselage_Measurement,Measurement_Row,File,ldi,hdi,ld,hdr,hdt,Figure_Count,Sweep_An
s);
        end

        %The damaged frequencies and strains are declared as variables, otherwise
        %there will be a conflict with the undamaged variables
        Damaged_Freq = Patran_Ana_Nat_Freq(NF_Mode_Numbers);
%         Damaged_Strain_x1 = MStrain_x1_NF_Loc;
```

```
        Damaged_Strain_x1 = MStrain_x1_NF_Loc_Normalised;

        %The SCDF is calculated directly from the strain measurements
        Measured_Nodes = [Node_Measured_Right Node_Measured_Middle Node_Measured_Left]; %The nodes at which measurements were
carried out

        %Extract the measurement x-locations
        File = 'D:\Nagraads\Meesters\Patran FEM\FEM models\Predator wing\Predator_parametric_wing_Original.bdf';
        [x_Loc,y_Loc] = Read_Elements_Node_Data(File,Measured_Nodes,N_Elem,N_Nodes);
        %Extract the family of wings' profile to superimpose on measurement
        %locations
        Data = dlmread('D:\Nagraads\Meesters\Patran FEM\FEM models\Predator wing\Model_Parameter_Predator_Wing_Nodes.txt');
        x = Data(1:13);
        y = Data(14:end);

        %The natural frequencies are compared to one another and the % change in
        %natural frequencies is determined
        Delta_Freq = abs(Undamaged_Freq - Damaged_Freq);
        Percentage_Delta_Freq = Delta_Freq./Undamaged_Freq*100;
        Spaces = '    ';
        for ii = 1:length(Undamaged_Freq)
            Damaged_Spaces_Vec(ii,:) = '   ';
            Undamaged_Spaces_Vec(ii,:) = '     ';
            Change_Spaces_Vec(ii,:) = '                  ';
            Percentage_Spaces_Vec(ii,:) = '       ';
        end
        disp(['Undamaged',Spaces,'Damaged',Spaces,'Change in Frequency',Spaces,'% Change']);
        disp([Damaged_Spaces_Vec,num2str(Undamaged_Freq,6),Undamaged_Spaces_Vec,num2str(Damaged_Freq,6),...
              Change_Spaces_Vec,num2str(Delta_Freq,6),Percentage_Spaces_Vec,num2str(Percentage_Delta_Freq,3)]);
        disp(' ');

        %Calculate the curvature from the strain measurement
        for N_Modes_CDF = 1:size(Undamaged_Strain_x1,1)
            for ii = 1:N_Modes_CDF %ii counts the modes used to calculate the CDF
                Undamaged_Curvature(ii,:) = -Undamaged_Strain_x1(ii,:);%Originally ./y;
                Damaged_Curvature(ii,:) = -Damaged_Strain_x1(ii,:);%Originally ./y;
%                 Damaged_Curvature(ii,8:9) = Damaged_Curvature(ii,8:9)./1.5;
            end

            %Calculate the CDF at each measurement location
            if N_Modes_CDF == 1
                yCDF(N_Modes_CDF,:) = (abs(abs(Undamaged_Curvature)-abs(Damaged_Curvature)))/N_Modes_CDF;
            else
                yCDF(N_Modes_CDF,:) = sum(abs(abs(Undamaged_Curvature)-abs(Damaged_Curvature)))/N_Modes_CDF;
            end

            %Calculate the SCDF at each measurement location
            if N_Modes_CDF == 1
                Averaged_Strain = abs(Damaged_Strain_x1(1:N_Modes_CDF,:))/N_Modes_CDF; %Have the measured vertical strains
averaged
%                 Averaged_Strain = abs(Undamaged_Strain_x1(1:N_Modes_CDF,:))/N_Modes_CDF; %Have the measured vertical
strains averaged
            else
                Averaged_Strain = sum(abs(Damaged_Strain_x1(1:N_Modes_CDF,:)))/N_Modes_CDF; %Have the measured vertical
strains averaged
%                 Averaged_Strain = sum(abs(Undamaged_Strain_x1(1:N_Modes_CDF,:)))/N_Modes_CDF; %Have the measured vertical
strains averaged
            end
            SCDF(N_Modes_CDF,:) = yCDF(N_Modes_CDF,:)./Averaged_Strain;

            %The parameter, SFDL, is calculated
            SCDF_rms = sqrt(sum(SCDF(N_Modes_CDF,:).^2)/size(SCDF,2));
            yCDF_rms = sqrt(sum(yCDF(N_Modes_CDF).^2)/size(yCDF,2));
            Averaged_Delta_Freq(N_Modes_CDF,1) = sum(Percentage_Delta_Freq(1:N_Modes_CDF))/N_Modes_CDF;
            DI(N_Modes_CDF,1) = SCDF_rms*Averaged_Delta_Freq(N_Modes_CDF,1);
            DI_yCDF(N_Modes_CDF,1) = yCDF_rms*Averaged_Delta_Freq(N_Modes_CDF,1);
        %     disp(' ');
        %     disp(['The value of the yCDF_rms at ',num2str(N_Modes_CDF),' number of modes is
',num2str(yCDF_rms(N_Modes_CDF),8)]);
        %     disp(['The value of the DI at       ',num2str(N_Modes_CDF),' number of modes is ',num2str(DI(N_Modes_CDF),8)]);
        end

        Averaged_Delta_Freq_Complete(Count,1) = Averaged_Delta_Freq(end,1);

        %Calculate the area of the damage to be saved with the SFDL values
        [Ratio_Dam_Wing,Ratio_Dam_Tot,Damaged_Area] = Wing_area_calculation(ld,hdr,hdt);

        %Keep the calculated SFDL values
        DI_Cases(:,Count) = [Count;Damaged_Area;Damaged_Thickness;Measure_Loc_Inside_Damage;DI];
        DI_Cases_yCDF(:,Count) = [Count;Damaged_Area;Damaged_Thickness;Measure_Loc_Inside_Damage;DI_yCDF];


        %Create a variable to save the SCDF graph for 6 modes
        SCDF_Tot(Run_No,:) = SCDF(end,:);
        x_Loc_Tot = x_Loc;

        %Save the *.mat file for the deterministic cases
        save(Mat_File,'Freq','Strain_x1','Node_Measured_Right','Node_Measured_Middle',...
                      'Node_Measured_Left','MStrain_x1_NF_Loc',...
                      'Damage_Corner_Nodes','Damaged_Thickness','Elements_Inside_Damage',...
                      'Measured_Elements_Data','Measured_Nodes','Measurement_Row',...
                      'NF_Mode_Numbers','N_Fuselage_Measurement','N_Wing_Measurement',...
                      'Theta_Right','Theta_Left','hdi','hdr','hdt','ldi','ld','DI','yCDF_rms',...
                      'SCDF_rms','Averaged_Delta_Freq','Measure_Loc_Inside_Damage',...
                      'Ana_Nat_Freq','MStrain_Freq_NF_Loc','NF_Strain_x1',...
                      'Patran_Ana_Nat_Freq','Patran_NF_Pos','Ana_Acc_Z','Ana_FRF_Freq',...
                      'Strain_x1_Normalised','MStrain_x1_NF_Loc_Normalised','SCDF');

        disp('------------------------------------------------------------');
        disp(' ');

        clear Averaged_Delta_Freq Averaged_Strain Change_Spaces_Vec DI Data Damage_Corner_Nodes Damaged_Curvature ...
```

```
            Damaged_Freq Damaged_Spaces_Vec Damaged_Strain_x1 Damaged_Thickness Data Delta_Freq ...
            Elements_Inside_Damage File File_Location Freq ii MStrain_x1_NF_Loc Mat_File Mat_File_No_Damage ...
            Measured_Elements_Data Measured_Nodes Measurement_Row NF_Mode_Numbers N_Elem N_Fuselage_Measurement ...
            N_Modes_CDF N_Nodes N_Wing_Measurement Nat_Freq_Pos Node_Measured_Left Node_Measured_Middle ...
            Node_Measured_Right Percentage_Delta_Freq Percentage_Spaces_Vec SCDF SCDF_rms Spaces Strain_x1 ...
            Theta_Right Theta_Left Undamaged_Curvature Undamaged_Freq Undamaged_Spaces_Vec ...
            Undamaged_Strain_x1 hdi hdr hdt ld ldi wn x x_Loc y yCDF yCDF_rms y_Loc Ratio_Dam_Wing ...
            Ratio_Dam_Tot Damaged_Area Theta_Left Measure_Loc_Inside_Damage Ana_NF_Fit_Mag_Avg Ana_Nat_Freq ...
            DI_yCDF MStrain_Freq_NF_Loc NF_Strain_x1 Patran_Ana_Nat_Freq Patran_NF_Pos Ana_Acc_Z ...
            Ana_FRF_Freq MStrain_x1_NF_Loc_Normalised Strain_x1_Normalised
    end
end

%Compute curve fits to the graph that relates the DI values to the average
%difference in natural frequencies
Avg_Del_Freq_Curve_Fit = linspace(0,max(Averaged_Delta_Freq_Complete),5000);

%Fit the exponential curve (y = be^(ax)) only when the damage include one
%measurement location
Count = 0;
DI_Cases_Inside = [];
for ii = 1:size(DI_Cases,2)
    if DI_Cases(4,ii) == 1
        Count = Count + 1;
        DI_Cases_Inside(:,Count) = DI_Cases(:,ii);
        Averaged_Delta_Freq_Complete_Inside(Count,:) = Averaged_Delta_Freq_Complete(ii,:);
    end
end

%Exponential fit y = be^(ax)
if ~(isempty(DI_Cases_Inside))
    Fit_Type1 = fittype('b*exp(a*x)','coeff',{'b','a'});
    Fit_Opt1 = fitoptions('Method','NonLinearLeastSquares','Lower',[-Inf -Inf],'Upper',[Inf Inf],'StartPoint',[2.e-03 9.e-
02]);
    [FittedModel1,Goodness1] = fit(Averaged_Delta_Freq_Complete_Inside(:,end),DI_Cases_Inside(end,:)',Fit_Type1,Fit_Opt1);
    a1 = FittedModel1.a;
    b1 = FittedModel1.b;
    DI_Est_1 = b1*exp(a1*Avg_Del_Freq_Curve_Fit);
    r1 = Goodness1.rsquare;
end

%Fit the exponential curve (y = bx^(a)) only when the damage exclude all
%the measurement location
Count = 0;
DI_Cases_Outside = [];
for ii = 1:size(DI_Cases,2)
    if DI_Cases(4,ii) == 0
        Count = Count + 1;
        DI_Cases_Outside(:,Count) = DI_Cases(:,ii);
        Averaged_Delta_Freq_Complete_Outside(Count,:) = Averaged_Delta_Freq_Complete(ii,:);
    end
end

%Exponential fit y = bx^(a)
if ~(isempty(DI_Cases_Outside))
    Fit_Type2 = fittype('b*x^a','coeff',{'b','a'});
    Fit_Opt2 = fitoptions('Method','NonLinearLeastSquares','Lower',[-Inf -Inf],'Upper',[Inf Inf],'StartPoint',[1e-05 2]);
    [FittedModel2,Goodness2] = fit(Averaged_Delta_Freq_Complete_Outside(:,end),DI_Cases_Outside(end,:)',Fit_Type2,Fit_Opt2);
    a2 = FittedModel2.a;
    b2 = FittedModel2.b;
    DI_Est_2 = b2*(Avg_Del_Freq_Curve_Fit).^a2;
    r2 = Goodness2.rsquare;
end

if upper(Answer_Plot_DIvsDI) == 'Y'
    y3 = DI_Cases(end,:);
    x3 = DI_Cases_yCDF(end,:);
    n = length(x3);
    DI_yCDF_Est = linspace(0,max(x3),5000);
    if ~(isempty(DI_Cases_Outside))
        %Linear fit y = ax + b for the DI computed from the yCDF and the SCDF
        a3_est = (n*sum(x3.*y3) - sum(x3)*sum(y3)) / (n*sum(x3.^2) - (sum(x3))^2);
        Fit_Type3 = fittype('a*x','coeff',{'a'});
        Fit_Opt3 = fitoptions('Method','NonLinearLeastSquares','Lower',-Inf,'Upper',Inf,'StartPoint',a3_est);
        [FittedModel3,Goodness3] = fit(DI_Cases_yCDF(end,:)',DI_Cases(end,:)',Fit_Type3,Fit_Opt3);
        a3 = FittedModel3.a;
        b3 = 0;
        DI_Est_3 = a3*(DI_yCDF_Est) + b3;
        r3 = Goodness3.rsquare;
    else
        %Exponential fit y = b*exp(a*x)
        y5 = log(DI_Cases(end,:));
        x5 = DI_Cases_yCDF(end,:);
        n = length(x5);
        lnb = (sum(x5.^2)*sum(y5) - sum(x5.*y5)*sum(x5)) / (n*sum(x5.^2) - (sum(x5))^2);
        b5_est = exp(lnb);
        a5_est = (n*sum(x5.*y5) - sum(x5)*sum(y5)) / (n*sum(x5.^2) - (sum(x5))^2);
        Fit_Type5 = fittype('b*exp(a*x)','coeff',{'b','a'});
        Fit_Opt5 = fitoptions('Method','NonLinearLeastSquares','Lower',[-Inf -Inf],'Upper',[Inf Inf],'StartPoint',[b5_est
a5_est]);
        [FittedModel5,Goodness5] = fit(DI_Cases_yCDF(end,:)',DI_Cases_Inside(end,:)',Fit_Type5,Fit_Opt5);
        a5 = FittedModel5.a;
        b5 = FittedModel5.b;
        DI_Est_5 = b5*exp(a5*DI_yCDF_Est);
        r5 = Goodness5.rsquare;
        Fit_Type6 = fittype('a*x*x+b*x','coeff',{'a','b'});
        Fit_Opt6 = fitoptions('Method','NonLinearLeastSquares','Lower',[-Inf -Inf],'Upper',[Inf Inf],'StartPoint',[3e18
3e07]);
        [FittedModel6,Goodness6] = fit(DI_Cases_yCDF(end,:)',DI_Cases_Inside(end,:)',Fit_Type6,Fit_Opt6);
        a6 = FittedModel6.a;
        b6 = FittedModel6.b;
        DI_Est_6 = a6.*DI_yCDF_Est.^2+b6.*DI_yCDF_Est;
```

Appendix A: MATLAB scripts

```
        r6 = Goodness6.rsquare;
    end

    %Exponential fit y = bx^(a)
    y4 = log(DI_Cases(end,:));
    x4 = log(DI_Cases_yCDF(end,:));
    n = length(x4);
    lnb = (sum(x4.^2)*sum(y4) - sum(x4.*y4)*sum(x4)) / (n*sum(x4.^2) - (sum(x4))^2);
    b4_est = exp(lnb);
    a4_est = (n*sum(x4.*y4) - sum(x4)*sum(y4)) / (n*sum(x4.^2) - (sum(x4))^2);
    Fit_Type4 = fittype('b*x^a','coeff',{'b','a'});
    Fit_Opt4 = fitoptions('Method','NonLinearLeastSquares','Lower',[-Inf -Inf],'Upper',[Inf Inf],'StartPoint',[b4_est
a4_est]);
    [FittedModel4,Goodness4] = fit(DI_Cases_yCDF(end,:)',DI_Cases(end,:)',Fit_Type4,Fit_Opt4);
    a4 = FittedModel4.a;
    b4 = FittedModel4.b;
    DI_Est_4 = b4*(DI_yCDF_Est).^a4;
    r4 = Goodness4.rsquare;
end

%Calculate the damage percentage values
Damage_Percentage = (0.01 - DI_Cases(3,:))/0.01*100;
```

Appendix B: SCDF normalised with undamaged averaged strain values

In paragraphs 3.1.2.1 and 3.1.3.1, the scaling of the SFDL values was compared for two different calculation methods. For the first method the SCDF and subsequently the SFDL value were calculated from equation 2.10 and 2.11. It was stated that it might be possible to calculate the SCDF values from the difference in strain values divided by the undamaged strain values and this serves as the second method. The comparisons were made in the respective paragraphs, but the results for the second method were not shown. This appendix serves as a reference to the curves and curve fits obtained for the SFDL values calculated from the SCDF values when the difference is divided by the undamaged strain values.

The two deterministic cases of paragraphs 3.1.2.1 and 3.1.3.1 were used for the investigation. The curve fits obtained for the variation of the SFDL values with respect to the level of damage and average difference in natural frequency is shown in Figure B-1 and Figure B-2. The power law curve fits are used in Figure 3-12 to compare the scaling of the two calculation methods.

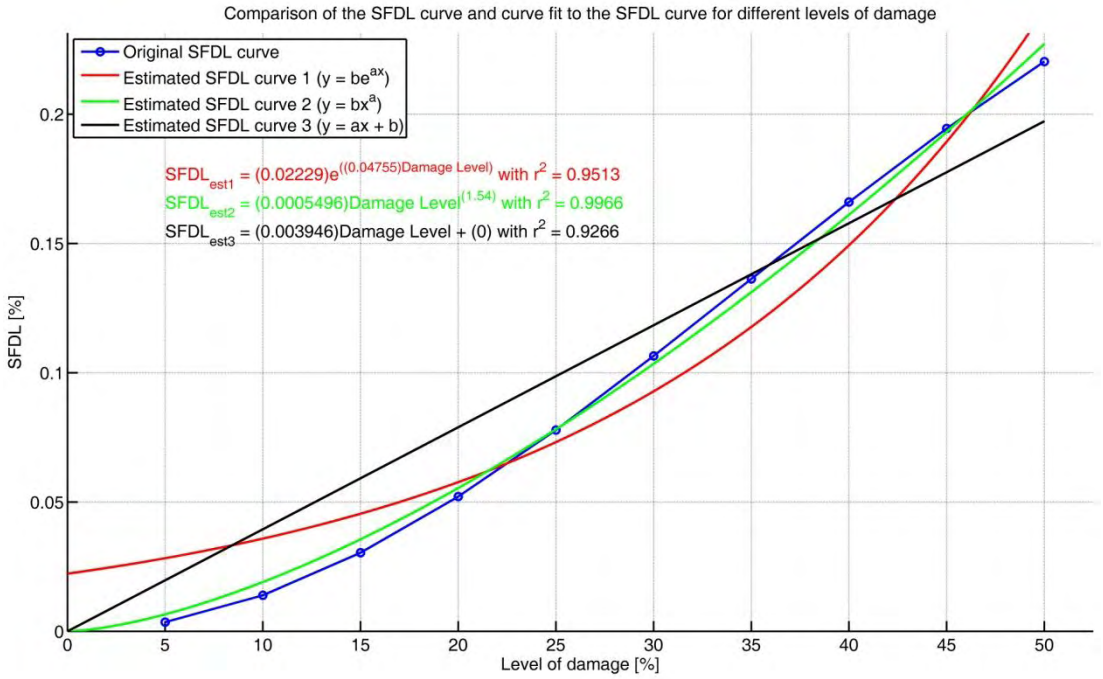

Figure B-1: Curve fits for the SFDL value compared to the level of damage for case 1 computed from the undamaged normalised SCDF

Appendix B: SCDF normalised with undamaged averaged strain values

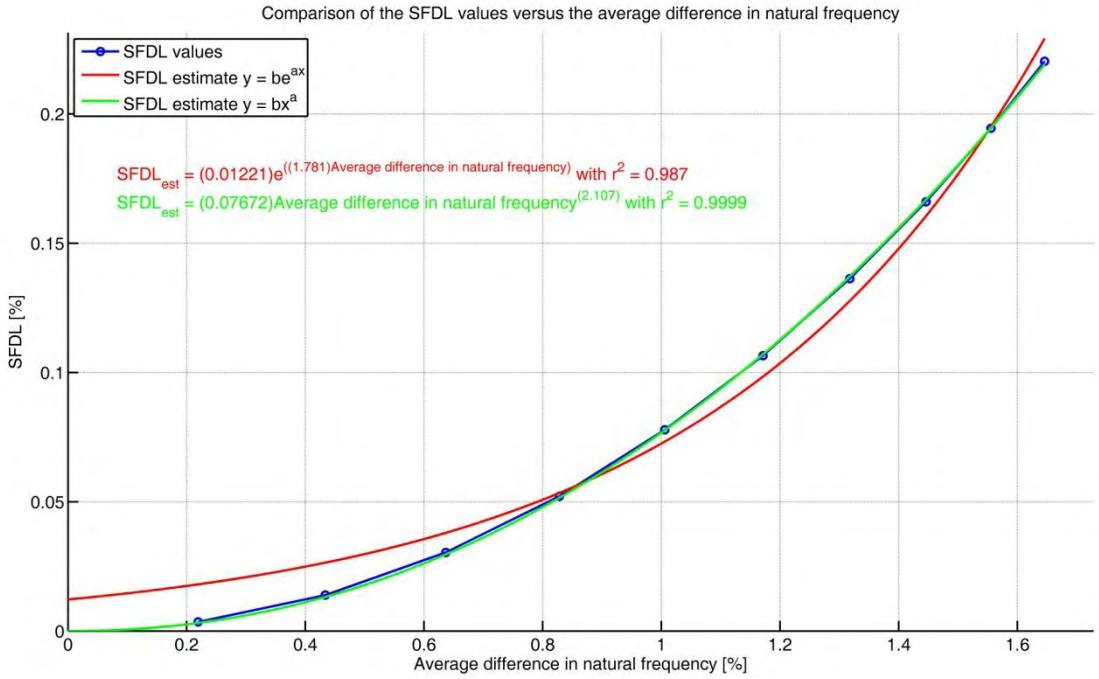

Figure B-2: Curve fits showing the relation between the SFDL value and the average difference in natural frequency for case 1 computed from the undamaged normalised SCDF

The same curve fits with respect to the damage level and average difference in natural frequency were made for the second deterministic case and is shown in Figure B-3 and Figure B-4, respectively. The power law curve fit of Figure B-3 and the exponential curve fit of Figure B-4 were used in the scaling comparison of Figure 3-23.

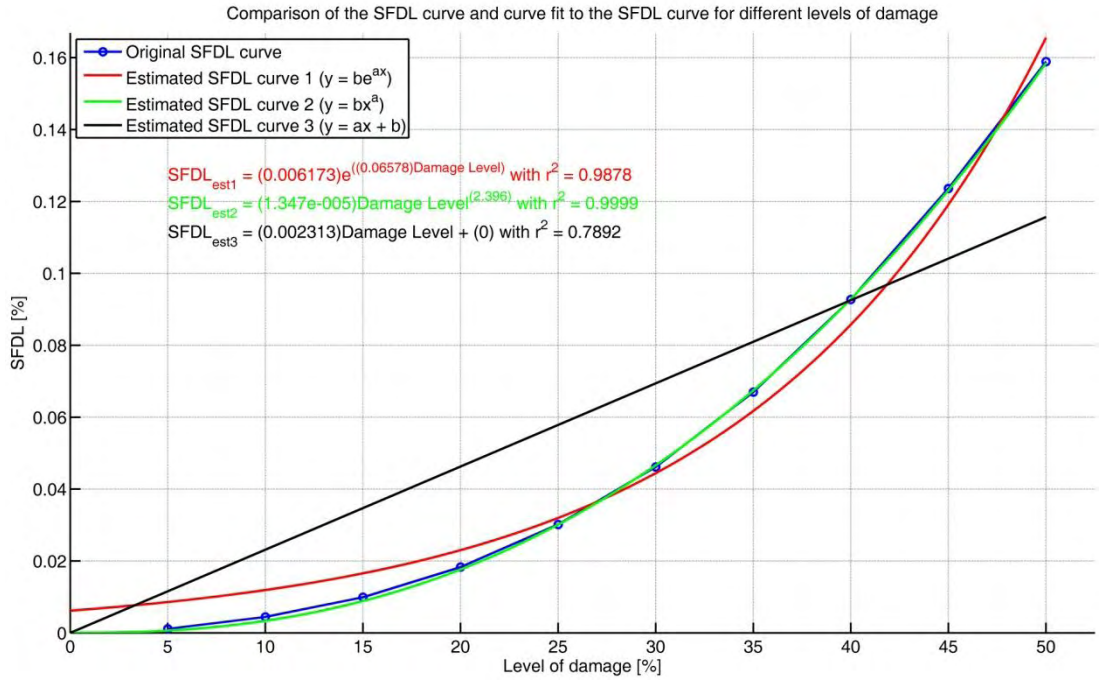

Figure B-3: Curve fits for the SFDL value compared to the level of damage for case 2 computed from the undamaged normalised SCDF

Appendix B: SCDF normalised with undamaged averaged strain values

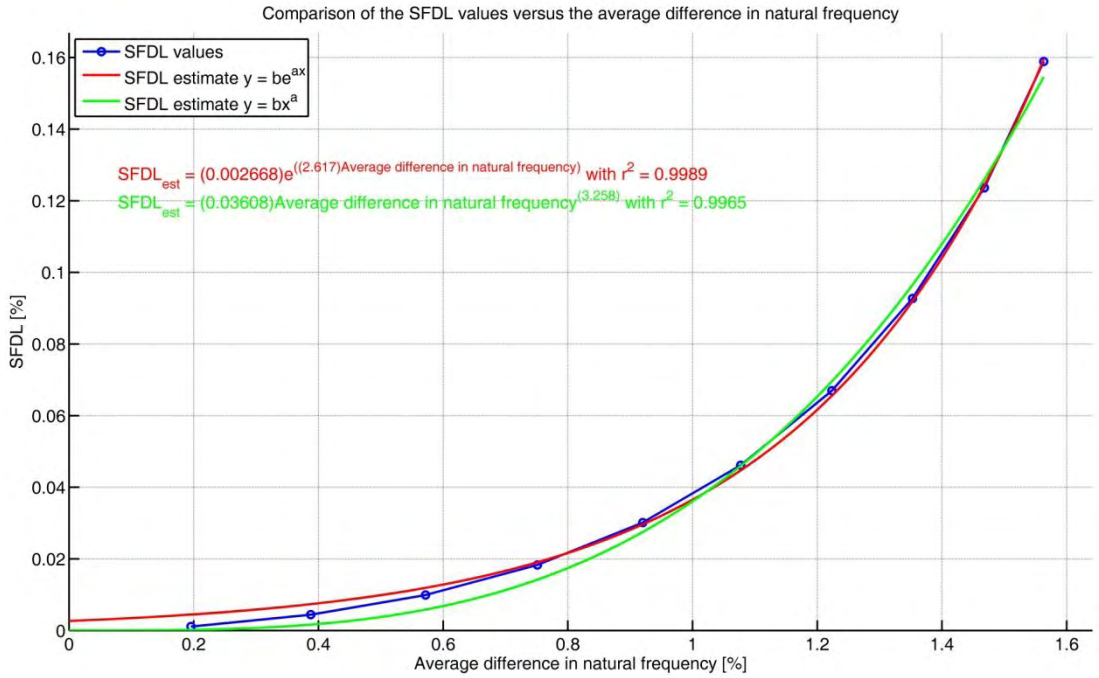

Figure B-4: Curve fits showing the relation between the SFDL value and the average difference in natural frequency for case 2 computed from the undamaged normalised SCDF

The best curve fits to the SFDL values for the two deterministic cases are compared to one another in Figure B-5. It is evident that when the damaged area encloses one or more measurement locations, the SFDL value increases gradually. The SFDL value scaled quicker when the difference in strain values was divided by the damage strain values as in the study in paragraph 3.4 and therefore this calculation is preferred.

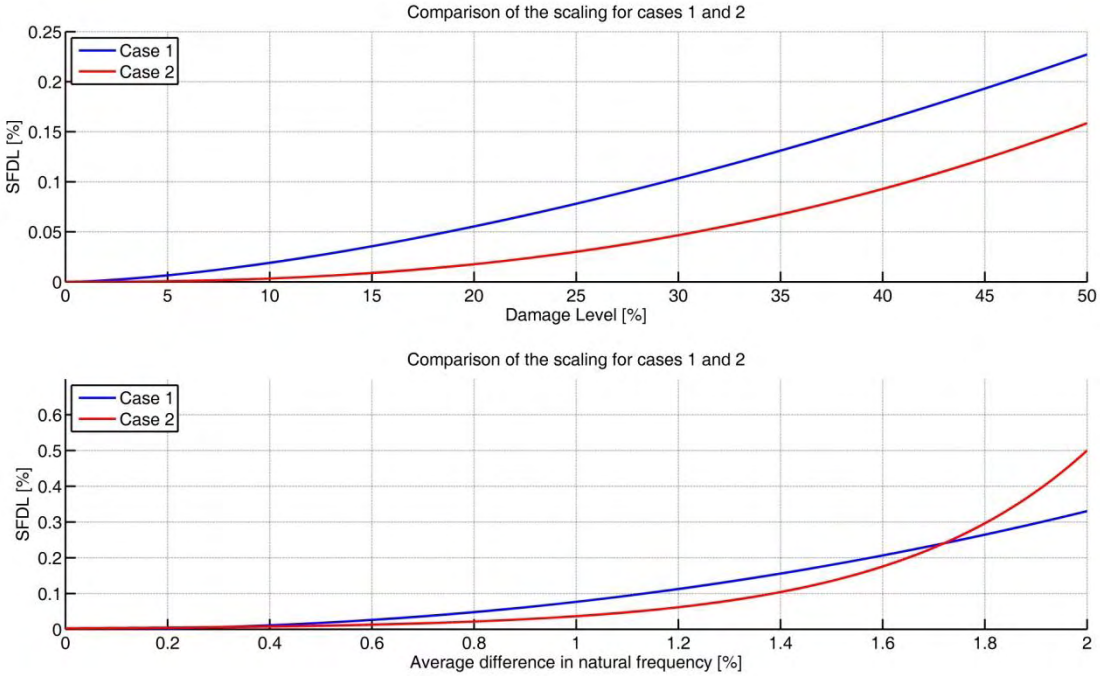

Figure B-5: Comparison the the SFDL value scaling for cases 1 and 2 with the SCDF normalised by the undamaged averaged strains

Appendix C: SFDL calculated from yCDF and SCDF

C.1 Deterministic case 1

If the yCDF and the SCDF plots appear to give the same form and can both indicate the location of the damage, the question arises why the yCDF is not used in the calculation of the SFDL value in stead of the SCDF value. This was explained in paragraph 1.3 and has to do with the relative scaling, but for interest sake these two parameters are compared in Figure C-1.

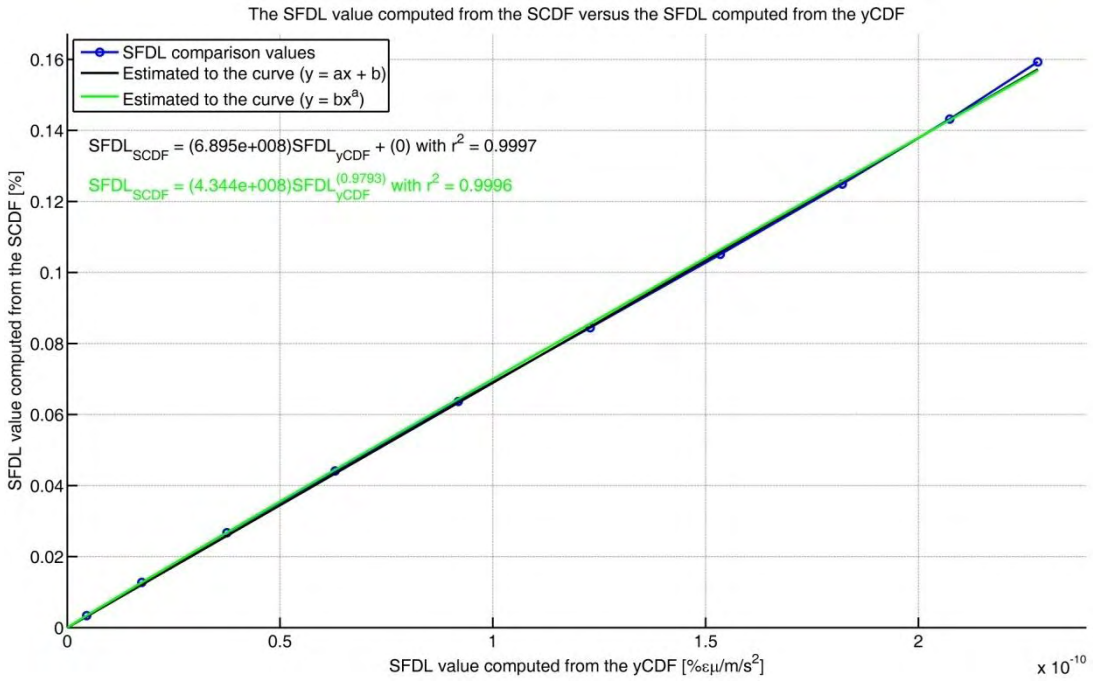

Figure C-1: Curve fits to the comparison between the SFDL values computed from the SCDF and the yCDF values for case 1

When the curve fits of Figure C-1 is examined, it can be seen that the SFDL value computed from the yCDF and SCDF appears to have a correlation through the power series fit or a linear relation as the correlation coefficient (r^2) is close to 1 for both of them. It can therefore be said that the SFDL value scales evenly when computed from either the yCDF or the SCDF value when the damaged area does not enclose any measurement locations. It appears as if there is no difference in computing the SFDL value from either the yCDF or the SCDF value when the damage is located close to the measurement locations without including such a measurement location.

C.2 Deterministic case 2

The same comparison of the SFDL value computed from the SCDF and yCDF is made in Figure C-2 for the second deterministic case. In case 1 (Figure C-1) this plot showed a linear relationship. It is interesting to note that in this case there is a non-linear relationship, which appears to be close to a quadratic polynomial fit. This can perhaps be attributed to the strain measured within the damage location. The strain value starts decreasing very rapidly as the level of damage increases due to the reduction in load carrying capability. The SCDF is divided by this rapidly decreasing strain value, which leads to the SFDL value, calculated from the SCDF, to have a non-linear relationship to the SFDL value calculated from the yCDF which is effectively divided by 1.

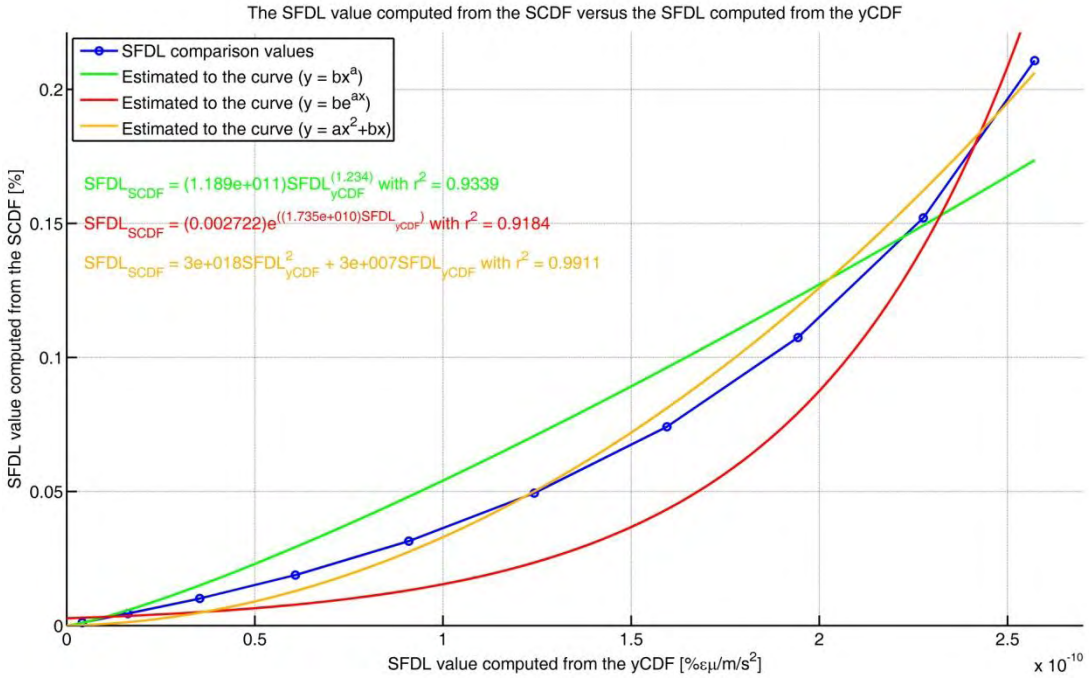

Figure C-2: Curve fits to the comparison between the SFDL values computed from the SCDF and the yCDF values for case 2

When the two cases are compared by comparing the change in the SFDL value as the damage level is increased, it can be seen that for case 1 the SFDL value scales linearly in comparison with the SFDL value computed from the yCDF value whereas the SFDL value for case 2 scales as a quadratic polynomial. The calculation of the SFDL values from the SCDF value is preferred as it scales faster when the damaged area encloses one or more measurement locations.

Appendix D: Method applied to other wing-like structures in the family of wings

The family of wings was introduced in paragraph 2.1.2. The method was developed for a complete family of wings, but a detailed numerical and experimental study was performed on only one family member. This appendix serves as a justification in the use of a family of wings. The method is applied to two other family members to verify whether the method is valid for other family members. The results of these cases are shown, without any further discussion.

D.1 Neptune wing

The first family member that is investigated is the Neptune wing (Figure 2-4). The parameters defining the geometry of the Neptune wing is given in Table 2-4 and the normalised values used in the FE model are summarised in Table D-1. The excitation and acceleration measurement position are summarised in Table D-2 with the strain measurement positions shown in Figure D-1 and Figure D-5. The damping value used to perform the simulation is equal to 0.2% of critical damping. The first 10 natural frequencies together with the type of mode shape obtained for the Neptune wing are given in Table D-3.

The geometry of the Neptune wing poses other challenges than the Predator wing, in the sense that the natural frequencies of different types of modes lie closer to one another. During the simulations difficulty was experienced when all 10 modes are included in the calculation. It was suspected that natural frequency crossovers occurred and results from different modes were compared to one another. For this reason only modes 1, 2 and 5 were included in the subsequent analysis and investigation. Since the geometry of the wing is larger in width, than the Predator wing, two damage cases are investigated. In the first case the damage is close to the measurement positions. In the second case the damage is located further from the measurement positions and is much smaller.

Table D-1: Parameters defining the Neptune wing geometry

Parameter	Original value	Normalised value
Wing span (b) [m]	2.13	1
Length of fuselage (l_f) [m]	0.604	0.28357
Sweep angle (Λ_{LE}) [°]	32	32
Chord at root (c_r) [m]	0.774	0.36338
Chord at tip (c_t) [m]	0.339	0.15915

Table D-2: Excitation and acceleration position used in FE model of the Neptune wing

Position name	x-coordinate [m]	y-coordinate [m]	FE node
Excitation	-0.123	-0.329	5037
Acceleration	-0.487	-0.237	7995

Table D-3: Type of mode shapes for the undamaged Neptune wing

Mode number	Frequency [Hz]	Type
1	66.598	VB
2	122.05	T
3	178.58	VB
4	234.35	VB
5	323.4	VB
6	362.61	T
7	503.33	VB – Upwards
8	514.42	VB
9	542.32	T
10	687.67	T

D.1.1 Deterministic damage case 1

The damage size and location is shown in Figure D-1 with the parameters defining this damage case summarised in Table D-4. The results obtained for the SCDF and SFDL values as the damage level is increased are shown in Figure D-2 to Figure D-4. It is clear that the presence of damage and the location can be established from the SCDF and SFDL values. The same type of scaling with respect to the damage level and average difference in natural frequency that was observed in the numerical study of chapter 3 is observed from the results.

Table D-4: Parameter values defining the damaged area for case 1 of the Neptune wing

Parameter	Value
l_{di}	186.165 mm
h_{di}	133.061 mm
l_d	100.716 mm
h_{dr}	63.643 mm
h_{dt}	52.830 mm
Λ_{LE}	24.071°
A_d	5.865×10^{-3} m^2
Ratio of damaged area to the area of right wing section	6.267%
Ratio of damaged area to the area of the complete wing	2.021%

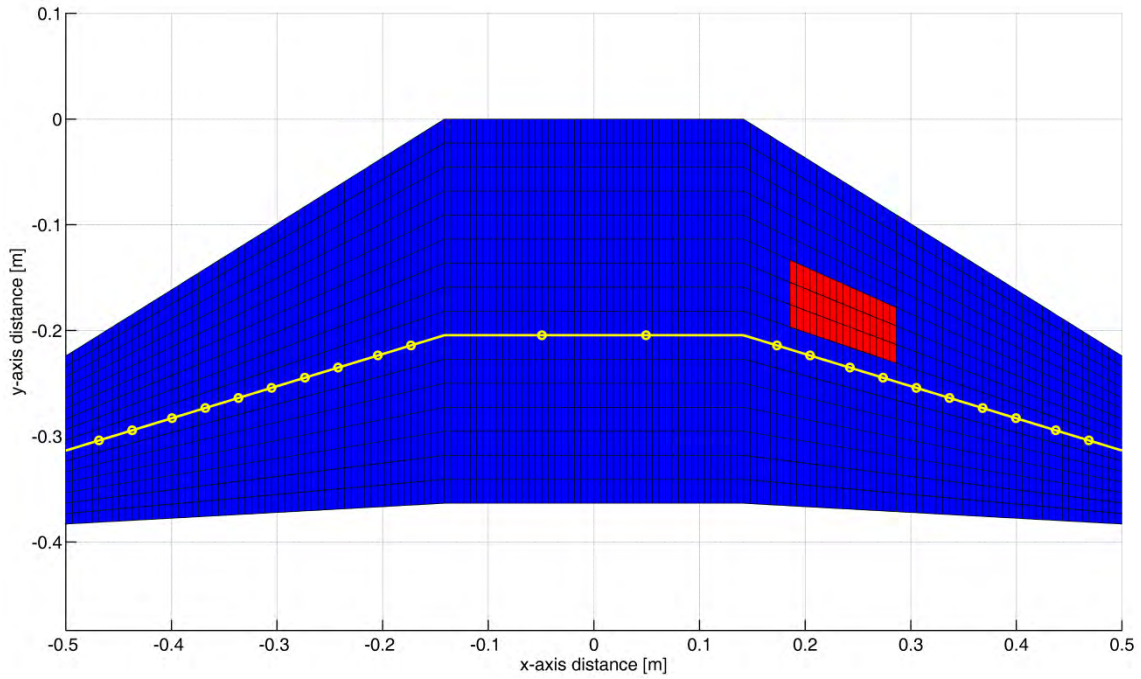

Figure D-1: Damage location with measurement locations for deterministic damage case 1 of the Neptune wing

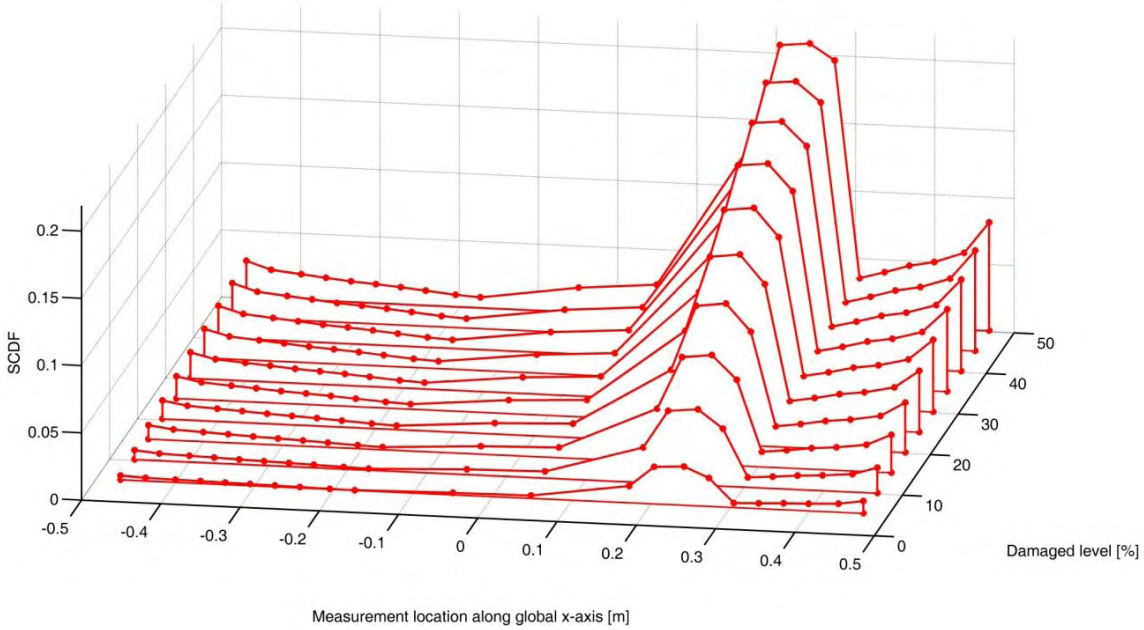

Figure D-2: Variation of the SCDF values, when 3 modes are included in the calculation, as the damage level is increased for case 1 of the Neptune wing

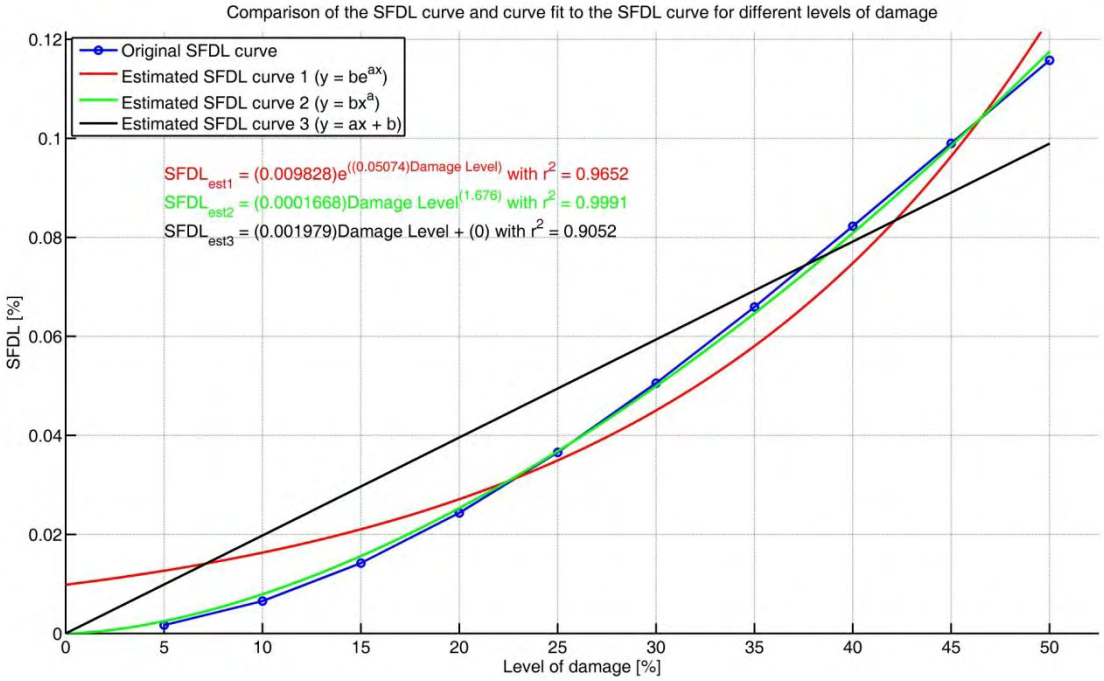

Figure D-3: Curve fits for the SFDL value compared to the level of damage for case 1 of the Neptune wing

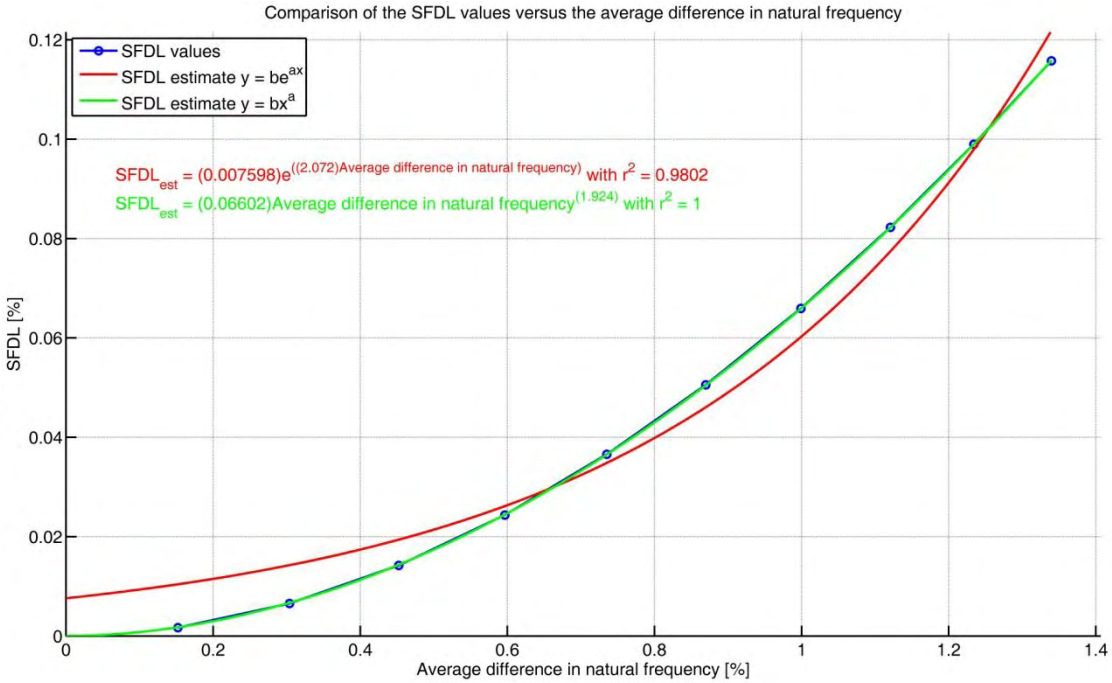

Figure D-4: Curve fits showing the relation between the SFDL value and the average difference in natural frequency for case 1 of the Neptune wing

D.1.2 Deterministic damage case 2

The damage size and location is shown in Figure D-5 with the parameters defining this damage case summarised in Table D-5. The results obtained for the SCDF and SFDL values as the damage level is increased are shown in Figure D-6 to Figure D-8. It is clear

that the presence of damage and the location can be established from the SCDF and SFDL values. The same type of scaling with respect to the damage level and average difference in natural frequency that was observed in the numerical study of chapter 3 is observed from the results.

Table D-5: Parameter values defining the damaged area for case 2 of the Neptune wing

Parameter	Value
l_{di}	149.065 mm
h_{di}	26.506 mm
l_d	49.516 mm
h_{dr}	44.635 mm
h_{dt}	41.845 mm
Λ_{LE}	30.508°
A_d	2.141×10^{-3} m^2
Ratio of damaged area to the area of right wing section	2.288%
Ratio of damaged area to the area of the complete wing	0.738%

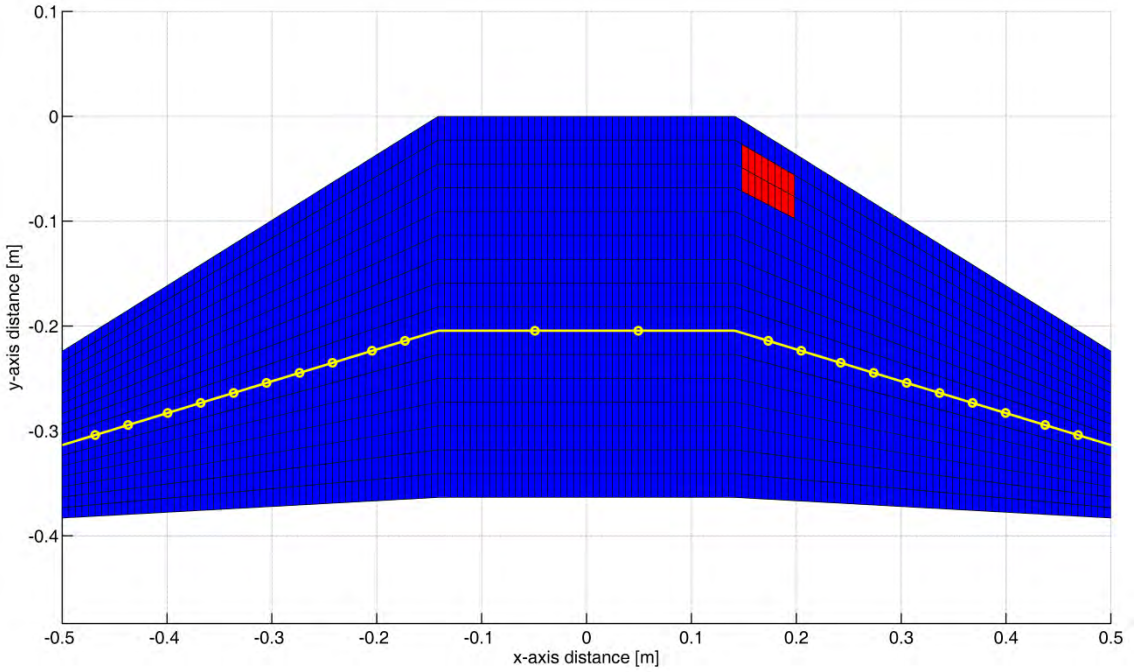

Figure D-5: Damage location with measurement locations for deterministic damage case 2 of the Neptune wing

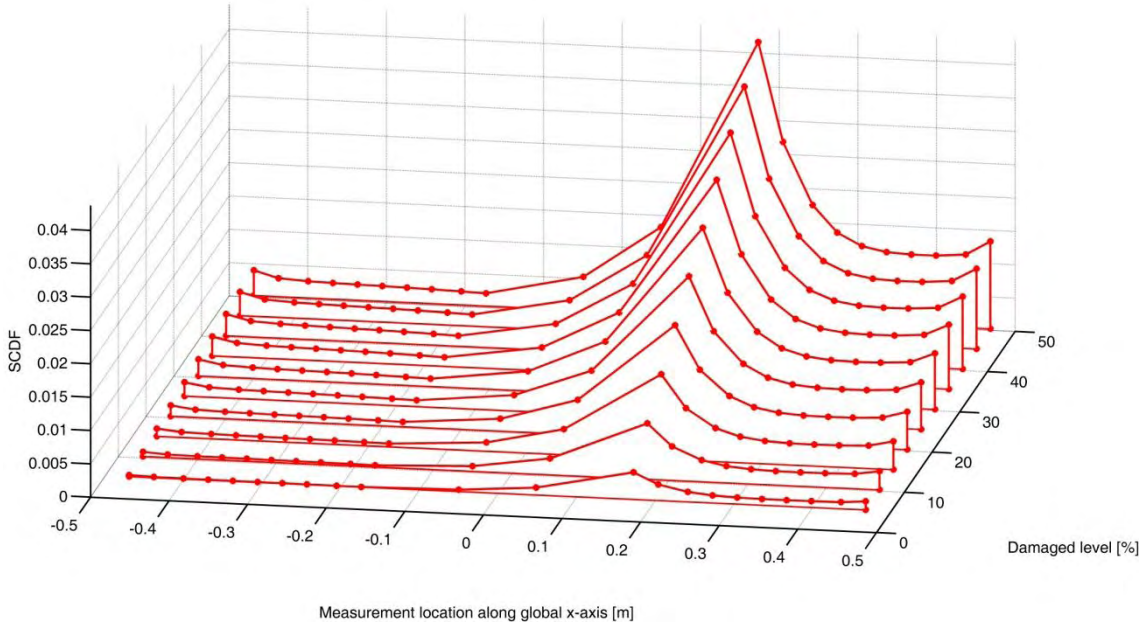

Figure D-6: Variation of the SCDF values, when 3 modes are included in the calculation, as the damage level is increased for case 2 of the Neptune wing

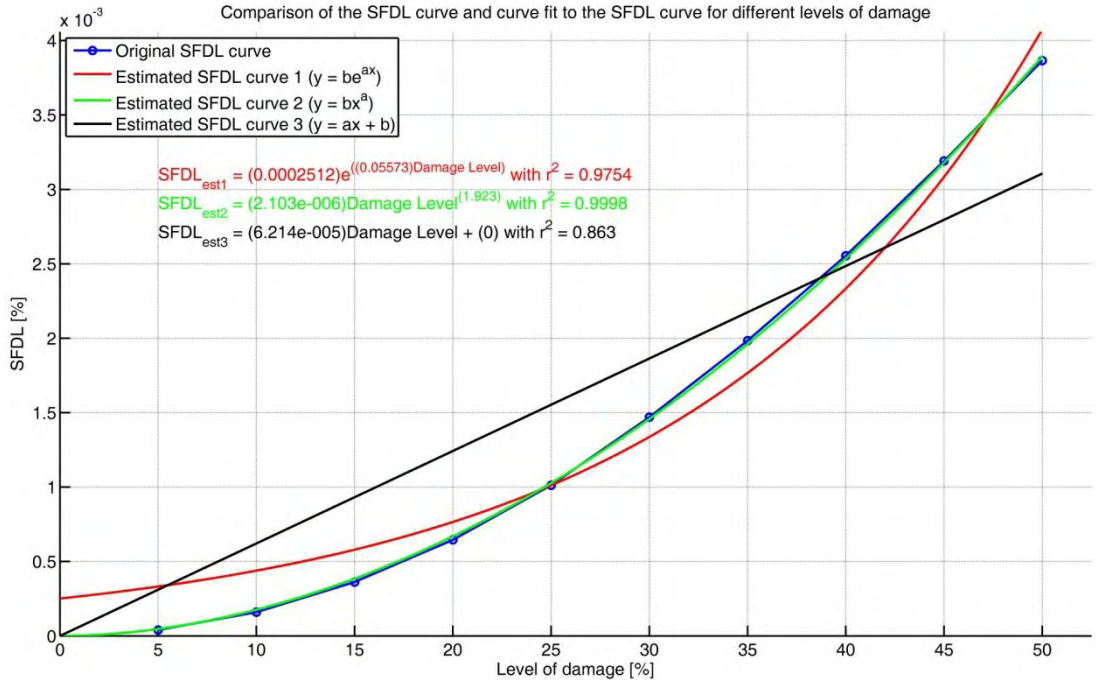

Figure D-7: Curve fits for the SFDL value compared to the level of damage for case 2 of the Neptune wing

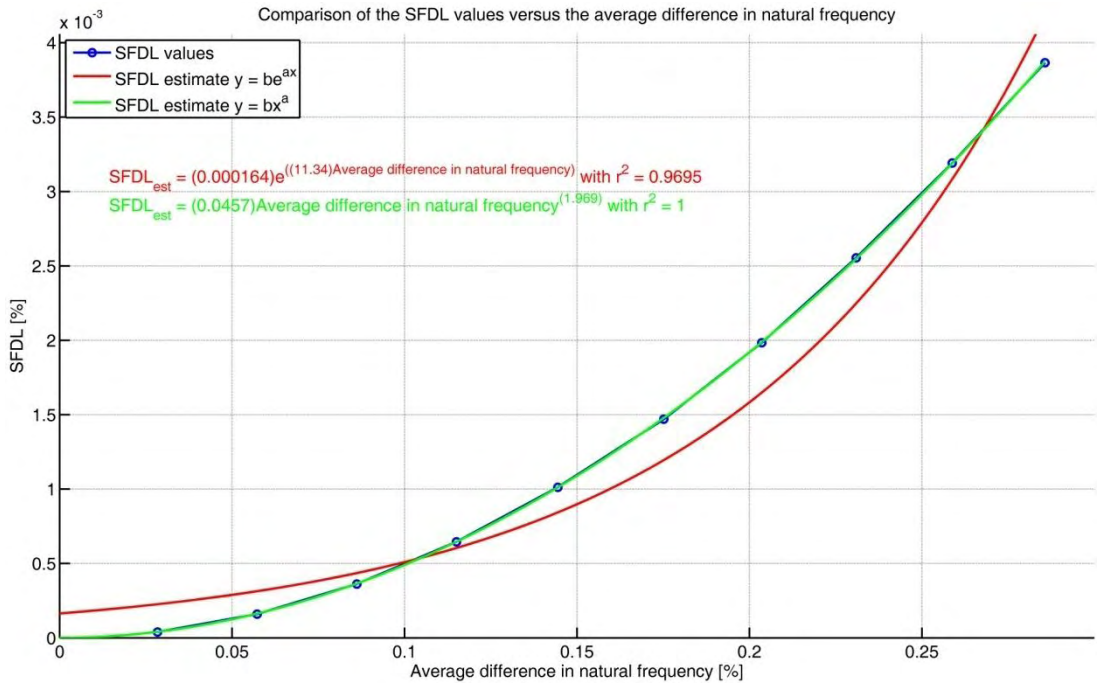

Figure D-8: Curve fits showing the relation between the SFDL value and the average difference in natural frequency for case 2 of the Neptune wing

D.2 Global Hawk wing

The second family member that is investigated is the Global Hawk wing (Figure 2-4). The parameters defining the geometry of the Global Hawk wing is given in Table 2-4 and the normalised values used in the FE model are summarised in Table D-6. The excitation and acceleration measurement positions are summarised in Table D-7 with the strain measurement positions shown in Figure D-9. The damping value used to perform the simulation is equal to 0.2% of critical damping. The first 11 natural frequencies together with the type of mode shape obtained for the Global Hawk wing are given in Table D-8.

The Global Hawk wing is similar to the Predator wing and during the analysis all the vertical bending modes and torsional modes up to mode 11 were included. The in-plane bending modes are ignored due to the fact that they would not have been measurable during an experimental analysis.

The damage size and location is shown in Figure D-9 with the parameters defining this damage case summarised in Table D-9. The results obtained for the SCDF and SFDL values as the damage level is increased are shown in Figure D-10 to Figure D-12. It is clear that the presence of damage and the location can be established from the SCDF and SFDL values. The same type of scaling with respect to the damage level and average difference in natural frequency that was observed in the numerical study of chapter 3 is apparent from the results.

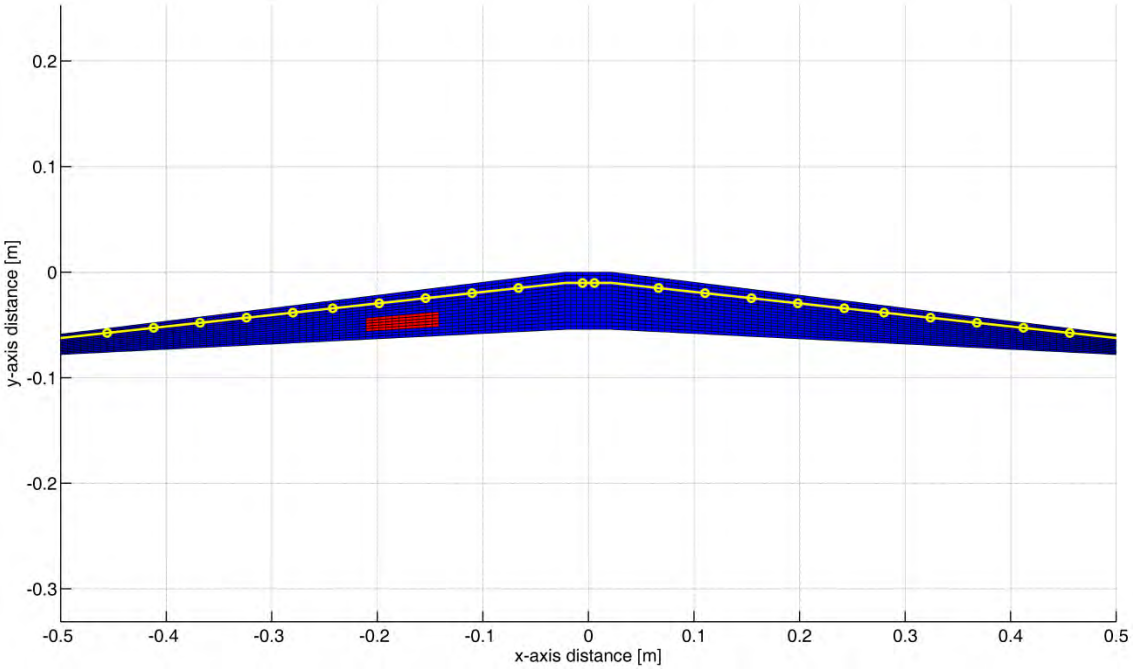

Figure D-9: Damage location with measurement locations for damage to the Global Hawk wing

Table D-6: Parameters defining the Global Hawk wing geometry

Parameter	Original value	Normalised value
Wing span (b) $[m]$	35.42	1
Length of fuselage (l_f) $[m]$	1.579	0.04458
Sweep angle (Λ_{LE}) [°]	7	7
Chord at root (c_r) $[m]$	1.922	0.05426
Chord at tip (c_t) $[m]$	0.687	0.01940

Table D-7: Excitation and acceleration position used in FE model of the Global Hawk wing

Position name	x-coordinate $[m]$	y-coordinate $[m]$	FE node
Excitation	-0.0167	-0.0492	4187
Acceleration	-0.493	-0.0604	8045

Table D-8: Type of mode shapes for the undamaged Global Hawk wing

Mode number	Frequency $[Hz]$	Type
1	88.224	VB
2	158.86	VB
3	285.28	IPB
4	305.42	VB
5	486.33	VB
6	599.88	IPB
7	720.94	VB
8	995.29	VB
9	1093.90	T
10	1096.10	IPB
11	1320.10	VB

Table D-9: Parameter values defining the damaged area for the Global Hawk

Parameter	Value
l_{di}	-141.436 mm
h_{di}	37.357 mm
l_d	-69.140 mm
h_{dr}	14.475 mm
h_{dt}	12.629 mm
Λ_{LE}	4.9318°
A_d	0.937×10^{-3} m^2
Ratio of damaged area to the area of right wing section	5.325%
Ratio of damaged area to the area of the complete wing	2.491%

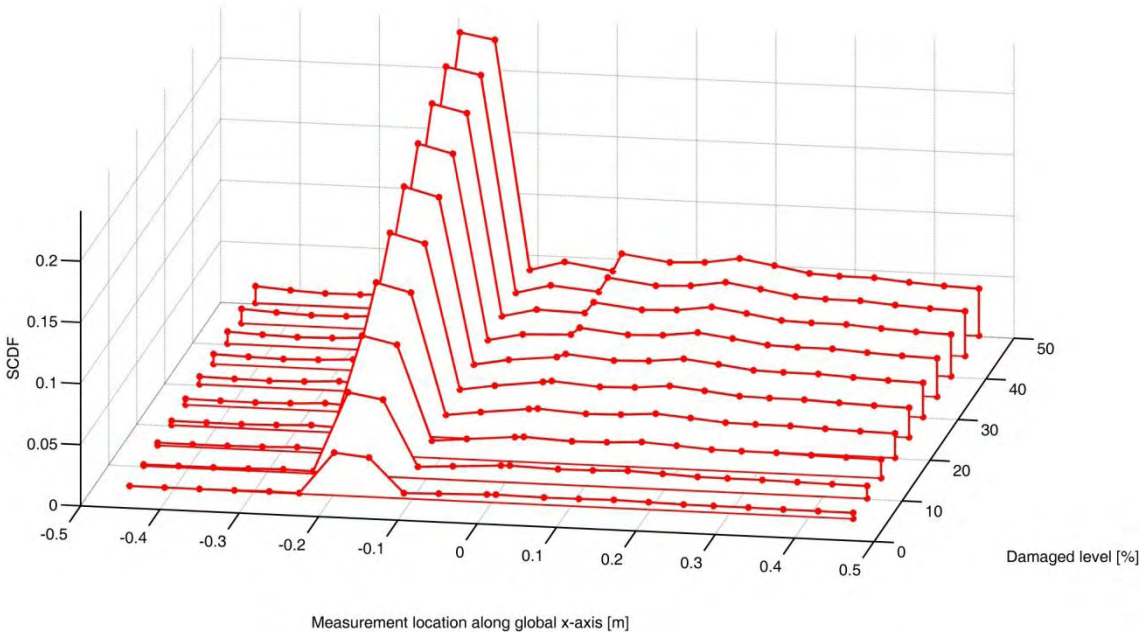

Figure D-10: Variation of the SCDF values, when 8 modes are included in the calculation, as the damage level is increased for the Global Hawk wing

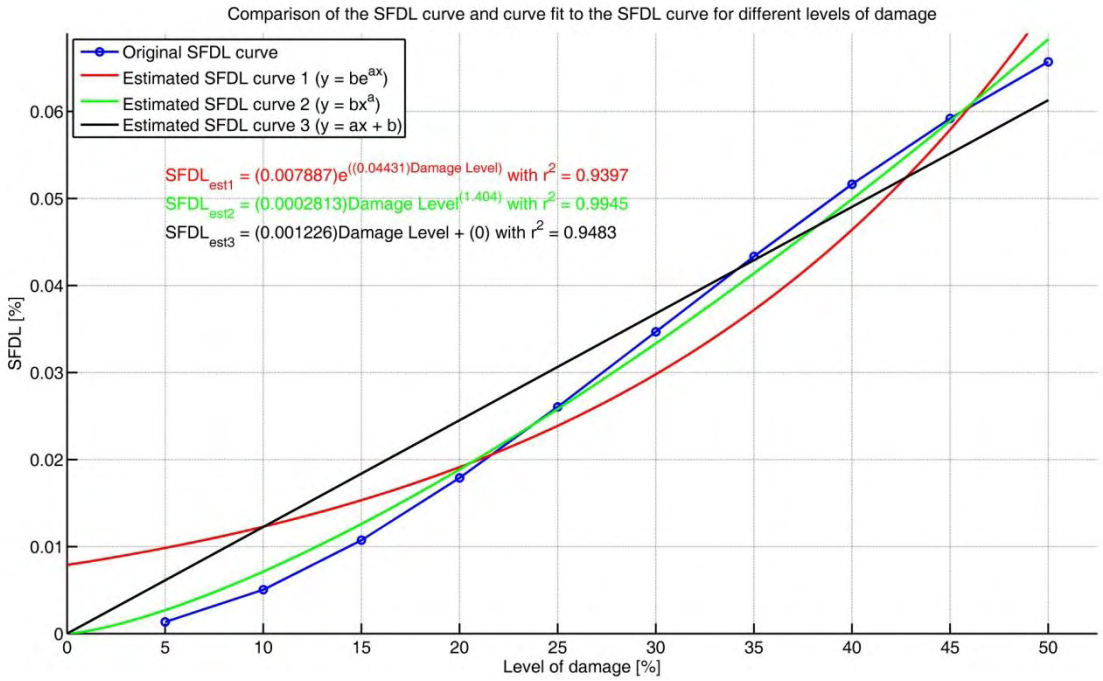

Figure D-11: Curve fits for the SFDL value compared to the level of damage for the Global Hawk wing

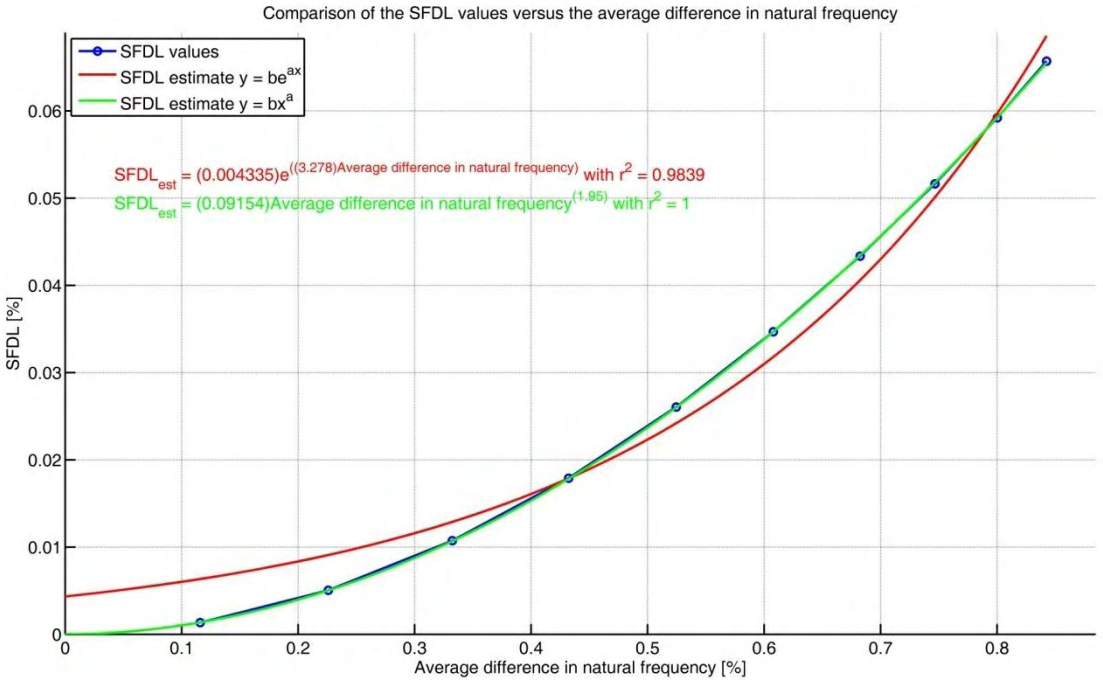

Figure D-12: Curve fits showing the relation between the SFDL value and the average difference in natural frequency for the Global Hawk wing